INELASTIC DYNAMIC BEHAVIOR AND DESIGN OF HYBRID COUPLED WALL SYSTEMS

by

MOHAMED HASSAN
M.S. Alexandria University, Egypt, 1998

A dissertation submitted in partial fulfillment of the requirements
for the degree of Doctor of Philosophy
in the Department of Civil and Environmental Engineering
in the College of Engineering and Computer Science
at the University of Central Florida
Orlando, Florida

Spring Term

2004

ABSTRACT

A key consideration in seismic design of buildings is to ensure that the lateral load resisting system has an appropriate combination of strength, stiffness and energy dissipation capacity. Hybrid coupled wall systems, in which steel beams are used to couple two or more reinforced concrete shear walls in series, can be designed to have these attributes and therefore have the potential to deliver good performance under severe seismic loading. This research presents an investigation of the seismic behavior of this type of structural system.

System response of 12- and 18-story high prototypes is studied using transient finite element analyses that accounts for the most important aspects of material nonlinear behavior including concrete cracking, tension stiffening, and compressive behavior for both confined and unconfined concrete as well as steel yielding. The developed finite element models are calibrated using more detailed models developed in previous research and are validated through numerous comparisons with test results of reinforced concrete walls and wall-beam subassemblages.

Suites of transient inelastic analyses are conducted to investigate pertinent parameters including hazard level, earthquake record scaling, dynamic base shear magnification, interstory drift, shear distortion, coupling beam plastic rotation, and wall rotation. Different performance measures are proposed to judge and compare the behavior of the various systems. The analyses show that, in general, hybrid coupled walls are particularly well suited for use in regions of high seismic risk.

The results of the dynamic analyses are used to judge the validity of and to refine a previously proposed design method based on the capacity design concept and the assumption of

behavior dominated by the first vibration mode. The adequacy of design based on the pushover analysis procedure as promoted in FEMA-356 (2000) is also investigated using the dynamic analysis results. Substantial discrepancies between both methods are observed, especially in the case of the 18-story system. A critical assessment of dynamic base shear magnification is also conducted, and a new method for estimating its effects is suggested. The method is based on a modal combination procedure that accounts for presence of a plastic hinge at the wall base. Finally, the validity of limitations in FEMA-368 (2000) on building height, particularly for hybrid coupled wall systems, is discussed.

ACKNOWLEDGEMENTS

I would like to express my deepest gratitude to my academic advisor, Dr. Sherif El-Tawil, for his guidance, encouragement and moral during the course of this research. Despite his overwhelming responsibilities, Dr. El-Tawil has dedicated a great deal of his precious time to guide me towards completion of this research. Truly, without him, this work would not have been possible.

Special thanks are due to Dr. Manoj Chopra who accepted to serve as my co-advisor. Dr. Chopra sincerely offered critical support to help completing the requirements of my degree.

This research was conducted under Project No. CMS 9870927 and many thanks are due to the U.S. National Science Foundation for their continued sponsorship over the past several years. They provided the means to accomplish this research effort.

The financial support from the Department of Civil& Environmental Engineering is sincerely appreciated.

I would like to thank Dr. David Nicholson, Dr. Okey Onyemelukwe and Dr. Ashraf El-Bahy who accepted to serve in my dissertation committee and helping me whenever the need arose.

Special thanks are due to Dr. Essam Radwan, Dr. Ayman Okeil and Dr. Hesham Mahgoub for their support and friendly advise.

t*o the soul of my father*

to my mother

to Sarah

TABLE OF CONTENTS

LIST OF TABLES xiv

LIST OF FIGURES xvi

CHAPTER 1: INTRODUCTION 1

1.1 Objective 4

1.2 Scope of Work 4

CHAPTER 2: LITERATURE REVIEW 6

2.1 Analysis Methods for Coupled walls Structures 6

2.1.1 Continuous Medium Method 6

2.1.2 Equivalent Frame Method 8

2.1.3 Analogue Truss Model 10

2.1.4 Macro Element Models 13

2.1.4.2 Nonlinear Parameter Estimation 16

2.1.5 Finite Element Method 19

2.2. Current Engineering Practice for Composite Coupled Walls 19

2.3 Experimental Studies Conducted on Coupling Beams 23

2.3.1 Steel Coupling Beams 23

2.3.1.1 Shahrooz et al, 1993 23

2.3.1.2 Harries et. al., 1993 26

2.3.2 Composite Coupling Beams 30

2.3.2.1 Gong and Shahrooz, 1998 30
2.4 Connections between Steel Beams and Reinforced Concrete walls 32
2.4.1 Steel Beams attached to steel plates embedded in Reinforced Concrete Walls 32
2.4.2 Steel Beams Embedded into Reinforced Concrete Columns or Walls 33
2.5 Experimental Investigations on Reinforced Concrete Shear Walls 33
2.5.1 Walls Tested by the Portland Cement Association 34
2.5.2 Experimental Studies Conducted at the University of California, Berkeley 36
2.5.3 Experimental Studies Conducted in Japan 39
2.5.3.1 Other Shear Wall Test Programs Conducted in Japan 42
2.5.4 Test Programs Performed in the United Kingdom 43
2.5.5 Test programs performed in Mexico 45
2.6 Summary 45
CHAPTER 3: SYSTEM DESIGN ISSUES 47
3.1 The Coupling Ratio – *CR* 47
3.2 Description of Prototypes 50
3.3 Summary of Previous Research by El-Tawil et al (2002) and Kuenzli (2001) 51
3.3.1 Economy of Coupled Systems 51
3.3.2 12-Story System Performance 52
3.3.3 6-Story System Performance 53
3.4 Choice of Building Height and Prototype Naming Convention 54
3.5 Analysis of the system for Design Purposes 55
3.5.1 Seismic Design Criteria 55
3.5.2 Analysis Procedures 57

3.5.2.1 Equivalent Lateral Force Procedure: *ELFP* 58
3.5.2.2 Modal Analysis Procedures: *MAP* 62
3.5.3 Longitudinal Design Analysis 64
3.5.4 Transverse Design Analysis 69
3.6 Design of the Coupling Beam 70
3.7 Shear Wall Design 73
3.7.1 Design for Shear Force 73
3.7.2 Check for maximum drifts 76
3.7.3 Design for flexure and axial force 79
3.7.4 Check for transverse reinforcement at the boundary regions 80
3.8 Summary 85
CHAPTER 4: Finite Element modeling and Constitutive Formulation 86
4.1 Finite Element Modeling 86
4.1.1 Modeling of Shear Wall 87
4.1.2 Modeling of Reinforcing Steel 90
4.1.3 Modeling of the Coupling Beam 91
4.2 Constitutive Model for Reinforced Concrete 94
4.2.1 Crack Modeling 95
4.2.1.1 Crack Representation 96
4.2.1.2 Crack Initiation and Propagation 98
4.2.1.3 Constitutive Formulation for Cracked Concrete 99
4.2.1.4 Crack Orientation 100
4.2.1.4.1 Fixed Crack Model 101

4.2.1.4.2 Rotating Crack Model 102
4.2.1.4.3 Non-Orthogonal Multi Crack Model 103
4.2.1.5 Proposed Crack Model 104
4.2.1.6 Normal Stress-Strain Relationship 104
4.2.1.6.1 Effect of Tension Stiffening 106
4.2.1.6.2 Crack Initiation, Closing and Reopening 107
4.2.1.6.3 Compression Behavior 110
4.2.1.6.4 Stress-Strain Relationship for Unconfined Concrete 112
4.2.1.6.5 Stress-Strain Relationship for Confined Concrete 113
4.2.1.6.6 Determination of the Confinement parameters 114
4.2.1.6.7 Degradation of Concrete under Cyclic Loading 119
4.2.1.7 Shear Stiffness Relationship 121
4.2.1.8 Separation of Shear Strain 123
4.3 Constitutive Model for Reinforcing and Structural Steel 125
4.4 Incremental –Iterative Procedure 128
4.4.1 Convergence Criteria 130
4.4.2 Solution Algorithm 131
4.5 Verification Study 133
4.5.1 PCA Wall Tests 133
4.5.1.1 Evaluation of the Analytical results 138
4.5.1.1.1 Load-Deflection Plots 139
4.5.1.1.2 Average Shear Strains 143
4.5.1.1.3 Failure Modes 143

4.6 Summary 148
CHAPTER 5: TENSION FLANGE EFFECTIVE WIDTH IN RC SHEAR WALLS 149
5.1 Effective Width Concept 149
5.1.1 Summary of Previous Research 151
5.1.2 ACI 318-2002 Provisions 152
5.2 Parametric Study 154
5.3 Finite Element Modeling 155
5.4 Verification of the model using Flanged Walls in Wallace (1996) 156
5.5 Analysis Results 157
5.5.1 Elastic Results 159
5.5.2 Inelastic Results 160
5.6 Design Implications and Recommendations 164
5.7 Impact of Analysis Results on HCW Modeling 166
5.8 Summary 167
CHAPTER 6: ANALYSIS RESULTS 169
6.1 Parametric Study 169
6.2 Performance Level 170
6.3 Level of Seismic Hazard 171
6.4 Performance Objective 172
6.5 Ground Motions Used 173
6.5.1 Strong Motion Duration 176
6.5.2 Scaling of Records 177
6.6 Finite Element Modeling 183

6.1.1 Gravity Loads 188
6.1.2 Floor Masses 188
6.1.3 Damping 188
6.1.4 Direct Time Integration 189
6.7 Analysis Results 191
6.7.1 Scaled vs. Unscaled Ground Motions 192
6.7.1.1 Results for HCW-12-30 193
6.7.1.2 Results for HCW-18-30 194
6.7.2 Maximum Roof Displacement 197
6.7.2.1 Results for HCW-12-30 and HCW-12-U 198
6.7.2.2 Roof Displacement Results for HCW-18-30 201
6.7.2.3 Deflection Amplification Factor 202
6.7.3 Base Shear Magnification 203
6.7.3.1 Results for HCW-12-30 and HCW-12-U 204
6.7.3.2 Base Shear Results for HCW-18-30 208
6.7.4 Concrete Crushing at Base 211
6.4.1.1 Results for HCW-12-30 and HCW-12-U 211
6.7.4.2 Results for HCW-18-30 212
6.7.5 Interstory Drift 212
6.7.5.1 Results for HCW-12-30 and HCW-12-U 212
6.7.5.2 Results for HCW-18-30 213
6.7.5.3 Comment on the Drifts as a Performance Measure 214
6.7.6 Shear Deformation 216

6.7.6.1 Results for HCW-12-30 and HCW-12-U 217
6.7.6.2 Results for HCW-18-30 218
6.7.7 Wall Rotations 220
6.7.7.1 Results for HCW-12-30 and HCW-12-U 221
6.7.7.2 Results for HCW-18-30 222
6.7.8 Coupling Beam Rotation 227
6.7.8.1 Results for HCW-12-30 and HCW-12-U 227
6.7.8.2 Results for HCW-18-30 228
6.7.9 Stiff Behavior of HCW-18-30 232
6.7.10 Deformed Shape 235
6.7.11 Crack Patterns 236
6.8 Rational Method for Computing Shear Magnification Factor 239
6.9 Limitation of FEMA-368 on Building Height 243
6.10 Evaluation of the Capacity Design Method 244
6.11 Summary 245
CHAPTER 7: SUMMARY, CONCLUSIONS and Recommendation for Future Work 247
7.1 Summary 247
7.2 Conclusions 249
7.2.1 Finite Element Analysis and Constitutive Modeling 249
7.2.2 Effective Width of Tension Flanges 250
7.2.3 Inelastic Behavior of HCW Systems 251
7.3 Recommendation for Future Work 253
APPENDIX A: PCA WALLS: TEST RESULTS vs. ANALYTICAL RESULTS 255

APPENDIX B: SELECTED OUTPUT FROM TIME HISTORY ANALYSIS 262

LIST OF REFERENCES 289

LIST OF TABLES

Table 3.1: Lateral Forces at Floor Levels According to FEMA-368.....61

Table 3.2 Modal Contribution Factors to Base Shear for a Cantilever with Different base Conditions.....73

Table 4.1 Properties of PCA Wall Specimens.....135

Table 4.2 Failure Modes: Experimental vs. Analytical.....144

Table 4.2 Failure Modes Comparison (Continued).....145

Table 5.1 Model Designations for the Parametric Study.....155

Table 5.2 Effective Width for the 6-Story Wall.....163

Table 5.3 Effective Width for the 12-Story Wall.....164

Table 6.1 Original SAC Record for 2/50 Ground Motions.....175

Table 6.2 Original SAC Record for 50/50 Ground Motions.....175

Table 6.3 Original and Scaled PGA's in g for the 2 /50 Records For 12-Story Systems.....181

Table 6.4 Original and Scaled PGA's in g for the 50 /50 Records For 12-Story Systems.....181

Table 6.5 Original and Scaled PGA's in g for the 2% /50 Records For 18-Story System.....182

Table 6.6 Original and Scaled PGA's in g for the 50% /50 Records For 18-Story System.....182

Table 6.7 Original and Scaled PGA's in g for the 2% /50 Records For 18-Story System (Scaled at a fundamental period of the inelastic system).....183

Table 6.8 Summary of all Performed Nonlinear Time History Analyses.....192

Table 6.9 Base Shear for All Analyses in kips.....204

Table 6.10 Comparison with FEMA-356 Wall Rotation Limits at the collapse prevention limit225

Table 6.11 Modal Combinations for Base Shear in HCW-18-30 system softened at the base.....241

Table 6.12 Modal Combinations for Base Shear in HCW-12-30 system softened at the base.....242

Table 6.13 Modal Combinations for Base Shear in HCW-12-U system softened at the base.....242

LIST OF FIGURES

Figure 2.1 Continuous Medium Model of Coupled Walls 7

Figure 2.2 Equivalent Fram model of Coupled Walls 10

Figure 2.3 Truss Model for Shear Walls.....11

Figure 2.4 Original Macro Model by Kabeyasawa 1992.....13

Figure 2.5 Multi-Component Wall Models 15

Figure 2.6 Nonlinear Flexural Behavior of Wall Cross Section.....17

Figure 2.7 Boundary element elongation over first story versus base shear 18

(ACI 1984).....18

Figure 2.8 Simplified hysteretic model for outer springs (Linde 1993) 19

Figure 2.9 RC Wall-Steel Beam Connection for Low Rise Buildings (Gong and Shahrooz, 1998)21

Figure 2.10 A Typical Steel Coupling Beam RC Wall Connection for Mid-Rise Buildings

(Courtesy of Kramer Gehlen Associates Inc. (Gong and Shahrooz, 1998)) Associates Inc. 22

Figure 2.11 Wall Steel Coupling Beam Connection With Steel Boundary Column for High-Rise

Buildings (Gong and Shahrooz, 1998).....23

Figure 2.12a Displacement History (Shahrooz et. al 1993).....24

Figure 2.12.b Moment Curvature Hysteretic for Wall No. 1 (Shahrooz et. al 1993) 25

Figure 2.13 Coupled Wall Segment Tested by Harries et al. (1993).....28

Figure 2.14 Segment Test Setup (Harries et al., 1993).....28

Figure 2.15 Energy Dissipation in Steel Beams Tested by Harries et al. (1993) 29

Figure 2.16 Test Setup (Gong and Shahrooz 1998).....31
Figure 2.17 Experimental Setup for Tests Conducted by Aktan and Bertero (1984).....39
Figure 2.18 Layout of the Seven-Story Building Tested by Okamoto et al 1985 41
Figure 3.1 Comparison between (a) isolated and (b) coupled shear walls. 48
Figure 3.2 Plan View of Theme Structure 4 51
Figure 3.3 Concrete and Steel Weights vs. Coupling Ratio, Kuenzli (2001) 52
Figure 3.4 12-Story System Target Displacement and Base Shear vs. Coupling Ratio Kuenzli (2001).....53
Figure 3.5 6-Story System Target Displacement and Base Shear vs. Coupling Ratio Kuenzli (2001).....54
Figure 3.6 Design Response Spectrum 56
Figure 3.7 Lateral Force Distribution at Story Levels in 12-story Building.....60
According to FEMA-368 60
Figure 3.8 Lateral Force Distribution of Linear Static Procedure and Linear Dynamic Procedure in HCW-18-30 63
Figure 3.9 Shear Force Distribution of Linear Static Procedure and Linear Dynamic Procedure in HCW-18-30.....63
Figure 3.10 Longitudinal Elastic Model 67
Figure 3.11 Coupling Beam, Forces and Dimensions 72
Figure 3.12 Mode Shapes 75
Figure 3.13 Design Moment Envelope 79
Figure 3.14 Interaction Curve for the Wall Cross Section.....80
Figure 3.15 Reinforcement layout of the Shear Walls.....82

Figure 3.16 LSW&RSW Designs 83
Figure 3.17 MSW Designs 84
Figure 4.1 Element Connectivity and Natural Coordinate System 87
Figure 4.2 Representation of Steel Reinforcement 90
Figure 4.3 4-Node Beam Element 92
Figure 4.4 Integration Scheme for the Beam Element 93
Figure 4.5 One-Directional Crack 98
Figure 4.6 Tension Stiffening Model 107
Figure 4.7 Stress vs. Strain (Stevens et. al., 1987) 108
Figure 4.8 Rule for Crack Closing 109
Figure 4.9 Rule for Crack Reopening 110
Figure 4.10 Arbitrary Loading-Unloading Sequence 110
Figure 4.11Thorenfeldt Compression Curve 111
Figure 4.12 Confined Concrete Model 112
Figure 4.13 Confinement Due to Hoop and Cross Tie Reinforcement 115
Figure 4.14 Confined Concrete Strength as a Function of Confining Pressures 118
(Mander et al., 1988) 118
Figure 4.15 Typical Cyclic Stress-Strain Relationship (Sittipunt, 1995) 120
Figure 4.16 Rules For Unloading and Reloading 121
Figure 4.17 Shear Stiffness vs. Crack Normal Strain 122
Figure 4.18 Shear Strain Separation (Sittipunt 1995) 125
Figure 4.19 Kinematic Hardening Model For Reinforcing Steel 126
Figure 4.20 Kinematic Hardening vs. Isotropic Hardening in Principal Stress Space 127

Figure 4.21 Cyclic Stress-Strain Curve (Brown, 1998) 127
Figure 4.22 Energy Norm Convergence Criteria 131
Figure 4.23 Newton-Raphson Algorithm 132
Figure 4.24 Tangent Stiffness vs. Secant Stiffness on the Element Level 133
Figure 4.25 Dimensions for Walls B1-B5 134
Figure 4.26 Typical Reinforcement Details for Dimensions for PCA Walls 135
Figure 4.27 Static Cyclic Loading for Walls B1, B2, B3, and B5 (Oesterle et al., 1976) 137
Figure 4.28 Finite Element Mesh for the PCA Walls 137
Figure 4.29 Determination of Shear Strains 139
Figure 4.30 Load vs. Displacement Comparison for Wall B1 141
Figure 4.31 Load vs. Displacement Comparison for Wall B2 142
Figure 4.32 Load vs. Shear Distortion Comparison for Wall B1 146
Figure 3.33 Load vs. Shear Distortion Comparison for Wall B2 147
Figure 5.1 Symmetric simply supported beams represented by two cantilevers 154
Figure 5.2 Deformed FE meshes. Walls pushed to 2% drift. 156
Figure 5.3 Cross Section and Mesh Layout for Wallace (1996) wall 158
Figure 5.4 Load vs. Top Displacement 158
Figure 5.5 Measured and computed tension flange strain profile for specimen TW2 159
Figure 5.6 Elastic stress distribution in tension flange 161
Figure 5.7 Steel tensile stresses along flange of 12-story wall with 30 ft flange. 162
Figure 5.8 Effective Width vs. Drift Ratio and Level of Axial Load 168
Figure 6.1 Strong Motion Duration 177

Figure 6.2 Elastic Response Spectra (5% damped) Scaled to median spectral Acceleration at The fundamental Period of the 12-Story System 179
Figure 6.3 Refined and coarse finite element meshes (deformed).....185
Figure 6.4 Contact Element in the Connection.....186
Figure 6.5 Base shear versus roof displacement for refined and coarse models 187
Figure 6.6 Lumped Masses and Dashpot Dampers 189
Figure 6.7 Wilson-θ Scheme of Time Integration 191
Figure 6.8 Maximum Roof Displacement in HCW-12-30 for Scaled and Unscaled Records for 2/50 records.....194
Figure 6.9 Maximum Base Shear in HCW-12-30 for scaled and unscaled ground motions for 2/50 records.....195
Figure 6.10 Maximum Roof Displacement and Base Shear in HCW-18-30 for Different Scaling Schemes 196
Figure 6.11 Determination of Initial and Effective Lateral Stiffnesses.....198
Figure 6.12 Displacement History for Ground Motion LA31 199
Figure 6.13 Maximum roof displacement in HCW-12-U for 2/50 records 200
Figure 6.14 Displacement History for Ground Motion LA33 in HCW-18-30 202
Figure 6.15 Maximum Base Shear in HCW-12-U for 2/50 records.....205
Figure 6.16 Displacement and Drift Profiles at the Maximum Base Shear and Adjacent Time Intervals for Earthquake LA31 (HCW-12-30).....207
Figure 6.17 Floor Forces at Maximum Base Shear for 2/50 Records in HCW-12-30 208
Figure 6.18 Push Over Base Shear Versus Roof Displacement for HCW-18-30.....209

Figure 6.19 Displacement and Drift Profiles at the Maximum Base Shear and Adjacent Time Intervals for Earthquake LA29 (HCW-18-30).....210
Figure 6.20 Floor Forces at Maximum Base Shear for LA29 Record in HCW-18-30.....211
Figure 6.21 Story drift ratios along height for HCW-12-30 for 2/50 records.....215
Figure 6.22 Story drift ratios along height for HCW-12-U for 2/50 records.....215
Figure 6.23 Story drift ratios along height for HCW-18-30 for 2/50 records.....216
Figure 6.24 Calculation of Average Shear Distortions.....217
Figure 6.25 Shear Distortion for 2%50 Records.....219
Figure 6.26 Calculation of Plastic Wall Rotations.....220
Figure 6.27 Wall Rotation Along Height in HCW-12-30 for 2/50 Earthquakes (LSW).....222
Figure 6.28 Wall Rotation Along Height in HCW-18-30 for 2/50 Earthquakes (LSW).....223
Figure 6.29 Comparison Between Pushover and Time History at the Maximum Roof Displacement In HCW-18-30.....226
Figure 6.30 Calculation of Coupling Beam Rotation.....227
Figure 6.31 Coupling Beam Rotation Along Height in HCW-12-30 for 2/50 Earthquakes.....228
Figure 6.32 Coupling Beam Rotation Along Height in HCW-18-30 for 2/50 Earthquakes.....229
Figure 6.33 Coupling Beam Shear Force History along Time in HCW-18-30.....231
Figure 6.34 Analysis of Moment and Strain Profiles for LSW/HCW-18-30.....234
Figure 6.35 Interaction Diagram for LSW/HCW-12-30 at the Base.....235
Figure 6.36 Deformed Shape at Time 5.9 second for Earthquake LA31 (HCW-12-U).....237
Figure 6.37 Deformed Shape at Time 5.9 second for Earthquake LA31 (HCW-12-30).....237
Figure 6.38 Deformed Shape at Time 4.05 second for Earthquake LA33 (HCW-18-30).....238
Figure 6.39 Magnified View for Detail “A”.....238

CHAPTER 1: INTRODUCTION

Early attempts to develop and implement earthquake engineering started by the early 1950's at a time of intense construction activity. Then existing earthquake provisions were rather crude and based on many assumptions about structural behavior. In addition, there was a lack of proper analytical tools and earthquake records that could be used in research and practice.

Since then, a great deal of research has been performed providing a better understanding of the behavior of structures under seismic loading and at the same time laying the foundation for rational design procedures. Progress in earthquake engineering has been fueled by advances in: 1) laboratory testing of structural elements and subassemblies, which provided insight into structural behavior at the component level; 2) observations of the behavior of structures subjected to real earthquakes; 3) advances in theoretical and computational techniques; and 4) the accumulation of earthquake records of different levels of intensity. When combined together, these advances resulted in a full circle of knowledge about earthquake engineering and rationalized the practice of earthquake-resistant structural design.

The ductile moment resisting frame system was probably the first earthquake-resistant system to be developed. This system was primarily used for multistory construction of both steel and concrete and remained a popular solution for both engineering and construction industries till the late 1970's (Fintel 1995).

Most of the analytical research in the 1950's and 1960's on the seismic response of structures emphasized the importance of a ductile moment resistant frame to reduce the base

shear demand on the building. Assuming higher seismic forces in rigid structures and assuming that shear walls are necessarily brittle, it was concluded that shear walls would undergo severe damage during earthquake events. Based on this erroneous conclusion, shear walls were considered undesirable for earthquake resistance and, consequently, buildings were built primarily with moment resistant frames. However, observations made on real buildings where shear walls served as the main lateral load resisting system cast more light on the real behavior of structural shear walls and showed their potential for use in regions of high seismic risk.

Fintel, M (1995) summarized the performance of shear wall buildings. His comments are based on observed damage that occurred during the Chile earthquake of May 1960, San Fernando (1971), Managua (December 1972), and Chile (1985). He emphasized the good performance of shear wall buildings and made the following specific observations:

- Instances of widespread shear wall cracking occurred. However, the cracking did not affect the overall performance of the buildings.
- Shear wall structures showed a superior response to earthquakes compared with frame-type structures by limiting inter-story drifts.
- Minimal damage was observed in structural wall systems in the Chile earthquake of 1985 despite poor detailing requirements compared to the strict requirements of the then-current ACI building code.

In cantilever RC shear walls, inelastic behavior of the entire wall is dependent on the plastic hinge zone at the wall base, where large rotations and yielding of reinforcement takes place. As a result, the entire structural system's stiffness, strength, ductility, and means of dissipating energy are wholly contingent on the response of this region. Brittle failure mechanisms and deformation modes with limited ductility are not permitted to control behavior

during the design seismic event. Examples of undesirable response include: concrete crushing in boundary elements, diagonal tension or compression caused by shear, sliding shear along construction joints, shear or bond failure along lapped splices or anchorages, instability of thin walled sections, and bar buckling of the principal compression steel.

Reinforced concrete coupling beams that connect two or more walls in series are employed to better distribute load and deformation demands throughout the wall system rather than concentrate it at the plastic hinge region. This solution also evolved as a practical means to provide openings through otherwise solid shear walls. Coupling beams provide a transfer of vertical forces between adjacent walls, which creates a coupling action that resists a portion of the total overturning moment induced by the base shear. This coupling action has two beneficial effects. First, it reduces the moments that must be resisted by the individual walls and therefore results in a more efficient structural system. Second, it provides a means by which energy is dissipated over the entire height of the wall system as the coupling beams undergo inelastic deformations (Aristizabal-Ochoa 1987).

Reinforced concrete coupling beams are subjected to severe demands during the design seismic event. These high demands, coupled with the brittle nature of unconfined concrete, have forced designers to provide special reinforcement detailing in the vicinity of the coupling beams, which complicates erection and increases construction costs. To mitigate these problems, engineers have turned to structural steel coupling beams as an alternative to reinforced concrete beams. The ends of the steel coupling beams are embedded in the wall boundary elements and the resulting structural system is called a hybrid coupled wall (HCW) system.

HCW systems have been studied both experimentally and analytically in the US and Canada since the early 1990's. In the US, research on HCW systems was conducted under the

auspices of the US-Japan Program on Composite and Hybrid Structures funded by the US National Science Foundation. The US and Canadian studies suggest that hybrid coupled walls are well suited for use in earthquake prone regions (El-Tawil et al 2002a, 2002b, 2003, Gong and Shahrooz 2001a, 2001b, 2001c, and Shahrooz et al 1993, and Harries et al 2000, 1998, and 1993). Although these previous studies produced a wealth of information about HCW systems, detailed information needed to: 1) develop a better understanding of structural behavior under severe seismic loading, and 2) develop performance-based design guidelines, is still missing.

1.1 Objective

The principal objective of this study is to investigate the seismic behavior of *hybrid-coupled wall systems* using detailed and comprehensive analytical tools that account for all the major aspects of structural behavior. In light of the results obtained from the analysis, current provisions and code requirements for design of new buildings are critically assessed and new provisions are proposed to replace provisions perceived as deficient. Aspects of behavior that are not addressed in the current US codes are also addressed.

1.2 Scope of Work

This dissertation is divided into six chapters in addition to the current chapter. Chapter 2 presents a brief literature survey to cast light on the previous analytical and experimental studies performed on coupled RC shear wall systems with special focus on the behavior of steel coupling beams. In Chapter 3, system design issues are discussed and the design provisions of current US and some international codes are summarized. Design details of prototype systems used in this work are given at the end of this chapter.

In Chapter 4, the solution methodology and related analytical procedures are explained. The finite element method is presented and constitutive models for concrete, reinforcing and structural steel are introduced. The implementation of the model into a finite element code is discussed. Chapter 5 represents parametric study performed on isolated flanged wall with the intention of simplifying the finite element model. In chapter 6, analysis results are presented and different analysis procedures are compared to asses the validity of the simplified procedure versus more comprehensive ones. Some current design issues are also addressed and discussed in chapter 6. Conclusions and recommendation for future work are finally presented in Chapter 7

CHAPTER 2: LITERATURE REVIEW

Extensive experimental and analytical studies have been conducted to investigate the behavior of coupled and uncoupled shear wall systems. Steel, concrete and composite beams were utilized to provide the coupling action needed. In this chapter, some of the state of the art work conducted on shear walls and coupled wall systems is reviewed

2.1 Analysis Methods for Coupled walls Structures

A number of analysis methods have been developed in order to analyze shear wall structures. Coull and Smith (1967), Gong and Shahrooz (1998) provided a historical review of these methods. Cheng et al. (1993) suggested alternative analysis methods for analysis based on an interaction surface of moment, shear and curvature or moment, shear and shear strain. Furlong (1996) presented an analytical method based on the concept of truss analogy for composite shear walls where steel members are used in the wall boundary elements. This section describes the different approaches used for analysis of shear walls.

2.1.1 Continuous Medium Method

In the *Continuous Medium Approach,* the discrete coupling beams are replaced by a continuous medium. The method was first used to solve coupled wall systems by Chitty (1947), and subsequently by Chitty and Wan (1948).

The continuous medium method assumes the coupling beam to have a point of inflection at the midspan, where the flexural moment reaches zero. In addition, the beam is assumed not to

experience axial deformation. Based on these assumptions, the behavior of the system as a cantilever can be described by a single fourth-order-differential equation, which leads to a general closed form solution. For the coupled wall system shown in Figure 1.1, the governing differential equation for the system, expressed in terms of the lateral displacement, y, with respect to the wall height, z, measured from the wall base can be expressed as:

$$\frac{\partial^4 y}{\partial z^4} - (k\alpha)^2 \frac{\partial^2 y}{\partial z^2} = \frac{1}{EI}\left[\frac{\partial^2 M}{\partial z^2} - (k\alpha)^2 \frac{k^2 - 1}{k^2} M\right] \tag{2.1}$$

Where,

M = external moment applied to the system;

EI = collective elastic flexural stiffness of walls

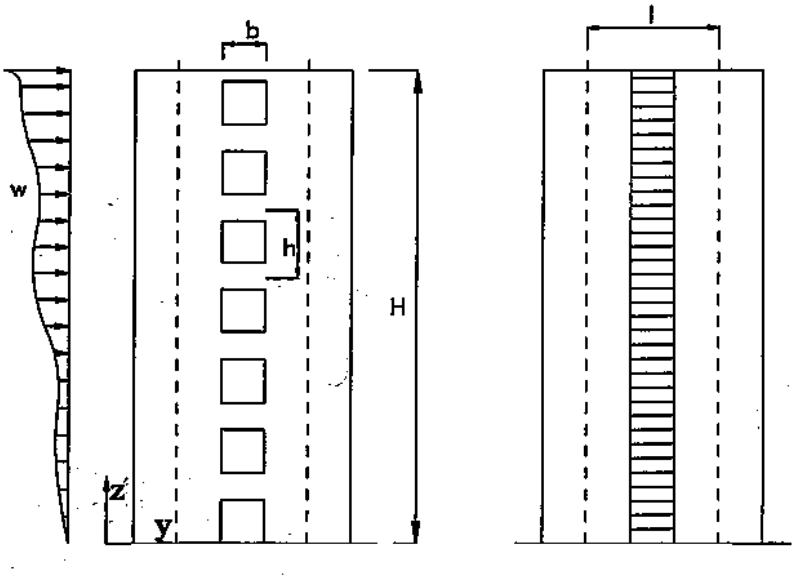

Figure 2.1 Continuous Medium Model of Coupled Walls

$$k = \sqrt{1 + \frac{AI}{A_1 A_2 l^2}} \tag{2.2}$$

$$\alpha = \sqrt{\frac{12 I_c l^2}{b^3 h I}} \tag{2.3}$$

I_c = equivalent moment of inertia of coupling beam = $\frac{I_b}{1+r}$

$$r = \frac{12 E I_b}{b^2 G A} \lambda \tag{2.4}$$

Where:

λ = cross sectional factor for shear, equal 1.2 for a rectangular section

I_b = elastic moment of inertia of coupling beam

E = elastic modulus of concrete

G = shear modulus of rigidity

I = collective second moment of inertia for wall segments = I_1+I_2

A = collective cross sectional area of wall segments = A_1+A_2

h = story height

b = half length of the coupling beam

l = center to center distance of wall piers.

By applying the proper boundary condition to the given differential equation, at the top and the base, and by imposing a known loading pattern onto the wall system, the solution of the equation can be obtained and expressed as a relationship describing displacement along the wall height. More comprehensive research (Rosman, 1964) was carried out to account for the difference in thickness for different wall segments as well as the effect of foundation rigidity.

2.1.2 Equivalent Frame Method

Although the continuous medium method presented above is appropriate for relatively simple coupled shear walls, the method becomes impractical in case of more complex coupled

shear walls systems. For instance, irregularity in wall configuration, presence of openings or a system comprised of three wall piers coupled together will cause the closed form solution in equation 1.1 to become difficult to reach. The equivalent frame method was introduced to deal with such complex and irregular wall systems. The method can also be applied for a combined system (dual system) of coupled wall and a perimeter frame (MacLeod, 1967 and Schwaighofer, 1969).

The equivalent frame method reduces the coupled wall system into a series of frame members with nonlinear properties lumped at the end nodes. These nonlinear properties are calibrated to provide a degrading hysteretic behavior that agrees with data obtained from test results or those obtained from more refined analysis techniques.

Shear walls are modeled as column members located at the centroid of each wall and having the cross sectional properties of the wall. Coupling beams are modeled with frame members that take into consideration both shear and flexural deformation. The beam member spans over a length equal to the net distance between the wall faces while rigid members are used to connect the coupling beam member to the column members at the center of the wall piers, i.e. to simulate the physical dimensions of the wall. Figure 2.2 shows the equivalent frame model of the coupled walls. Despite its simplicity, the method suffers some drawbacks;

- The centroid changes position dramatically as loading progresses; this change can be severe for reversed loading as can occur during earthquakes.
- It is difficult to calibrate stiffness characteristics and degradation in structural properties under cyclic loading (i.e. hysteretic model) for walls and beams
- Shear/flexure/axial interaction that occurs in walls is difficult to account for.

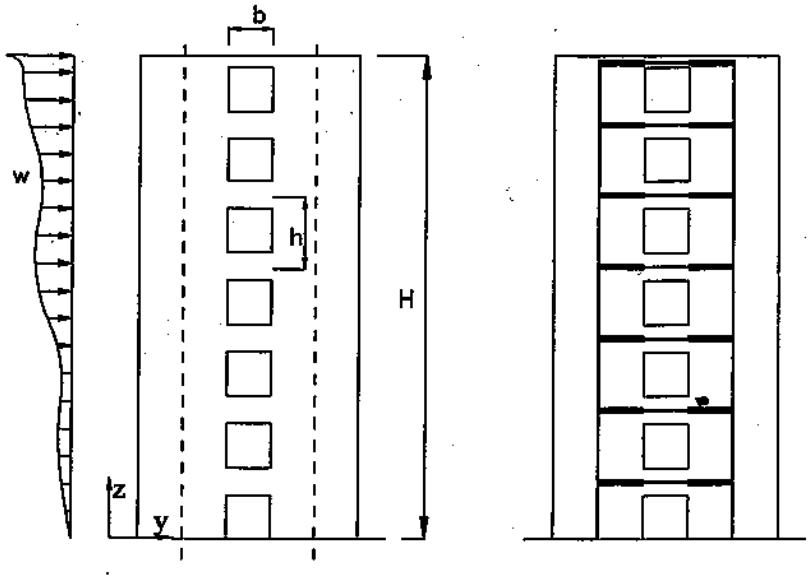

Figure 2.2 Equivalent Fram model of Coupled Walls

2.1.3 Analogue Truss Model

The analogue truss model is a simple analytical tool in which the shear wall continuum is replaced by a series of compression members (struts) and tension members (ties) forming a plane truss. For a shear wall, lateral load migrates through both flexural and shear to the base of the shear wall. Using the concept of truss analogy, flexural stiffness is modeled by two vertical truss members located at the extreme fibers of the structural wall, whereas the shear stiffness is represented by diagonal members connecting the top and bottom floor for every wall panel as shown in Figure 2.3 (Furlong, 1996)

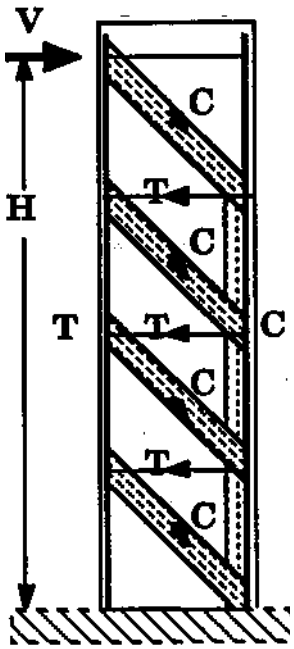

Figure 2.3 Truss Model for Shear Walls

Based on an extensive experimental study by Oesterle et. al. (1984), it was reported that high shear force is transmitted through concrete in between cracks and that the carrying capacity is directly dependent on average compressive strength of concrete struts. The study suggested that failure is initiated by crushing of compression struts. Upon failure of a strut, its load is transferred to adjacent struts depending on their relative stiffness. Upon further loading, the adjacent struts fail progressively and ultimately lead to overall failure of the wall.

The representative members' sectional properties can be accounted for as following (Furlong, 1996):

- Cross sectional area for the vertical members is computed as the entire flange area in addition to one half of the web area
- Steel reinforcement can be counted for by transforming steel into equivalent concrete area using the modular ration Es/E_c.

- Similarly, horizontal stiffness of floor system can be computed as the tributary area of the floor system carried by the shear wall. The area of these horizontal members however is likely to be very high and so it is reasonable to consider the horizontal members as totally rigid members.
- Lateral displacement of the top of the shear panel can be computed using a reduced modulus of rigidity for cracked concrete as well as second moment of inertia for the concrete cracked section. Steel reinforcement is considered when the second moment of inertia is computed. Based on the lateral displacement calculation, the cross sectional area of an equivalent diagonal member is estimated and the equivalent truss model for the wall system can be established.

Although truss analogous system can be simply established and analyzed, the method has some drawbacks that limit its use. First, under moderate and high seismic forces, the part of the wall web in compression is significantly less than one half of the web length as assumed by the method. Second, pre-processing for the diagonal member properties must be carried out before the analysis can be performed. Third, steel reinforcement in the web will either be assumed to have the same level of strains and stress in the main flexural reinforcement placed in the boundary region of the wall, or it will be completely ignored. In other words, a realistic strain distribution along the wall length is not possible. Forth, the flexural stiffness of the wall is based on a fixed second moment of inertia for the entire cracked section and doesn't consider any changes in Young's modulus of concrete. This means that the flexural stiffness of the system is constant through out the analysis and equal to the cracked section flexural stiffness. The method best suits the analysis of shear walls subjected to monotonic loading where the system lateral stiffness does not change dramatically from the point of cracking until the initiating of steel

yielding. Also, the method can be more reliable if the tension and compression properties of the system are equal or nearly equal. This is only possible in composite walls where steel sections are embedded in the shear wall boundary elements.

2.1.4 Macro Element Models

The Macro model Element is basically a refinement of the equivalent frame method. It was originated in the 1980's within the US-Japan Cooperative Earthquake Research Program (ACI-SP84, 1994). The model was developed to create an analytical representation for a full-scale seven-story building tested in Japan by Okamoto et al (1985). The first model of this type was suggested by Kabeyasawa et al (1982) to model a single story wall segment. This model comprises of five nonlinear springs connected by rigid beam members at the top and bottom of the wall panel. As depicted in Figure 2.4, the element consists of two outer springs representing the axial stiffness and strength of the boundary elements while a central spring represents the axial properties of the wall web. Shear stiffness of the wall web is represented by a horizontal spring and finally, the moment strength and flexural stiffness of the web is represented by a central rotational spring.

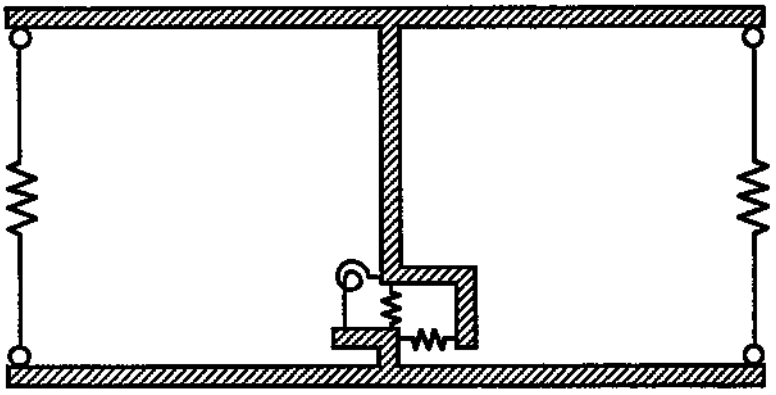

Figure 2.4 Original Macro Model by Kabeyasawa 1992

Many other researchers have attempted to refine this modeling technique (Shimazaki et al 1998, Fajfar and Fischinger 1991, Vulcano et al 1987, Cheng et al 1994, Colotti 1993, Kunnath et al 1992, Charney 1991 and Otani 1980). Figure 2.5 shows some examples of these models. The axial, shear and bending behavior of the wall panel and the stiffness and strength characteristics of these aspects of behavior are either assigned to individual nonlinear springs (Figure 2.5.a, b and d) or inherent in a single beam-column element (Figure 2.5.c)

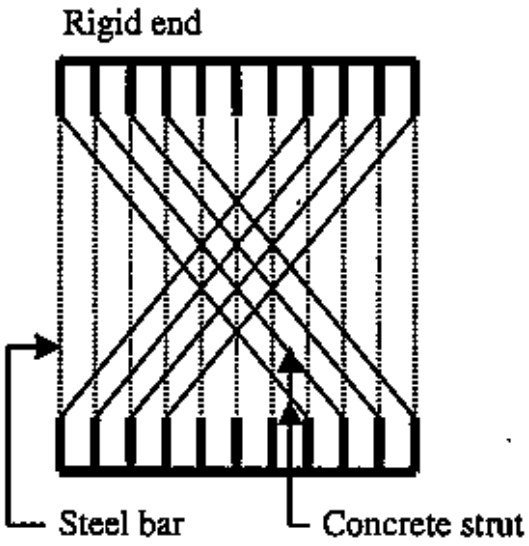

a) Shimazaki et al 1998

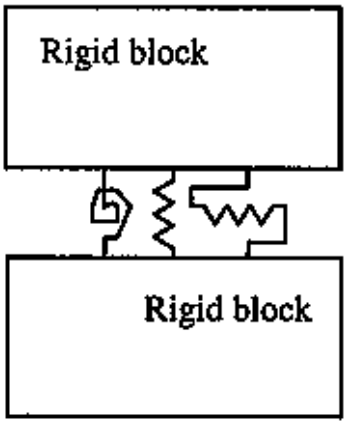

b) Cheng et al 1993

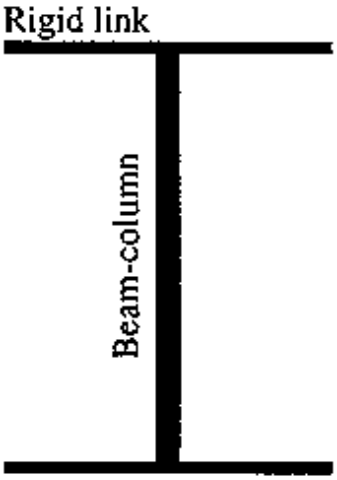

c) Kunnath et al 1992

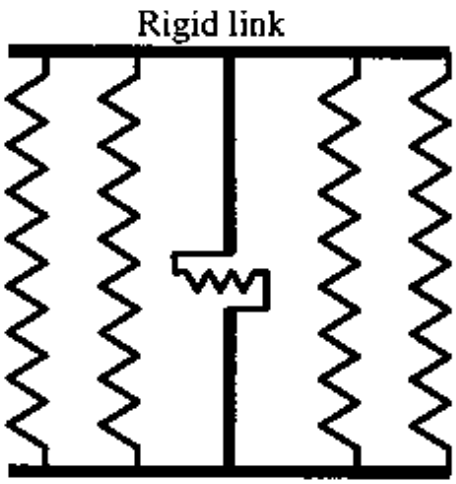

d) Colotti 1993

Figure 2.5 Multi-Component Wall Models

Multi-spring or equivalent beam-column models are efficient from a computational point of view. In addition, they have been used in several inelastic dynamic analyses of shear walls and frame-wall systems. (Bolander and Wight 1991, Shahrooz et al 1993) However, macro elements suffer from the following drawbacks:

- They require extensive pre-analysis to determine the structural properties of the individual components.
- Because they rely on extensive calibration to capture interaction between the individual components, they can only simulate simple failure mechanisms. Hence, most elements of this sort cannot precisely capture inelastic wall behavior.
- The presence of the rigid beam implies that the plane cross-section remains plane. Although this can be reasonable assumption in tall or slender walls, it imposes kinematic constraints on walls subject to large lateral loads. This assumption becomes more critical in walls with low aspect ratios.
- Macro elements are not capable of capturing the moment gradients along the height of a wall panel. Furthermore, they do not provide sufficient information on localized damage such as crack propagation and direction, crushing, etc.

2.1.4.2 Nonlinear Parameter Estimation

Customarily, nonlinear behavior of a spring is represented by a *force-axial deformation* relationship depicted in Figure 2.6.b. The relationship between the axial force in spring F_s, bending moment in wall panel M and length of wall l is expressed as following (Linde 1993):

$$F_s = \frac{M}{l} \tag{2.5}$$

Similarly, the relationship between the spring axial deformation δ_v and the wall rotation θ is expressed as:

$$\delta_a = \frac{\theta\, l}{2} \tag{2.6}$$

Hence, the nonlinear force-deformation relationship of the spring could be obtained based on the *moment-rotation* relationship of the wall cross section. The later relationship can be easily obtained based on the concept of fiber analysis considering the effect of material nonlinearity in concrete and reinforcing steel behavior. Figure 2.6.a shows a typical *moment-rotation* relationship for a reinforced concrete cross section under bending.

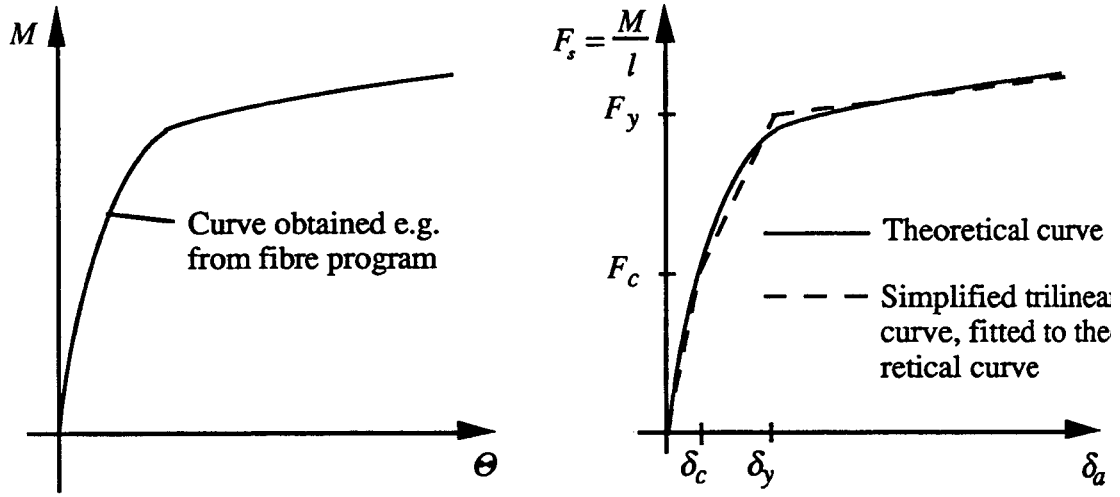

(a) Moment-Rotation Relation (from Fiber Analysis)

(b) Spring Force-Deformation Relationship

Figure 2.6 Nonlinear Flexural Behavior of Wall Cross Section

The previous procedures establish the monotonic behavior of the springs under flexural conditions. For cyclic loading, additional model parameters are needed in order to describe the unloading-reloading behavior under reversed loading. At this point, test results of shear walls

under cyclic condition can be used to calibrate the required spring parameters. Figure 2.7 shows a schematic of cyclic response (shear-displacement relationship) of walls tested within the US-Japan Cooperative Research Program (ACI 1984). Based on experimental observations of these tests, different stiffnesses under load reversals such as initial (elastic stiffness), cracked section stiffness, unloading and reloading stiffness as well as reloading stiffness from an unloading load path can be assessed and different model parameters can be assigned to the springs of the macro model. Figure 2.8 displays a schematic of the material model by Linde (1993) for both large and small cycles load amplitudes. In the figure, the terms K_e, K_{cr}, K_y and K_u, denote elastic, cracking, yield and unloading stiffnesses of the wall respectively. The Terms F_y and δ_y denote the spring yield strength and yield displacement respectively while $a_{cl}\, F_y$ denotes the load at which an open crack is completely closed.

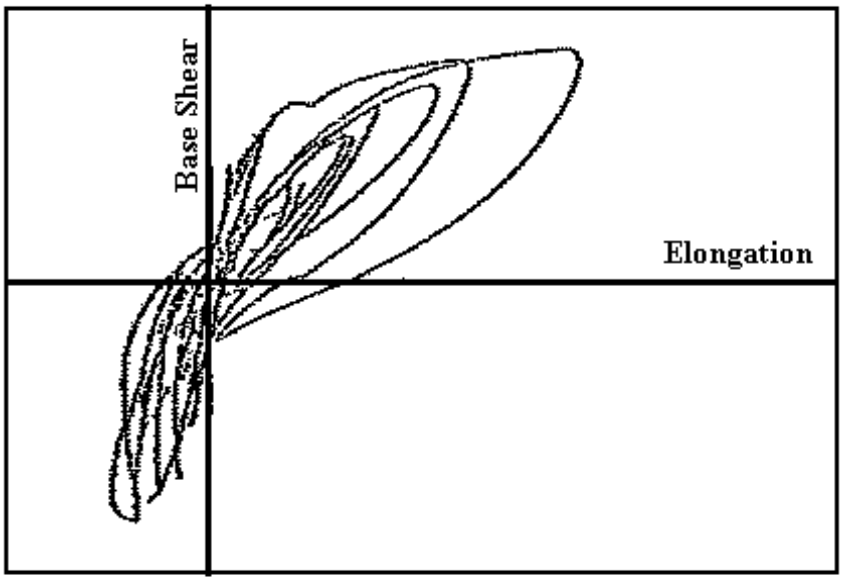

Figure 2.7 Boundary element elongation over first story versus base shear (ACI 1984)

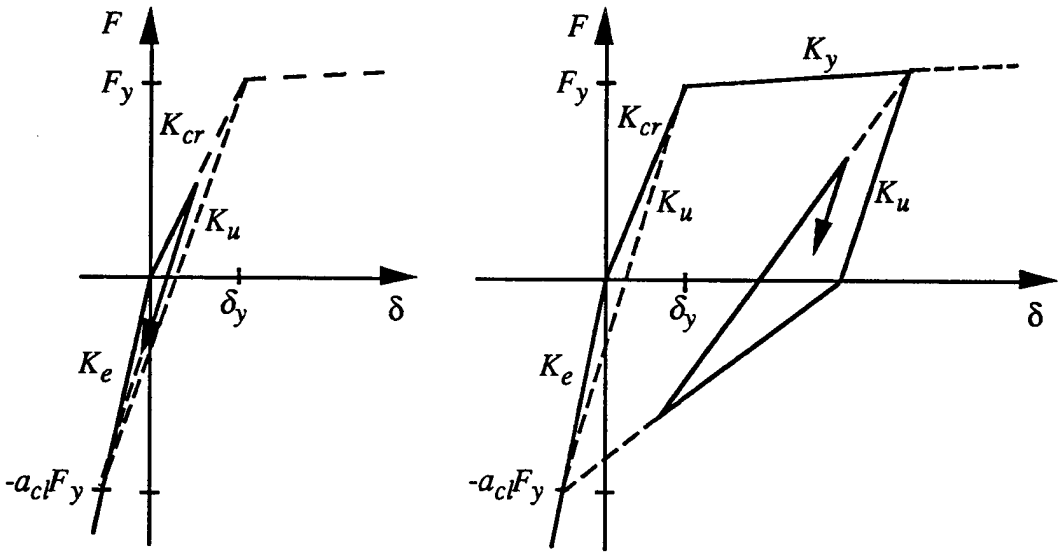

a) Small Amplitude Cycles b) Large Amplitude Cycles

Figure 2.8 Simplified hysteretic model for outer springs (Linde 1993)

2.1.5 Finite Element Method

While the equivalent frame approach considerably reduces the computational degrees of freedom of a structure as well as the amount of computational effort required to account for nonlinearity, this approach suffers from fundamental drawbacks as discussed previously. Continuum finite element analysis naturally addresses many of these drawbacks and has been used in spite of its large computational demands (Blonder and Wight, 1991), (El-Tawil et.al, 2002a)

2.2. Current Engineering Practice for Composite Coupled Walls

Steel coupling beams are used to couple RC walls when story heights do not allow the use of conventional deep reinforced concrete coupling beams, or when reinforced concrete beams are perceived to be incapable of providing the necessary strength, ductility of deformation

capacity. Steel beams are usually encased inside door lintels or unencased across elevator lobbies.

Although, some studies have been conducted to investigate the behavior of steel beam coupled wall system, design codes do not specify detailed design methods for system and the design process relies heavily on engineering judgment. Existing provisions that are applicable to hybrid-coupled walls were first published in the 1994 NEHRP provisions. Subsequent updates were published in the 1997 and 2002 AISC seismic provisions.

Transfer of shear forces from the coupling beam to the wall is achieved through a number of different schemes:

- When connection ductility is not critical, steel beams are welded to steel plates embedded in the concrete wall. Steel anchors similar to those used in base plate connections anchor the plates into the concrete walls. The anchors and steel plates are designed in a manner similar to the design of column base plates (Figure 2.9).
- For systems with higher ductility demands, the coupling beam is embedded into the wall pier or interfaced with the boundary element, if present in the system. Some illustrative details for this type of connection are shown in Figure 2.10. The embedment length is computed based on the PCI guidelines for steel brackets embedded inside reinforced concrete columns (PCI, 1985). Shear studs or steel rebars are welded to the flanges of the coupling beam to ensure smooth transfer of shear forces from the beam to the surrounding concrete.
- An alternative system that can be used when high ductility is required makes use of a steel column embedded into the wall boundary element. The coupling beams are welded directly to the column (Figure 2.11). However, the Northridge earthquake

steel connection failures (FEMA 267A, 1995) suggests that unless the welding is done correctly, the sought ductility may not be achieved in this type of connection.

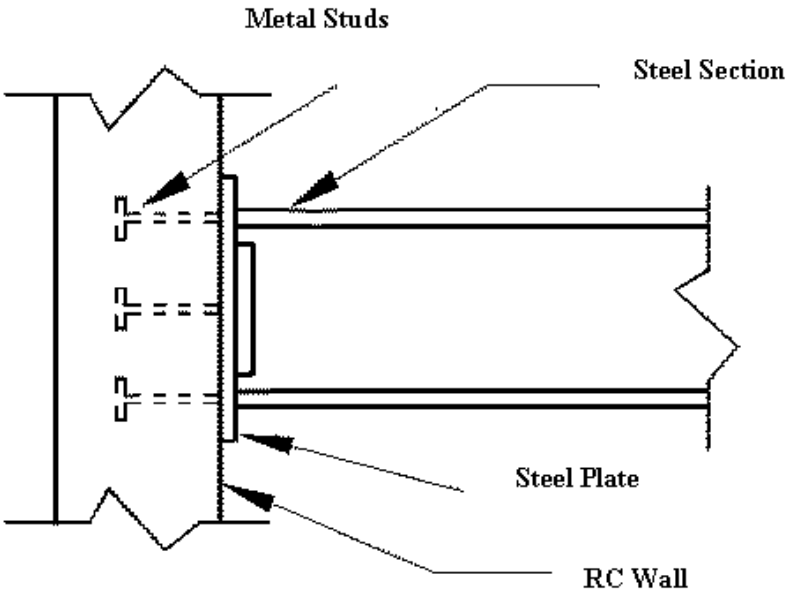

Figure 2.9 RC Wall-Steel Beam Connection for Low Rise Buildings (Gong and Shahrooz, 1998)

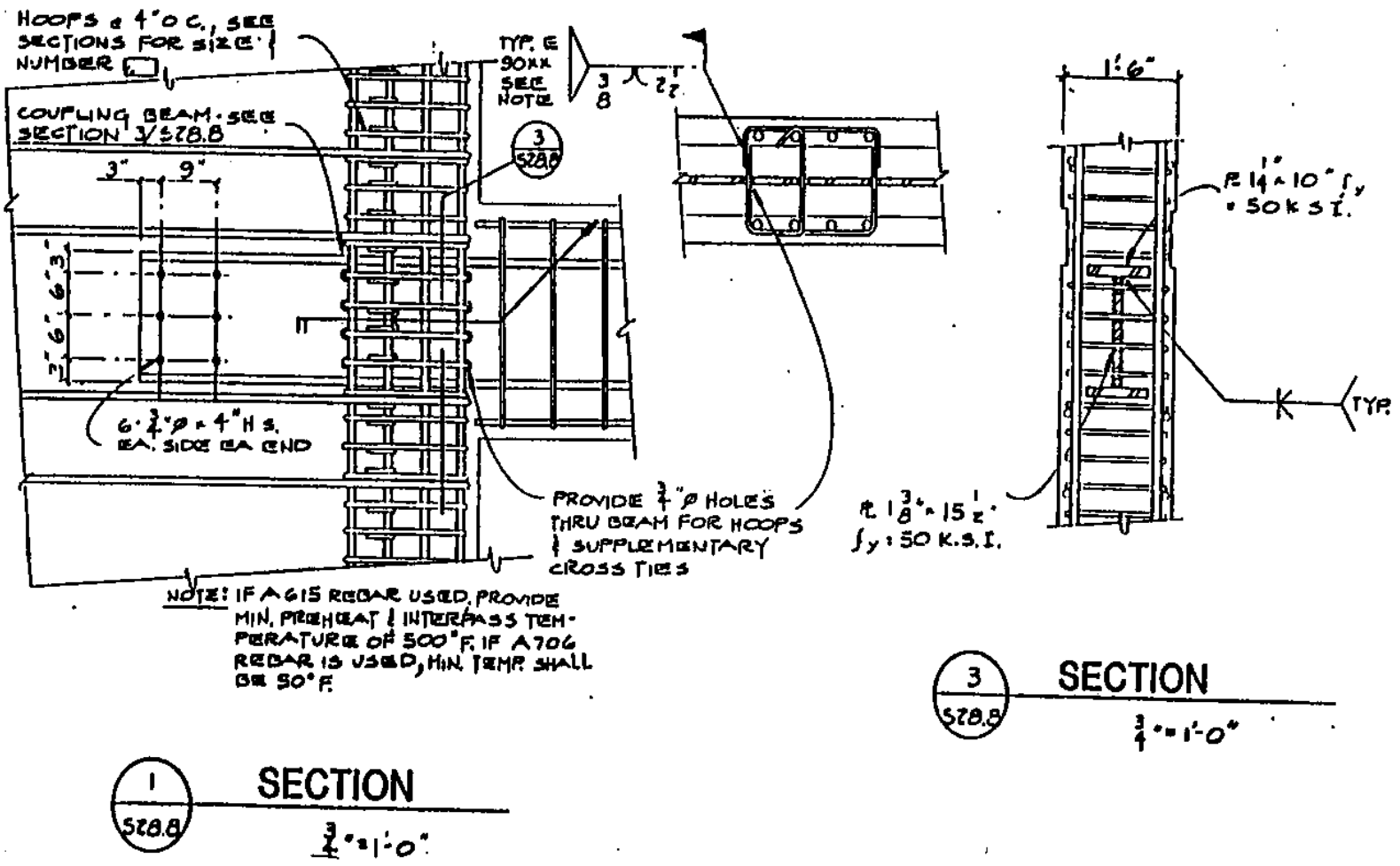

Figure 2.10 A Typical Steel Coupling Beam RC Wall Connection for Mid-Rise Buildings (Courtesy of Kramer Gehlen Associates Inc. (Gong and Shahrooz, 1998)) Associates Inc.

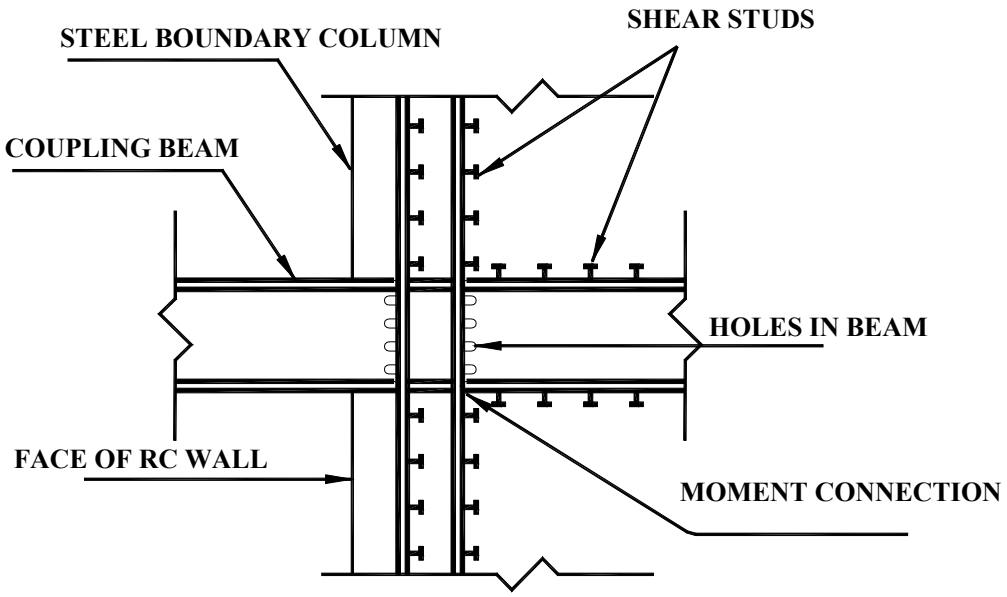

Figure 2.11 Wall Steel Coupling Beam Connection With Steel Boundary Column for High-Rise Buildings (Gong and Shahrooz, 1998)

2.3 Experimental Studies Conducted on Coupling Beams

2.3.1 Steel Coupling Beams

2.3.1.1 Shahrooz et al, 1993

Transfer of cyclic shear forces between steel coupling beams and reinforced concrete walls was investigated experimentally. In this study, tests were conducted on three one half-scale subassemblages proportioned based upon a prototype coupled wall structure. The coupling beams were embedded into the boundary elements of the wall and interfaced with the wall vertical and transverse reinforcement. In order to simulate the effect of seismic lateral load on the sub-assemblage, two vertical loads were applied to the test specimens.

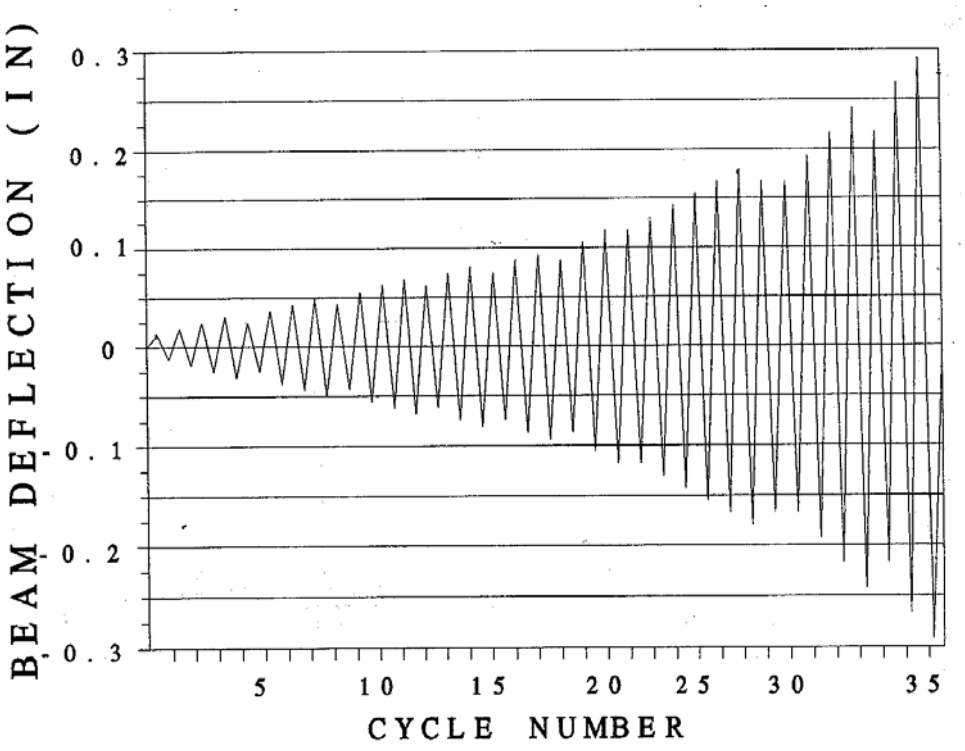

Figure 2.12a Displacement History (Shahrooz et. al 1993)

A master actuator was positioned vertically at the end of the coupling beam while another dependant (slave) actuator was positioned eccentrically on the wall to simulate the effect of the gravity loads as well as the effect of the overturning moment from the lateral load. The master actuator was programmed to enforce a cyclic displacement history on the end of the coupling beam while the other actuator was programmed to apply a force history that depended on the reaction at the master actuator (Figure 2.12a). The vertical stresses in the boundary element varied as a result of the variation in the shear force in the coupling beam. Based on this study, the following major observations and conclusions were drawn:

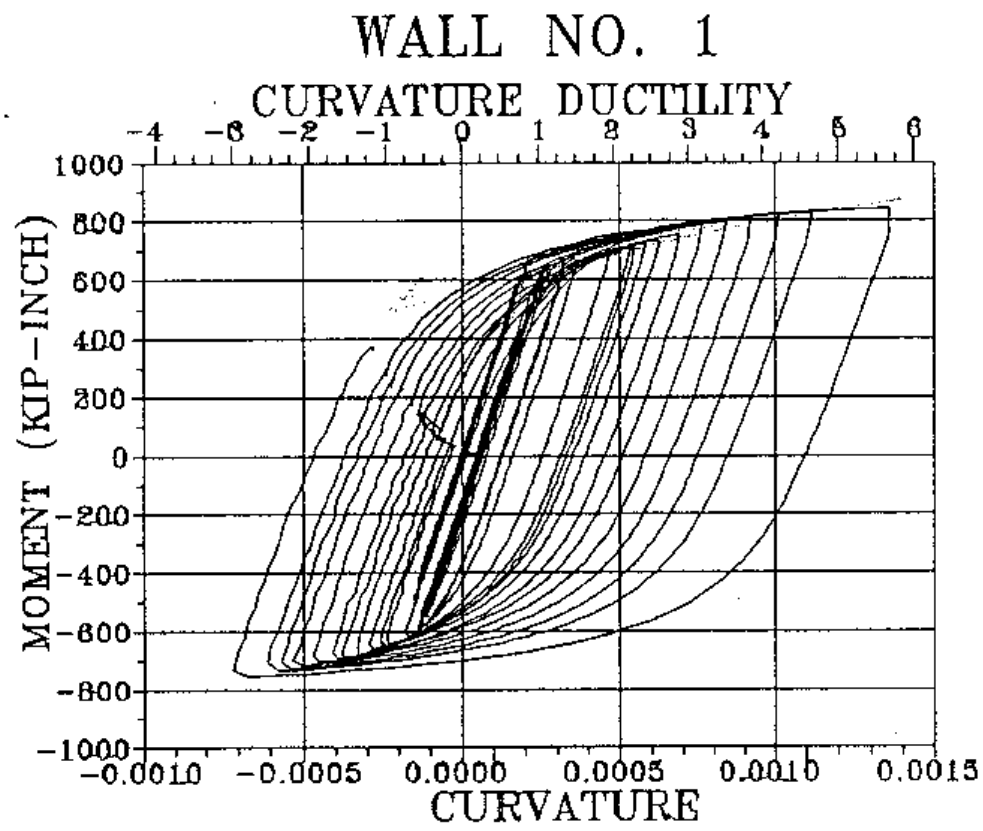

Figure 2.12.b Moment Curvature Hysteretic for Wall No. 1 (Shahrooz et. al 1993)

- The steel coupling beams had stable hysteresis curves with little loss of strength. The theoretical plastic moment capacity could be reached and exceeded when the connection region was under compressive stresses. When the boundary elements were subjected to large tensile stresses, the resulting cracks reduced the stiffness, and the moment that could be developed in the beam became smaller. Welding of vertical bars to the beam flanges resulted in larger and more symmetrical distribution of strength and stiffness. These bars also helped to maintain the overall stiffness.

- Between 65% and 80% of energy was dissipated through plastic hinges in the exposed portion of the coupling beams. The contributions of both flexural and shear deformation in the coupling beams were significant (see Figure 2.12.b).
- The initial stiffness of all beams was smaller than the value computed assuming the beam fully fixed at the face of the wall. The coupling beams were found to be effectively fixed at a point inside the boundary element.

2.3.1.2 Harries et. al., 1993

This research was conducted at the McGill University on four specimens representing reinforced concrete walls coupled by steel beams. The steel beams were embedded into the walls. Unlike the previous study by Shahrooz et. al. (1993), The walls didn't have boundary elements. The amount of vertical bars in the embedment region was increased over the flexural requirements to control cracks that result from large bearing stresses. The coupling beams were designed and detailed as steel beams in eccentric braced frames. Full depth stiffener plates were welded to the web. Three of the specimens were designed such that the beam remains elastic in flexure when the ultimate shear capacity was developed. While for the fourth specimen, the thickness of the flanges and web were selected such that the beam yields in flexure before it yields in shear. In one of the four specimens, the web thickness was increased in the embedment region to ensure that the beam in this region would remain elastic. The clear span to depth ration ranged from 1.29 to 3.43 for the first three specimens dominated by shear yielding and 3.43 for the specimen dominated by flexural yielding.

To simulate the effect of the shear forces transmitted through the coupling beam, one of the walls was clamped to the floor while the other wall was lifted and lowered to deform the

coupling beam. The gravity axial load was simulated by post-tensioning the walls to the floor. Figure 2.13 shows the tested segment of the coupled walls and Figure 2.14 shows the test setup. The results were satisfactory particularly when the web thickness was increased in the embedment region. The investigators reported that:

- The reinforced concrete embedment region must be designed for a shear and bending moment corresponding to the development of the full capacity of the coupling beam
- Concrete cover spalling at the inside face of the wall reduces the embedment length of the beam. This effect must be taken into consideration when the embedment length is estimated.
- Results showed that energy dissipation in the steel coupling beams was similar to that observed in steel link beams in eccentrically braced frames tested by Engelhardt and Popov (1989). Greater energy dissipation was observed than that in traditionally reinforced and diagonally reinforced concrete coupling beams tested by Shiu et al. (1978). Both of these results are shown in Figures 2.15a and 2.15b, respectively. Harries et al. (1993) recommended a design procedure that ensured the structural steel coupling beams would plastify in shear prior to flexural yielding.

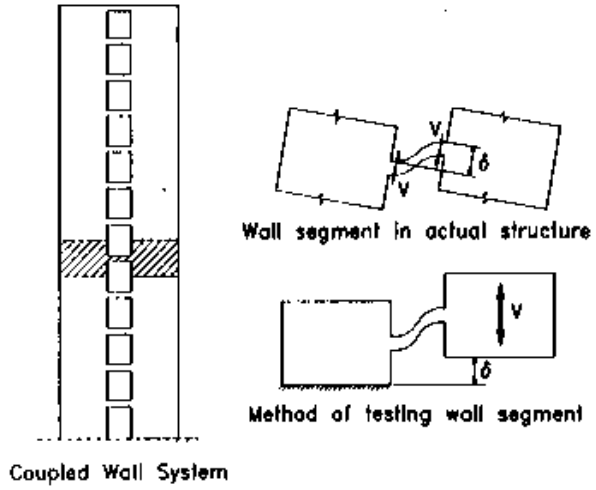

Figure 2.13 Coupled Wall Segment Tested by Harries et al. (1993)

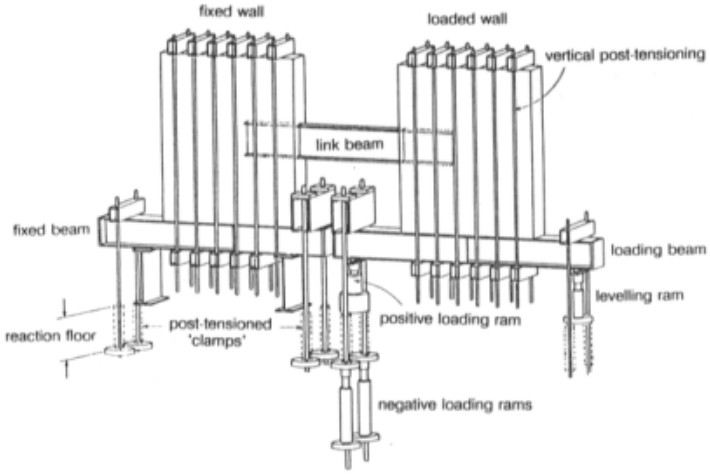

Figure 2.14 Segment Test Setup (Harries et al., 1993)

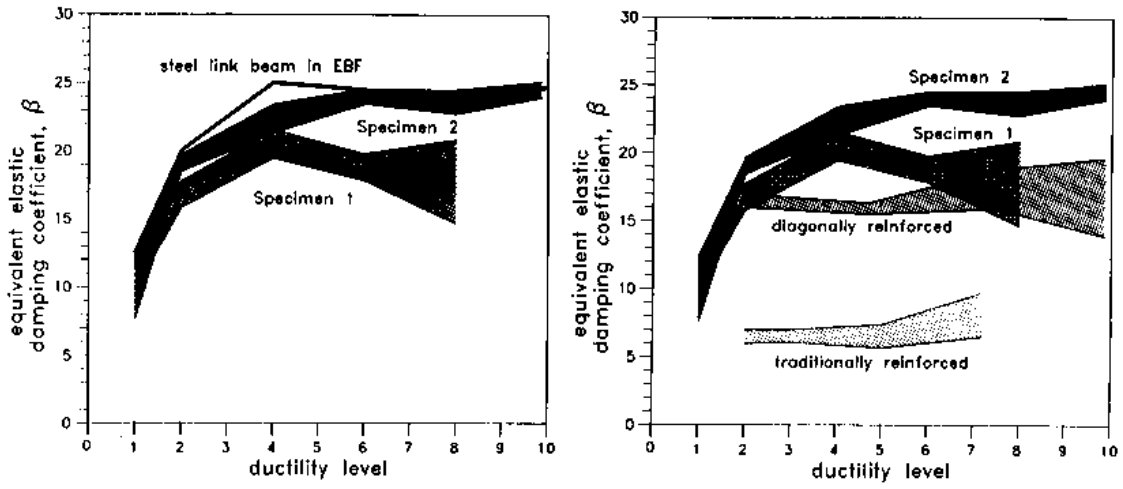

(a) Test Specimens vs. EBF Link Beam (b) Test Specimens vs. RC Beams

Figure 2.15 Energy Dissipation in Steel Beams Tested by Harries et al. (1993)

The study did not address the effects of wall overturning moments and only gravity loads were applied to the wall piers. Overturning moments cause an increase of compressive loads on one pier while the other pier will experience lower compressive stress or perhaps tensile stresses. At the same time, the level of the wall normal stresses in the extreme fibers changes depending on the direction of the lateral load. However, this important aspect of behavior was ignored and only the effects of cyclic shear as well as the effect of constant axial loads were considered. As in the study carried out by Shahrooz et. al. (1993), the coupling beams exhibited very stable hysteresis loops.

2.3.2 Composite Coupling Beams

2.3.2.1 Gong and Shahrooz, 1998

Gong and Shahrooz, (1998) conducted an experimental study on a series of steel/steel composite coupling beams. A series of one-third-scale models of steel coupling beams encased in concrete were tested. Test specimens consisted of one-half of a coupling beam and small portion of the wall pier. Some of the test specimens were tested ignoring the effect of wall overturning moment and only the effect of cyclic shear force on the coupling beam as well as the gravity load on the wall pier was simulated. For the remaining specimens, the effect of overturning moments on the wall was introduced through an eccentric cyclic load applied on the wall pier. Test variables included (a) the presence or lack of nominally reinforced encasement around the steel coupling beams (b) the number and spacing of web stiffener plates (c) the method by which the required embedment length is calculated and (d) presence of floor slab. Figure 2.16 depicts the test setup for assemblies where overturning moments were accounted for.

The nominal encasement around the coupling beam was found to enhance both stiffness and strength considerably. It was found that a significant amount of energy is dissipated by the inelastic deformation in the connection region especially if the contribution of the encasement was not considered in estimating the beam shear capacity. Therefore, the increased strength and stiffness due to the surrounding concrete could have detrimental effects on the overall performance. However, Nominal encasement around the coupling beam was found to effectively prevent web buckling and hence eliminating the need for web stiffeners.

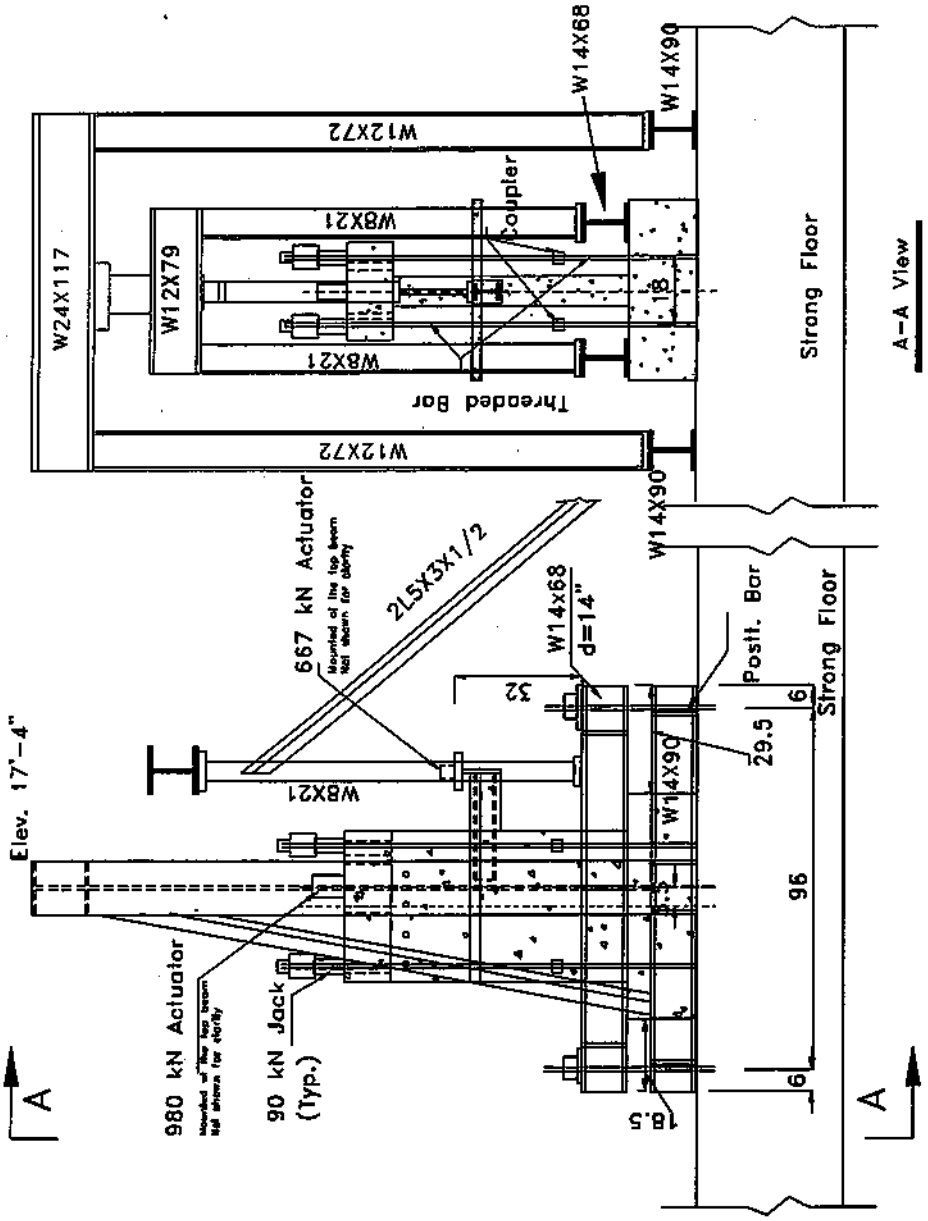

Figure 2.16 Test Setup (Gong and Shahrooz 1998)

Although the presence of the nominal encasement significantly enhances both stiffness and strength of the coupling beam, its effect on the beam ductility is considered undesirable. The strength of the encased beams experienced degradation after the shear angle reached 3% while the unencased beam kept a constant strength plateau beyond yield point. Since coupling beams are expected to exhibit extremely ductile performance, it is anticipated that a significant loss in strength will be experienced by encased beams at higher level of shear deformations. In addition to the loss in the beam stiffness, patterns of failure such as concrete spalling and concrete crushing were observed at these high levels of deformations.

2.4 Connections between Steel Beams and Reinforced Concrete walls

Different schemes are used to connect the coupling beam to the walls depending on the ductility requirements as previously mentioned. The connection between the beam and wall was subject to a number of experimental studies conducted by Mattock and Gaafar (1982), Hawkins et. al. (1980), Sheikh et. al. (1989) and Kanno (1993). Beam-wall connections may be categorized into one of the following types:

2.4.1 Steel Beams attached to steel plates embedded in Reinforced Concrete Walls

The specimens tested consisted of structural steel beams welded or bolted to steel plates that were embedded in reinforced concrete elements with metal headed studs (Hawkins et. al., 1980). It was found that the connection could not develop the full moment capacity required for moment resisting connections. Metal studs could not provide the required ductility and a brittle failure mode was observed. Cyclic loading resulted in a significant loss of stiffness and strength. Considering the considerable loss of both stiffness and strength and the inadequate ductility of

the metal studs, it was concluded that this type of connections is not an effective technique for connecting steel coupling beams to reinforced concrete walls.

2.4.2 Steel Beams Embedded into Reinforced Concrete Columns or Walls

The strength of embedded steel sections in precast or cast-in-place concrete columns has been the subject of a number of past studies (Raths 1974, Marcakis and Michell 1980 and Mattock and Gaafar 1982). All of these studies were based on variations of the Prestressed concrete institute guidelines for design of steel brackets attached to concrete columns (PCI, 1985). Cyclic behavior was not considered. Yamanouchi et. al. (1988) tested half scale models of steel beam-reinforced concrete column subassemblage. The assemblage was loaded with four concentrated cyclic loads at the end of its four member. The tests showed that the joint panel of such systems possesses quite large ductility and no significant loss in strength was noticed up to a drift angle of 0.05 radians.

2.5 Experimental Investigations on Reinforced Concrete Shear Walls

Prior to the 1970's very limited research work was dedicated to investigating behavior of reinforced concrete shear walls under lateral loading. Due to the lack of sufficient test data on shear walls and lack of understanding of behavior, reinforced concrete shear walls were not considered efficient as lateral load carrying systems during earthquake events. However, since 1970, researchers started to focus more on the behavior of shear walls, either isolated or coupled with a structural frame. In this section, some of the most important research work on the testing of reinforced concrete walls is outlined.

2.5.1 Walls Tested by the Portland Cement Association

Researchers at the Portland Cement Association (PCA) were among the pioneers of reinforced concrete shear wall testing. Cardenas (1973) tested thirteen one-half scale shear wall models. The aspect ratio of the walls (height to length), amount, location and distribution of flexural reinforcement were chosen as test variables. The amount of shear reinforcement was kept constant for all walls. The results indicated that: 1) axial load imposed on specimens was found to increase moment capacity yet decrease the ultimate curvature and ductility 2) Higher ductility was achieved when the flexural reinforcement was concentrated near the edge boundaries of the shear walls 3) minimum shear reinforcement was found to provide sufficient shear strength 4) specimens with lower aspect ratios were demonstrated to experience higher amounts of shear stresses which was attributed to the higher contribution of concrete to shear forces.

Oesterle, Fiorato and Corley, (1983) and Oesterle and Fiorato (1984) conducted an extensive test study on a series of one-third scale isolated shear wall models with the primary objective of studying the strength, ductility and energy dissipation characteristics of the shear walls under cyclic loading. The tested walls had a length of 75 inches, thickness of 4 inches and a height to length ratio of 2.4. A total number of twenty-one tests were done on this wall series (Oesterle and Fiorato, 1984). Test variables included axial load, amount of flexural and shear reinforcement, concrete compressive strength and loading history. Also, walls with flanged, rectangular cross-section as well as barbell cross sections were considered in tests.

It was reported that both flanged and barbell types of sections were found vulnerable to web crushing. One of the rectangular sections experienced out-of-plane instability. Near-horizontal cracks and flexural failure modes were observed in wall with low nominal shear

strength (less than 0.25 $\sqrt{f'_c}$ M pa). While those with high nominal shear strength (more than 0.58 $\sqrt{f'_c}$ Mpa) were found to develop inclined cracks in the web portion of the wall and diagonal compression strut was formed to transfer shear forces to the wall base. The failure modes for those walls were reported to be either web crushing or diagonal tension. A case of sliding shear was reported in only one of the test specimens.

A comparison between flexural strength of walls subject to different loading schemes showed that walls under cyclic loads have flexural capacities 15% less than identical walls tested under monotonic loads. In addition, monotonic loading yielded larger deformation capacities. Deformation capacity in cyclic tests was observed to be dependent on the prior maximum deformation and no significance influence of the load sequence was found to affect wall deformation capacity.

The moment capacity and corresponding maximum shear were found to be dependent on both the amount and the distribution of flexural reinforcement. The actual capacity of a shear wall was higher than the design capacity since the nominal material strength specified for design was less than the actual properties. Therefore, the actual shear force that a wall would experience might be significantly more than that on which the shear design was based on. Similar to the results reported by Cardenas (1973), higher moment capacities as well as more deformation capacity were found when flexural reinforcement was concentrated in the wall boundary regions rather than uniformly distributed along the wall length. The reported study showed that shear reinforcement provided based on an estimate of the actual shear force corresponding to maximum possible flexural capacity (considering the effect of material over strength) is sufficient to avoid shear failure. Extra shear reinforcement beyond this estimate would have minor effect on failure modes such as diagonal tension, web crushing and sliding shear.

Hoop reinforcement in the wall boundary regions was found to considerably enhance the inelastic behavior of reinforced concrete walls. Oesterle et al (1983) summarized the benefits of hoop reinforcement as followings:

- Prevent buckling of flexural reinforcement in the compression side of the wall
- Due to its confining effect, it improves concrete properties in the boundary region
- Increases shear strength and stiffness of the boundary elements

Axial loads of less than 10% of the wall axial capacity proved to considerably increase the moment capacity. Axial loads also tend to retard the initiation of cracking and reduce crack openings or even help closing some of the concrete open cracks. This particularly enhances shear properties of concrete in cyclic loading. Consequently, larger base rotation is sustained prior to the occurrence of web crushing. Concrete strength was found to enhance web-crushing capacity for those specimens dominated by this mode of failure. Concrete shear strength along crack interfaces was significantly enhanced.

Daniel et al (1986) investigated effect of openings in shear walls. They tested two one-third-scale wall models under cyclic loading. One of the walls had an opening while the other one was solid. Shear deterioration was observed in the first specimen after it reached the flexural capacity. It was concluded that frequent load reversals causes strength degradation beyond the elastic range due to the deterioration of shear strength in that specimen.

2.5.2 Experimental Studies Conducted at the University of California, Berkeley

Considerable research effort has been dedicated to the testing of shear walls at the Earthquake Engineering Research Center of the University of California at Berkeley EERS/UCB) in the 1970's. Wang, Bertero and Popov (1975) tested two one-third-scale models

with barbell cross section-type walls with spiral hoops reinforcement in the boundary element. The tested walls represented three stories of a ten-story building designed according to the Uniform Building Code of 1973. Walls were loaded incrementally until failure was reached and then repaired and re-tested. Valenas, Bertero and Popov (1979) conducted a parametric study on four shear walls. Two of them had a similar configuration as those tested in the previous study. In addition, two rectangular shape walls were tested. Study parameters included the cross section shape, amount of transverse reinforcement in the boundary element, shear stress and loading history. As observed in the previous studies at the Portland Cement Association, the study reported that moment capacities of walls were higher than those predicted based on the nominal material properties. However, it was concluded that estimation of moment strength based on realistic material properties leads to gives better predictions of the wall flexural capacity.

The major finding of the study can be summarized as following:

- Walls with higher flexural capacities, developed wide flexural and diagonal cracks in the tension side of the neutral axis. Very low shear stresses were able to migrate along the interfaces of these widely opened cracks and hence, mainly, the concrete in the compression side resists shear. It was suggested that shear stress capacity of concrete is considerably higher than what the design codes generally prescribe.
- Due to the grinding effect of frequent load reversals on crack interfaces, the amount of shear resisted by concrete through aggregate interlock degraded significantly compared to walls subjected to monotonic loading.
- Wall base rotations were found to increase the total deflection of the wall by 7 to 11 percent

- The participation of shear deformation in the total deflection of the wall was found to be significant. Shear deflection was found to range between 0.43 and 0.87 of the deflection caused by flexure.
- Local buckling of vertical reinforcement bars was suggested to be related primarily to the diameter of longitudinal reinforcement, spacing of transverse reinforcement and strain levels in the boundary zones of the wall.

The effect of amount and distribution of web reinforcement on the hestereteic behavior of walls was investigated by Iliya and Bertero (1980). Two flanged walls were tested under cyclic loading and good agreement between predicted and actual flexural capacity was reported. They concluded that boundary confinement has significant impact on ductility whereas the distribution of web reinforcement has a little effect on the wall ductility and deformation capacity. Diagonal web reinforcement was found to enhance ductility noticeably.

Similar to past studies, they suggested that in order to achieve better estimates of the wall flexural capacity, realistic material properties should be accounted for rather than the nominal properties customarily used in engineering practice.

Aktan and Bertero (1984) conducted analytical and experimental studies on a 15-story reinforced concrete frame coupled wall structure. The Building is identified as a typical mid-rise office building located in the western United States. The experimental study was carried out on a four-story one-third-scale model subassemblage of the coupled wall system as shown in Figure 2.17. The lateral load was applied on both walls by a system of two horizontal actuators coupled to four other vertical actuators. The six actuators were programmed to simulate the lateral shear, vertical gravity and coupling force, as well as bending moment on the forth story. They concluded that when the coupling girders were designed to provide 60 percent of the total

overturning moment of the entire system, severe compressive axial loads could develop in the wall in the compression side. This resulted in premature crushing in the wall panel in compression. Thus, the level of coupling was judged as too severe.

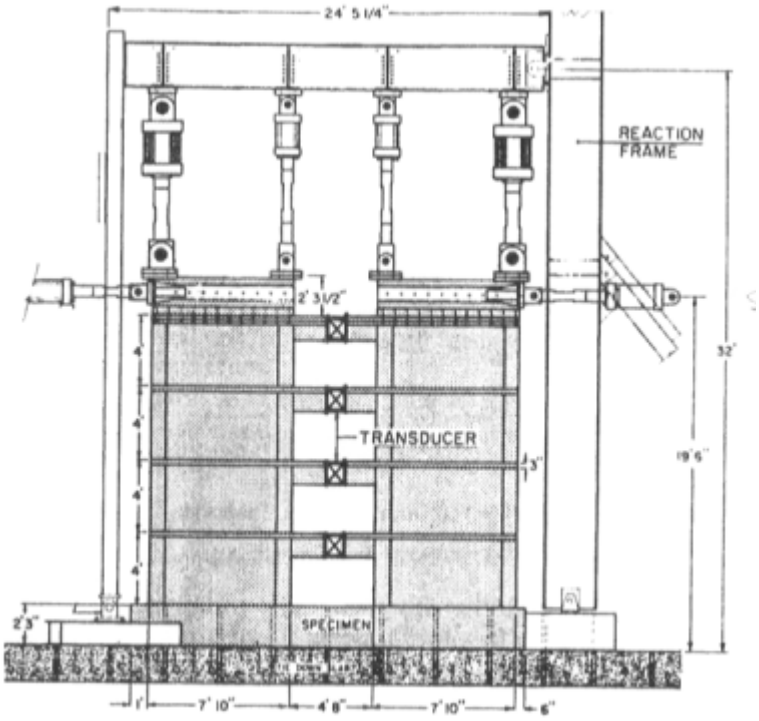

Figure 2.17 Experimental Setup for Tests Conducted by Aktan and Bertero (1984)

2.5.3 Experimental Studies Conducted in Japan

As part of the US-Japan Cooperative research program (US-Japan Joint Technical Coordinating Committee 1984), a full-scale reinforced concrete building was tested. The tests were conducted in the large size structural laboratory of the Building Research Institute, Tsukuba, Japan in 1981.

The test structure was a reinforced concrete seven-story full-scale building. The Building had three moment frames along the loading direction. The outside frames were open frames having three bays each while the center frame had a shear wall in the middle bay. Figure 2.18 shows a plan and elevation view of the building and the elevation of the center frame. In addition, four walls were built in the transverse direction of the building, along with four moment frames in that direction in order to support the building against lateral deflection or twisting. A strong floor system of 5 cm slab and supporting beams was considered to act as a rigid diaphragm connecting the lateral frames and the shear wall.

Lateral loading was enforced on the building using a set of electro-hydraulic actuators. At each of the first six floor levels, an actuator of a capacity of 220 kips capacity (100 metric ton) and a stroke of 20 inches (500mm) was installed. At the seventh floor, two actuators each of 440 kips capacity and 40 inches stroke were installed parallel to each other. Complete details of the testing procedure and instrumentation is provided by Okamoto et al (1985)

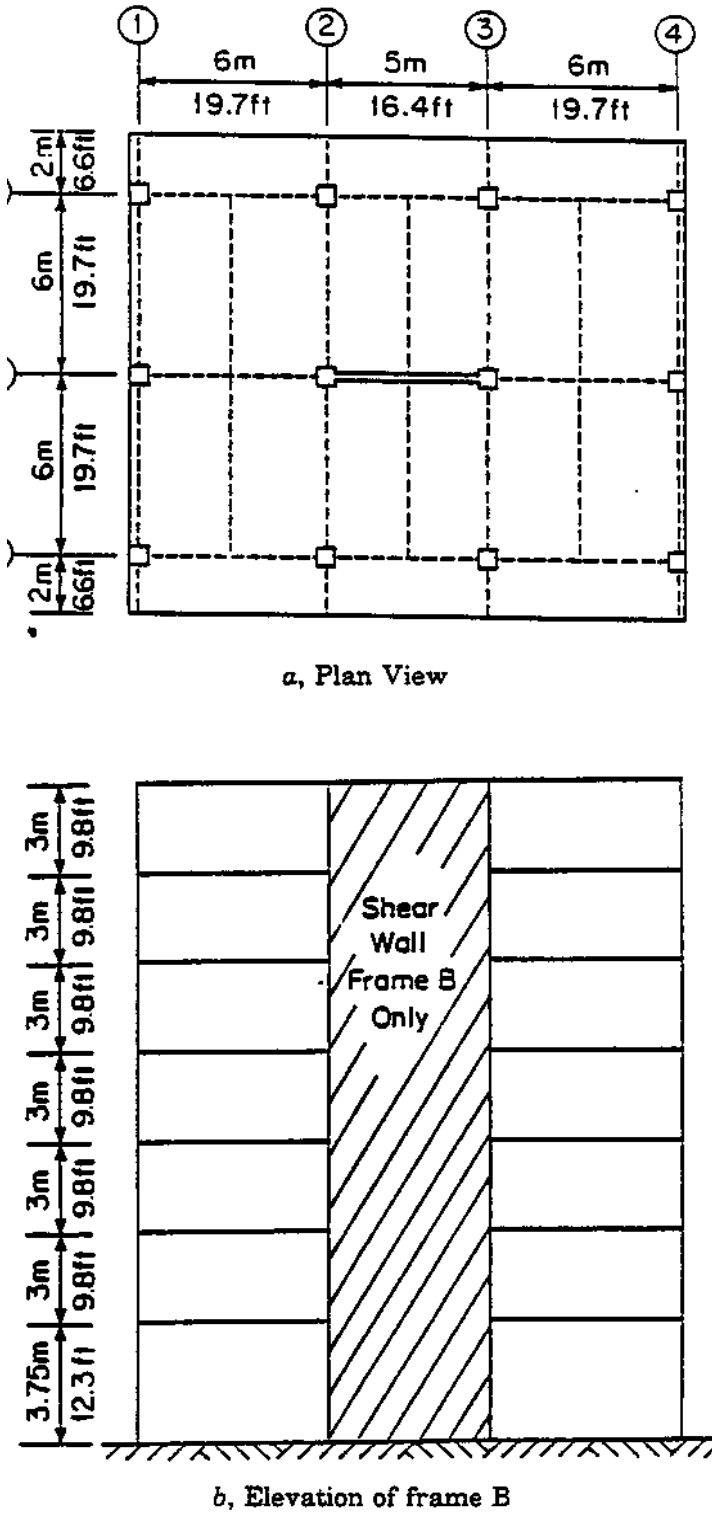

Figure 2.18 Layout of the Seven-Story Building Tested by Okamoto et al 1985

The Building was tested four times using a psedo dynamic technique (PSD). Each time, a different ground acceleration record was simulated by displacement time histories applied by the actuators at the different floor levels. The PSD method employed a single degree of freedom nonlinear system with mass and stiffness characteristics equivalent to those of the building. For each time step, the equivalent single degree of freedom system was subjected to the desired ground motion record, then as an approximation, a straight-line displacement profile was imposed onto the building. Feedback from the actuator is used to solve the SDOF for the next time step. Okamoto et al (1985) summarized the extent of the structural damage that took place during the different pseudo dynamic tests. The first PSD test did not result in any noticeable cracks in the shear wall; the second PSD produced cracks in the lower part of the shear walls as well as in beams and slab adjacent to the wall. During the third PSD, existing cracks widened and new flexural and diagonal cracks formed in the web panel and the boundary columns of the wall. Concrete cover spalling was observed in the lower parts of the boundary columns. Cracks also developed in the transverse beams due to upward force emerging from the vertical displacement of the shear wall edges. After the fourth PSD, crack pattern basically remained the same but cracks start to intensify and their widths increased. As the structural damage progressed, the building natural fundamental period lengthened and by the end of the fourth test, it tripled in value.

2.5.3.1 Other Shear Wall Test Programs Conducted in Japan

A number of experimental studies on the previous full-scale seven-story building were conducted at the Building Research Institute, Japan. Hiraishi et al (1985) carried out six tests on one-half models of the wall beam assemblies of the prototype; two static cyclic, two on the shake

table and two pseudo dynamic tests. Morgan, Hiraishi and Corley (1985) tested 1:3.5 scale models of isolated walls and wall-beam assemblies.

Yamaguchi et al (1980) tested sixteen one-fifth models of isolated shear walls with barbell cross-sections. Test variables included moment to shear force ratio (shear span), axial stress and the amount of longitudinal reinforcement. The tests were carried out using cyclic displacements, which were progressively increased. It was concluded that type of failure depends on the flexural to shear capacities ratio. A ratio of less than 0.86 was proposed to result in shear-type failure while flexural-type failure is expected for ratios more than 1.10.

2.5.4 Test Programs Performed in the United Kingdom

Tests on reinforced concrete isolated shear walls were conducted at the Imperial College of London by Lefas and Kotsovos (1990). Thirteen two-fifth-scale models of walls of aspect ratio one and two were subjected to monotonic and cyclic loading. The parameters under investigation were the amount of axial load, concrete strength and amount of shear reinforcement as the amount and distribution of flexural reinforcement was kept unchanged in all the tested walls. All the walls failed due to concrete crushing in the compressive area. As reported by previous researchers above, presence of axial load increased moment capacity of the wall and reduced the yield and ultimate displacement of walls. In all tests, the obtained flexural strengths was significantly higher than those predicted by analysis based on the nominal strength of concrete. It was concluded that confinement effect of transverse reinforcement in the boundary elements enhance concrete strength and ductility considerably. In certain cases, ultimate strength of concrete was founded to be three times as the uniaxial cylinder strength of concrete.

Pilakoutas (1990) conducted an experimental study on nine shear walls of one-fifth and two-fifth scales. One of the tested walls was subjected to earthquake loading on a shaking table whilst the other walls were subjected to displacement controlled cyclic loading of large amplitudes. Different ratios of flexural reinforcement were used in walls. Also, shear reinforcement was varied in order to investigate the effect of various degrees of safety margins in shear. The flexural reinforcement was concentrated in the boundary elements such that the moment capacity is maximized; whereas a minimal ratio of vertical reinforcement was used in wall webs.

Shear reinforcement was activated only after the initiation of cracking. Inadequacy of shear reinforcement in certain walls led to a brittle shear failure in these specimens. While inadequate anchorage of the same reinforcement led to shear deterioration in one specimen after reaching its moment capacity. In one wall, shear reinforcement reached its yield limit but that. Yet, the deformational behavior of that wall was not affected. Base wall rotations accounted for less than 2% of the total displacement at ultimate conditions. Out-of-plane deformations were demonstrated not to have any significant effect on the in-plane behavior. Increase in axial loads was found to increase the moment capacity of the walls accompanied by a reduction of ductility. Tensile axial loads demonstrated the opposite but imposed higher tensile strain demand on the flexural reinforcement. Most of the energy dissipated in the main flexural reinforcement at the wall base while the contribution of pre-yield cycling and shear deformations to the overall energy dissipation capacity was low

2.5.5 Test programs performed in Mexico

Hernandez and Zermeno (1980) tested twenty-two scales one-eighth models of isolated - reinforced concrete walls under cyclic loading. All the tested walls were intended to fail in shear. The parameters of the study included wall cross section (rectangular and barbell sections were considered), shear span ratio, concrete strength, amount of axial loads, ratio, distribution of flexural reinforcement and the presence of intermediate slabs along wall height. The tested walls were observed to experience progressive deterioration in strength under cyclic loading, Hysteretic behavior of the walls as well as their energy dissipation capacities were inadequate due to the pinching effect and the significant loss in strength and stiffness degradation. Slabs were observed to act as stiffeners and increase the initial stiffness of the system

2.6 Summary

An overview of the past studies conducted on coupling beams and shear walls was presented in this chapter. The studies show that if properly designed and detailed, shear walls can provide the necessary balance of stiffness and ductility during an earthquake event. Special attention is required to ensure ductile behavior of the wall and to avoid possible brittle failure pattern caused by shear forces rather than bending moments. Different analysis approaches of isolated and coupled wall systems were overviewed with emphasis on the drawbacks of each one. Among these analytical approaches, finite element method stands as the most efficient approach that can reflect different aspects of nonlinear behavior without many of the assumption inherent in the other approaches.

Experimental studies on steel coupling beams proved that they posses ductility and energy dissipation capacity higher than reinforced concrete or composite coupling beams. A

great deal of energy is dissipated through the plastic hinges in the exposed portion of the coupling beam.

CHAPTER 3: SYSTEM DESIGN ISSUES

Seismic design of hybrid coupled shear walls requires a thorough understanding of the seismic behavior under the transient lateral loading imposed by an earthquake. In addition to the variables associated with ground motion, structural response is influenced by a multitude of parameters pertaining to RC walls; steel coupling beams and the interaction between the walls and the coupling beams. The existence of so many design parameters complicates system design to achieve the basic requirements of strength, stiffness and ductility.

This chapter presents a critical discussion and evaluation of the effects of various parameters as observed in previous research, in particular the work of El-Tawil, Kuenzli and Hassan (2002a) and El-Tawil and Kuenzli (2002b). Also presented are the procedures taken to design the prototype systems analyzed later on in chapter 6.

3.1 The Coupling Ratio – *CR*

A comparison is made between system behavior of a series of 3 isolated walls and a series of 3 coupled walls in Figure 3.1. The walls are designated LSW (left shear wall), MSW (middle shear wall), and RSW (right shear wall). Three walls are used because the prototypes considered in this study have a similar configuration. As discussed in Paulay and Priestly (1992), there is a fundamental difference in how each system resists the overturning moment induced by the lateral forces. In the isolated wall system, the overturning moment ($h.V_{Base}$) is resisted entirely by the moment reactions developed at the base of the individual shear walls. However,

in the coupled walls, the transfer of shear forces through the coupling beams induce tensile (T) and compressive (C) forces in LSW and RSW, creating a couple moment that resists a portion of the total overturning moment. Assuming a symmetric system, then $C = T$, and MSW is not subjected to a net axial force because the coupling beam shear forces on the left and right cancel out. Hence

$$h.V_{Base} = m_1 + m_2 + m_3 + (C \text{ or } T).S \quad (1)$$

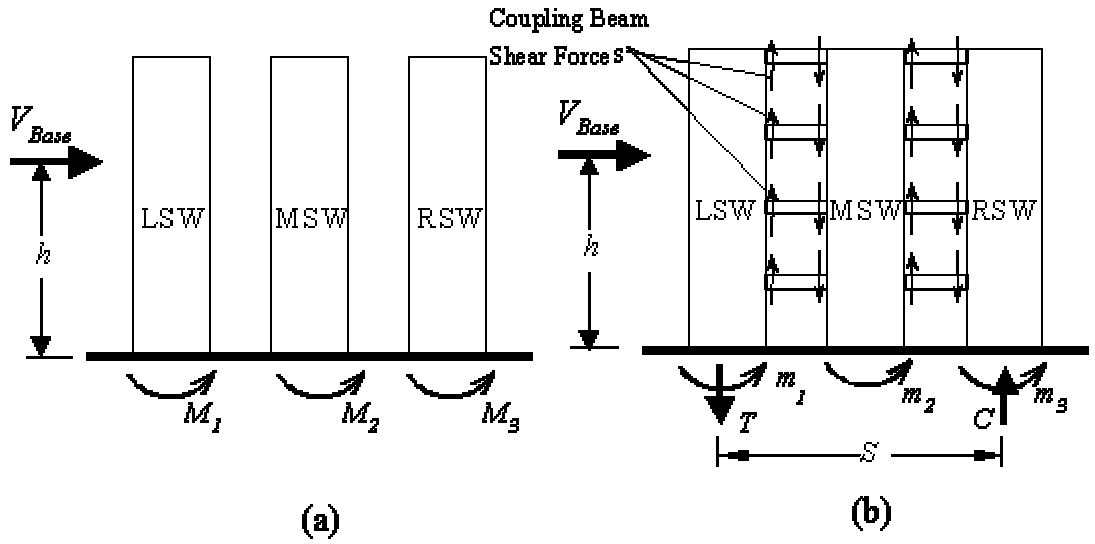

Figure 3.1 Comparison between (a) isolated and (b) coupled shear walls.

Where L is the couple moment arm (i.e. the distance between the centroids of walls LSW and RSW. The moment reactions of the individual walls decrease compared to the isolated wall system since a significant portion of the total moment is taken by the coupling action. The proportion of system overturning moment resisted by the coupling action is defined as the coupling ratio, CR:

$$CR = \frac{C.S}{m_1 + m_2 + m_3 + C.S} \quad (3.1)$$

The coupling ratio is a key parameter in the design and behavior of coupled walls. Too little coupling (i.e. too small a coupling ratio) will yield a system that behaves in a manner similar to uncoupled walls and benefits due to wall coupling will be minimal. Too much coupling (i.e. too large a coupling ratio) will add excessive stiffness to the system, causing the coupled walls to perform as a single pierced wall. The optimum amount of coupling lies in between these two extremes.

El-Tawil et. al. (2002) conducted a parametric study on a series of systems with different coupling ratios. The plan of the systems is similar to that considered here as discussed in section 3.2. Coupling ratios of 0 (uncoupled), 30%, 45% and 60% were chosen. It was observed that since coupling induces tension force on LSW and compression on RSW, cracking and concrete crushing were more widespread in cases with higher coupling ratios, which were considered detrimental to the behavior. On the other hand, under coupled system can also lead to poor behavior. For example, of all the prototypes considered, the uncoupled system suffered the highest base wall rotations, story drifts, shear distortions, deflections, and underwent concrete crushing in the plastic hinge region.

Based on these observations, El-Tawil et al (2002b) concluded that the system with *CR*=60% can be considered over coupled whereas better performance in terms of story drifts, wall rotations as well as crack patterns and prevention of extensive concrete and web crushing can be obtain using lower coupling ratios of 30% and 45%. Therefore, throughout the current work, walls with 30% coupling are chosen to represent walls with moderate coupling ratio. For the sake of comparison, an uncoupled system is chosen as a reference line.

3.2 Description of Prototypes

The prototype structures considered in this research are based upon plans developed for the US-Japan cooperative research program on Composite and Hybrid Structures sponsored by the US National Science Foundation (US-Japan Planning Group, 1992). The US-Japan theme structures have a regular floor plan and geometry. They are intended to provide common focus for the various components of the US-Japan research program.

Theme structure 4, designated as (S-SRC)+W-12, is selected for design and subsequent analysis It is similar to that used by El-Tawil et al (2002). The structural system consists of a core set of reinforced concrete walls coupled together via steel coupling beams and surrounded by perimeter steel moment resisting frames. A plan view of the theme structure is given in Figure 3.2. The structure is symmetric in both the longitudinal and transverse directions, measuring 126 ft by 115.54 ft. Two C-shaped reinforced concrete shear walls are coupled to a centered I-shaped wall. The walls are designated LSW, MSW, and RSW for left, middle, and right shear walls, respectively. Built-up structural steel I-shaped coupling beams are embedded in both walls and have clear spans of 5 ft. The perimeter steel moment resisting frame is connected to the interior wall system via structural steel beams supporting a metal deck concrete slab.

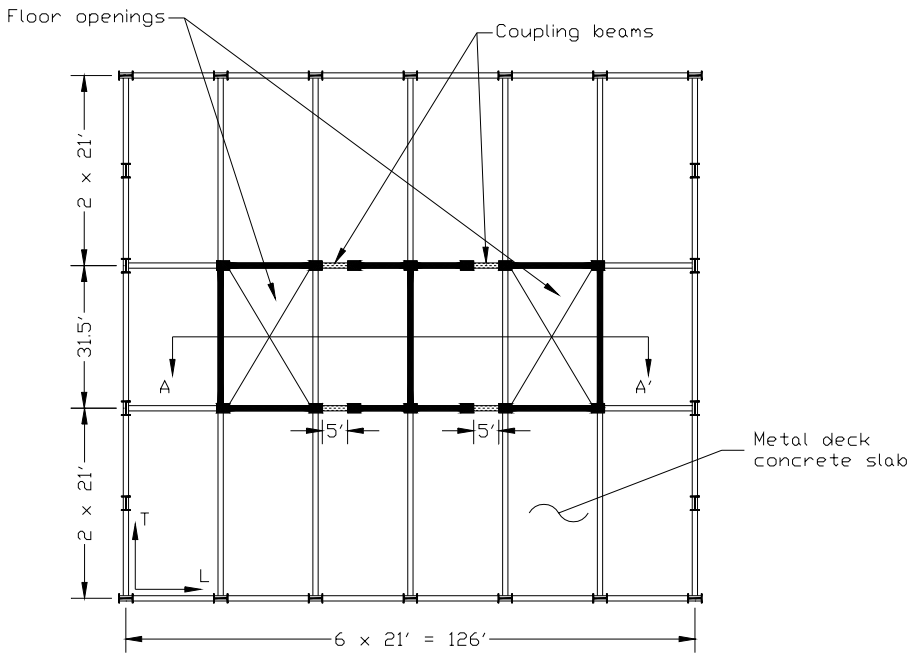

Figure 3.2 Plan View of Theme Structure 4

3.3 Summary of Previous Research by El-Tawil et al (2002) and Kuenzli (2001)

3.3.1 Economy of Coupled Systems

As discussed in section 3.2, El-Tawil et al (2002) conducted research on systems similar to that shown in Figure 3.2 with different coupling ratios varying from 0 to 60%. They observed that improvement in structural efficiency attributed to coupling also lead to improvement in economy. Increases in coupling ratio resulted in substantial reductions in total concrete and steel weights. As shown in Figure 3.3, an increase in CR from 0 to 60% resulted in a 00% reduction in concrete weight and a 00% reduction in rebar weight. Although more structural steel is used as CR increases, there is a net reduction in total steel weight (00%).

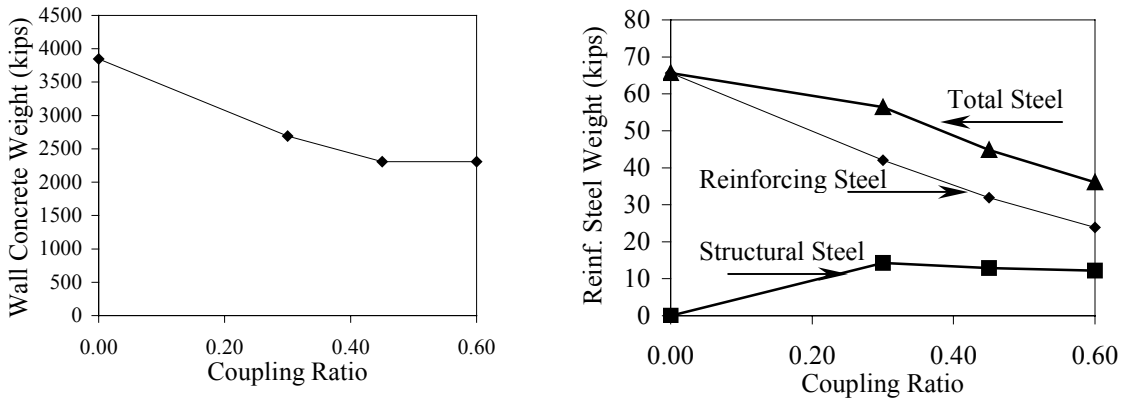

a) Concrete Weight b) Steel Weight

Figure 3.3 Concrete and Steel Weights vs. Coupling Ratio, Kuenzli (2001)

3.3.2 12-Story System Performance

Target Displacement: El-Tawil et al (2002b) observed that **i**ncreasing *CR* resulted in smaller target displacements at the roof level. As shown in Figure3.4a, significant reductions in target displacement from 28.1 in for the uncoupled system to 16.8 in, 14.8 in and 13.2 in for the 30%, 45% and 60% coupled system respectively for the 2/50 hazard level (defined in section 3.5.1). The figure also shows the displacement levels for the 10/50 hazard level (defined in section 3.5.1). The base shear for the four systems is also depicted in Figure 3.4b indicating that walls with different coupling ratios have almost the same strength.

Wall Rotation at the Base: Coupled systems showed average rotations at the wall base equal to 55% of that of the uncoupled system. However, since the allowable limit of wall rotation decreases with the amount of compressive force on the walls, wall rotation of the 60% coupled system with the highest compression exceeded the allowable limit on wall rotation. The uncoupled system also failed to satisfy the rotation limit of FEMA-356 but due to lack of stiffness

Story Drift: The analyses showed that increasing coupling significantly decreases the drift demands on the system. Maximum drift ratios were 1.7%, 1.0%, 0.9% and 0.8% for the uncoupled system, 30%, 45% and 60% coupled systems respectively.

Concrete Crushing: The uncoupled systems experienced crushing in the left and middle shear walls. The 60% coupled system also experienced concrete crushing. Systems with 30% coupling and 45% did not experience concrete crushing.

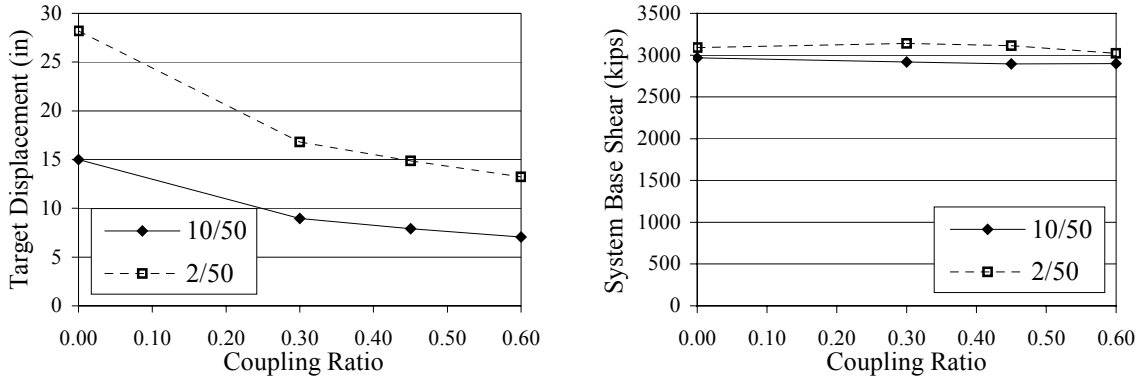

a) Target Displacement b) System Base Shear

Figure 3.4 12-Story System Target Displacement and Base Shear vs. Coupling Ratio Kuenzli (2001)

3.3.3 6-Story System Performance

The 6-story system behavior was observed to be fundamentally different, particularly in terms of the beneficial effects of coupling. For instance, the maximum roof displacement in this system was 8.3 in for the uncoupled system vs. an average of 7.7 in for the coupled systems, i.e. only a 7% reduction in roof (target) displacement (Figure 3.5a). Similar results were obtained for other deformation measures (e.g. wall rotations, story drifts). The maximum base shear on the other hand increased considerably from1226 kips to 3129 kips as the *CR* increases from 0 to 60% (Figure 3.5b). In general, the beneficial effect of coupling in the case of 6-story building was not

as clear as in the case of the 12-story system because the design was dominated by minimum thickness and steel requirements specified in ACI-318.

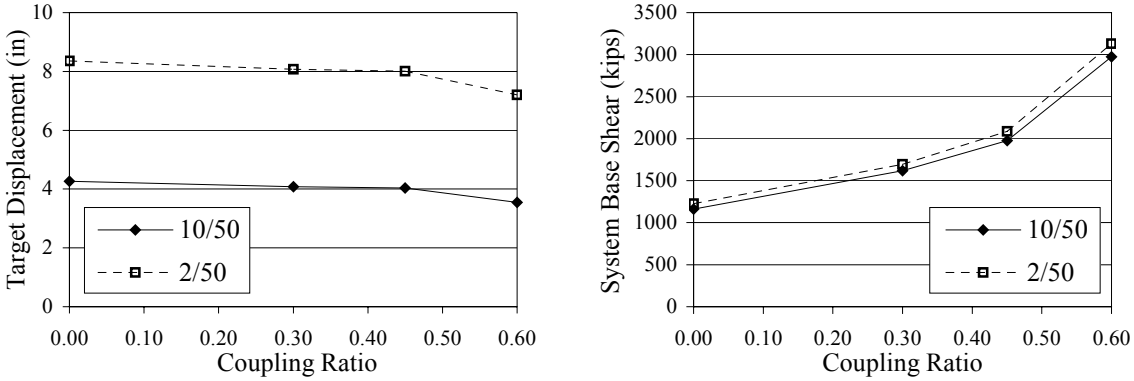

a) Target Displacement b) System Base Shear

Figure 3.5 6-Story System Target Displacement and Base Shear vs. Coupling Ratio Kuenzli (2001)

3.4 Choice of Building Height and Prototype Naming Convention

Two different heights are considered in this research: 12 stories and 18 stories representing mid rise construction. 6-story buildings are not considered based on the observation in El-Tawil et al (2002b) that the design is dominated by minimum requirements thus, does not accurately reflect the effect of coupling.

El-Tawil et al (2002) only conducted push over analysis, which does not represent true system behavior under strong seismic shaking. In this research, dynamic analysis that considers the true nature of ground shaking is conducted for both 12- and 18-story systems. The design procedures and detailing of both types of systems are summarized in this chapter. Detailed procedures for the design of the 12-story systems can be found in Kuenzli 2001 while a description of the 18-story system design is briefly discussed in the next section of this chapter.

For the 12-story and 18-story systems, the total height of the structure is 147 and 219 ft. respectively with a first floor of 15 ft and all upper floors 12 ft.

The different designs are designated HCW-N-CR, where N represents the number of stories, and CR the amount of coupling. For example, HCW-12-U is a 12-story uncoupled system, while HCW-18-30 is a 18-story building with 30% coupling

3.5 Analysis of the system for Design Purposes

3.5.1 Seismic Design Criteria

Among different levels of seismic hazards, design codes specify the *Maximum Considered Earthquake* for design of new buildings. A maximum considered earthquake is a ground motion with 2% probability of exceedance in 50 years referred to as 2% 50 hereafter.

Some major US design building codes categorize the US territories into seismic zones; each with a different level of seismic hazard (i.e. the spectral ground motion acceleration used to design a specific building). For example, the UBC 1997 categorizes the United States into four different seismic zones (zones 1, 2, 3 and 4). On the other hand, other design codes and documents, such as IBC2000, ASCE7-1997 and FEMA-368 (2000) determine the level of seismic hazard based on the exact location of the building site. For this purpose, spectral acceleration is represented by contour lines that cover the entire United States and determine the spectral accelerations S_S and S_1 at short period (0.30 second) and one-second period respectively.

In order to adjust these quantities (S_S and S_1) to the specific site conditions, a *site class* is defined based on the type of soil at the building site. Site classes A through F are defined according to soil parameters such as soil type (rock, sand), density, stiffness and other geo-

technical parameters. Among these categories, site class *D*, which represents a soil profile of average density and stiffness is assumed in this dissertation.

Upon determining the site class, spectral accelerations are adjusted with two coefficients; acceleration-based site coefficient F_a and velocity-based site coefficient F_v. The design spectral acceleration at short period S_{MS} and the design spectral acceleration at one-second period S_{M1} are then determined from which a design response spectrum can be derived as shown in Figure 3.6.

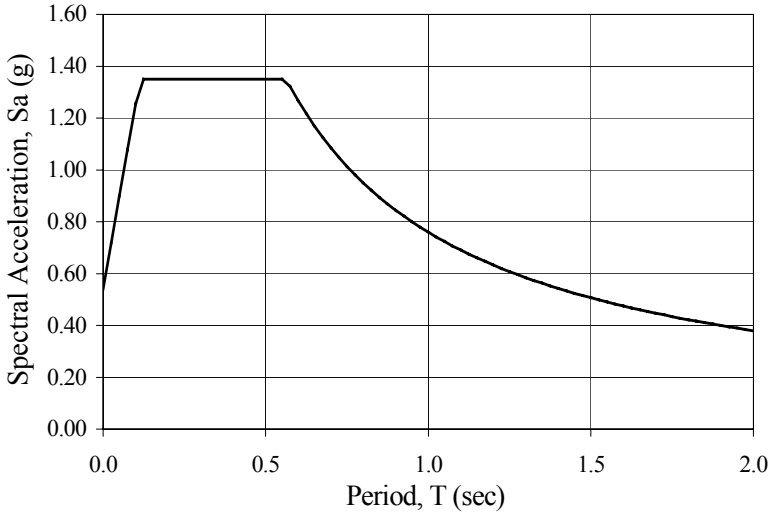

Figure 3.6 Design Response Spectrum

The prototype structure is then categorized as seismic design category *E* according to Tables 4.2.1.a and 4.2.1.b of FEMA-368 (2000). According to Table 5.2.2 in FEMA-368, the design coefficients R, Ω_o, and C_d are 5.5, 2.5, and 5, respectively with a limitation on the building height of 160 foot. To focus the research effort on the HCW response, the steel perimeter moment resisting frames are ignored and the coupled wall system is assumed as the sole lateral load-resisting element in the structure. The structure is categorized as a bearing wall system with special reinforced concrete shear walls.

The 12-story building is 147 ft high and can therefore be designed according to FEMA-368 (2000) provisions. The 18-story however is 219 ft high, which exceeds the limit set by table 5.2.2 for special concrete shear walls for design category *E*. However, wince the hybrid coupled wall system is fundamentally different than the special reinforced concert shear wall system prescribed in the table, it is not clear if the 160 ft limitation will also apply to hybrid coupled walls, which are stronger and stiffer than a corresponding uncoupled shear wall system. It was thus decided to ignore this limit in the design process and evaluate this limitation as part of the research.

The approximate fundamental period is calculated to be 0.84 seconds for HCW-12-30 and HCW-12-U, and 1.0 second for HCW-18-30. For the two 12-story systems, the required wall thickness decreased from 20 inches for the uncoupled wall design to 14 inches for the 30% coupled wall design. This caused some reduction in the total structure weight between the two designs, and thus, a reduction in the design base shears as calculated using the *Equivalent Lateral Force Procedure* (ELFP). The total structure weights were 24,617 kips, 22,219 kips for HCW-12-U and HCW-12-30 respectively.

3.5.2 Analysis Procedures

According to FEMA-368, two procedures are prescribed for the analysis of lateral force resisting system namely; the *Equivalent Lateral Force procedure*, *ELFP,* and the *Modal Analysis Procedure.*

3.5.2.1 Equivalent Lateral Force Procedure: *ELFP*

In *ELFP*, a set of static lateral forces representing the inertial forces of the floors at the fundamental period spectral level is applied to the structure. The basic assumption of the *ELFP* is that the system behavior is dominated by the first mode, and therefore, only the spectral acceleration corresponding to this period is needed to perform the analysis.

For prototype design, base shear is calculated and distributed over the building height according to the procedures in FEMA-368, section 5.3 and summarized below:

$$V = C_s W \tag{3.2}$$

$$C_s = \frac{S_{DS}}{R/I} \tag{3.3}$$

C_s need not exceed the following:

$$C_s = \frac{S_{D1}}{T(R/I)} \tag{3.4}$$

$$T = C_T h_n^{(3/4)} \tag{3.5}$$

Where V is the base shear, C_s is the seismic response coefficient, W is the total dead load of the building; R is the response modification factor defined in 3.1.1 and I is the occupancy importance factor as defined in table 1.4, T is the fundamental period of the structure and h_n is the total building height. For special reinforced concrete shear wall lateral system, C_T is taken as 0.02.

The total base shear calculated from 3.1 is then distributed over the building. At any given level, the lateral force induced at that level, F_x, is determined from the following equations:

$$F_x = C_{vx} V \tag{3.6}$$

$$C_{vx} = \frac{W_x \, h_x^{\,k}}{\sum_{i=1}^{n} w_i \, h_i^{\,k}} \tag{3.7}$$

$$k = 1 + \frac{T - 0.5}{2} \tag{3.8}$$

$1.0 \le k \le 2.0$

Where: C_{vx} is a vertical distribution factor, V is the total design lateral force at the base, w_i and w_x is the weight of floor i or x, hi or h_x is the height from the base to level i or x. Figure 3.7 shows a schematic for the lateral force applied to the different floor levels in the 12-story systems. The magnitudes of the force at each level of the 12-story and 18-story systems are summarized in table 3.1

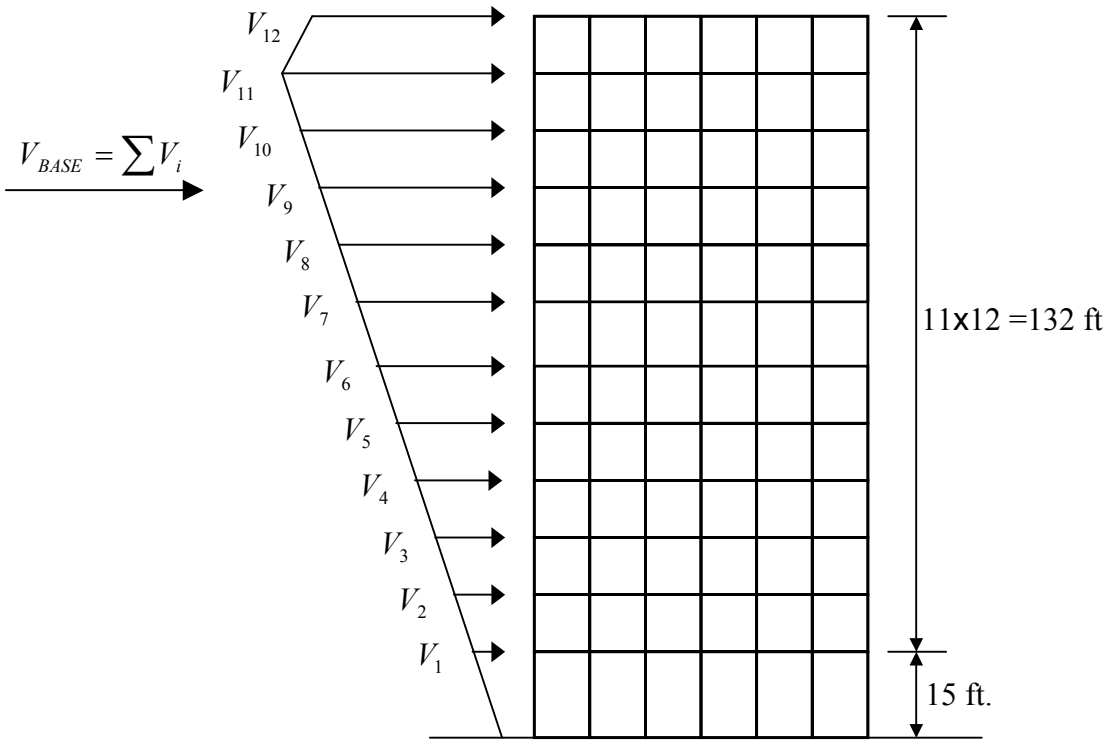

Figure 3.7 Lateral Force Distribution at Story Levels in 12-story Building According to FEMA-368

Table 3.1: Lateral Forces at Floor Levels According to FEMA-368
(a) 18-Story System (b) 12-Story Systems

HCW-18-30	
Floor	Force
1	8.4
2	18.1
3	29.5
4	42.0
5	55.4
6	69.8
7	84.9
8	100.6
9	117.0
10	134.0
11	151.5
12	169.5
13	188.0
14	207.0
15	226.3
16	246.1
17	266.3
18	176.5
V_{Base}	**2290.9**

HCW-12-U		HCW-12-30	
Floor	Force	Floor	Force
1	24.4	1	21.7
2	48.5	2	43.3
3	74.6	3	66.6
4	102.2	4	91.2
5	130.9	5	116.8
6	160.6	6	143.3
7	191.1	7	170.6
8	222.4	8	198.5
9	254.3	9	227.0
10	286.8	10	256.0
11	319.9	11	285.5
12	198.9	12	197.8
V_{Base}	**2014.5**	ΣF_i	**1818.2**

3.5.2.2 Modal Analysis Procedures: *MAP*

Modal Analysis Procedure is basically a dynamic procedure in which masses are assigned to each floor level and damping is defined to represent the dynamic characteristics of the building. The structure is analyzed using *n* number of modes. The number of modes is chosen such that at least 90% of the building mass is participating in the total shear determined at the base of the building.

Unlike the *ELFP* where only one mode (the fundamental mode or the first mode) is used to determine the total base shear and the lateral force distribution grows mostly linearly from the base to the roof, the MAP allows every one of the first n modes to participate in computing the total base shear. For each mode of the first n modes, the spectral acceleration is determined from the response spectrum derived in the previous sections and the total base shear of this mode is determined based on the spectral acceleration and the participation factor of this specific mode. Finally, these base shears are combined together to find the total base shear of all *n* modes.

The effect of the higher modes becomes more significant in taller building. Hence, a modal analysis is conducted to determine the total base shear of the 18-story building and most importantly, the distribution of the lateral force.

A comparison is made between the two procedures, *ELFP* and *MAP* in Figure 3.8. For the *ELFP* and *MAP*, The total base shear is 2290 kips and 2150 kips respectively with only 6% difference. However, The distribution of the lateral force differs significantly, especially at the roof level where the effect of higher modes became more significant. Although the variation in story lateral force is quite high between the two procedures, the variation in story shear force at floor levels is rather smaller (Figure 3.9). For example, the difference in lateral force at the 12^{th} floor reaches 46% while the maximum difference in shear force along the building height (except

for the roof level) is 15% at the 10th floor. At the roof level however, the difference in the story shear force becames more significant

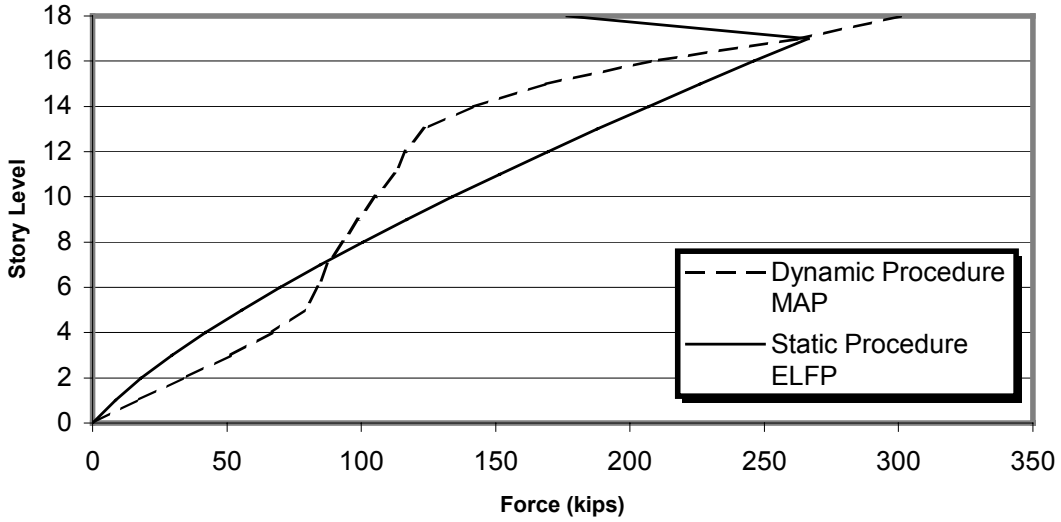

Figure 3.8 Lateral Force Distribution of Linear Static Procedure and Linear Dynamic Procedure in HCW-18-30

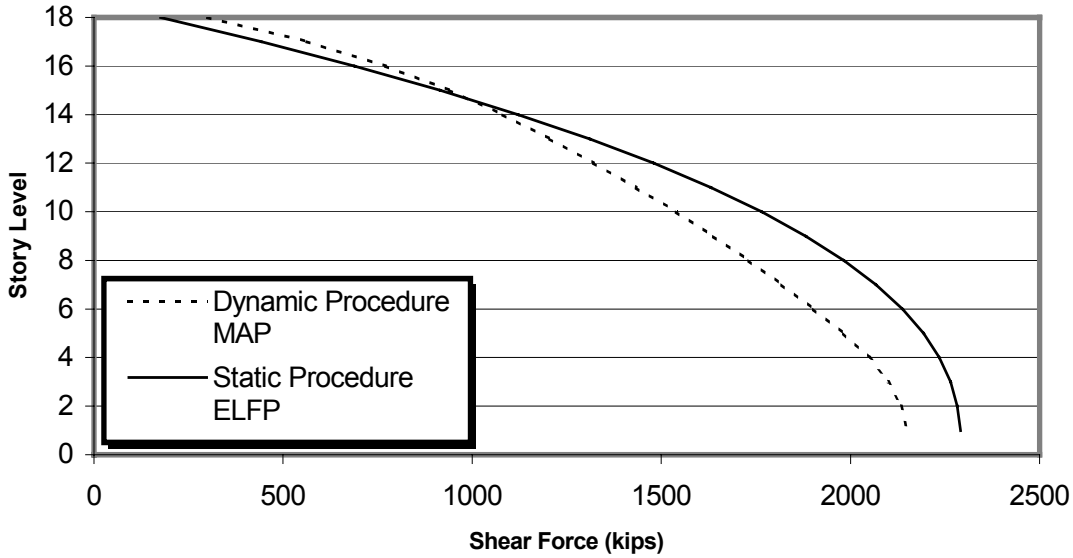

Figure 3.9 Shear Force Distribution of Linear Static Procedure and Linear Dynamic Procedure in HCW-18-30

In summary, except for the roof level, no significant change in the design story shear resulted from the two procedures in the longitudinal direction. Hence, the static procedure is

found to be sufficient in determining the design shear forces required for design of the building. However, as will be discussed in the next sections, the effect of higher modes becomes significant when the wall reaches yield. At that level, the contribution of higher modes to the total base shear increases substantially.

3.5.3 Longitudinal Design Analysis

In order to perform linear analysis on the structural system, reasonable assumption of geometric properties of the different members is necessary. Given that the layout of the structural wall is usually mandated by architectural requirements, the only parameter that is required to size the wall is its thickness. A minimum wall thickness could be estimated based on the ACI318-02 code, which requires wall to be of a minimum thickness $h/30$ where h is the story-height (ACI318-02 14.6.1). The minimum thickness required is also such that the nominal capacity of the section in shear does not exceed the limit specified by ACI318-21.7.4.4.

$$V_n \le 10\sqrt{f_c'}\, A_{cp}$$
$$V_n = V_s + V_c \qquad (3.9)$$

Where V_n, is the nominal shear strength of the wall, V_s and V_c are the web reinforcement and concrete nominal shear strength respectively. A_{cp}, is the cross sectional area of the wall segment.

Since shear demands on the different walls piers can be approximately estimated from the total base shear, V_{base}, based on their relative stiffness, analysis can start with reasonable assumption of the wall thickness. Moment demands obtained from analysis will only affect the

amount of flexural reinforcement required and will not affect the wall thickness based on the shear demands.

The second step before a linear analysis can be started is to assume cross sectional properties of the coupling beams. This assumption will then be checked at the end of the analysis and may need to be modified based on the analysis results. This implies that the design process will be iterative in nature and successive trial analyses need to be performed. Two difficulties are usually associated with such a technique; first the process might not lead to a stable solution. This means too many trials may be involved and a final estimation of shears and moments of the coupling beams that fit the chosen cross section is not obtained. Second, the overall coupling of the system might exceed the amount of coupling required for the system, i.e. there is no control over the coupling ratio.

Because of these inherent difficulties, a capacity design approach was followed such that the force in the coupling beams does not exceed certain limit corresponding to the required coupling ratio. Furthermore, using this procedure, all coupling beams can be designed such that they have the same cross sectional properties and therefore the same capacity, which simplifies construction.

The coupled systems are designed such that the coupling beams yield in shear rather than in flexure. As discussed in the previous chapter, tests have shown that shear-yielding beams are very ductile and are well suited for seismic applications. To achieve the desired amount of coupling in the system, the following design procedure is developed based on a method proposed by El-Tawil et al (2002). The procedure is founded on observations made from the nonlinear analyses reported in El-Tawil and Kuenzli (2001) where most of the coupling beams yielded in

shear prior to the formation of plastic hinges in the walls. This is a key assumption in the design method and is to be further discussed in the next sections.

To start the design process using this method, a suitable coupling ratio is defined and the seismic lateral loading is calculated based on the structure's weight. As noted before, for construction convenience, it is assumed that coupling beam properties are uniform over the height of the entire structure. Figure 3.10 shows this system and the forces induced by application of the seismic loading. With similar beams between both sets of walls, LSW-MSW and MSW-RSW, the tensile and compressive axial loads induced in the LSW and RSW by the coupling action are equal. Therefore, from Equations 3.10 and 3.11, the coupling ratio is:

$$CR = \frac{C.S}{V_{Base}.h} \tag{3.10}$$

From statics, vertical equilibrium of forces acting on the RSW yields:

$$C = T = N.V_{beam} \tag{3.11}$$

Where N is the number of floors. Substitution of Equation 3.11 into 3.10 and solving for the beam shear resulted in:

$$V_{beam} = \frac{CR.h.V_{Base}}{N.S} \tag{3.12}$$

Where:

V_{beam} is the shear demand on the coupling beams.

CR is the design-coupling ratio as defined previously

C and T are the axial compression and tension induced by the coupling action at the base of the walls.

h is the height of the resultant of the floor lateral forces

V_{base} is the total system base shear.

N is the number of stories.

S is the distance between the centroids of LSW and RSW.

With the coupling ratio, seismic lateral loading, and distances between wall centroids known, the required shear to be transmitted between adjacent walls by each coupling beam can be calculated readily using Equation 3.12. The coupling beams are then detailed to yield in shear at this load prior to flexural yielding.

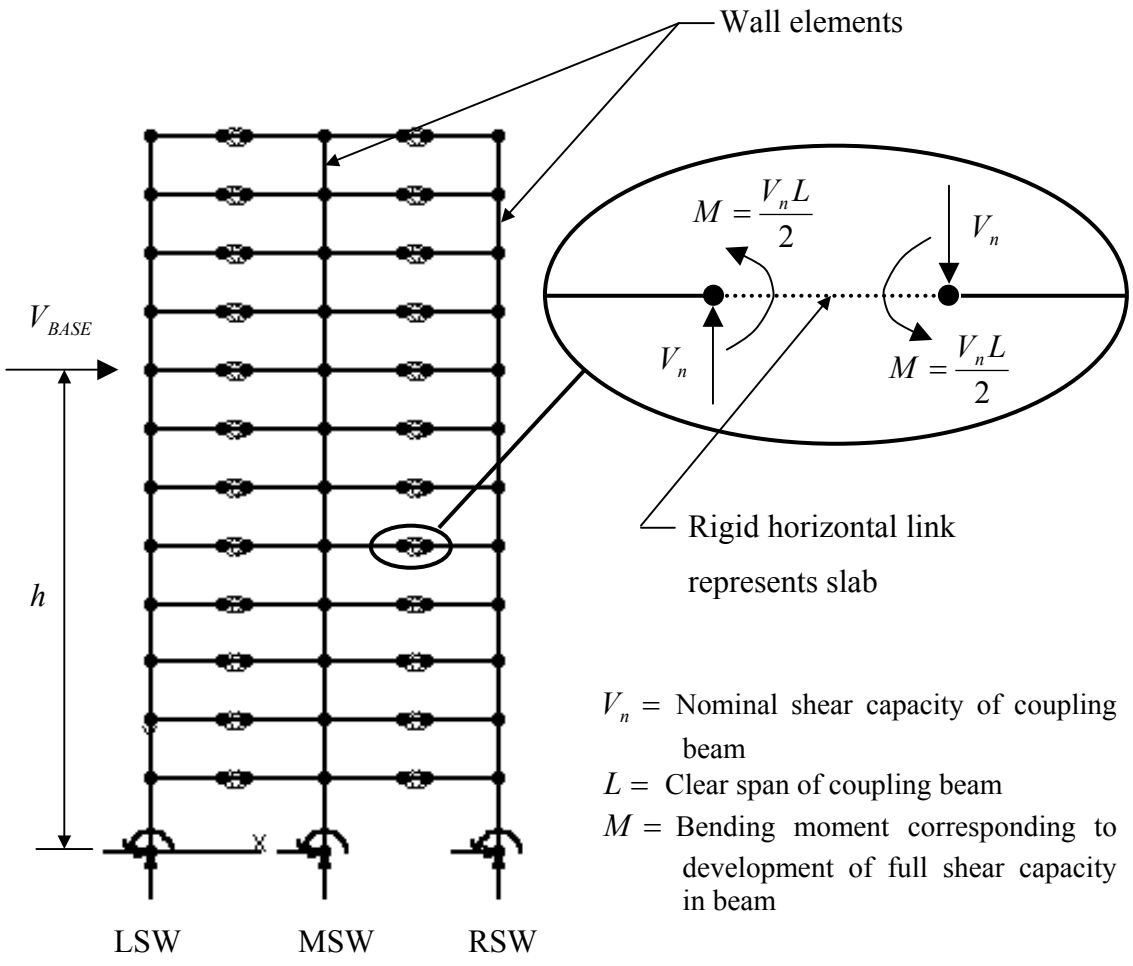

Figure 3.10 Longitudinal Elastic Model

An elastic frame model is used to determine wall forces. In the frame model shown in Figure 3.10, walls are represented by beam-column elements located at each wall's gross section centroid and rigid elements model the finite size of these walls. All beam-column elements specified are capable of deforming in both shear and bending. The base is assumed as fixed in accordance with FEMA-368 (2000) and the effective flange width is calculated in both tension and compression according to ACI (1999). To account for the cracking of concrete and the resulting drop in stiffness, a reduced moment of inertia as suggested in the ACI code (1999) is used for the walls.

$$I_{eff} = 0.35 I_g \tag{3.13}$$

Where: I_{eff} = Effective moment of inertia taking into effect crack of concrete

I_g = Gross moment of inertia

To further account for cracking, 75% of the wall web area was used for the shear area in the wall elements.

In accord with the assumption that all coupling beams will yield in shear prior to the shear walls reaching their flexural capacity, shear forces equal to the nominal shear strength of the coupling beams and corresponding moments are applied to the walls in place of the beams. The concrete slabs at the floor levels acted as rigid diaphragms that tie all the walls together such that all the walls have the same horizontal displacement at the floor levels. The resulting analysis setup for seismic loading is shown in Figure 3.10 Gravity loads calculated using each wall's tributary area are applied to the model, and factored design forces on the walls are then determined.

According to the load criteria given by FEMA-368 (2000), member forces caused by earthquake are calculated using the following expression:

$$E = \rho Q_E \pm 0.2 S_{DS} D \quad (3.14)$$

Where: $E =$ Member force due to horizontal and vertical seismic loading

$Q_E =$ Member force due to horizontal seismic loading from analysis

$\rho =$ Reliability factor calculated in accordance with FEMA-368 (2000)

$S_{DS} =$ Design short period spectral acceleration

$D =$ Member force due to dead loading from analysis

This latter term accounts for the vertical effect of the earthquake in calculation of the ultimate member forces. Combinations of loads for critical member forces are calculated in accordance with ASCE 7 (1995) as required by FEMA-368 (2000). Thus:

$$U = 1.2D + 1.0E + 0.5L \quad (3.15)$$

$$U = 0.9D \pm 1.0E \quad (3.16)$$

Where: $U =$ Ultimate load effect

$D =$ Dead load effect

$E =$ Earthquake load effect as calculated in equation 3.14

$L =$ Live load effect

Equation (3.15) is used when the effect of the seismic load, E, is additive to those of the gravity loads (D and L), while the latter equation is used when seismic and gravity effect counteract each other.

3.5.4 Transverse Design Analysis

The system is modeled in the transverse direction in the same fashion as in the longitudinal direction except that there are no coupling beams in this direction. Again, walls are

linked together by a rigid diaphragm to ensure that walls have the same horizontal displacement at the floor levels. Effective moments of inertia of the wall sections are used in order to assess the lateral deflection of the building based on the cracking properties. Ultimate member forces are calculated using the same expression in 3.15 and 3.16.

3.6 Design of the Coupling Beam

The coupling beams are designed to yield in shear in the web prior to reaching moment capacity according to the method proposed by Harries et al. (1993) in conjunction with the AISC Seismic Provisions (1997) for shear links in an eccentrically braced frame. This design procedure results in beams with thin webs and thick, heavy flanges. Built-up plate-girders are used since suitable sections cannot be found in the AISC (1993) tables. Additional steel reinforcement in the wall embedment region is not needed for crack control since vertical reinforcement provided from wall design is more than adequate. The Design procedures are briefly summarized below:

Step 1: As a start point, the thickness of the flange and the total height of the section is assumed. According to AISC-LRFD (1997), the thickness of the web is calculated based on the following formula:

$$V_u \le \phi_v V_n = \phi_v (0.60)(d - 2t_f) t_w f_y \qquad (3.17)$$

Where V_u and V_n is the ultimate shear force demand and the nominal shear capacity of the coupling beam respectively, ϕ_v is a strength reduction and is equal to 0.9, d the total height of the section, t_f is the assumed flange thickness and f_y is the yield stress of the structural steel.

Step 2: To ensure that the beam yields in shear prior to yielding in flexure, the moment demand on the beam is calculated based on a magnified nominal shear capacity of the beam V_p that

accounts for the potential over strength due to the strain hardening effect. Where V_p is equal to 1.25 V_n.

$$\phi_b M_n = \left(\frac{L}{2} + c\right) V_p \tag{3.18}$$

Where f_b is the bending strength reduction factor and is equal to 0.9, M_n is the nominal flexural strength of the beam corresponding to V_p, L is the clear length of the beam (5 feet), c is the concrete cover at the interface of the beam and the shear wall.

Step 3: Based on M_n, the plastic modulus of the section and the required flange width are calculated from the following equations:

$$z_x = \frac{M_n}{f_y} \tag{3.19}$$

$$b_f = \frac{z_x}{\left(d - t_f\right) t_f} \tag{3.20}$$

Step 4: The required embedment length of the beam inside the concrete shear wall is calculated based on the provisions of the PCI design handbook for steel brackets embedded in concrete.

$$V_c = \frac{0.85 f_c' b L_e}{1 + 3.6 e / L_e} \tag{3.21}$$

Where V_c is the nominal embedment of the concrete, f_c' is the concrete compressive strength, b is the width of embedment region and is equal to the width of the coupling beam flange, L_e is the embedment length and e is equal to half of the beam clear span + $L_e/2$. The coupling beam forces and dimensions are shown in Figure 3.11.a and 3.11b respectively. Since the shear demand on the coupling beams for both the 12-story and the 18-story is almost equal, identical coupling beams are used for both systems.

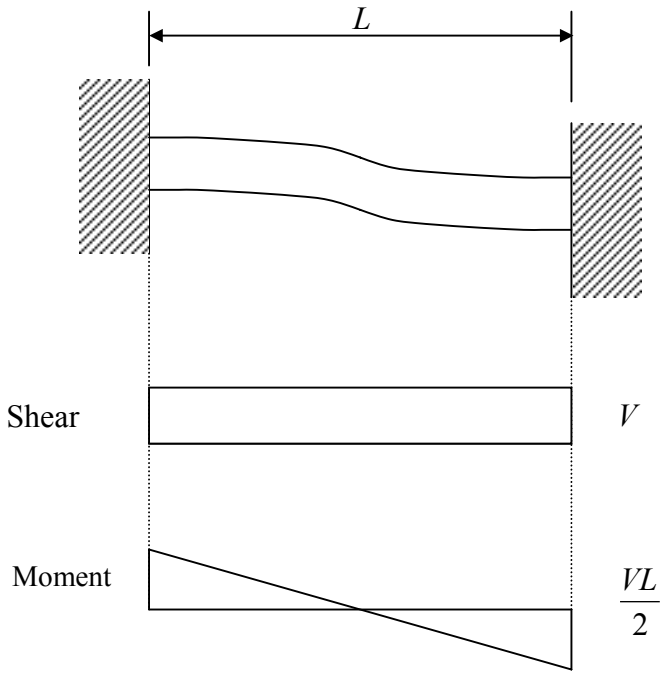

a) Coupling Beam Forces

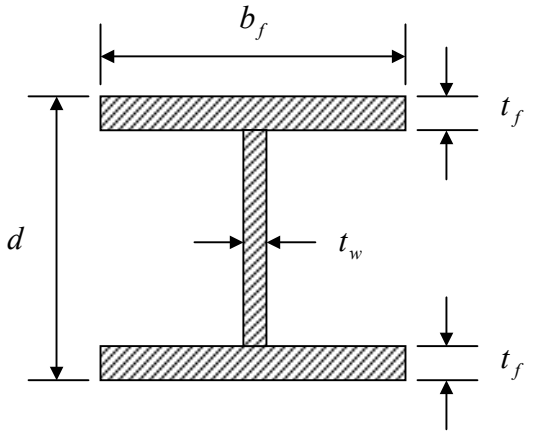

d =13 in.

b_f=6.5 in.

t_f=1.25 in.

t_w =0.3125 in.

L = 60 in.

Embedment length L_e= 20 in.

b) Coupling Beam Dimensions for both HCW-12-30 and HCW-18-30 systems

Figure 3.11 Coupling Beam, Forces and Dimensions

3.7 Shear Wall Design

The walls are designed as special reinforced concrete shear walls according to ACI-318 (1999) and FEMA-368 (2000). To ensure a flexural yielding mechanism, factored shear forces at each floor were magnified according to Paulay and Priestley's (1992) recommendation. To prevent rapid deterioration of the wall base at the compressive boundary due to crushing, certain parts of the system require heavy transverse reinforcement to confine the concrete according to ACI-318 (1999).

3.7.1 Design for Shear Force

When excited with ground shaking, a shear wall behaving in an elastic manner responds in a combination of several modal shapes as shown for the cantilever in Figure 3.12a. While it's true that the first modal shape dominates the dynamic response of shorter walls, the contribution of higher modes to the total response increases as the cantilever height increases. When a plastic hinge forms at the base of the cantilever, the participation of the first mode drops dramatically and the effect of the second and higher modes becomes important. This is illustrated in the following example.

Table 3.2 Modal Contribution Factors to Base Shear for a Cantilever with Different base Conditions

Base Condition	First Increment: Fixed Base				Second Increment: Plastic Hinged at Base			
Mode	T (sec)	r_n	S_a (g)	V_b/W	T (sec)	r_n	S_a (g)	V_b/W
1	2	0.64	0.38	0.24	11.66	0.75	0.06	0.045
2	0.31	0.20	1.35	0.27	0.46	0.2	1.35	0.27

To illustrate the effect of inelastic behavior on the base shear, the dynamic behavior of the cantilever in Figure 3.12c is considered. The cantilever is assumed to have a total length of 10 ft with concentrated unit masses lumped at each 1 ft of its height. Elastic material properties are arbitrary assumed so that the cross-sectional area is identical to the coupling beam area in Figure 3.12b. The problem is solved on incrementally on two steps; the first increment represents the response in elastic range before formation of plastic hinge at the base. In the second increment, a plastic hinge is created at the base of the cantilever and the incremental base shear is computed for the updated dynamic characteristics of the structure. The total response of the system after the plastic hinge is formed is obtained by adding the results of both increments. The plastic hinge at the base is created by reducing the stiffness of the lower part of the cantilever to 1% of its initial value.

Table 3.2 summarizes the obtained results from modal analysis for both systems. For fixed base condition, the fundamental period of the structure is 2 seconds while the 2^{nd} mode is 0.31 second. The modal participation factors r_n for the both modes are 64% and 20% for the first and second mode (other higher modes are ignored for simplicity) the spectral acceleration from the response spectrum in Figure 3.6 are 0.38g and 1.35g. The contribution of each mode to the base shear is calculated by multiplying the weight contributions of both modes with the spectral accelerations. The base shears of the first and second modes are $0.24W$ and $0.27W$ respectively.

To represent formation of a plastic hinge at the cantilever base, the element at the base of the cantilever is softened by reducing its stiffness to 1% of its original stiffness. As illustrated in Table 3.2, the fundamental period of the cantilever increases dramatically to 11.66 second while the second period decreases slightly to 0.46 second. The base shear contribution factors greatly change from the case of fixed condition. The spectral acceleration corresponding to the first

mode dramatically decreases to 0.06g while the one corresponding to the second mode is the same as before. Therefore, the majority of the base shear in this case comes from the second mode

Elastic analysis procedures provided by design codes do not recognize this issue and either prescribe linear static or at the best, linear dynamic procedures that will not capture such shear magnification caused by the second mode beyond the yield limit of the wall.

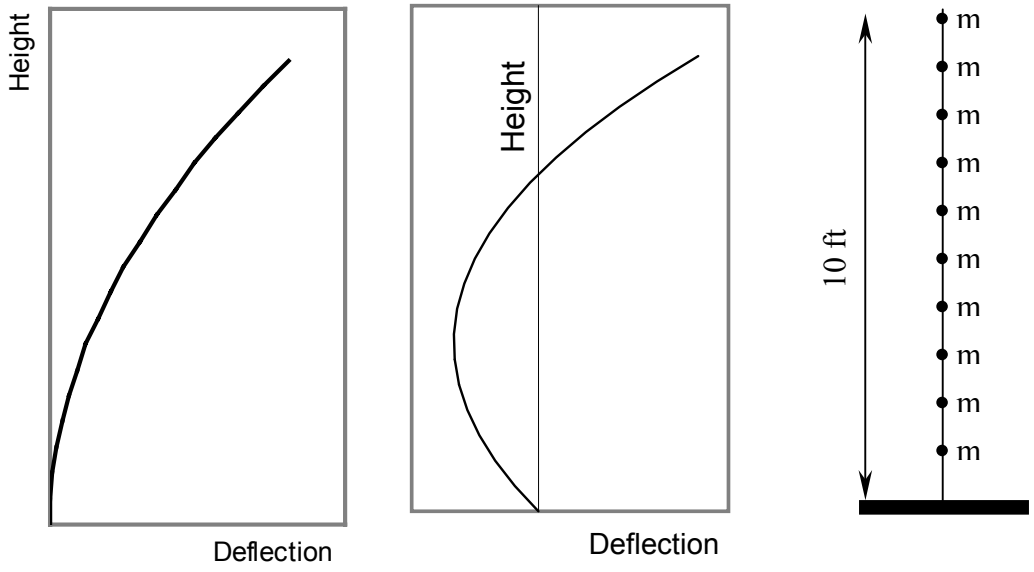

a) First Mode Shape b) Second Mode Shape c) Mass Distribution

Figure 3.12 Mode Shapes

From the above discussion, the worst case scenario for flexural design is to design the wall to take as much moment as attracted from the first mode (as specified by most design codes); while the worst case scenario for shear design is to take into account the effect of higher modes on the system base shear. Although, US major Design Codes (UBC 1997, IBC 2000) do not address the issue, it is addressed in the New Zealand Standard Code of Practice for the

Design of Concrete Structures (NZS, 1982) in an approximate manner as motioned in Paulay and Priestley's (1992):

$$V_u = \omega_v \phi_{o,w} V_E \tag{3.22}$$

Where: ω_v = Dynamic shear magnification factor

$\phi_{o,w}$ = Flexural over-strength factor

V_E = Code-specified lateral force

V_u = Total design shear

The flexural over-strength factor is taken as 1.25 and the dynamic shear magnification factor is calculated according to (NZS, 1982):

$$\omega_v = 1.3 + \frac{n}{30} \tag{3.23}$$

Where: n = Number of stories (for buildings 6 stories or more)

3.7.2 Check for maximum drifts

Following the procedures in section 3.4.1, the wall thickness is assumed to satisfy the shear strength requirements ($V_n \le 10\sqrt{f_c'}\, A_{cp}$), and an elastic model of the system is created considering the cracked section properties of the concrete shear walls (per equation 3.13) and the elastic properties of the steel coupling beams. The elastic displacements at the floor levels are obtained from the model. According to FEMA-368, the inelastic displacements are obtained by magnifying the elastic displacements from the linear elastic analysis using the following equation given by FEMA-368

$$\delta_x = \frac{C_d \delta_{xe}}{I} \tag{3.24}$$

Where: δ_{xe} = Elastic displacement at story x

δ_x = Anticipated inelastic displacement at story x

C_d = Deflection amplification factor as defined in 3.2.1.

Then, story drifts are determined at each floor level and compared to those prescribed in Table 5.2.8 in FEMA-368. If the anticipated story drifts exceed this limit, the wall thickness is increased and the system is reanalyzed. The effect of concrete cracking must be accounted for in assessing the elastic deformation as specified in ACI-318-02.

In the capacity design method used in designing the system, the steel coupling beams are assumed to reach their yield point early and hence, in the elastic model created in order to compute wall forces, coupling beams are replaced by a vertical force equal to their nominal capacity. This approach has yielded a reasonable solution for the 12-story system where drifts are found within the allowable limit of FEMA-368. For the 18-story system, the magnified displacement at the roof level (based on *Cd=5*) is 80 inches, which results in drifts that considerably exceed the allowable limits of FEMA-368. To resolve the situation, the thickness of the wall has to increase to nearly 30 inches or more instead of the current design of 20 in thick walls. For this reason, a critical evaluation of the method prescribed by FEMA-368 is made by comparing the results of the dynamic analyses (presented later in chapter 6) with the method as suggested by equation 3.24. It must be noted that by replacing the coupling beams with vertical loads equal to their nominal capacities, the inelastic deformation caused by the coupling beam yielding are implicitly accounted for and therefore, magnifying the entire displacement from the elastic model described above is simply double counting the inelasticity effect of the coupling beams.

To ensure that the inelastic deformation of the coupling beams are not counted twice, the total displacement of the system is resolved into two components, one that represents the contribution of the yielding coupling beam. This component need not be magnified by the factor, C_d, because it already results from a system with yielding beams. The second component represents the contributions of the cracked walls. This latter one is magnified because the properties of cracked concrete do not include the inelasticicity of the reinforcing steel. The following expression represents the concept:

$$\delta_x = \frac{C_d (\delta_{xe})_w}{I} + (\delta_{xe})_{cb} \tag{3.25}$$

Where: $(\delta_{xe})_w$ is the wall contribution to displacements from the elastic model, $(\delta_{xe})_{cb}$ is the contribution of the yielding coupling beams.

The first component can be computed by representing the coupling beams in another elastic model with their *'elastic'* properties, as if yielding of coupling beam will not occur, δ_1. The second component is the difference between the displacements computed from the original model, δ_2 (the one of the capacity design method) and the latter one with elastic properties for the coupling beams, δ_1 and will represent the effect of coupling beam yielding. For the 18-story system, $\delta_1 = 3.25$ *in* and $\delta_2 = 16.45$ *in. Hence:*

$$(\delta_{xe})_w = \delta_1 \tag{3.26}$$

$$(\delta_{xe})_{cb} = \delta_2 - \delta_1 \tag{3.27}$$

The maximum roof displacement based on the proposed method is *29.45 in* and the drifts are within the allowable limits. For the 12-story system with 30% coupling, $\delta_2 = 5.13$ *in* and $\delta_1 = 4.1$ *in.* Hence, maximum roof displacement is *21.5 in*. The proposed method will be evaluated later in chapter 6 in light of the results of dynamic analysis.

3.7.3 Design for flexure and axial force

Upon sizing the shear walls based on the requirements of both shear strength and story drift limit, the wall section is designed for combined axial force and bending moments. Demands at the different stories are determined from the linear analysis performed on the elastic model as explained in section 3.2.3. . In order to insure that the plastic hinge forms at the base of the wall while the rest of it remains elastic, a moment envelope is drawn as suggested by Paulay and Priestley (1992) where the moment at the wall base is considered constant for the first two floors. A linear relationship is assumed throughout the rest of the wall height as illustrated in Figure 3.13.

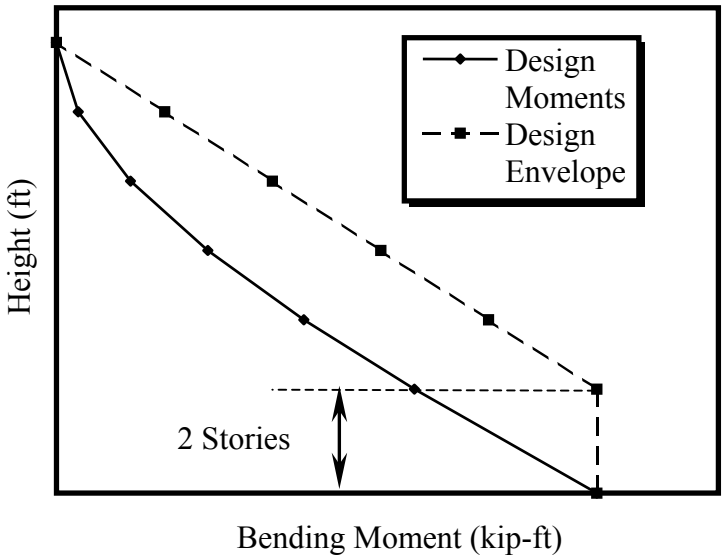

Figure 3.13 Design Moment Envelope

The flexural reinforcement in the wall boundary zones, wall flanges and wall web is determined based on the combined axial load and moments in both longitudinal and transverse directions. Then, an interaction diagram is created for the designed section and the demands are plotted versus the ultimate capacity of the section. An iterative procedure is needed to optimize

the design such that the demands on the wall section are close enough to the ultimate capacity of the section as illustrated in Figure 3.14.

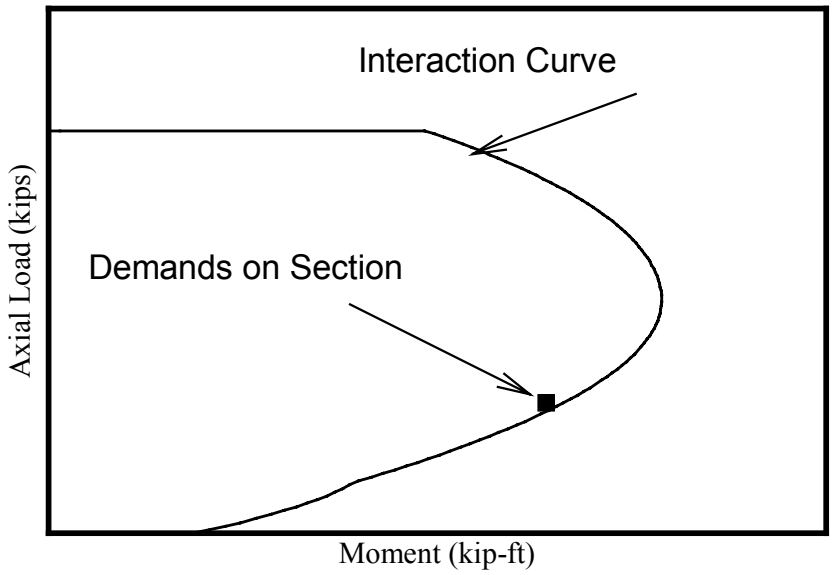

Figure 3.14 Interaction Curve for the Wall Cross Section

3.7.4 Check for transverse reinforcement at the boundary regions

One critical aspects of seismic design of shear walls is to evaluate the possibility of nonductile behavior at the boundary zones of the wall. Under cyclic loading, these regions become more vulnerable to concrete crushing, spalling and buckling of main flexural reinforcement, which increases the potential for non-ductile behavior of the wall. The cross sectional of the wall at the base is analyzed under the given bending moment and axial force and the depth of the neutral axis, *c*, is obtained. If c exceeds the limit set by ACI-318, as calculated by equation 3.25, special transverse reinforcement is provided per ACI-318, 21.7.6.4.

$$c_{\max} = \frac{l_w}{600\left(\delta_u / h_w\right)} \tag{3.28}$$

Where: l_w is the wall length, δ_w is the maximum inelastic wall deflection at the roof level as predicted by equation 3.24 and h_w is the total height of the wall. Equation 3.25 is based on a displacement based design approach where rotation of the wall at its base is approximated by the magnitude (δ_u / h_w) and the permissible unconfined concrete strain is limited to 0.003 radians. Based on this approach, increase of neutral axis depth beyond the limit in equation 3.28 implies increase of the concrete strain at the boundary zones beyond 0.003 radians and hence the need for confinement detailing. The assumption that the wall rotation at the base is equal to (δ_u / h_w) implies that the dynamic response of the wall is predominantly dictated by its first mode; an assumption to be evaluated based on the results obtained from dynamic analysis.

Reinforcement details for shear walls are presented in Figures 3.15 through 3.17

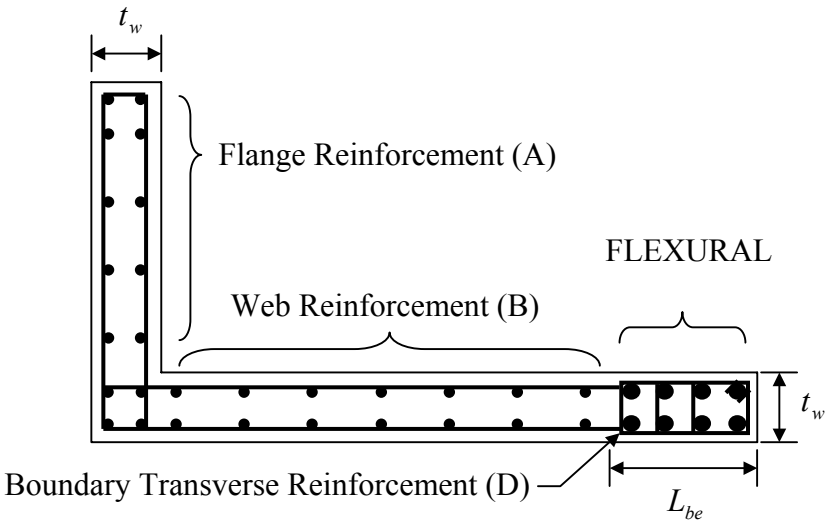

a) LSW and RSW

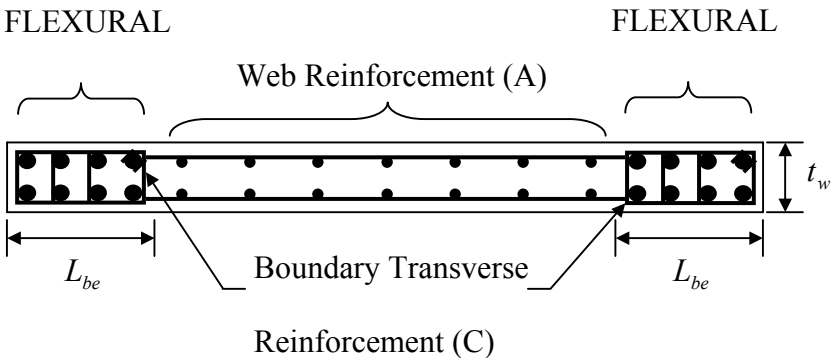

b) MSW

Figure 3.15 Reinforcement layout of the Shear Walls

		Dimensions		A		B			
System	Floors	t_w (in)	L_{be} (in)	Horiz.	Vert.	Horiz.	Vert.	C	D
HCW-12-U	1-2	20	46	#6@7.5"	#4@7.5"	#5@9"	#4@7.5"	16-#14	#5@3"
	3-4	20	40	#6@8.5"	#4@7.5"	#5@10"	#4@7.5"	14-#14	#4@8"
	5-6	20	40	#5@7"	#4@7.5"	#4@7.5"	#4@7.5"	14-#11	#4@8"
	7-8	20	28	#5@8.5"	#4@7.5"	#4@7.5"	#4@7.5"	10-#10	#3@8"
	9-10	20	28	#4@7.5"	#4@7.5"	#4@7.5"	#4@7.5"	10-#7	#3@8"
	11-12	20	--	#4@7.5"	#4@7.5"	#4@7.5"	#4@7.5"	--	--
HCW-12-30	1-2	14	42	#6@9"	#5@7.5"	#5@8"	#4@8"	8-# 11	#5@3.5"
	3-4	14	22	#6@10"	#5@8.5"	#5@8.5"	#4@9"	8-# 10	#3@8"
	5-6	14	22	#5@8"	#5@10.5"	#5@10"	#4@11"	8-# 9	#3@8"
	7-8	14	22	#5@9.5"	#4@8.5"	#4@8"	#4@11"	8-# 7	#3@8"
	9-10	14	10	#4@9.5"	#4@11"	#4@11"	#4@11"	4-# 6	#3@8"
	11-12	14	--	#4@11"	#4@11"	#4@11"	#4@11"	--	--
HCW-18-30	1-2	20	40	#6@6"	#7@6	#5@6"	#7@6	10# 14	#5@3"
	3-4	20	40	#6@6"	#6@5	#5@6"	#6@6	10# 14	#5@8"
	5-6	20	35	#6@6"	#6@7	#5@7"	#6@7	8# 14	#4@8"
	7-8	15	35	#6@7"	#6@8	#5@7"	#6@8	12# 11	#4@8"
	9-10	15	30	#6@8"	#6@12	#5@9"	#6@12	10# 9	#4@10"
	11-12	15	30	#6@10"	#5@12	#5@12"	#5@12	12# 6	#4@12"
	13-14	10	30	#5@9"	#5@12	#5@16"	#4@12	12# 6	#4@12"
	15-16	10	30	#4@10"	#4@12	#4@15"	#4@12	-	
	17-18	10	30	#4@15"	#4@12	#4@15"	#4@12	-	

Figure 3.16 LSW&RSW Designs

		Dimensions		A		B	C
Design	Floors	t_w (in)	L_{be} (in)	Horiz.	Vert.		
HCW-12-U	1-2	20	46	#5@10"	#4@7.5"	16-#14	#5@3"
	3	20	40	#5@10"	#4@7.5"	14-#14	#5@3"
	4	20	40	#5@10"	#4@7.5"	14-#14	#4@8"
	5-6	20	34	#4@7"	#4@7.5"	12-#11	#4@8"
	7-8	20	28	#4@7.5"	#4@7.5"	10-#9	#3@8"
	9-10	20	16	#4@7.5"	#4@7.5"	6-#6	#3@8"
	11-12	20	--	#4@7.5"	#4@7.5"	--	--
HCW-12-30	1-2	14	42	#5@9"	#4@7.5"	12-#11	#5@3.5"
	3	14	42	#5@9"	#4@7.5"	10-#11	#5@3.5"
	4	14	28	#5@9"	#4@7.5"	10-#11	#4@8"
	5-6	14	22	#5@10"	#4@7.5"	8-#9	#3@8"
	7-8	14	22	#4@8.5"	#4@10.5"	8-#7	#3@8"
	9-10	14	--	#4@11"	#4@11"	--	--
	11-12	14	--	#4@11"	#4@11"	--	--
HCW-18-30	1-2	20	40	#6@7"	#5@6"	16#14	#5@3"
	3-4	20	40	#6@7"	#5@6"	16#14	#5@3"
	5-6	20	35	#6@8"	#5@7"	14#14	#4@8"
	7-8	15	35	#6@9"	#5@9"	12#14	#4@8"
	9-10	15	30	#5@7"	#4@8"	16#11	#4@12"
	11-12	15	30	#5@9"	#4@12"	14#11	#4@12"
	13-14	10	20	#4@7"	#4@16"	14#9	#4@15"
	15-16	10	20	#4@14"	#4@16"	10#9	#4@15"
	17-18	10	-	#4@15"	#4@16"	-	-

Figure 3.17 MSW Designs

3.8 Summary

In this chapter, previous research conducted on the design of coupled wall system has been discussed. Based on the observed trends of behavior of both 6- and 12-story systems studied, the current work is dedicated to investigate the behavior of mid-rise systems more extensively. The capacity design method used to design the coupled systems is illustrated. The shortcomings of the static linear and nonlinear procedures are discussed and the motivation for performing dynamic analysis is illustrated. Design details for uncoupled and coupled12-story systems and coupled 18-story system are presented

CHAPTER 4: FINITE ELEMENT MODELING AND CONSTITUTIVE FORMULATION

4.1 Finite Element Modeling

The finite element method has been widely used for the analysis of reinforced concrete structures since the late 1960's. The essence of the method is to discretize the structure into a finite number of subdivisions or 'finite elements'. Elements share common boundaries and are connected to each other at their corners or edges at specific points (nodes). Different types of elements have been developed to represent the different components of reinforced concrete structures including elements that represent structural steel, reinforcing steel, concrete and the interaction between steel and concrete. Specification of applied loads, boundary conditions and constrains complete the definition of a finite element representation of a RC structure.

Throughout this dissertation, a software package called DIANA 7.1 (2001) is used to solve the finite element problem. DIANA is chosen because of its powerful capabilities for analyzing reinforced concrete problems. The program features a variety of elements and mateial models that were found to be particularly useful. Moreover, DIANA permits the use of user-defined material models, which allowed its capabilities to be customized for this research. This chapter describes the finite element modeling technique used in this work.

4.1.1 Modeling of Shear Wall

Walls are represented by the 4-node plane stress element shown in Figure 4.1.a. The element is based on an '*isoparametric'* formulation. The displacement field within the element is defined using bi-linear interpolation between the displacements at the four nodes such that:

$$\left.\begin{aligned} u &= N_1 u_1 + N_2 u_2 + ... + N_4 u_4 \\ v &= N_1 v_1 + N_2 v_2 + ... + N_4 v_4 \end{aligned}\right\} \quad (4.1)$$

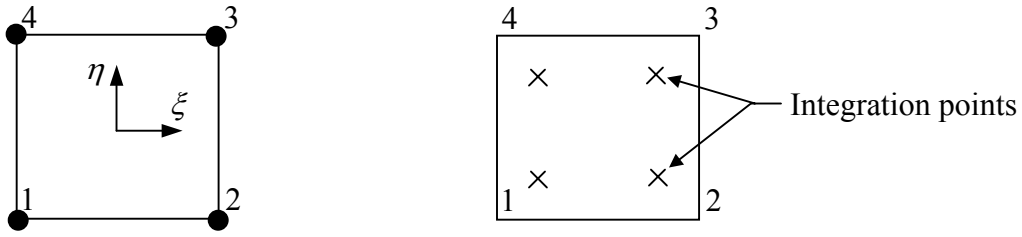

a) 4-Node Element Natural Coordinates b) 2x2 Integration Scheme

Figure 4.1 Element Connectivity and Natural Coordinate System

Where:

N_1, N_2, N_3 and N_4 are the displacement functions defined in equation 4.2

$$\left.\begin{aligned} N_1 &= \tfrac{1}{4}\ (1-\xi)\,(1-\eta) \\ N_2 &= \tfrac{1}{4}\ (1-\xi)\,(1+\eta) \\ N_3 &= \tfrac{1}{4}\ (1+\xi)\,(1-\eta) \\ N_4 &= \tfrac{1}{4}\ (1+\xi)\,(1+\eta) \end{aligned}\right\} \quad (4.2)$$

Where:

ξ and η are natural coordinates as shown in Figure 4.1a and range from –1 to 1

u_1, u_2, u_3 and u_4 are the nodal displacement of the element nodes in global x direction

v_1, v_2, v_3 and v_4 are the nodal displacement of the element nodes in global y direction

u and v are the displacements of any arbitrary point of coordinates ξ and η in x and y directions respectively.

Strains at any arbitrary point are then expressed in terms of the displacement obtained in 4.1.

$$\left.\begin{aligned} \varepsilon_{xx} &= \frac{\partial u_x}{\partial x} \\ \varepsilon_{yy} &= \frac{\partial u_x}{\partial y} \\ \gamma_{xy} &= \frac{\partial u_x}{\partial y} + \frac{\partial u_y}{\partial x} \end{aligned}\right\} \qquad (4.3)$$

The expression can be written in matrix form as follows:

$$\{\varepsilon\} = [B] \times \{\delta\} \qquad (4.4)$$

$$\{\varepsilon\} = \begin{Bmatrix} \varepsilon_{xx} \\ \varepsilon_{yy} \\ \gamma_{xy} \end{Bmatrix}, \quad \{\delta\} = \begin{Bmatrix} u \\ v \end{Bmatrix}, \quad [B] = \begin{Bmatrix} \frac{\partial}{\partial x} & 0 \\ 0 & \frac{\partial}{\partial y} \\ \frac{\partial}{\partial y} & \frac{\partial}{\partial x} \end{Bmatrix} \qquad (4.5)$$

Where ε_{xx} and ε_{yy} and are normal strains in x and y directions respectively, γ_{xy} is the shear strain at point (ξ, η). For elastic conditions, stresses at any point are related to the strains via the conventional elasticity matrix. For a plane stress element, this relationship is:

$$\{\sigma\} = [D] \times \{\varepsilon\} \qquad (4.6)$$

Where:

$$[D] = \frac{E}{(1+\nu)(1-2\nu)} \begin{bmatrix} 1-\nu & \nu & 0 \\ \nu & 1-\nu & 0 \\ 0 & 0 & \frac{1-2\nu}{2} \end{bmatrix} \tag{4.7}$$

Where E and ν are the Modulus of elasticity and the Poisson's ratio of the material. A Different [D] matrix is used to represent the inelastic behavior of concrete as discussed in section 4.2. Using well-known finite element procedures, the stiffness matrix of the element can be determined from the following double integration:

$$[K] = \int_{-1}^{+1}\int_{-1}^{+1} [B]^T D [B] |J| \, d\zeta \; d\eta \tag{4.8}$$

Where $|J|$ is the Determinant of the Jacobian matrix, J:

$$[j] = \begin{pmatrix} \frac{\partial x}{\partial \xi} & \frac{\partial y}{\partial \xi} \\ \frac{\partial x}{\partial \eta} & \frac{\partial y}{\partial \eta} \end{pmatrix} \tag{4.9}$$

The integration is carried out numerically at discrete points within the element (integration points). As shown in Figure 4.1.b, a 2x2 Gauss integration technique is used where four integration points are used to represent the entire element. The stiffness matrix is computed at these discrete locations from equation 4.8 and then the element stiffness matrix is derived from the following summation:

$$[K] = \sum_{i=1}^{4} W^i [K]^i \tag{4.10}$$

Where W^i is a weight factor that depends on the integration scheme used and equals 1.0 for a 2x2 Gauss integration scheme.

4.1.2 Modeling of Reinforcing Steel

Two types of finite elements are used to represent reinforcing steel; discrete and smeared steel elements. The discrete element (Figure 4.2.a) is basically, a 2-node truss element where only axial strain and stress is present. The stiffness of the member can be computed by the following equation:

$$[K] = \begin{bmatrix} \frac{E_s A_{cs}}{l} & -\frac{E_s A_{cs}}{l} \\ -\frac{E_s A_{cs}}{l} & \frac{E_s A_{cs}}{l} \end{bmatrix} \tag{4.11}$$

Where E_s, A_{cs} and l are the modulus of elasticity or reinforcing steel, bar cross sectional area and bar length respectively. The discrete element is used to represent main bar reinforcement, for example, within the boundary zone of the wall.

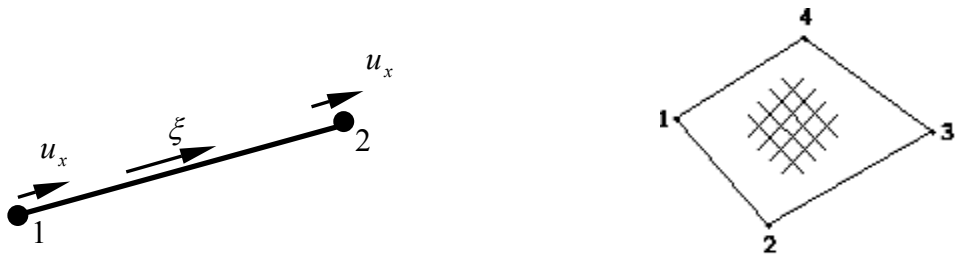

a) 2-Node Bar Element (Truss Element) b) Smeared Grid Element

Figure 4.2 Representation of Steel Reinforcement

Instead of individually modeling each steel bar within the steel mesh located within the wall web, a steel grid element is used to represent the reinforcement in a smeared manner (Figure 4.2.b). The stiffness of the grid element is formulated in a manner similar to the plane stress concrete element except that the element has no stiffness in shear and its Poisson's ratio is zero.

The stiffness of the smeared grid element is computed and then added to the stiffness of the concrete element encompassing it. The grid element can have different thickness in any two orthogonal directions to represent different amounts of vertical and horizontal reinforcement in the wall web.

4.1.3 Modeling of the Coupling Beam

The element used to represent the coupling beam must reflect the relating small length-to-depth ratio of the beam. The beam has a clear length of 60 inches while its total thickness is 14 inches and hence it is expected to deform appreciably in both shear and flexure. Therefore, a formulation based on *Mindlin-Reissner* theory where shear deformation is taken into account is chosen.

Figure 4.3 shows a schematic for the beam element used in the analysis. A 4-node beam element is used where the deflection and rotation at any point on the beam is determined from a third order displacement function

$$\left.\begin{aligned} u_x(x,y) &= a_o + a_1 x + a_2 x^2 + a_3 x^3 + \varphi_z(x)\, y \\ u_y(x) &= b_o + b_1 x + b_2 x^2 + b_3 x^3 \\ \varphi_z(x) &= c_o + c_1 x + c_2 x^2 + c_3 x^3 \end{aligned}\right\} \qquad (4.12)$$

Where: u_y and ϕ_z are the deflection and the rotation of the beam at point (x*)* in the plane of the shear wall respectively, u_x is the axial displacement at a point located at a distance x measured from the end of the beam and y is the distance measured from the centroid of the beam cross section (Figure 4.3.a)

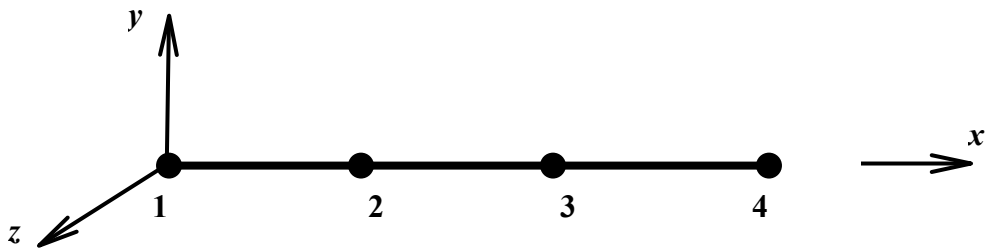

Figure 4.3 4-Node Beam Element

Unlike the conventional shallow beam formulation where only normal strain in the beam direction is considered, *Mindlin-Reissner* beam has two strain componenets, normal strain and shear strain. Both componenets are related to the displacement function in equation 4.12 via the following expressions:

$$\left.\begin{aligned} \varepsilon_{xx} &= \frac{\partial u_x}{\partial x} \\ \gamma_{xy} &= \frac{\partial u_x}{\partial y} + \frac{\partial u_y}{\partial x} \end{aligned}\right\} \qquad (4.13)$$

The rest of the formulation is similar to that of the 4-node element explained in section 4.1.2 except that normal strain in y direction ε_{yy} is not present for this element. Numerical integration is carried out using a number of four points through the beam cross section as shown in Figure 4.4.a and seven points along the beam axis; therefore the total number of integration points for this elements is 4 x 7 = 28.

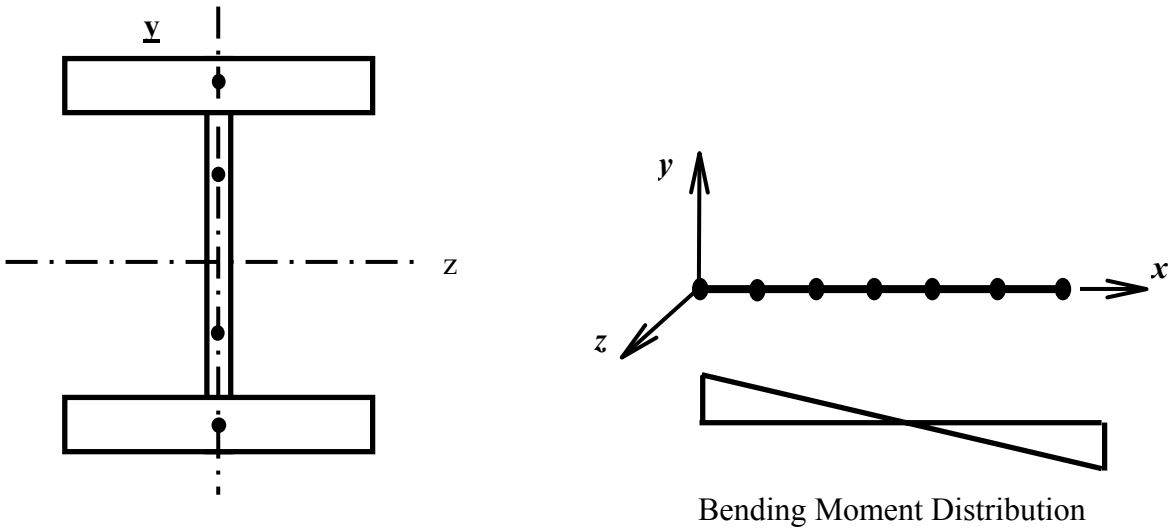

Figure 4.4 Integration Scheme for the Beam Element

Two of the integration points along the depth of the beam are in the flanges while the other two are in the web. It is important to have integration points in the flanges to account for the large axial force that develops there. The web integration points primarily account for the shear stresses.

A reduction factor is applied to the shear stiffness of the beam flanges so that they do not take shear stresses and therefore only the web carries the entire shear force acting on the section. This assumption is consistent with the shear design of the coupling beam where the web is designed to take all the shear force.

A parametric study is conducted to confirm that the choice of integration points along beam depth and beam length is reasonable. Along the beam, the number of integration points is varied from 3 to 11 points with only odd numbers allowed. The seven integration points are found to yield a shear that is of 99% of that corresponding to 13 points. Use of a lesser number of points (3 and 5) yield a shear force of 70% and 95% of that of the 13-point case. Therefore, seven integration points are deemed sufficient to obtain reasonable accuracy. For the number of points in the flanges, 1,3,5 and 7 integration points are tried and all resulted in the same exact shear force. Therefore, one integration point in the flange is satisfactory. For the number of points in the web, a number of 2 points resulted in a difference of only 1% compared to the case with 6 points. Hence, only 2 points through the web are utilized.

4.2 Constitutive Model for Reinforced Concrete

Numerous studies have been conducted to establish material constitutive models that are suitable for analysis of reinforced concrete members. Among these studies, few have focused on developing material models for reinforced concrete members subjected to cyclic loading. Some of the pioneers who established the basis for constitutive formulations for reinforced concrete suitable for application to finite element analysis include Cervenka, 1985, Darwin and Pecknold, 1976 and Aktan and Hanson, 1980. One of these studies is that conducted by Sittipunt, 1995 who developed a constitutive model for concrete under load reversals that is particularly suited for cantilever shear walls. Since all previous studies were limited to either static monotonic or static cyclic loading, adopting existing material models to analyze concrete shear walls under dynamic loading, where frequent and random load reversals are expected is not feasible necessitating developing of a new model.

The necessary aspects of the sought material model include the following features:

Simplicity: The model should reflect the important aspects of behavior of reinforced concrete cantilever shear walls subjected to cyclic loads. Fancy and detailed modeling of every aspect of behavior, no matter how insignificant, might generate numerical instability and yet have no significant effect on the behavior in the global sense and should be avoided

Efficiency: At the structural level, the model must yield acceptable results within a reasonable length of time.

In this chapter, inelastic cyclic material models for both concrete and reinforcing steel are established and verified by comparing the analysis results with published test results.

4.2.1 Crack Modeling

Tensile cracking is one of the important causes of nonlinearity in the behavior of reinforced concrete members. Since concrete has little tensile capacity, cracking occurs early during the loading history of the concrete member. In design practice, stiffness of a cracked member in flexure is conveniently taken as 35% of its original stiffness prior to cracking (ACI-318, 2000). However, this estimation of stiffness is approximate and a proper model that accounts for the stiffness of a cracked member is necessary in order to achieve reasonable accuracy. In the case of members controlled by shear cracking, design codes do not address the problem and no reduction factor is suggested given for the shear stiffness of such members. In order to accurately consider the behavior of cracked concrete, the following issues must be addressed:

- Representation of crack
- Crack Initiation and Propagation

- Material constitutive relationship for cracked concrete.

4.2.1.1 Crack Representation

Two approaches are commonly used to represent a crack; the *discrete crack approach* and the *smeared crack approach*. In the discrete approach, the discontinuity of the concrete matrix at the crack surface is modeled by generating finite elements at the opposite faces of the crack. This approach implies that the finite element mesh has to be continuously updated with the progress of cracks in the concrete matrix. The location of the crack, its orientation and width have to be identified first; then the finite element mesh is refined around the crack lines such that both sides of cracks are incorporated in the updated, refined model. The only way to avoid this continuous remeshing process is to define the cracks at the beginning of the analysis if the crack location can be reliably predicted from a previous analysis or test results. In cyclic loading, the model has to account for both crack opening, closing and reopening and the problem is turned into a *contact problem* where the distance between opposite faces of a crack has to be continuously monitored during the analysis. The stiffness of concrete at these faces undergoes frequent sudden changes with each opening and closing of the crack. The approach was used by Nelson (1968) and Hounde and Mirza (1974) to investigate the behavior of RC beams.

Though it's more realistic and more closely describes the physical behavior of cracked concrete, the discrete approach poses complex and intensive computational demands especially in case of 2 or more intersecting cracks. Hence, its use has been limited to certain applications when a few major cracks dominate the behavior of the system under investigation such as water dams.

In the smeared crack approach, which was introduced by Rashid (1968), the cracks are assumed to exist in a uniform continuous sense rather than discrete one. The existence of a crack at a point is accounted for by modifying the material properties at that point. Concrete is assumed to lose most of its stiffness and strength in the direction normal to the identified crack. A reduction in shear stiffness due to the presence of cracks is also accounted for by modifying the shear stiffness properties of the cracked concrete. Bolander and Wight (1989) summarized the characteristics of the smeared crack model in the following:

- A crack can occur at any direction.
- At any integration point, multiple cracks can take place simultaneously.
- The topology of the finite element mesh remains unchanged throughout the analysis
- Cracks within the same elements can be of different directions. Partial cracking, where cracks can occur at one or more integration point (a finite element is represented by several integration points) within the element, is also possible.

In addition to these advantages, the smeared crack approach can easily handle situations involving well-distributed cracking. It is therefore more suitable than the discrete crack approach for the problem at hand, where well-distributed cracking can occur. Figure 4.5 shows the concept of both methods of crack representation.

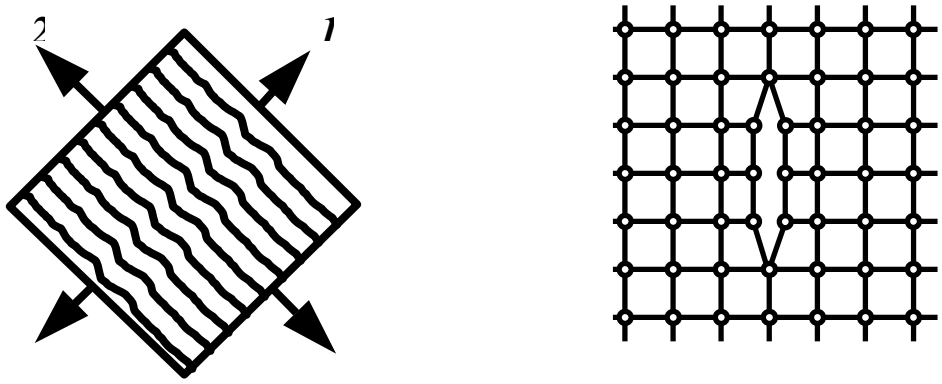

b) Smeared Crack Model b) Discrete Crack Model

Figure 4.5 One-Directional Crack

4.2.1.2 Crack Initiation and Propagation

The strength criterion has been widely used to identify the initiation of cracks in concrete. At a given integration point, the onset of a crack is identified as the time instance at which principal stress at this integration point reaches the tension capacity of concrete. For uniaxial loading conditions, the uniaxial tensile strength of concrete or the modulus of rupture are commonly used to identify crack initiation. However, for a state of biaxial stress, tension-tension or tension-compression strength envelopes such as that proposed by Kupfer et al (1969) are used.

Following the formation of a crack, the crack propagates to the adjacent concrete elements. The progress of a crack in concrete can be predicted using two approaches namely: strength criteria and fracture mechanics criteria.

In the strength approach, similar to the crack initiation criteria, the crack extends to the adjacent elements when the normal stress at its tip exceeds the concrete tensile capacity. In the fracture mechanics approach, the work exerted to make the crack extend a unit length is constant and the crack tip is assumed to progress to the next element when the energy released due to the

crack extension reaches a certain value called *"the fracture energy", G_f,* which is considered a unique material property.

The application of the fracture mechanics approach to the finite element analysis of reinforced concrete members was first suggested by Bazant and Cedolin (1980). Their work was driven by the fact that applying the strength approach to finite elements meshes with different element sizes yields different solutions for the same analysis. Therefore, they considered the strength approach as not an objective way to model crack propagation and introduced the fracture energy approach to eliminate the problem of mesh non-objectivity.

Schnobritch (1985) and the *Task Committee on Finite Element Analysis of RC Structures* (1982) reported that the application of the strength approach is acceptable as long as the response of the cracked member is not driven by a few major cracks. They argued that the fineness of the finite element meshes did not have much effect on the finite element analyses of different types of concrete members including shear walls since the crack length is small and fully encompassed within one finite element. This last results implies however that the usage of a coarse mesh, where the crack bandwidth is expected to remain within the same finite element, is necessary to obtain objective results. However, such coarse meshes might not yield satisfactory results in linear analysis due to different types of irregularities such as sudden changes in thickness or presence of openings where finer elements are needed in order to capture such changes.

4.2.1.3 Constitutive Formulation for Cracked Concrete

Constitutive modeling of cracked concrete consists of three major aspects namely:

- Crack Orientation
- Normal stress-strain relationship

- Shear stiffness relationship

4.2.1.4 Crack Orientation

Concrete under a uniaxial stress state, as in a case of one-dimensional concrete members (e.g. prismatic members) subjected to axial tension, will develop cracks that are oriented in a direction perpendicular to the longitudinal axis of the member. However, under a state of biaxial stresses, the maximum tensile stresses or strains (principal stresses or strains) occur on inclined planes (principal planes) that do not necessarily coincide with the global axes of the two-dimensional concrete member. A crack is assumed to occur on a principal plane when the normal tension stress at that plane exceeds the concrete tensile strength and hence, the potential direction of a crack generally deviates from the global directions.

The principal stresses σ_1, σ_2 and their inclination to the global direction, θ, are determined from the following well-known expressions:

$$\sigma_{1,2} = \frac{\sigma_x + \sigma_y}{2} \pm \sqrt{(\frac{\sigma_x - \sigma_y}{2})^2 + \tau_{xy}^2} \tag{4.14}$$

$$\tan(2\theta) = \frac{2\tau_{xy}}{\sigma_x - \sigma_y} \tag{4.15}$$

Similarly, the principal strains can be determined from the following equations, which can be derived from Mohr's circle:

$$\varepsilon_{1,2} = \frac{\varepsilon_x + \varepsilon_y}{2} \pm \sqrt{(\frac{\varepsilon_x - \varepsilon_y}{2})^2 + (\frac{\gamma_{xy}}{2})^2} \tag{4.16}$$

$$\tan(2\theta) = \frac{\gamma_{xy}}{\varepsilon_x - \varepsilon_y} \tag{4.17}$$

Where:

σ_x and σ_y are the normal stress in x and y direction, τ_{xy} is the shear stress in xy plane.

ε_x and ε_y are the normal strain in x and y direction, γ_{xy} is the shear strain in xy plan.

θ is the angle between the principal direction and the global x-axis direction

Under increasing load, the ratio between the three stress components, σ_x, σ_y and τ_{xy}, in linear analysis is constant and therefore, the principal directions at a given point within the element remain unchanged. Additional complexity arises in nonlinear analysis, where the ratio between the stresses is not constant and therefore, the principal planes are constantly changing throughout the loading history.

Three approaches have been used to determine the orientation of a crack at a given integration point within the finite element; Fixed crack model, rotating crack model and non-orthogonal multi crack model.

4.2.1.4.1 Fixed Crack Model

In the fixed crack model, the crack occurs normal to the direction of the principal tensile stress (or strain) when the principal stress exceeds the concrete tensile strength. Once a crack is identified at a given point, the crack direction is assumed fixed and cracking at that point is monitored at this plane and the plane perpendicular to it. Therefore, two orthogonal cracks are allowed at the integration point under consideration. The constitutive relationship at this point is expressed as following:

$$\begin{bmatrix} \partial\sigma_1 \\ \partial\sigma_2 \\ \partial\tau_{12} \end{bmatrix} = \begin{bmatrix} E1 & 0 & 0 \\ 0 & E2 & 0 \\ 0 & 0 & \beta G \end{bmatrix} \begin{bmatrix} \partial\varepsilon_1 \\ \partial\varepsilon_2 \\ \partial\gamma_{12} \end{bmatrix} \tag{4.18}$$

Where $\partial\sigma_1$, $\partial\sigma_2$ and $\partial\tau_{12}$ are stress increments on the crack direction, $\partial\varepsilon_1$, $\partial\varepsilon_2$ and $\partial\gamma_{12}$ are strain increments on the crack direction; E_1 and E_2 are the tangent and normal stiffnesses. G is

the elastic shear stiffness and β is a reduction factor to account for the amount of shear stiffness retained on the crack direction due to the effect of aggregate interlock.

The fixed crack model has been widely used by investigators (Balakrishnan and Murray, 1988, Cervenka, 1985, Darwin and Pecknold, 1976). In spite of its success in solving numerous types of concrete members, unsatisfactory results were reported by Vecchio and Collins (1986) when the model was used in the analysis of reinforced concrete shear panels tested by Vecchio and Collins (1982). Due to the constraint that the fixed crack model imposes on the crack direction, the predicted stiffness of the tested members is usually overestimated. According to Vecchio and Collins (1982), the test panels had highly anisotropic reinforcement and, contrary to the basic assumption of the fixed crack model, the crack directions were changing during the tests.

4.2.1.4.2 Rotating Crack Model

The concept of a rotating crack was adopted by a number of researchers including Milford (1984) and Vecchio and Collins (1986). The concept was backed by the results obtained from tests conducted by Vecchio and Collins (1982) in which concrete panels with anisotropic reinforcement were tested to failure. In the model, crack directions are continuously rotating with the principal planes, as the principal directions are determined during each new iteration throughout the nonlinear analysis. The constitutive formulation of the model expressed in the form of the constitutive matrix is similar to that in equation 4.18 except for the components of the matrix are always calculated at the principal planes. Shear retention factor, β, need not be assumed and the shear rigidity is related to the normal stiffness E_1 and E_2 by the following expression:

$$G = \frac{E_1 E_2}{E_1 + E_2} \tag{4.19}$$

However, the model was criticized by Bazant (1983) who argued that change in crack directions with load progress means that the old crack no longer exists which implies that the damage in concrete is temporary and dependent on the strain state; an assumption that violates the basic concept of permanency of damage in concrete members. Another logical drawback of the model is that the model considers the stress-strain history of the new crack planes the same as the history on the old planes; unless the entire stress-strain history of the new principal planes is generated at the moment the cracks hit these planes. In addition to these inherent complications, from a computational point of view, the continuous change in the crack planes especially in cyclic nonlinear analysis slow down the convergence rate and sometimes causes cause divergence to occur.

4.2.1.4.3 Non-Orthogonal Multi Crack Model

This Model was proposed by De Borst and Nauta (1985) in an attempt to avoid the drawbacks of the fixed and rotating crack models. The total strain increment, $\Delta\varepsilon$, at a given integration point is decomposed into two components, concrete strain increment $\Delta\varepsilon_c$ and crack strain increment $\Delta\varepsilon_{cr}$.

$$\Delta\varepsilon = \Delta\varepsilon_c + \Delta\varepsilon_{cr} \tag{4.20}$$

Decomposition of strain into a crack strain and concrete strain in such a way allows the separation of intact concrete strain and crack strain. Multiple cracks can occur at the same integration point and the final crack strain, $\Delta\varepsilon_{cr}$, is the summation of all contributions of individual cracks taking place at that point. The Model was used by Bolander and Wight (1989)

in the analysis of shear walls. However, only monotonic loading condition was considered. The drawbacks of the multiple non-orthogonal crack model arise from the mathematical complexity involved when applying the model to finite element analysis. A considerable computational effort is needed to keep track of the stress-strain history at each individual crack. Compared to the fixed crack and the rotating crack approaches, applying the multiple crack model would double or even triple the computation time required and the analysis cost might not be feasible especially if the analysis is performed on systems with large number of finite element such as the systems considered in the current study. In addition to the high cost, Crisfeild and Wills (1990) encountered numerical difficulties implementing the model to nonlinear finite element analysis.

4.2.1.5 Proposed Crack Model

Recognizing the advantages and drawbacks of each of the crack models discussed in the above sections, as well as the simplicity and efficiency requirements as discussed in the introduction of this chapter, the fixed crack approach was chosen for conducting the analyses presented in chapters 5 and 6. The model is simple to formulate and apply in a finite element code. In addition, it provides faster and more stable solution and higher convergence rate because crack directions, once established, remain unchanged throughout the nonlinear analysis.

4.2.1.6 Normal Stress-Strain Relationship

The normal stress-strain relationship describes the constitutive relationship in the direction perpendicular to the crack direction. Since cracking is assumed smeared and continuous over the entire concrete element, the relationship between normal stress and strain is assumed continuous for both cracked and intact concrete. For simplicity, Poisson's ratio is assumed zero

for concrete after cracking occur. This assumption has been used by many researches (Task Committee, 1982).

Concrete is assumed to behave uni-axially; that is, stresses and strains on each direction are treated separately and no strength enhancement or reduction is accounted for due to the co-existing stress on the perpendicular direction. The major effect of the bi-axial behavior of concrete occurs at the boundary zones of the shear walls, where heavy transverse reinforcement is provided. For elements in these zones, the stress-strain relationship is modified to reflect the increase in strength and ductility due to confinement. In the rest of the shear wall (the web part), the effect of co-existing perpendicular stresses on the global behavior of the shear wall was found to be minimal. Although this assumption is made in order to primarily fulfill the simplicity and efficiency requirements, analysis results confirm its validity compared with test results as will be shown in the verification study in section 4.5.

The state of stresses at a given integration point can change due to the change of loading magnitude and direction, or redistribution of stresses due to frequent nonlinear changes occurring in the vicinity of that integration point. Therefore, a particular finite element is subjected to frequent loading-unloading-reloading sequences. The normal stress function must be able to describe all these potential loading situations. Also, the function must represent various aspects of nonlinear response of reinforced concrete namely:

- Effect of tension stiffening
- Crack initiation, closing and re-opening
- Compression behavior
- Confinement effect of reinforcing steel
- Stiffness degradation due to cyclic loading.

4.2.1.6.1 Effect of Tension Stiffening

Although plain concrete posses little tensile capacity after cracking, concrete confined between cracks can still convey some tensile stresses to the steel reinforcing bars through bond stresses. This ability of cracked concrete to transfer such stresses is termed "*tension stiffening*." Some researchers included the effect of tension stiffening by modifying the stress-strain relationship of the reinforcing bars such that it reflects the stress in the bar in addition to the extra force in the surrounding concrete due to tension stiffening. No tensile stresses are carried by concrete in that approach (Gilbert and Warner, 1978). Most researchers however, include the effect of tension stiffening in the concrete model itself rather than in the reinforcing bars. Concrete retains a portion of its tensile capacity after cracking. Then, concrete strength decreases gradually with the increase in tensile strains. This latter approach was suggested by Scanlon and Murray (1974) and was commonly used thereafter to represent the tension stiffening effect (Balakrishnan and Murray, 1988, Barzegar, 1989, Cervenka, 1985).

In the current work, the stress-strain relationship is developed according to the second approach. As shown in Figure 4.6, a linear stress-strain relationship is assumed up to the cracking limit, σ_{cr}, which represent the onset of the crack with a constant modulus of elasticity equals to E_c, according to the following equation given by ACI-318:

$$E_c = 57000\sqrt{f_c'} \tag{4.21}$$

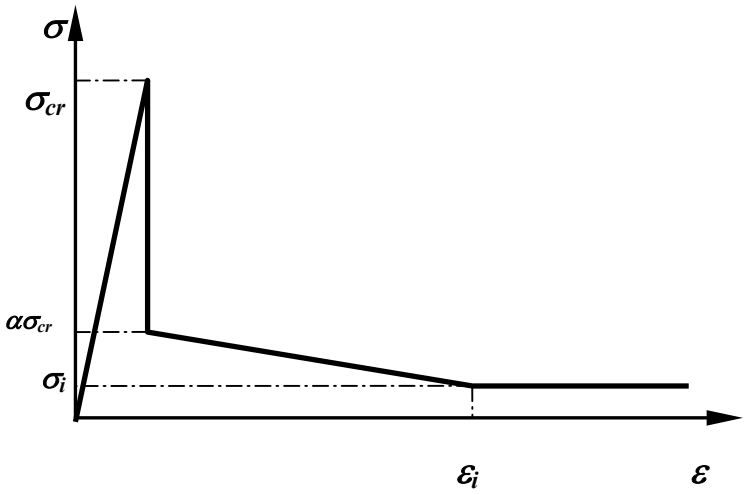

Figure 4.6 Tension Stiffening Model

Immediately after the occurrence of a crack, the concrete tensile strength decreases suddenly from σ_{cr}, to $\alpha\ \sigma_{cr}$; where α is a reduction factor. Following that sudden drop in tensile strength, normal stress decreases steadily while the normal strain increases until the strain reaches a value ε_i, at which stress remain constant at a corresponding value σ_i. This simplified tension stiffening model was used by Inoue and Koshika, (1985) Yamaguchi and Nomura (1980) and Sittipunt (1995) in the analysis of shear walls.

4.2.1.6.2 Crack Initiation, Closing and Reopening

Cyclic loading causes cracks to be constantly under states of opening, closing and reopening. With the constant change in crack status, the stiffness of cracked concrete experiences extreme change from near zero to the initial modulus of elasticity. Figure 4.7 shows typical results obtained from cyclic tests on concrete members (Stevens et. al. 1987). As described in Stevens et al (1987), a common characteristic of the loading-unloading curves is that the monotonic stress-strain curve encompasses all the cyclic curves in the tension side. Unloading

(crack closing) begins at the envelope curve with a tangent stiffness approximately equal to the initial modulus E_c (initially stiff region). As the stress becomes close to zero, the unloading follows a straight path with zero stiffness (softened region) before the unloading picks up gradually and the unloading curve eventually merges onto the compression curve at a low compressive strain (stiffened region). In reloading (crack reopening), compressive stress decreases to a small value until a zero strain is achieved at which the stress-strain relationship follows a straight path until it merges with the envelope curve at the previous unloading point.

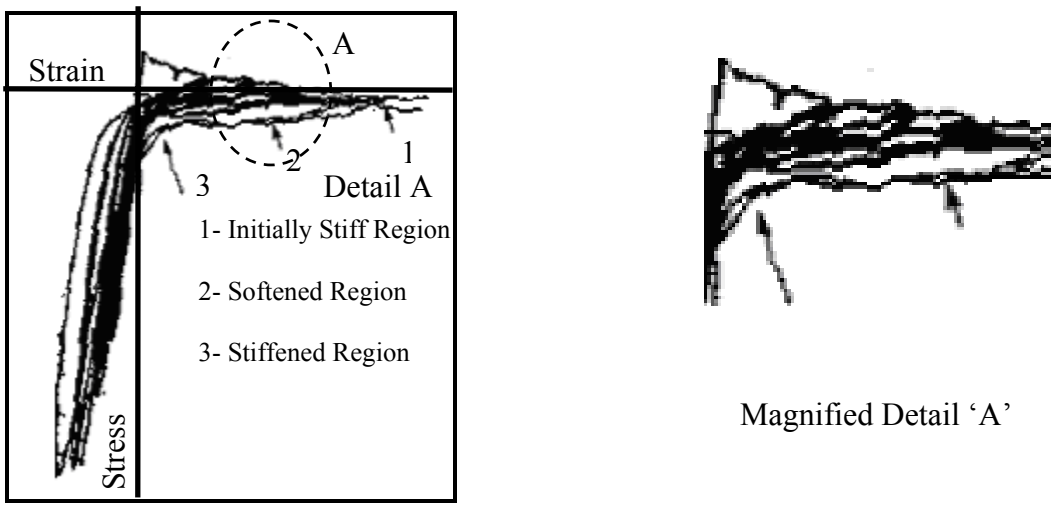

Figure 4.7 Stress vs. Strain (Stevens et. al., 1987)

This behavior is mathematically expressed as following:

- In unloading (Figure 4.8), the curve starts from point 'A' with a tangent stiffness equals to E_c. At point 'B', the curvs turns horizontally towards 'O'.
- In reloading (Figure 4.9), The Curve follows a straight path from 'O' to 'C' where 'C' is the previous unloading point.

For a random load reversal situation when unloading does not proceed to point 'O' or when reloading does not star from point 'O', (Figure 4.10):

- Whenever unloading occurs (points 1 or 4), the tangent modulus is equal to E_c until stress is equal to zero (points 2 or 5). Then a straight line towards 'O' is followed (lines 2-O or 5-O)
- Whenever reloading occurs, (points 3 or 6), a straight path is followed to the point of maximum attained stress (point 1)

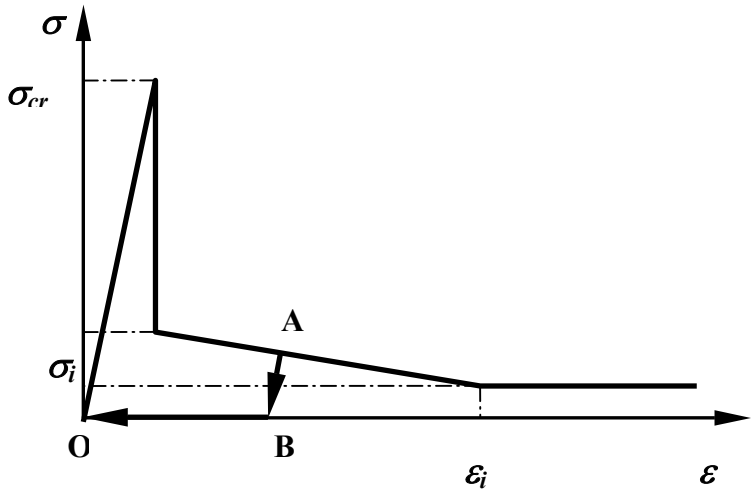

Figure 4.8 Rule for Crack Closing

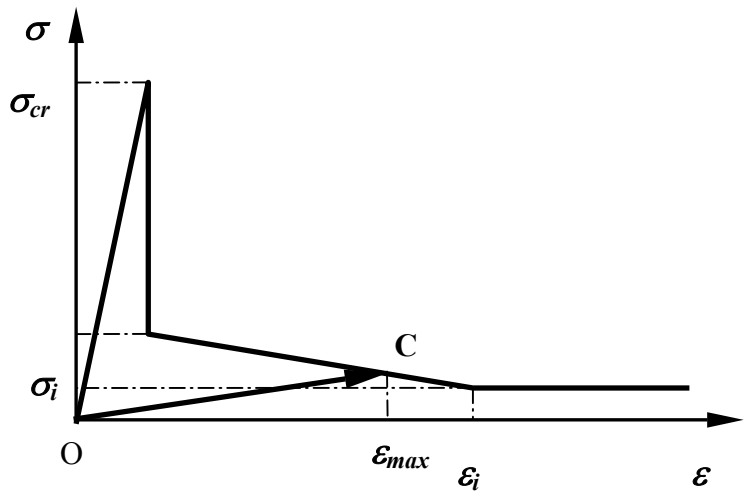

Figure 4.9 Rule for Crack Reopening

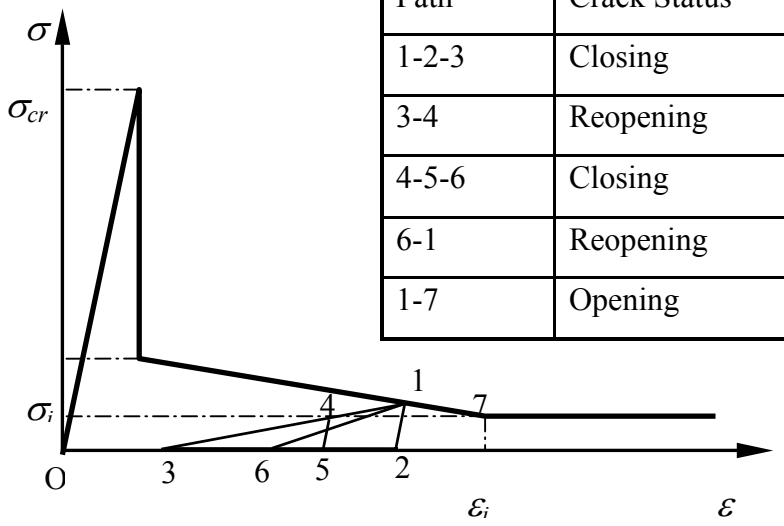

Path	Crack Status
1-2-3	Closing
3-4	Reopening
4-5-6	Closing
6-1	Reopening
1-7	Opening

Figure 4.10 Arbitrary Loading-Unloading Sequence

4.2.1.6.3 Compression Behavior

The stress-strain relationship of concrete is approximately linear when concrete is subjected to low compressive stresses (commonly taken below $0.7\ f_c^{'}$). Beyond that limit, the

stress-strain relationship begins to lose stiffness gradually until the stress reaches the compressive strength of concrete, $f_c^{'}$ at a corresponding ultimate strain ε_0. The compressive stress then begins to decrease as the strain increases. Such degradation in strength reflects the accumulated damage in concrete when subjected to high compressive strains.

For unconfined concrete, the behavior of concrete as represented by figure 4.11, is essentially brittle. The descending branch of the curve shows a high rate of strength degradation which implies that once concrete stress reaches the ultimate strength, significant loss of the concrete carrying capacity is experienced and hence, the concrete element contribution to the global strength and stiffness is almost lost.

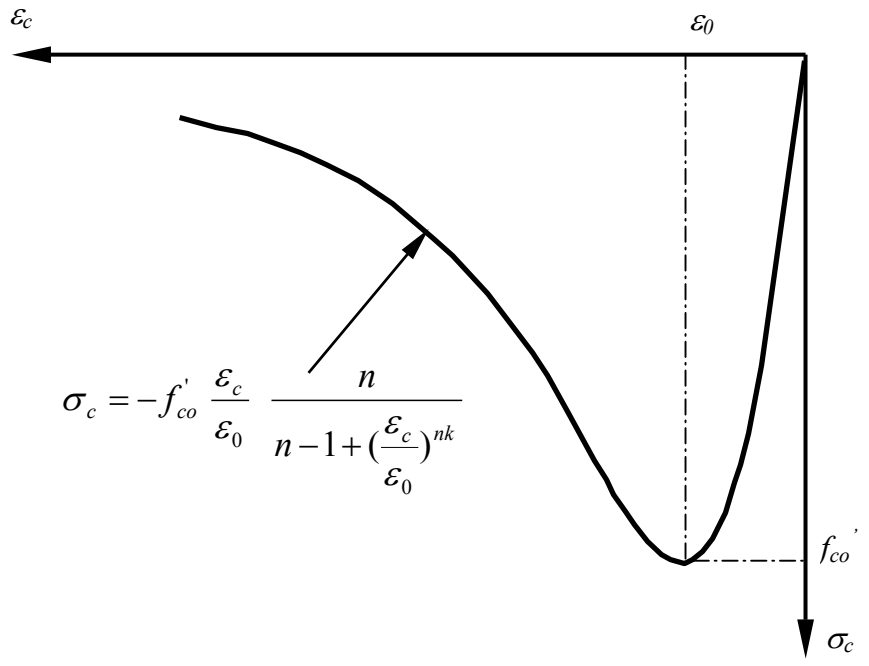

Figure 4.11Thorenfeldt Compression Curve

For confined concrete however, concrete gains more strength in the axial direction of the member (parallel to the direction of the applied load) due to the confining stresses resulting from heavy transverse reinforcement or in other cases, due to the bi-axial stress state that the concrete

element is subjected to. In addition to the enhancement in strength (and accordingly, stiffness as expressed in equation 4.21), strength degradation rate beyond the ultimate strength limit is significantly slower than that for unconfined concrete (Figure 4.11). Slower strength degradation causes confined concrete to respond to compressive loads in a more ductile manner than unconfined concrete.

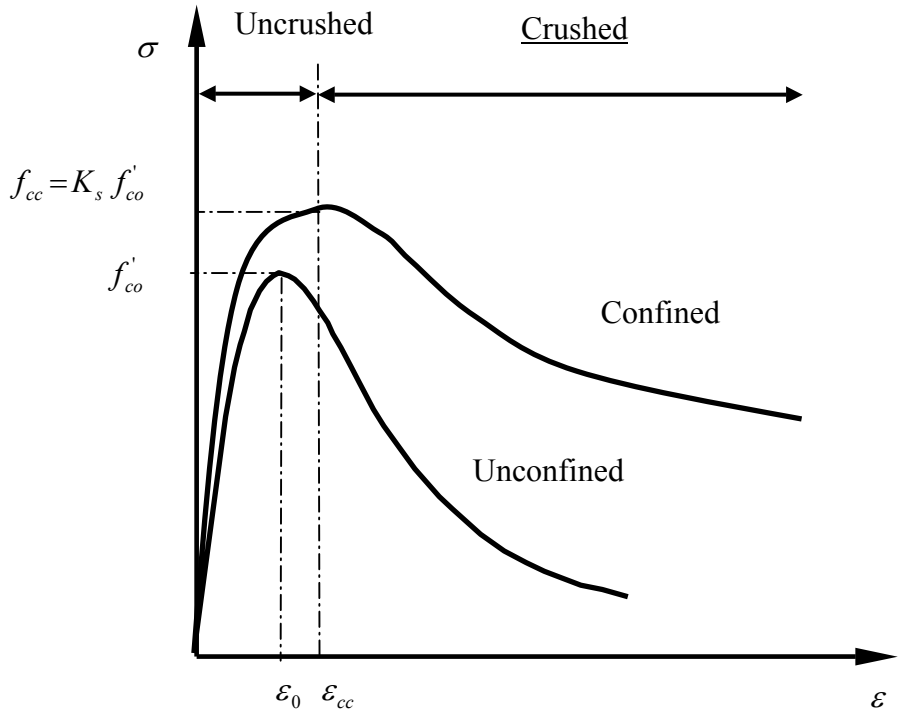

Figure 4.12 Confined Concrete Model

4.2.1.6.4 Stress-Strain Relationship for Unconfined Concrete

Several stress-strain relationships have been proposed by researchers during the past few decades (Popovics, 1973) to represent the compressive behavior of concrete subjected to uni-axial compression. For the current work, the formula originally proposed by Popocics in 1973 (Collins et al., 1993) and lately modified by Thorenfeldt (Thorenfeldt et. al. 1987) to account for more rapid degradation beyond the peak point is used.

$$\sigma_c = -f_{co}^{'} \frac{\varepsilon_c}{\varepsilon_0} \frac{n}{n-1+(\frac{\varepsilon_c}{\varepsilon_0})^{nk}} \quad (4.22)$$

$$n = 0.8 + \frac{f_{co}^{'}}{2.37} \quad (4.23)$$

$$k = 1 \qquad for\ 0 > \varepsilon_c \geq \varepsilon_o \quad (4.24.a)$$

$$k = 0.67 + \frac{f_{co}^{'}}{8.66} \qquad for\ \varepsilon_o \geq \varepsilon_c \quad (4.24.b)$$

In the original formula by Popovics, *k* was taken as 1.0 in both cases above. In the subsequent modification proposed by Thorenfeldt, k is greater than 1.0, which results in a higher rate of strength decay.

$$\varepsilon_o = -\frac{n}{n-1} \frac{f_{co}^{'}}{E_c} \quad (4.25)$$

Where:

$f_{co}^{'}$: uni-axial concrete compressive strength (ksi)

ε_o: ultimate compressive strain

σ_c and ε_c: concrete compressive stress and strain respectively

E_c: Young's modulus of concrete

4.2.1.6.5 Stress-Strain Relationship for Confined Concrete

Three parameters are needed to describe the behavior of confined concrete as shown in Figure 4.12 namely: The enhanced concrete strength f_{cc}, corresponding to concrete strain ε_{cc} and the parameter *k* in equation 4.24 which accounts for the strength degradation rate.

In order to obtain the enhanced strength of confined concrete, Mander et al (1988) proposed the following expression:

$$f'_{cc} = k_s \, f'_{co} \tag{4.26}$$

Where the strength enhancement factor is determined according to the following section

4.2.1.6.6 Determination of the Confinement parameters

For a cross-section of reinforced concrete with hoop and tie reinforcement, shown in Figure 4.13, the core area, A_c, is defined as the cross-sectional area bounded by the hoop centerlines (Mander et al., 1988). Thus:

$$A_c = b_c h_c \tag{4.27}$$

Where: b_c = Hoop center-to-center dimension in x-direction

h_c = Hoop center-to-center dimension in y-direction

This core area contains both confined and unconfined concrete. According to Mander et al. (1988), arching action occurs horizontally and vertically between longitudinal bars and transverse hoops, respectively. It can be traced by parabolas with beginning and ending slopes of 45° (dashed lines in Figure 4.13). Within these boundaries lies the effectively confined portion of concrete. As shown in Figure 4.13, the total unconfined portion of concrete located within the core area at the level of transverse hoops is (Mander et al., 1988):

$$A_u = \sum_{i=1}^{n} \frac{w_i^2}{6} \tag{4.28}$$

Where: n = Number of unconfined parabolic areas

w_i = Width of parabolic area (between tied longitudinal bars)

A_u = Unconfined portion of core area

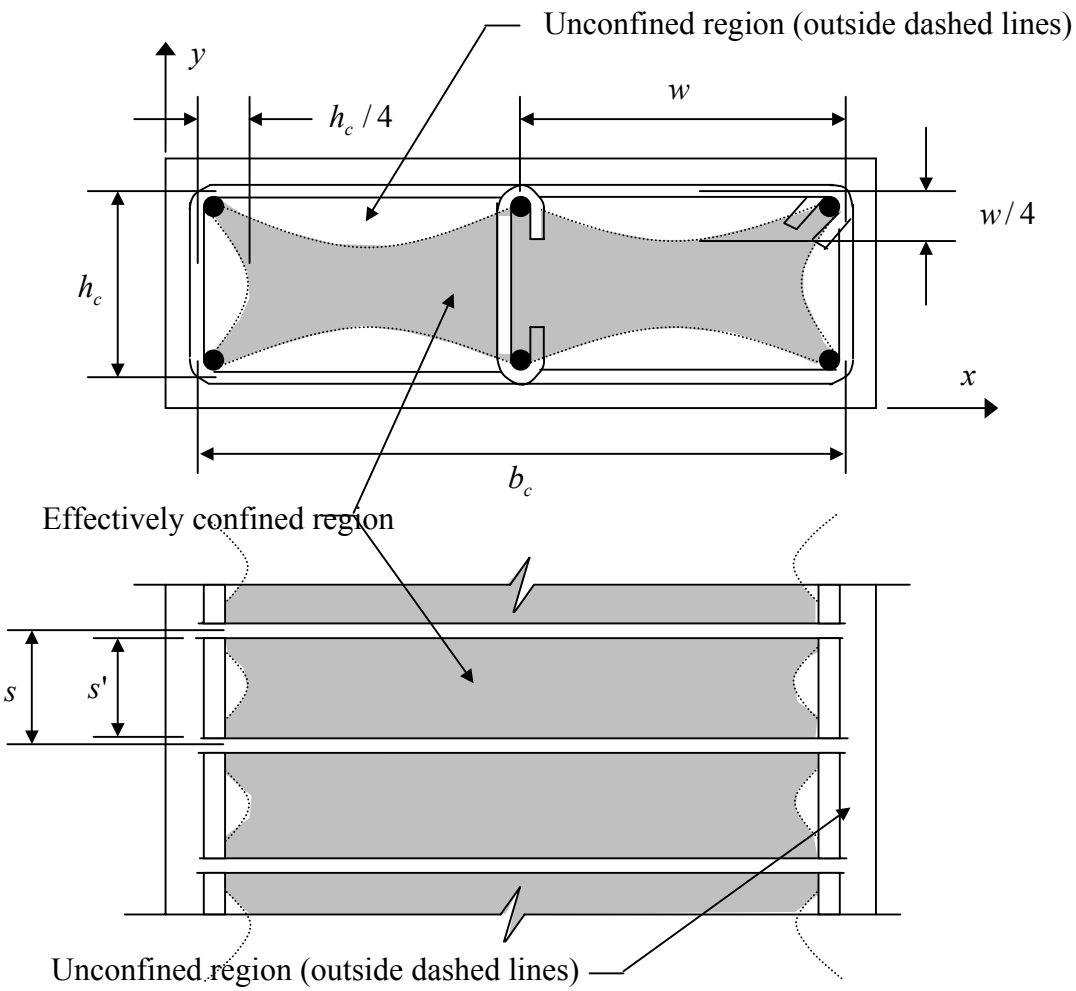

Figure 4.13 Confinement Due to Hoop and Cross Tie Reinforcement

Taking account of the unconfined concrete in the vertical direction, between hoop layers, the minimum effectively confined concrete cross-sectional area, A_e, is defined as (Mander et al., 1988):

$$A_e = \left(b_c h_c - \sum_{i=1}^{n} \frac{w_i^2}{6} \right) \left(1 - \frac{s'}{2b_c} \right) \left(1 - \frac{s'}{2h_c} \right) \tag{4.29}$$

Where: s'= Clear spacing between hoop levels

Mander et al. (1988) defines the confinement effectiveness coefficient, k_e, as the ratio of effectively confined concrete cross-sectional area to the core concrete area. Thus:

$$k_e = \frac{A_e}{A_{cc}} \tag{4.30}$$

Where: $A_{cc} = A_c(1 - \rho_{cc})$ (4.31)

ρ_{cc} = Longitudinal reinforcement ratio

For the rectangular section in Figure 4.13, differing amounts of reinforcement in the *x* and *y* directions yield different reinforcement ratios in these directions as follows (Mander et al., 1988):

$$\rho_x = \frac{A_{shx}}{sh_c} \tag{4.32}$$

$$\rho_y = \frac{A_{shy}}{sb_c} \tag{4.33}$$

Where: A_{shx} = Area of transverse reinforcement in x direction

A_{shy} = Area of transverse reinforcement in y direction

s = Center-to-center spacing of hoop levels

The confining pressures in the x and y directions are thus defined (Mander et al., 1988):

$$f_{lx} = k_e \rho_x f_y \tag{4.34}$$

$$f_{ly} = k_e \rho_y f_y \tag{4.35}$$

Where: f_y = Yield strength of steel reinforcement

The confined concrete strength under tri-axial compression as a function of the confining pressures is given in Figure 4.14. From the calculated pressures, f_{lx} and f_{ly}, the larger is taken as $f_{l2}^{'}$ and the smaller as $f_{l1}^{'}$, while $f_{co}^{'}$ in the figure is the unconfined concrete strength. For ease of determining the confined strength, $f_{cc}^{'}$, El-Tawil and Deierlein's (1996) interpolation

between the upper and lower bounds of the solution as presented in Figure 4.14 is used. The upper bound strength gain (when $f_{l2}^{'} = 0.3 f_{co}^{'}$) is given by (El-Tawil and Deierlein, 1996):

$$k_u = 1.3 + 5.55 \frac{f_{l1}^{'}}{f_{co}^{'}} - 7.5 \left(\frac{f_{l1}^{'}}{f_{co}^{'}} \right)^2 \tag{4.36}$$

Where: $f_{l1}^{'}$ = Smaller confining pressure

$f_{l2}^{'}$ = Larger confining pressure

k_u = Upper bound strength gain factor

The lower bound strength gain (when $f_{l1}^{'} = f_{l2}^{'}$) is given by (Mander et al., 1988):

$$k_l = -1.254 + 2.254 \sqrt{1 + \frac{7.94 f_{l1}^{'}}{f_{co}^{'}}} - 2 \frac{f_{l1}^{'}}{f_{co}^{'}} \tag{4.37}$$

Where: k_l = Lower bound strength gain factor

El-Tawil and Deierlein's (1996) interpolation equation is:

$$k_s = k_l + (k_u - k_l) \sqrt{\frac{\left(\frac{f_{l2}^{'}}{f_{co}^{'}} - \frac{f_{l1}^{'}}{f_{co}^{'}} \right)}{\left(0.3 - \frac{f_{l1}^{'}}{f_{co}^{'}} \right)}} \tag{4.38}$$

Where: k_s = Strength increase factor

Thus, the confined concrete strength is calculated from:

$$f_{cc}^{'} = k_s f_{co}^{'} \tag{4.39}$$

Once the confined concrete strength is determined, the corresponding ultimate strain is computed from the following formula:

$$\varepsilon_{cc} = \varepsilon_o \left[1 + 5 \left(\frac{f_{cc}^{'}}{f_{co}^{'}} - 1 \right) \right] \tag{4.40}$$

And the strength degradation rate, $k^{'}$, in equation 4.24 is computed from the following expression proposed by El-Tawil and Deierlein (1996):

$$k^{'} = 1.0 + (k-1)\sqrt{\frac{f_{cc}^{'} - \sigma_c}{f_{cc}^{'}}} \tag{4.41}$$

Where k is the degradation rate for unconfined concrete according to equation 4.24. The rate computed from 4.30, k', is variable and represents the slow strength decay rate of confined concrete as shown in Figure 4.12.

Incorporating the three parameters, f_{cc}, ε_{cc} and $k^{'}$ into Thorenfeldt formula in equation 4.22, the following expression is used to compute the stress-strain relationship of confined concrete:

$$\sigma_c = -f_{cc}^{'} \frac{\varepsilon_c}{\varepsilon_{cc}} \frac{n}{n-1+(\frac{\varepsilon_c}{\varepsilon_0})^{nk^{'}}} \tag{4.42}$$

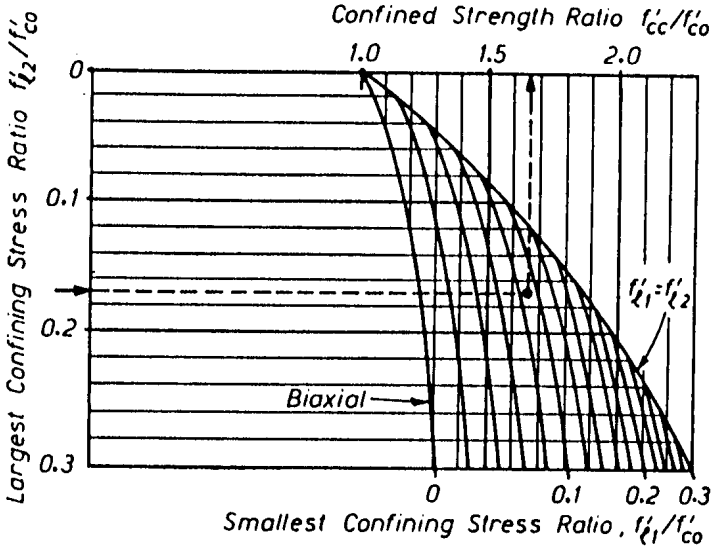

Figure 4.14 Confined Concrete Strength as a Function of Confining Pressures (Mander et al., 1988)

4.2.1.6.7 Degradation of Concrete under Cyclic Loading

The stress-strain relationships defined in the preceding sections describe the response of concrete under monotonic compressive loading. Under cyclic loading, stress-strain relationship of concrete in unloading and reloading status must be defined. As shown in Figure 4.15, unloading path starts (points P_1, P_2 and P_3) straight with a tangent modulus close to the initial Young's Modulus, E_c. As the unloading proceeds to a stress level of $0.3 f'_{co}$, the stress-strain path bends gradually such that the tangent stiffness decreases until the stress is equal to zero at a certain residual strain (plastic strain). In reloading, concrete stress increases almost linearly up to a certain point (Points P6 and P7) then bends sharply and merges onto the envelope curve (points P_4 and P_5). The model shown in Figure 4.15 (Sittipunt, 1995) was based on test results obtained from Karsan and Jirsa (1969) and Sinha et al (1964). As stated earlier in this chapter, although dynamic analysis is cyclic in nature, the potential stress-strain path is more complex than the paths usually followed in the tests or those followed to perform '*static*' cyclic analyses which are characterized by equal and increasing displacement amplitudes in both directions of loading. In dynamic loading on the other hand, similarity of loading paths in both directions of loading does not commonly occur. On top of that, the potential occurrence of unloading at the middle of a reloading path; which in turn could be initiated at the middle of another unloading path adds complication to the situation.

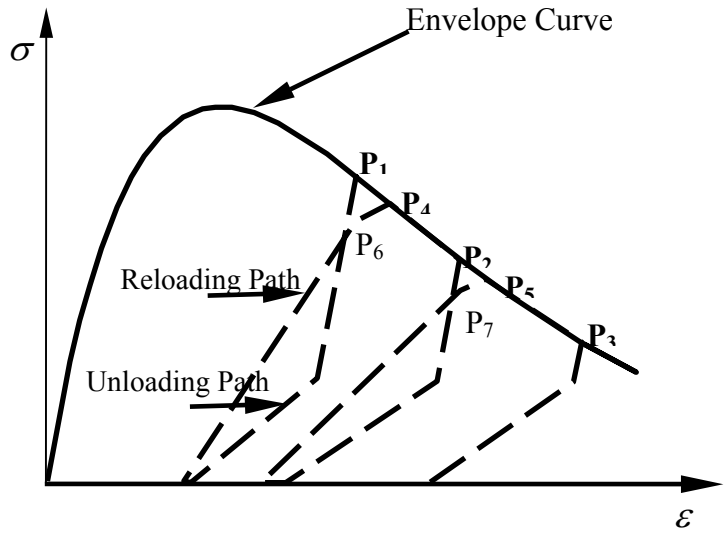

Figure 4.15 Typical Cyclic Stress-Strain Relationship (Sittipunt, 1995)

Because of all these inherent complexities in load reversals, simplifying the unloading and reloading paths is necessary in order to avoid unneeded complication in the formulation as well as to avoid any possible numerical instability caused by the complexity of the stress-strain path. The stress-strain path used in this study is shown in Figure 4.16. Whether the unloading starts from the envelope curve or from another unloading or reloading path, the unloading tangent modulus is equal to E_c until the point of zero stress (points B, E or H) is reached. Once the path hits the zero stress point, it follows the horizontal axis towards the origin (0,0) where the reloading rule in the tensile side governs. Similarly, the reloading path starts from anywhere (in the compression side) straight towards the previous unloading point (points A, D or G) after which the monotonic relationships defined in the previous sections governs the response. The same rules are followed for both confined and unconfined concrete.

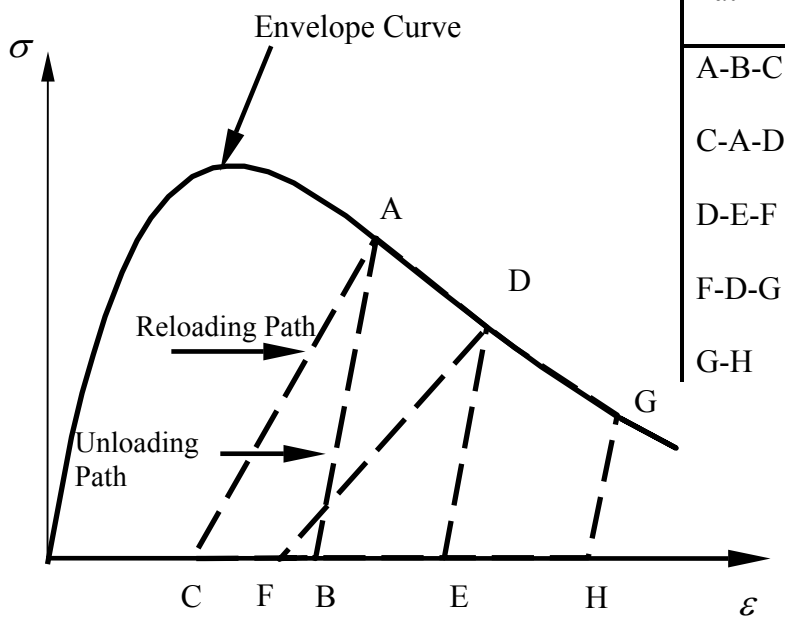

Path	Status
A-B-C	Unloading
C-A-D	Reloading
D-E-F	Unloading
F-D-G	Reloading
G-H	Unloading

Figure 4.16 Rules For Unloading and Reloading

4.2.1.7 Shear Stiffness Relationship

Concrete exhibits a significant reduction in its shear stiffness immediately after crack formation. Unlike uncracked concrete where shear stresses are transferred by both material cohesion and internal friction, cracked concrete loses the cohesion property at the location of the crack. The main mechanism that transfers shear stresses between the opposite sides of a crack is the aggregate interlock. The opposite faces of a crack are usually rough and characterized by a series of summits and sags (Figure 4.17). Hence, the interlock between summits on one side of a crack and sags on the other side creates resistance to shear stresses. As the crack widens, the summits and sags move away from each other and the shear resistance provided by the aggregate interlock becomes smaller.

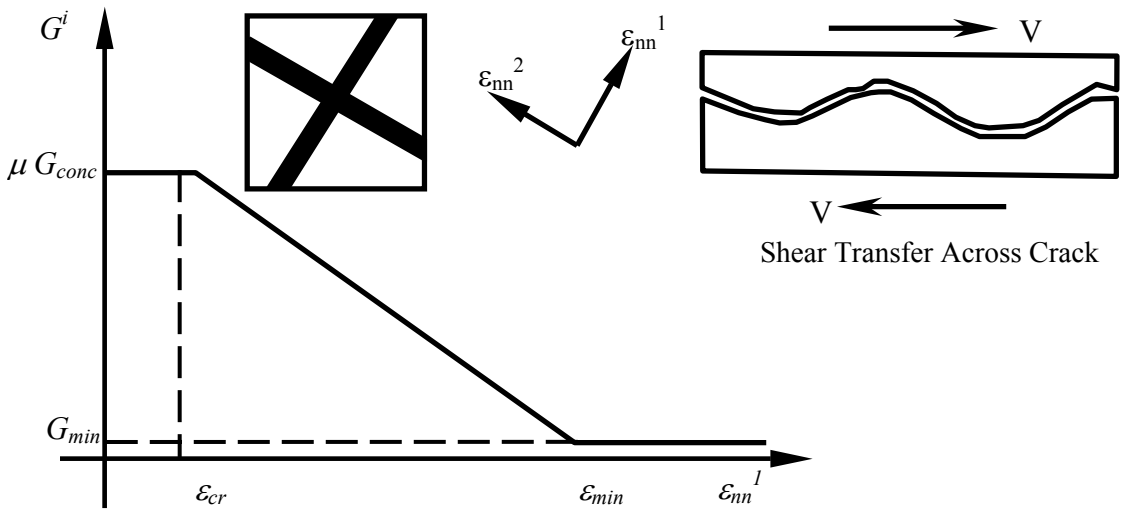

Figure 4.17 Shear Stiffness vs. Crack Normal Strain

Early models developed for shear transfer in reinforced concrete used crack width and shear slip as parameters to simulate the shear transfer. However, such approach implies the use of a discrete crack model where the crack width can be calculated. In the smeared crack model, shear stiffness of cracked concrete is represented by applying a reduction factor (also known as *shear retention factor*) to the shear stiffness G_{conc} of elastic concrete. Two approaches have been commonly used in the past to specify the shear retention factor. In the first one, the reduction factor is considered constant and usually taken as a value ranging from 0 to 0.5. In the second approaches, shear stiffness varies and depends on the normal strain at the cracked integration point. Figure 4.17 shows the relationship between the retained shear stiffness of concrete G^i, and the normal stain of the crack in i direction where "*i*" is an index for the crack direction. Shear stiffness for cracked concrete is assumed to decrease to a value equal to $\mu\, G_{conc}$ immediately after the crack formation at a given integration point. Then, the shear stiffness decreases gradually with the increase in crack strain until a minimum value, G_{min}. Based on the recommendation of Sittipunt (1995), μ, ε_{min} and G_{min} are taken as 0.2, $12.5\varepsilon_{cr}$ and $0.005\, G_{conc}$ respectively; where ε_{cr} is the concrete cracking strain.

The shear stiffness is calculated for each crack direction (for i= 1 and i= 2), then the total shear stiffness at the integration point is calculated from the following expression:

$$G_{cr} = 2.0[\frac{1}{G^1} + \frac{1}{G^2}]^{-1} \tag{4.43}$$

$$G^i = \mu G_{conc} \qquad for\ \varepsilon^i_{nn} < \varepsilon_{cr} \tag{4.44}$$

$$G^i = \mu G_{conc} \frac{\left|\varepsilon_{\min} - \varepsilon^i_{nn}\right|}{\left|\varepsilon_{\min} - \varepsilon_{cr}\right|} \qquad for\ \varepsilon_{cr} \le \varepsilon^i_{nn} < \varepsilon_{\min} \tag{4.45}$$

$$G^i = G_{\min} \qquad for\ \varepsilon^i_{nn} \ge \varepsilon_{\min} \tag{4.46}$$

$$G_{conc} = \frac{Ec}{2(1+\nu)} \tag{4.47}$$

Where E_c and ν are the elastic Young's Modulus and Poisson's ratio of concrete respectively.

4.2.1.8 Separation of Shear Strain

In the conventional fixed crack model, similar to the normal stiffness, shear stiffness is computed on the crack direction and then the entire stiffness matrix for this direction is transformed back to the global coordinate system. Thus, shear stiffness of the global system depends not only on the shear stiffness component of the crack direction (βG_c) but also on the normal stiffness components of that direction (E_1 and E_2)

To illustrate this idea, a numeric example is given below where the crack direction is assumed at an angle of 45 degrees, Normal stiffness E_1 is assumed zero since principal strain ε_1 is positive while E_2 is assumed equal to E_c as the principal strain ε_2 is compression. Shear stiffness on that direction is βG_c. The stiffness matrix of the crack direction [D_{cd}] is then

transformed to obtain the stiffness matrix of the global system $[D_g]$ via the transformation Matrix *A*.

$$[D_{cd}] = \begin{bmatrix} 0 & 0 & 0 \\ 0 & E_c & 0 \\ 0 & 0 & \beta G_c \end{bmatrix} \tag{4.48}$$

$$[D_g] = [A]^T \begin{bmatrix} 0 & 0 & 0 \\ 0 & E_c & 0 \\ 0 & 0 & \beta G_c \end{bmatrix} [A] \tag{4.49}$$

$$[A] = \begin{bmatrix} Cos^2\theta & Sin^2\theta & Cos\theta\, Sin\theta \\ Sin^2\theta & Cos^2\theta & -Cos\theta\, Sin\theta \\ -2\,Cos\theta\, Sin\theta & 2\,Cos\theta\, Sin\theta & Cos^2\theta - Sin^2\theta \end{bmatrix} \tag{4.50}$$

Surprisingly, for all values of β, the global shear stiffness obtained is unchanged and always equal to $E_2/4$. This result means that in certain cases where the element is under predominant shear strains, shear stiffness is dictated by the value of normal stiffness E_2 no matter what the value of the shear stiffness reduction factor β is taken. Hence, the element is expected to exhibit a stiff response in terms of shear deformation even if the shear retention factor is taken as zero. Shear stiffness will decrease only when the concrete crushes and the normal stiffness E_2 is reduced dramatically and then the element can experience high shear deformations.

Realizing this difficulty, and in order to allow the wall to experience high shear deformations without causing premature concrete crushing, Sittipunt (1995) proposed the idea of separating shear stiffness from normal stiffness, that is, the shear stiffness computed from equation 4.43 above overrides the one computed from equation 4.49. Figure 4.18 shows the concept of separating shear strain

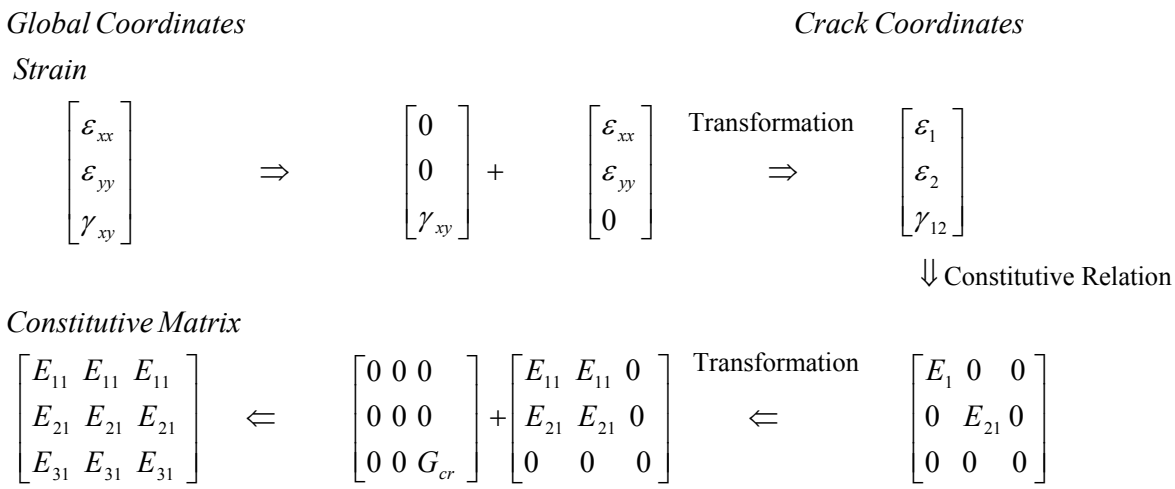

Figure 4.18 Shear Strain Separation (Sittipunt 1995)

4.3 Constitutive Model for Reinforcing and Structural Steel

The stress-strain relationship of steel under monotonic loading is conventionally represented by a bi-linear model where the stress-strain relationship remains elastic up to the yield stress of steel with a constant modulus of elasticity E_s. Beyond the yield limit, the steel hardens with a tangent modulus E_{sh} that is taken as a fraction of E_s (Figure 4.19). Steel rebars in the shear walls are well supported laterally by the heavy transverse reinforcement, while for structural steel, i.e. the coupling beams, design considerations are taken to avoid possible buckling modes such as local buckling and lateral torsional buckling as prescribed by ASCE-LRFD 1997. Hence, buckling is not included in the steel modeling.

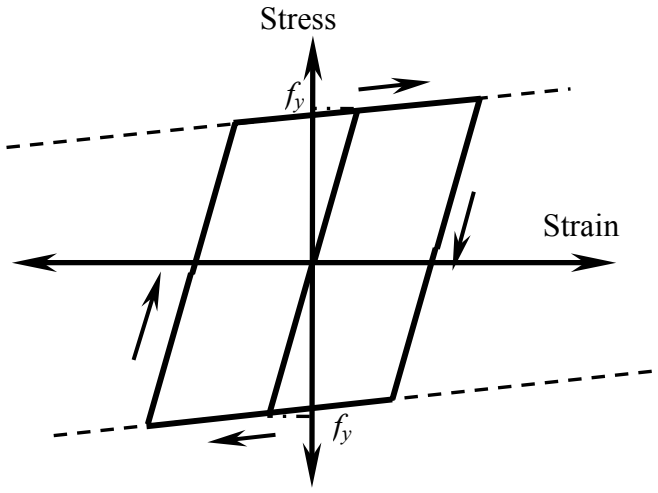

Figure 4.19 Kinematic Hardening Model For Reinforcing Steel

The stress-strain relationship for a bi-axial state of stress is defined by a yield surface function where a mathematical expression is used to predict the state of stresses based on the increments in strains. The original yield surface of steel can be represented by the dashed ellipse in Figure 4.20a. With the progress of loading beyond the yield limit, the yield surface starts to move (kinematic hardening) and/ or expand (isotropic hardening) such that the location of the new surface (the solid line ellipse) predicts the new values of stresses. The test results presented in Figure 4.21 shows that yield surface translates and expands simultaneously but the expansion of the surface is less significant in determining the new location of the surface.

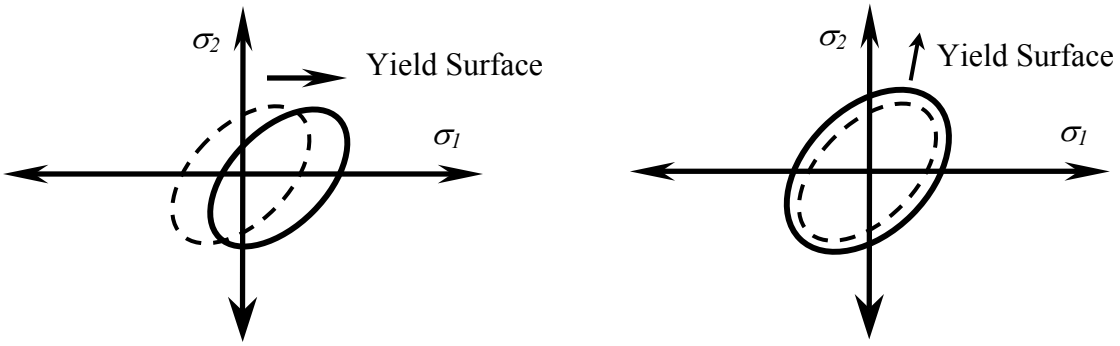

a) Kinematic Hardening b) Isotropic Hardening

Figure 4.20 Kinematic Hardening vs. Isotropic Hardening in Principal Stress Space

Because the yield surface shows little change in size, a pure kinematic hardening model is used where the expansion is ignored and the yield surface is only allowed to translate (Figure 4.19 and 4.20a). The yield stress for reinforcing bars and coupling beam is taken as 60 and 36 ksi respectively with an initial modulus of elasticity of 29000 ksi as is typically used for steel. The hardening modulus is taken as 0.5% of the initial modulus.

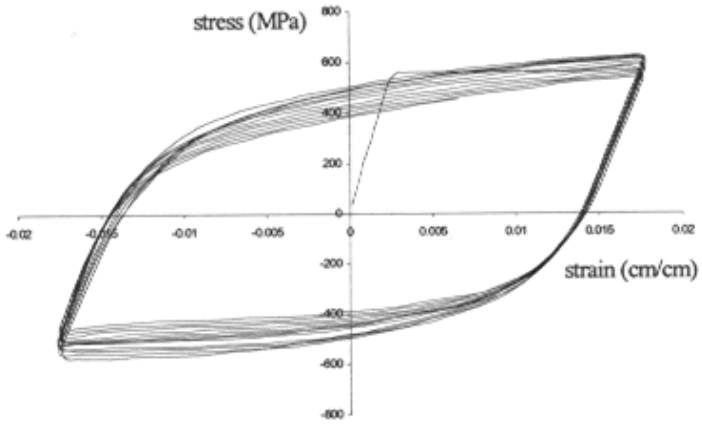

Figure 4.21 Cyclic Stress-Strain Curve (Brown, 1998)

4.4 Incremental –Iterative Procedure

The analysis is carried out in an incremental iterative manner. For static loading where forces are applied directly to the structure, the magnitude of the applied force is divided into increments whereas in dynamic analysis, the total time of the dynamic load is divided into small intervals. Within each increment, a solution for the equilibrium equations is sought by iterative means, i.e., by constantly adjusting the stiffness of the finite elements and repeatedly updating the state of stress and strains until the solution converges and equilibrium requirements are satisfied.

The Incremental procedure, which is essentially a Newton-Raphson procedure, can be described in the following steps:

Phase A, Increment #1, Iteration #1:

1. To find a start point, all elements are assumed elastic, and the structure is solved for the increment of forces applied.
2. Nodal displacements are computed and strains for each element are determined
3. Based on the obtained strains, stresses are found based on the stress-strain relationship (according to Figures 4.10 and 4.16) and the constitutive model of the element.
4. A new stiffness matrix is formulated for the element based on its current stress-strain state and the nodal forces for the element are computed by integrating the stresses on the element area. The total internal forces acting on the structure are found by adding up the individual element forces.

5. The external forces applied at the current increment are compared to the internal forces resulting from the previous step and the difference (the unbalanced forces) is determined.

Phase B, Increment #1, Iteration #2:

1. The unbalanced forces are applied to the structure with the modified stiffness and the new displacement increments are solved for.
2. The total displacement is found by adding up the displacement increments from the previous step to the current displacement
3. Steps 3A and 4A are repeated
4. Before proceeding to step 5A, the unbalanced forces are checked. If they are small enough then the solution is considered satisfactory and a new load increment is applied. Else, proceed with step 5A and repeat phase B with a new iteration (iteration 3)

Phase C, Increment #2, Iteration #1:

1. Elements are assumed to have the most recent stiffness calculated from the last iteration and the structure is solved for the increment of forces applied plus the previous increments.
2. Repeat 2A, 3A, 4A and 5A
3. Repeat Phase B With Increment #2, Iteration #2
4. Change increment number and proceed with phase C

4.4.1 Convergence Criteria

In step 4B, the computed unbalanced forces are checked against convergence criteria to determine if the solution accuracy is sufficient. The convergence is based on energy norm criteria shown in Figure 4.22. The gain in energy in the current iteration is divided by the gain of energy at the very first iteration within the increment considered. The solution is said to convergence if the energy norm is less than a certain convergence tolerance specified by the user.

$$Energy\ Norm\ Ratio = \frac{\delta E_1}{\Delta E_o} = \left| \frac{\{\delta u_i\}^T (\{f_{\text{int},i+1}\} + \{f_{\text{int},i}\})}{\{\Delta u_i\}^T (\{f_{\text{int},1}\} + \{f_{\text{int},0}\})} \right| \tag{4.51}$$

Where:

$\delta u_{i:}$ Incremental displacement vector at iteration *i*

$\Delta u_{o:}$ Incremental displacement vector at iteration *0*

$f_{int,i:}$ internal force vector at iteration *I*

$f_{int,+1i:}$ internal force vector at iteration *i+1*

$f_{int,1:}$ internal force vector at iteration 1

$f_{int,0:}$ internal force vector at iteration *0*

At the same time, a maximum number of iterations per increment is specified by the user so that the analysis proceeds to the next increment if the maximum number of iteration or the convergence tolerance whichever comes first is achieved

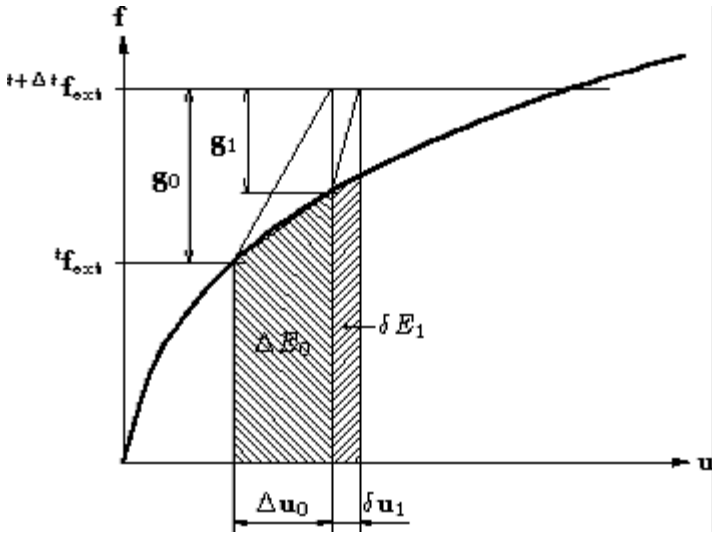

Figure 4.22 Energy Norm Convergence Criteria

4.4.2 Solution Algorithm

Figure 4.23 shows a schematic for the iterative procedure used in analysis. The Newton-Raphson algorithm is used, where the structure stiffness matrix is updated every iteration until convergence is achieved. The structure stiffness matrix is assembled from the element stiffness matrices upon the determination of the stress-strain state as explained in step 4A. Since the solution is incremental in nature, the fastest path to move from point 1 to point 2 is to follow a line tangent to the point 1. This implies that use of tangent stiffness approach would be the fastest solution algorithm to achieve convergence. Although this is true at the element level, at the structure level, negative stiffness coefficients in a large stiffness matrix cause the solution to numerically fail and diverge instead of converging. To avoid the presence of negative coefficients in the structure stiffness matrix, element stiffness is based on the secant stiffness rather than tangent stiffness where the stiffness coefficients are always positive (Figure 4.24).

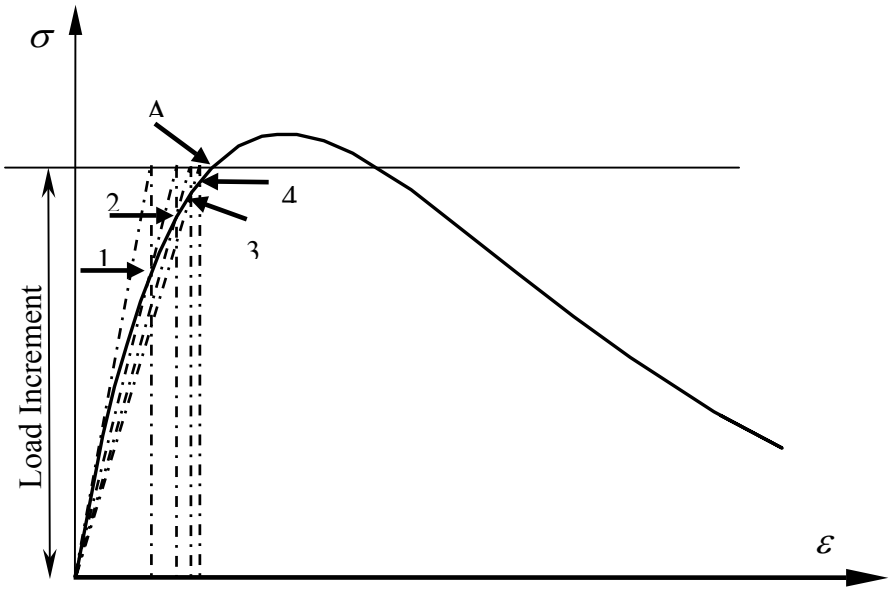

Figure 4.23 Newton-Raphson Algorithm

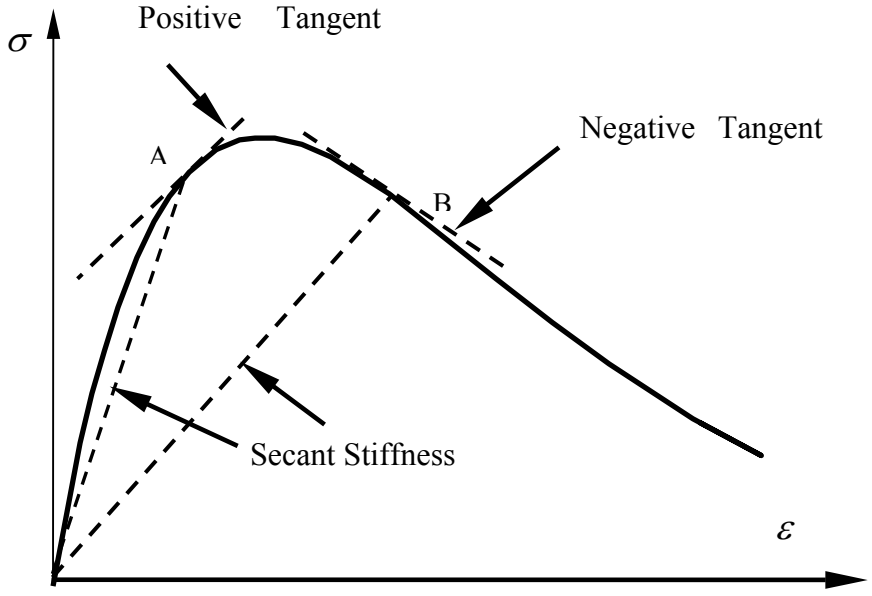

Figure 4.24 Tangent Stiffness vs. Secant Stiffness on the Element Level

4.5 Verification Study

Extensive experimental studies on shear walls were conducted at the Portland Cement Association (PCA) by Oesterle et al. (1976 and 1979). The test results obtained from these studies are used in order to evaluate the analytical model described in this chapter.

4.5.1 PCA Wall Tests

The PCA experimental program was designed to investigate the inelastic behavior of reinforced concrete shear walls. A successful finite element model is expected to properly represent pertinent aspects of the observed nonlinear behavior of the wall samples. The objective is to insure that the model can reproduce the behavior of shear walls with various design parameters, such as ratio of flexural and shear reinforcement, concrete compressive strength, loading history etc. If the model is successful for such task, it can be used to investigate the

behavior of walls different from the test specimens. The test specimens included a series of rectangular cross sectional walls with and without thickened boundary elements. Five walls out of the whole set was chosen to compare to the analytical model. They are labeled B1; B2 through B5.Nominal dimensions of the wall specimens is shown in Figure 5.25.

The parameters considered in the PCA wall test specimens include:

- The amount of the flexural reinforcement
- The amount of horizontal shear reinforcement
- The amount of transverse reinforcement in the boundary element
- The loading history
- The concrete compressive strength

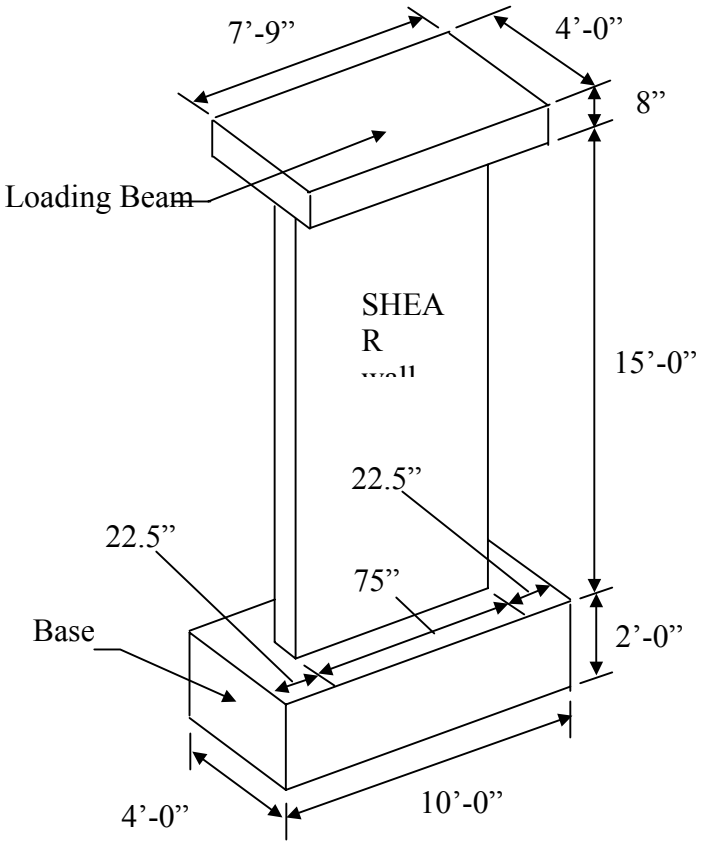

Figure 4.25 Dimensions for Walls B1-B5

Figure 4.26 shows typical reinforcement details of the wall cross-section. Table 4.1 summarizes the wall properties such as reinforcement and material models of each wall.

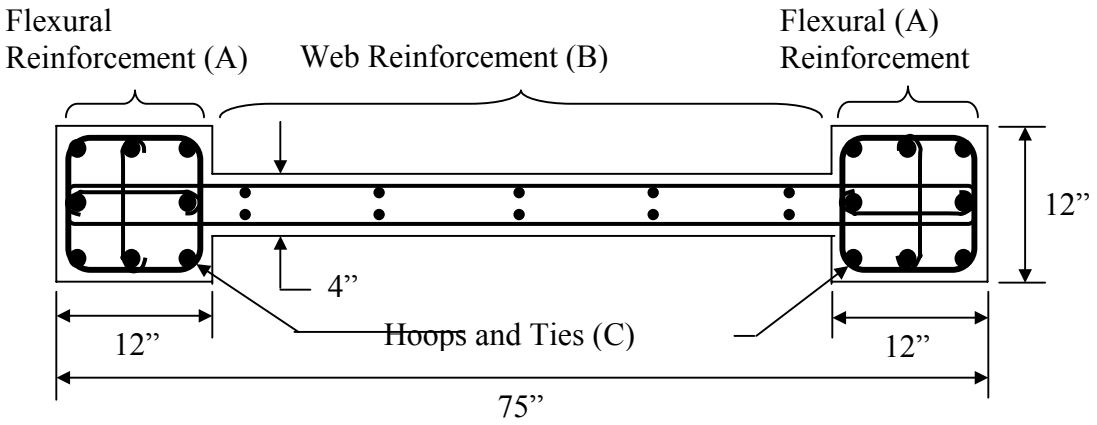

Figure 4.26 Typical Reinforcement Details for Dimensions for PCA Walls

Table 4.1 Properties of PCA Wall Specimens

Wall	Loading Type	f_c’(psi)	f_y(psi)	Reinforcement[3] (%)			
				ρ_v	ρ_h	ρ_n	ρ_s’
B1	IR[1]	7685	65.2	1.11	0.31	0.29	0
B2	IR	7775	59.6	3.67	0.63	0.29	0
B3	IR	6860	63.5	1.11	0.31	0.29	1.28
B4	MN[2]	6530	65.3	1.11	0.31	0.29	1.28
B5	IR	6570	64.4	3.67	0.63	0.29	1.35

[1] IR: Increasing reversed loading

[2] MN: Monotonic loading

[3] ρ_v: Ratio of flexural reinforcement (A) to area of the boundary element

ρ_h: Ratio of horizontal web reinforcement (B) to area vertical section through the web

ρ_n: Ratio of vertical web reinforcement (B) to area horizontal section through the web

ρ_s': Ratio of volume of confinement reinforcement (C) to the volume of core

Test specimens were designed according to the 1977 ACI building code. Specimens B1, B3 and B4 had minimum web reinforcement. In specimens B2 and B5, web reinforcement was selected such that the nominal shear strength is equal to the nominal flexural strength. Although the specified concrete compressive strength for all walls is the same, the actual measured strength for the walls vary as shown in Table 4.1. Transverse reinforcement was provided in the lower 6 feet of walls B3, B4 and B5 while the rest of the boundary element was reinforced with ordinary ties.

Lateral load was applied through a top loading-beam (Figure 4.25). Two types of loading were used, monotonic load (MN) and increasing incremental loading (IR). In the monotonic loading, the specimen was subjected to monotonically increasing load up to failure. In the IR loading, the amplitude of the applied displacement cycles was increased incrementally as indicated in Figure 4.27. The finite element mesh for the walls is shown in figure 4.28. 2-node bar (truss) elements are used to represent the flexural reinforcement in the boundary element while 4-node plane stress element is used for the modeling of the concrete wall, while smeared steel grid elements represent the web reinforcement. A detailed description of the elements is given in section 4.1 of this chapter. Because of the large dimensions of the top and bottom beams, elastic material properties are assigned to the elements that represent them.

Material properties are assigned to the elements according to table 4.1. For confined concrete in walls B3, B4 and B5, the confined concrete strength due to the presence of the transverse reinforcement is taken 9660 psi using equation 4.38. For the reinforcing steel, a strain hardening modulus of 0.5% of the steel's initial modulus of elasticity is used with a kinematic hardening model as explained in section 4.3

The entire wall is fixed at the base. The nodes at the wall base are considered fixed to the base beam. This fixity is modeled by restraining the wall base nodal points against translation in all directions.

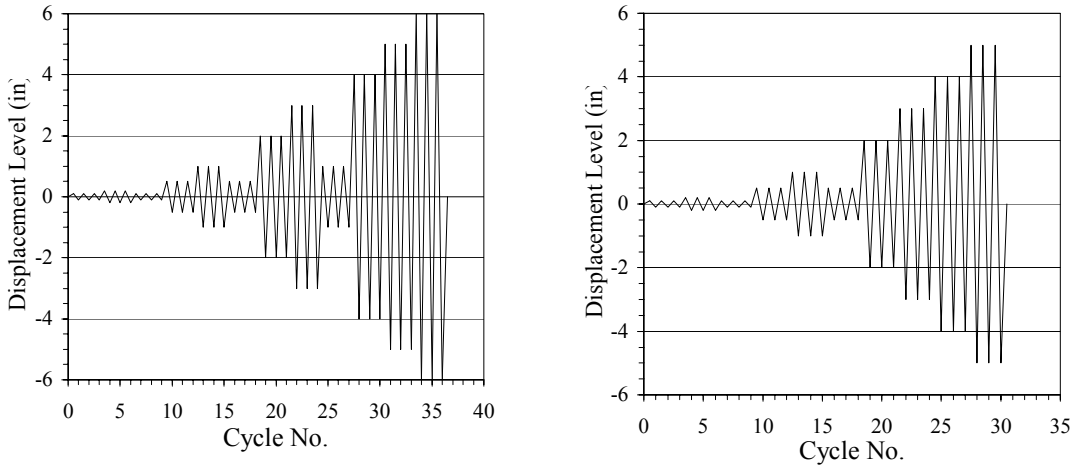

a) Walls B1 and B3 b) Walls B2 and B5

Figure 4.27 Static Cyclic Loading for Walls B1, B2, B3, and B5 (Oesterle et al., 1976)

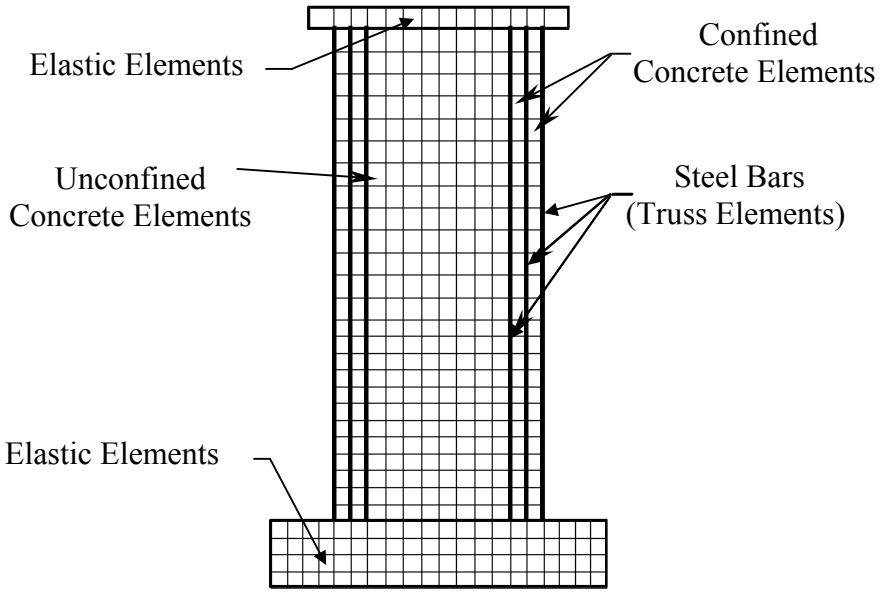

Figure 4.28 Finite Element Mesh for the PCA Walls

4.5.1.1 Evaluation of the Analytical results

The analytical results from the finite element analyses include nodal displacements, wall base reaction, stresses and strains in concrete elements and steel bar elements. The relationship between the lateral load and the displacement at the wall top is a considered a general indicator of the response of the wall. Wall strength can easily be measured from the load-deflection curve. Wall stiffness can be quantified as the tangent of the load-deflection curve. In addition, the load-deflection curve indicates the energy dissipation characteristics of the tested wall. Nonlinear behavior aspects such as strength and stiffness degradation are also represented by the load-deflection curve.

The total displacement at the top of the wall is a summation of two components: flexure and shear. The importance of monitoring the shear distortion contribution stems from the fact that significant shear strains are usually associated with brittle, undesirable modes of behavior and hence, such high strains are an indicator for potential brittle failure mechanism that should be avoided in the design. Average shear strains are measured using information extracted from the wall nodal displacement. The average shear distortion of the lower part of the wall is calculated using the equation proposed by (Oesterle et al., 1976):

$$\gamma = \frac{\delta_1 d_1 - \delta_2 d_2}{2hl} \tag{4.51}$$

Where: $\delta_1, \delta_2 =$ Change in lengths of diagonals 1 and 2

$d_1, d_2 =$ Original lengths of diagonals 1 and 2

$h =$ Height of region for which shear distortion is calculated

$l =$ Length of region for which shear distortion is calculated

The average shear distortion for the entire 6 ft. high region is calculated according to (Oesterle et al., 1976):

$$\gamma_{avg} = \frac{\gamma_1 h_1 + \gamma_2 h_2}{h_1 + h_2} \tag{4.52}$$

Where: $\gamma_1, \gamma_2 =$ Shear distortions for regions 1 and 2 as shown in Figure 4.19

$h_1, h_2 =$ Heights of regions 1 and 2 as shown in Figure 4.29.

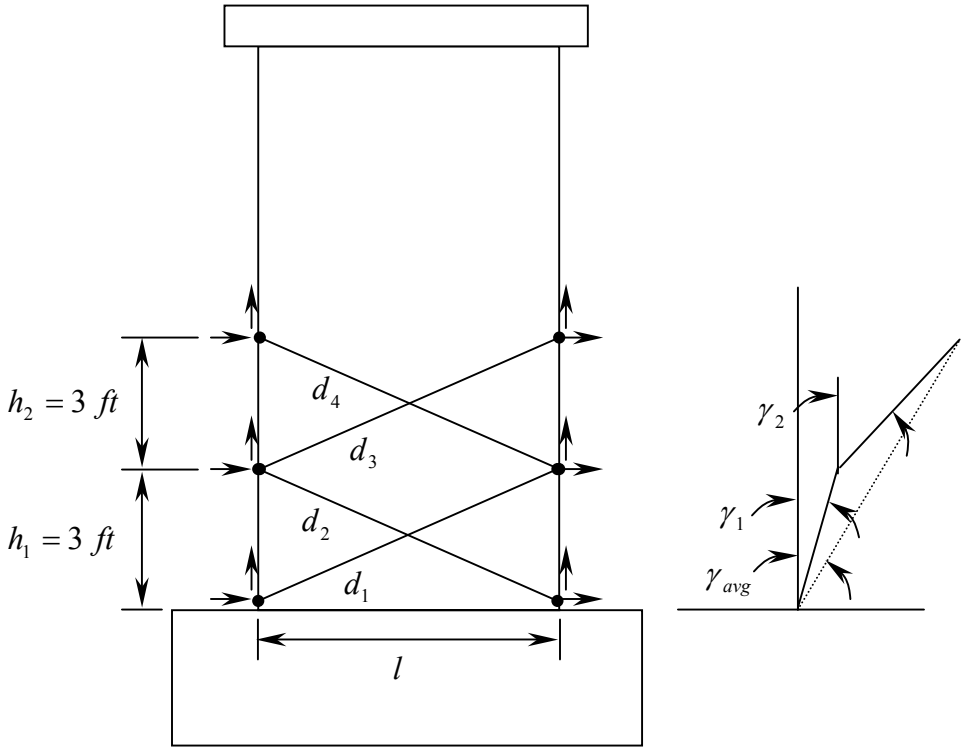

Figure 4.29 Determination of Shear Strains

4.5.1.1.1 Load-Deflection Plots

A comparison is made between three sets of data. The first set is the test results obtained from Oesterle et al (1976 and 1979). The second set of results are obtained by using a built-in-DIANA material model in which the shear reduction factor is constant and taken as 0.25 ($\beta =$

0.25 in equation 4.47). The third set of results represented by the continuous-line plots are obtained from the analytical model described in section 4.2 of this chapter.

Representative load-deflection curves for walls B1 and B2 are shown in Figures 4.30 and 4.31 where all three sets match well. However, it's observed that the results predicted by the analytical model better captures the stiffness degradation of the wall while it is unloading (pinching effect). The unloading stiffness and the size of loops of the analytical mode suggest better representation of the wall response. Moreover, in the DIANA model, the predicted strengths in both direction of loading are not the same. For wall B1, the strength is 60 kips when the wall is pushed to the right vs. 70 kips if the wall is pushed to the left which introduces a bias to the analytical results. The load deflection curve for wall B3 (Figure A.1, appendix A) also experiences the same bias in DIANA results. Results obtained from the analytical model are symmetric in both direction of loading for all walls. The initial stiffness of analytical results matches the experimental results better than those predicted by DIANA; which slightly underestimates the initial response of the wall. In wall B2, The analytical model shows better pinching than the DIANA built-in model does does. For further reference, load-deflection plots for walls B3, B4 and B5 are shown in Figures A.1, A.3 and A.5, appendix A respectively.

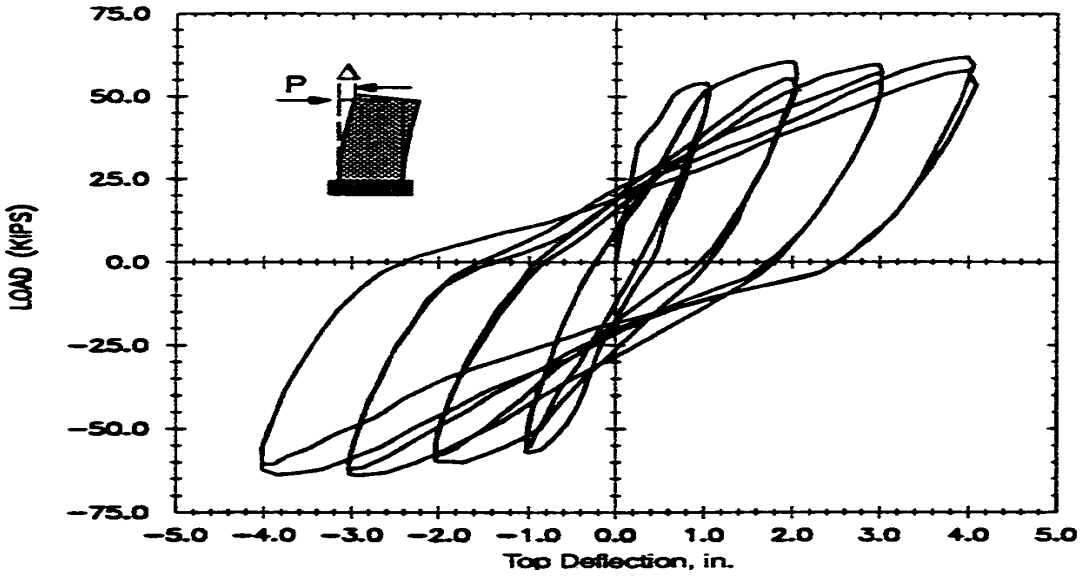

a) Experimental Result

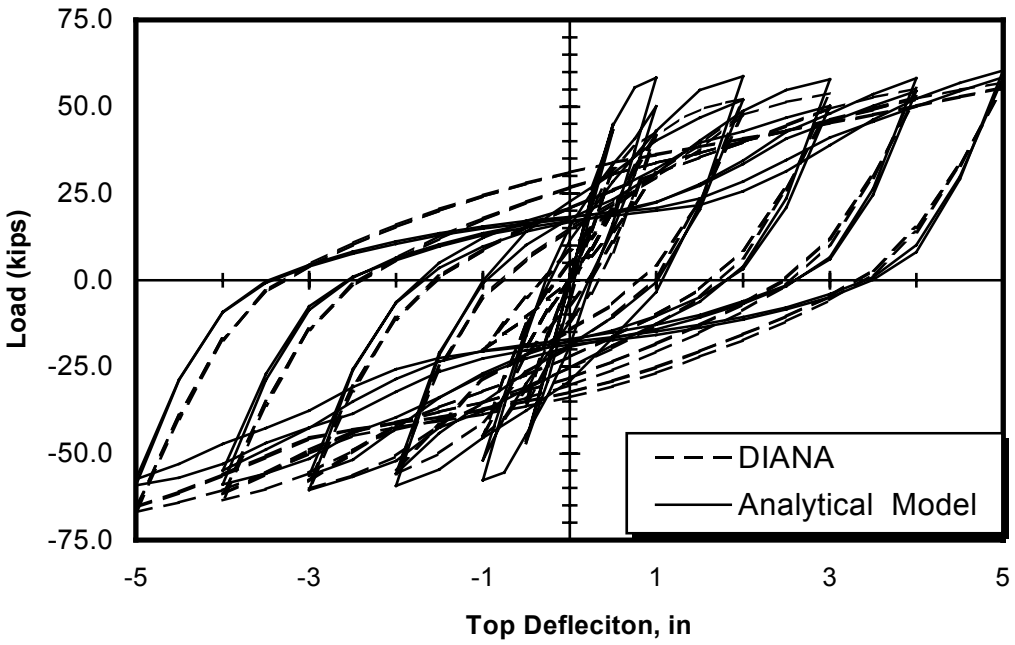

b) Analytical Result

Figure 4.30 Load vs. Displacement Comparison for Wall B1

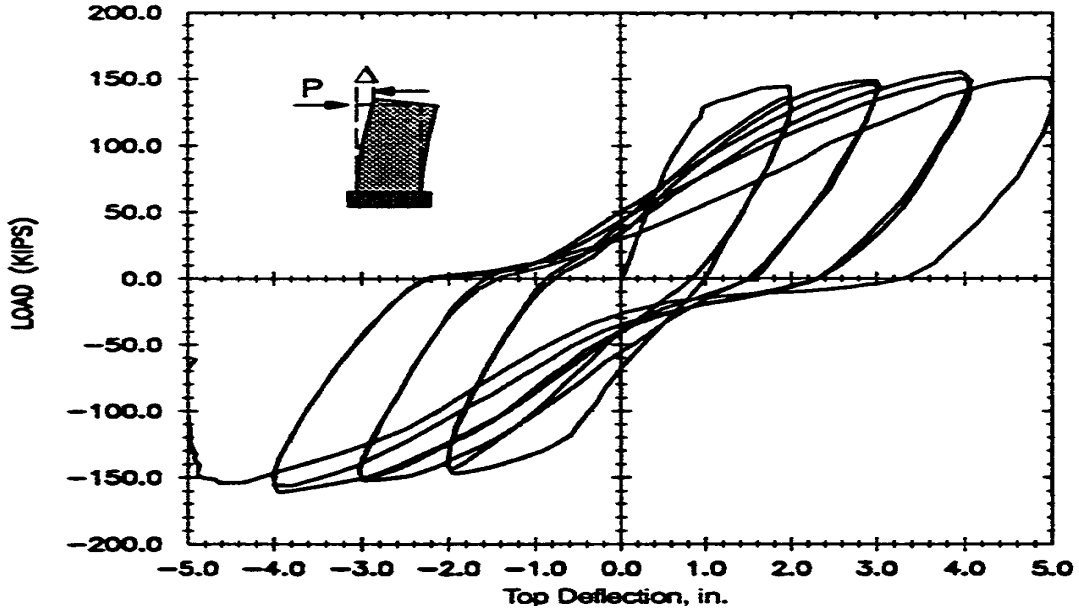

a) Experimental Result

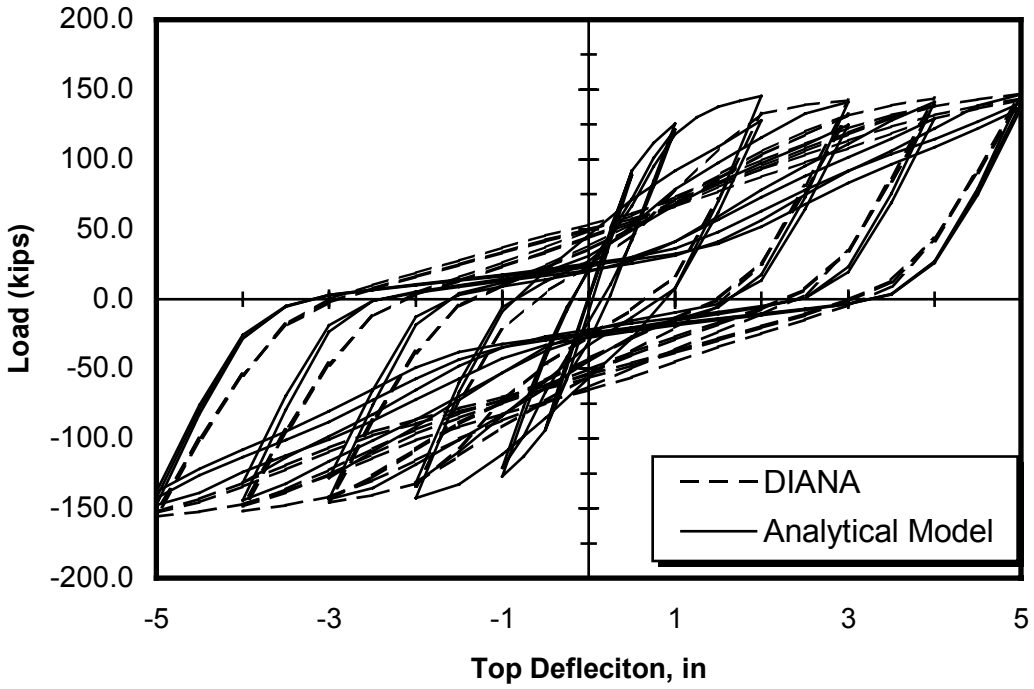

b) Analytical Result

Figure 4.31 Load vs. Displacement Comparison for Wall B2

4.5.1.1.2 Average Shear Strains

Figures 4.32 and 4.33 show comparison between average shear strains obtained from the test results and those obtained from the analytical model. Results obtained from the built-in DIANA model are also shown in dashed lines. Shear strains predicted by the analytical model show better representation compared to test results. In wall B1, DIANA underestimates the shear deformation of the specimens and introduces bias to the analytical results by computing less shear strains in the negative load cycles than it does in the positive cycles. In Wall B2, DIANA underestimates the shear strains compared to other sets of results but with symmetric behavior on both positive and negative load cycles. Wall B2 experiences significant pinching effect compared to wall B1 due to the large increase of the flexural reinforcement. As mentioned above, large shear strains and, consequently, pinching effect is undesirable mode of behavior in shear walls since it is associated with potential brittle failure modes, less energy absorption capacity and less ductility capacity. The size of the loops of both B1 and B2 is also another indicator to the amount of energy consumed by both systems. The load-deflection plot of B1 is characterized with relatively wider loops than those obtained from B2. Average shear strains for Walls B3, B4 and B5 are illustrated in Figures A.2, A.4 and A.6, Appendix A for further reference.

4.5.1.1.3 Failure Modes

Table 4.3 illustrates the failure modes from both test results and analytical solution. Good agreement is obtained in computing the steel yielding point for all walls as well as the ultimate strength of the wall. Determination of crushing criteria of both sets of results also matches well

except in wall B3 where discrepancy is encountered in matching the web crushing point obtained from analysis and test results.

Table 4.2 Failure Modes: Experimental vs. Analytical

Specimen	Failure Mode	Experimental Results	Analytical Results
B1	Steel Yielding	+0.56 in. DL Cycle 10 Load = 45.1 kips	0.50 in. DL Cycle 10 Load = 44.8 kips
	BE Crushing	+3.0 in Cycle 22	+2.0 in. Cycle 14
	Web Crushing	None	None
	Wall Strength	Load = 61.0 kips -4.0 in.	Load = 60 kips -5.00 in.
B2	Steel Yielding	+0.84 in. Cycle 13 Load = 119.7 kips	+1.0 in. Cycle 14 Load = 125 kips
	BE Crushing	+3.0 in. Cycle 22	+2.0 in. Cycle19
	Web Crushing	-5.0 in. Cycle 28	-5.0 in. Cycle 28
	Wall Strength	Load = 152.8 kips -4.0 in.	Load = 148 kips 5.00 in.
B3	Steel Yielding	+0.55 in. Cycle 10 Load = 45.2 kips	0.50 in. Cycle 10 Load = 47 kips
	BE Crushing	+7.00 in. DL (Cycle 38)	None
	Web Crushing	-4.0 in. DL (Cycle 28)	None
	Wall Strength	Load = 62.0 kips +6.00 in. DL	Load = 62 kips 6.00 in. DL

Table 4.2 Failure Modes Comparison (Continued)

Specimen	Failure Mode	Experimental Results	Analytical Results
B4	Steel Yielding	0.50 in. Load = 45.3 kips	0.5 in Load = 43.9 kips
	BE Crushing	2.0 in.	3.0 in
	Web Crushing	None	None
	Wall Strength	Load = 75.3 kips 8.5 in.	Load = 73 kips 8 in.
B5	Steel Yielding	+0.84 in. Cycle 13 Load = 112.3 kips	.75 in. Cycle 13 Load = 124 kips
	BE Crushing	+2.0 in. DL Cycle 19	+3.00 in. Cycle 24
	Web Crushing	-5.00 in. DL Cycle 29	-4 in. Cycle 28
	Wall Strength	Load = 171.3 kips -5.0 in.	Load = 175 kips - 5.0 in.

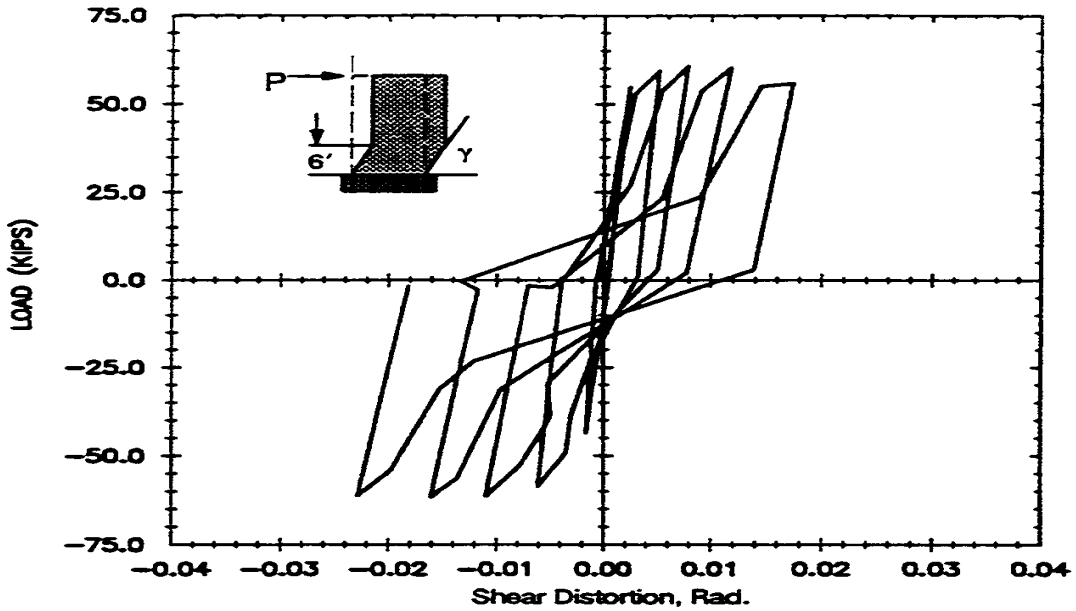

a) Experimental Result

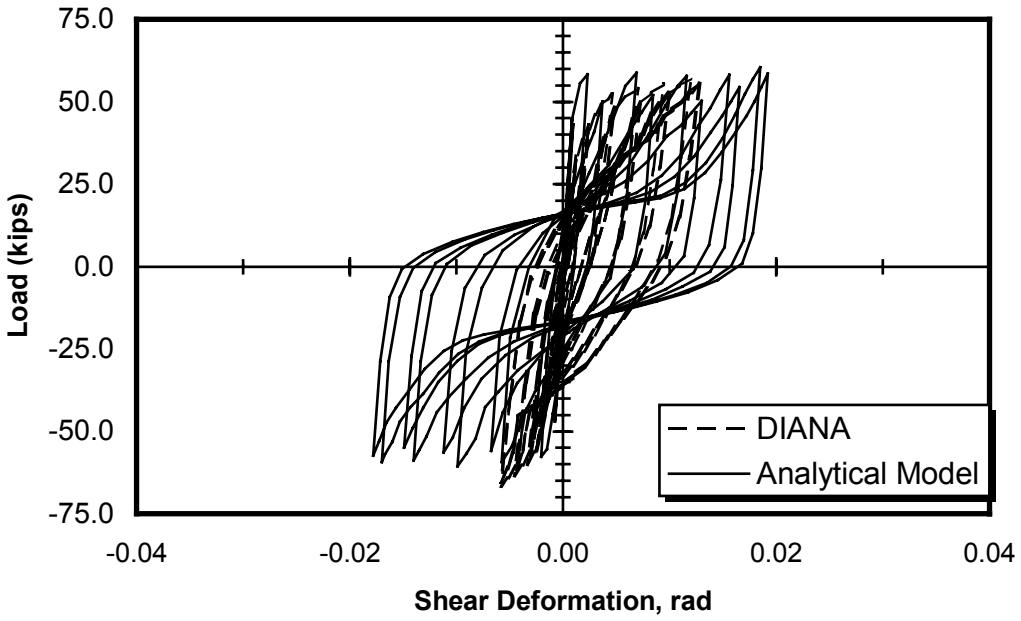

b) Analytical Result

Figure 4.32 Load vs. Shear Distortion Comparison for Wall B1

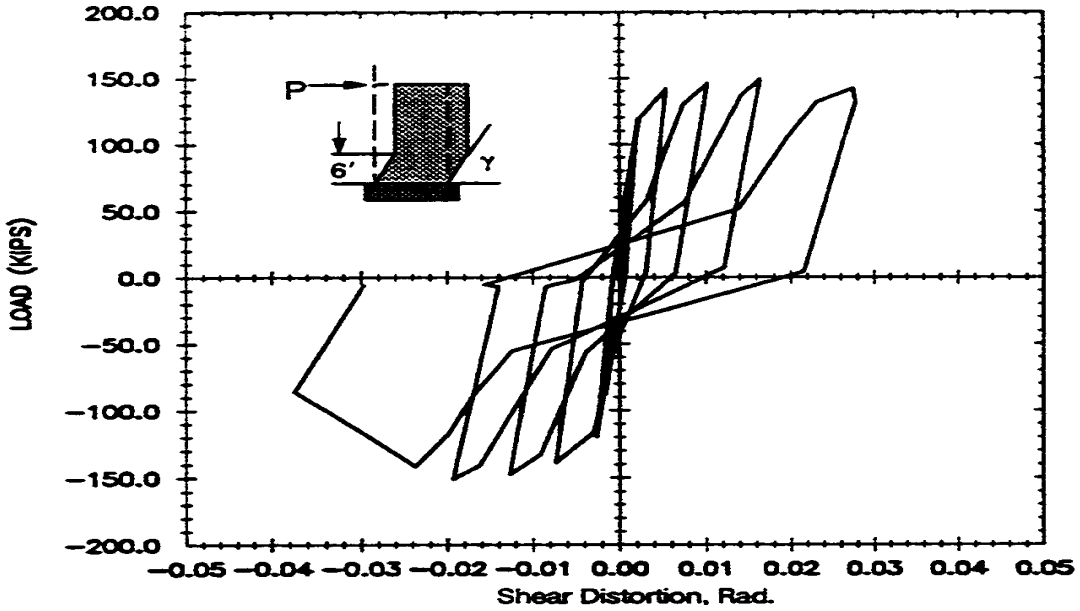

a) Experimental Result

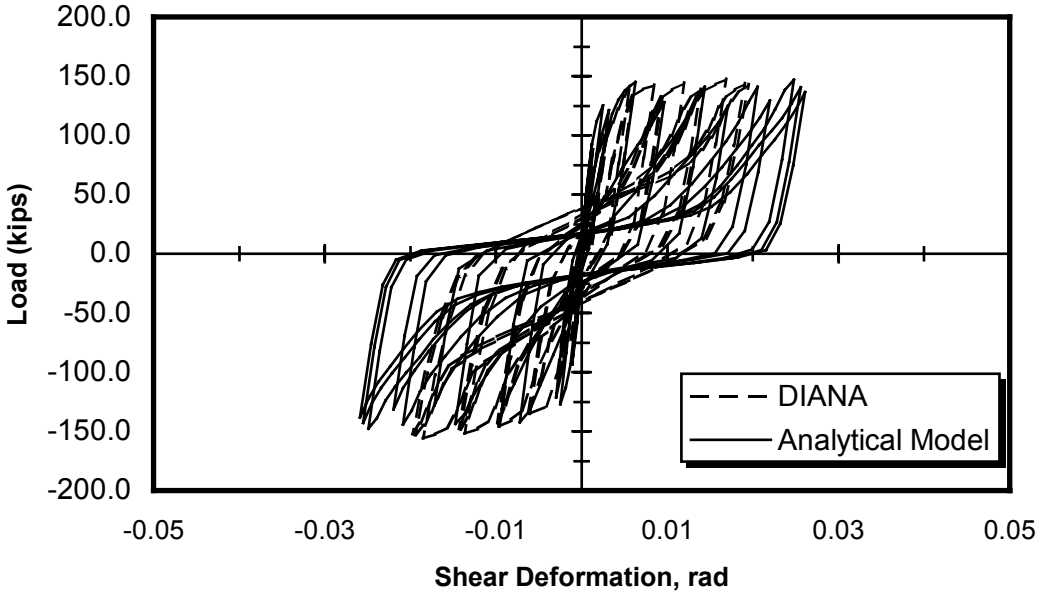

b) Analytical Result

Figure 3.33 Load vs. Shear Distortion Comparison for Wall B2

4.6 Summary

A review of the aspects of nonlinear behavior of reinforced concrete reinforcing and structural steel is presented. For concrete, important aspects of nonlinear behavior such as cracking, tension stiffening, concrete crushing, shear stiffness reduction, compressive behavior are discussed. Both discrete and smeared approaches in modeling cracks in concrete are presented. Smeared crack approach is found suited for the type of problem considered in this work. Concrete compressive behavior is simulated via using the stress-strain curve suggested by Thorenfeldt. Behavior of confined concrete at the boundary zones of shear walls is also accounted for by enhancing the concrete strength and ductility. For the shear behavior, shear stiffness is reduced based on the extent of cracking in concrete. Moreover, following the work of Sittipunt, shear strains are separated from normal strains to avoid premature compressive failure in concrete while allowing concrete to undergo high shear strains.

Although many material models were successfully used in analysis of reinforced concrete, they were chiefly implemented for concrete under static monotonic or cyclic loading with regular load reversals. To avoid possible problems associated with the random load sequence that characterize dynamic loading, further simplification is made to the existing models by assuming simple load paths for the concrete in both loading and unloading conditions.

The constitutive model for steel consists of bilinear model with initial stiffness and strain hardening parts. Kinematic strain hardening is implemented where the failure surface is traveling in the principal stress space without expanding.

The model is validated through a comprehensive verification study where results obtained from the model are compared to well-known test results. The model is found capable of capturing aspects of nonlinear behavior satisfactorily.

CHAPTER 5: TENSION FLANGE EFFECTIVE WIDTH IN RC SHEAR WALLS

One of the concerns in nonlinear finite element analysis is the efficiency and practicality of the model. This concern becomes critical in nonlinear dynamic analysis where the load duration is divided into a number of time intervals, each requiring incremental solution of the nonlinear problem. When the specified time steps are small, the number of time intervals necessary to perform the analysis becomes large. Furthermore, compared to static analysis, dynamic nonlinear analysis involves many random load reversals chapter 1, which could hinder convergence in larger models. As discussed in chapter 1, the finite element models developed by Kuenzli (2001) were so large that they could not be effectively used in the nonlinear dynamic analyses conducted herein. As described later on in Chapter 6, one of the tactics undertaken to reduce the size of the model is to eliminate the flanges, and lump their effect through specification of an effective width. This chapter describes the effective width concept and the means by which it can be implemented.

5.1 Effective Width Concept

One of the important parameters that influence behavior, analysis, and design of flanged reinforced concrete shear walls is the transverse distribution of the strains in the tension flange. The shape and magnitude of the strain distribution plays an important role in both serviceability behavior and ultimate strength behavior. Since the distribution of strains in the flange is nonlinear, the corresponding stress distribution is also nonlinear, which considerably complicates

analysis and design. To avoid direct consideration of the shape of the nonlinear stress distribution, engineers resort to the concept of effective width, in which only a uniformly stressed 'effective' portion of the flange is considered to participate in structural behavior. The length of the effective width is calculated such that the behavior of a fictitious wall in which only the 'effective' portion of the flange is present is equivalent to the flanged wall being represented. Code committees are keenly conscious of the practical importance of the effective width concept, but they have struggled to specify what they perceive to be a conservative yet fixed value that is suitable for a wide range of design conditions. The difficulty encountered in specifying a fixed width arises because the effective width varies as a function of several influential parameters.

The design philosophy for walls recently changed from prescriptive to deformation-based and consequently, the effective width provisions and the philosophy behind them also underwent a dramatic change. As recently as 1994 (UBC 1994), the tension effective width was required to be not greater than one-tenth of the wall height, which is now generally considered to be a low value. The reasoning behind this provision appears to be that it is conservative to underestimate tension flange effective width, which leads to conservative flexural design. Wallace (1996) pointed out that a low estimate is not necessarily safe and could lead to inadequate shear reinforcement and insufficient seismic reinforcement in the wall web opposite the flange in tension. He suggested a tension flange effective width of one-quarter the wall height, which was subsequently adopted in the ACI (2002) seismic provisions.

Previous research has shown that the main parameters that influence tension flange effective width include 1) design drift, 2) geometry of the flanged wall, and 3) applied axial load. Of these 3 parameters, the first two have been studied to some extent as a result of research into the behavior of reinforced concrete T-sections. The main conclusions from these studies are

discussed in the following section. The last parameter (axial load) has been rarely studied, and is investigated in this chapter. The motivation for this study stems from the fact that coupled walls are subjected to axial forces that vary during an earthquake as a result of the coupling action. Under seismic conditions, the net axial force acting on a wall can become quite high and can possibly reverse direction subjecting the wall to axial tension. The purpose of the study presented in this chapter is to use nonlinear finite element modeling to quantify the effect of axial load (including tension) along with other parameters on the tension flange effective width for a limited number of flanged walls, and to discuss the implications regarding current effective width provisions.

5.1.1 Summary of Previous Research

The nonlinear distribution of flange stresses results from the phenomenon known as *shear lag*, in which high stresses are generated or *concentrated* at the junction between the flange and the web and the stresses decrease in value at locations away from the flange/web junction. The effect of shear lag in simple linear elastic systems has been investigated using the theory of elasticity (Timoshenko and Goodier 1970). However, rigorous theory of elasticity investigations of shear lag problems are of theoretical value only and are too complex to use for estimating the effective of width in practical engineering problems. Approaches that make use of empirical approximations have proved to be more successful in developing simplified equations to estimate the effective flange width for design purposes. For example, based on experimental observations, Reisner (1964) made effective width calculations by assuming that the distribution of flexural normal stresses in a flange plate can be approximated by a second order parabolic curve. Other notable investigations that made simplifying assumptions in the calculation of the *elastic*

effective width include Schade (1951), Sechler (1952), Fan and Heins (1974), and Song and Scordelis (1990).

When nonlinearity in material behavior is present, the effective width can no longer be accurately calculated using elastic techniques. Material nonlinearity is common in reinforced concrete walls and results from nonlinear compressive behavior of concrete, concrete cracking, steel yielding, reinforcement slip, etc. Most of the recent investigations have focused on the effective flange width in reinforced concrete T-sections under pure flexural loading. However, this situation is not representative of flanged walls, which are under the effect of axial forces in addition to flexure. The main conclusions from research on T-beams under pure flexure reported in Ehsani and Wight (1985), Pantazopoulou and Moehle (1990), Qi and Pantazopoulou (1991), Shahrooz and Pantazopoulou (1992), Hosoya et. al. (1994), and Pantazopoulou and French (2001) can be briefly summarized as follows:

- The degree of participation of the flange in the tension zone can be quite high and results in simultaneous increases in both stiffness and strength of the cross section.
- Increasing beam depth mobilized more of the flange thereby increasing the effective flange width. Since beam depth is usually a function of span, it is reasonable to define effective width as a ratio of span.
- Tension flange participation is a drift-controlled problem, increasing in the amount and significance with increasing plastic rotation.

5.1.2 ACI 318-2002 Provisions

It is instructive to compare ACI *seismic* provisions for tension flange effective width in beams and walls. In the case of T-beams, Section 21.4.2.2 specifies that the flange effective

width (for flange under compression or tension) should be taken as the smaller of 1) 25% of the beam span, 2) center-to-center spacing of the beams, or 3) sixteen times the slab thickness plus the beam width. In the case of walls, Section 21.6.5.2 specifies that unless a more detailed analysis is conducted the overhanging effective flange width (measured from the face of the web) should be taken as the smaller of 1) one-half the distance to an adjacent wall web or 2) 25% of the total wall height. The wall provisions are based primarily on data pertaining to the tension flange effective width, but the commentary suggests that they are applicable to the flange under compression as well. The rationale behind this is that the compression effective width has little impact on flexural strength and ductility and so determination of a precise value is not necessary and is therefore avoided for the sake of simplicity.

As shown in Figure 5.1, a symmetric simply supported flanged beam (span L) is structurally equivalent to two flanged cantilevers (each of span L/2) joined at their fixed ends. In the case of the simple beam, the effective width according to ACI-318 beam provisions is L/4 assuming that the other criteria pertaining to the slab thickness and centerline spacing do not control. In the case of the cantilever, the ACI-318 wall provisions suggest that the effective width is L/2/4 on either side plus the web width, i.e. L/4 + web width. Since the web width is generally small compared to L/4, it appears that the ACI-318 provisions do not substantially differentiate between the effective width of walls and beams and therefore ignore the effect of axial loads, which are present in walls. Hence, the following sections of this chapter are devoted to investigating the effect of axial load along with other parameters on the effective width.

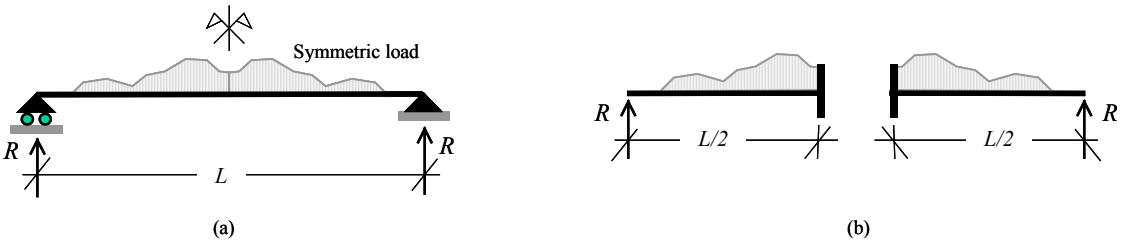

Figure 5.1 Symmetric simply supported beams represented by two cantilevers

5.2 Parametric Study

The shear walls used in this study are based on the design for the 12-story coupled wall system designated HCW-12-30 as discussed previously in the chapter 3. Using the left C-wall of the system as a starting point, additional analysis configurations are created by varying the following parameters: flange width, wall height, and axial load level. The overhanging flange width (half the total flange width) is varied from a nominal 15 ft to 22.5 ft and then to 30 ft. Other parameters including flange reinforcement per unit length, for example, are assumed to remain constant as the flange width is varied. The applied axial loads are carefully chosen based on analyses of several 6- and 12-story prototype systems reported in El-Tawil et al (2002b) to bound load levels that can occur during a severe seismic event. Four levels of axial load are considered: 1) tension that represents the significant uplift observed when coupling ratios are high (represented by a tensile force causing $0.4f_y$ in the wall steel); 2) zero axial load, i.e. pure flexure case; 3) compression resulting in a wall compressive stress of $0.05f'_c$; and 4) compression resulting in a wall compressive stress of $0.08f'_c$. Two wall heights are considered: 6 and 12 stories. The 6-story walls are obtained by simply removing the top half of the12-story walls while keeping wall reinforcement constant to avoid changing more than one parameter at a time.

A total of 24 models are created. Each wall model is then subjected to a uniform lateral load and pushed to three levels of drift: namely 0.5%, 1%, and 2%. The last drift level is widely considered representative of demands imposed by a severe seismic event (Pantazopoulou and French 2001). Table 5.1 shows the parameter combinations that resulted in 24 models; each model is designated by the number of stories, flange width and level of axial force on the wall. For example, W-12-15-T indicates a model with 12 stories; 15 ft flange and a tension load applied to the wall.

Table 5.1 Model Designations for the Parametric Study

Wall Height	12 Stories			6 Stories		
Flange Width / Axial Load[1]	15 ft	22.5 ft	30 ft	15 ft	22.5 ft	30 ft
$-0.4 f_y A_s$	W-12-15-T	W-12-22-T	W-12-30-T	W-6-15-T	W-6-22-T	W-6-30-T
0.0	W-12-15-0	W-12-22-0	W-12-30-0	W-6-15-0	W-6-22-0	W-6-30-0
$0.05 f_c' A_c$	W-12-15-C5	W-12-22-C5	W-12-30-C5	W-6-15-C5	W-6-22-C5	W-6-30-C5
$0.08 f_c' A_c$	W-12-15-C8	W-12-22-C8	W-12-30-C8	W-6-15-C8	W-6-22-C8	W-6-30-C8

[1] Negative sign indicates tension

5.3 Finite Element Modeling

Finite element mesh for both wall are shown in figure 5.2. The wall web was divided into 4 x 48 in-plane elements while the 15 ft flange was divided into a similar number of elements. For the 22.5 ft and 30 ft flanges, number of elements increases proportionally to 6 x 48 and 8 x 48 elements respectively. For the 6-story wall, elements numbers in vertical direction are half those of the 12-story wall (i.e. 24). Steel reinforcement is represented by grid reinforcement in

both the web and the flange as explained in chapter 4. Reinforcing bars in the boundary element are represented by discrete bar (truss) elements.

Lateral loads are distributed uniformly along the wall height and the walls are pushed over until a maximum drift level of 2% is achieved. Results are then extracted at drift levels of 0.5% and 1% drift levels as well.

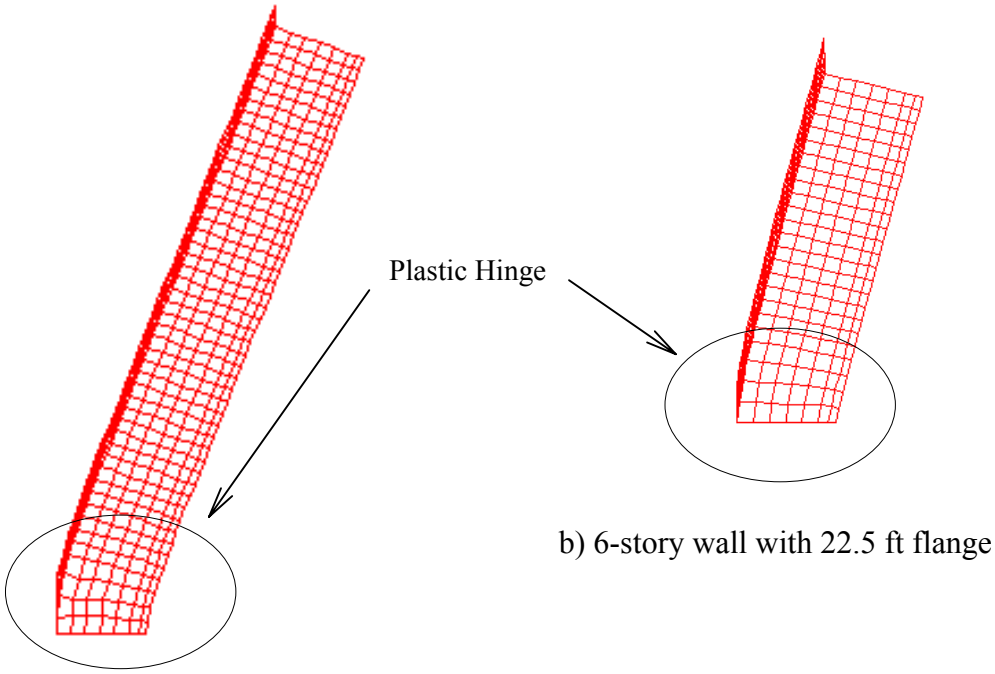

a) 12-story wall with 22.5 ft flange

b) 6-story wall with 22.5 ft flange

Figure 5.2 Deformed FE meshes. Walls pushed to 2% drift.

5.4 Verification of the model using Flanged Walls in Wallace (1996)

Wallace (1996) conducted tests of T-shaped RC walls subjected to axial compression and cyclic lateral loading. Using concrete compressive strength of 4 ksi and steel yield strength of 60 ksi, the monotonic and cyclic responses of wall TW2 are calculated and compared to the test results. The wall is12 ft high, 48 inches deep and has a flange of 48 wide. Wall reinforcement is

shown in Figure 5.3a where the finite element mesh used is depicted in Figure 5.3b. The measured and calculated load-deflection curves match well as presented in Figure 5.4. As shown in Figure 5.5, the measured strain distribution in the flange under tension also compares well to the computed strains for various drift levels. Since the model cannot capture local bar buckling nor web instability because of the type of elements used, it is unable to predict the initiation of these modes of failure as observed in the tests. Nevertheless, the analytical results correlate well to the test data prior to the occurrence of these local modes of failure.

5.5 Analysis Results

The effective tension flange width is calculated using the following equation:

$$b_{eff} = \frac{\sum_{i=1}^{n} \sigma_i w_i}{\sigma_{\max}} \qquad (5.1)$$

Where σ_i = tensile steel stress in element i, w_i = width of element i and $\sigma_{\max}$ = maximum tensile steel stress at web-flange interface. The stresses in Equation 1 are computed at the centroid of elements located at mid-height of the first floor close to the center of the wall plastic hinge.

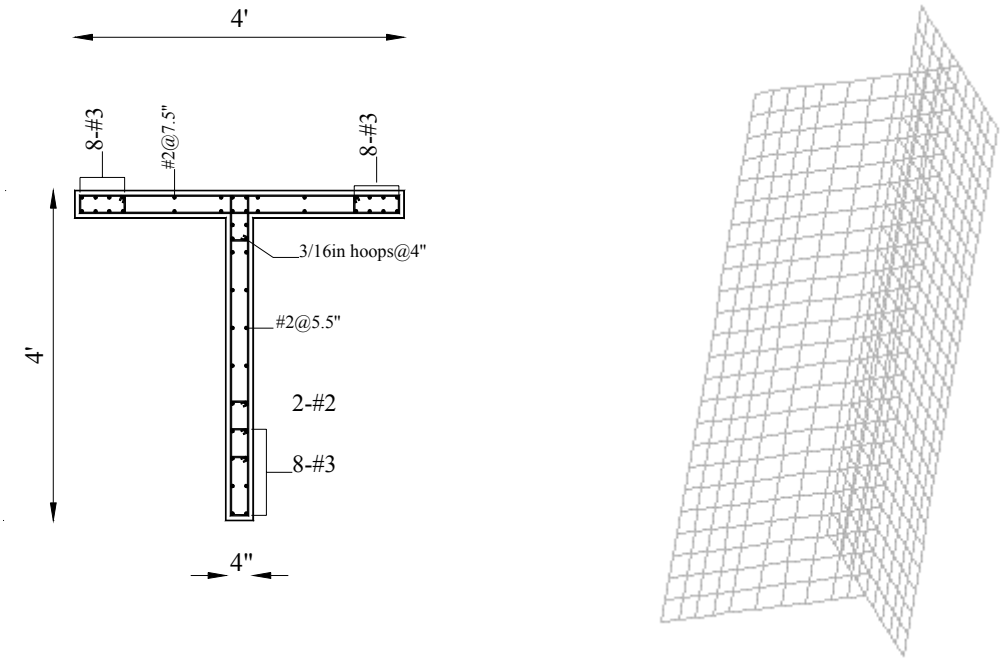

a) Cross Section b) Mesh Layout

Figure 5.3 Cross Section and Mesh Layout for Wallace (1996) wall

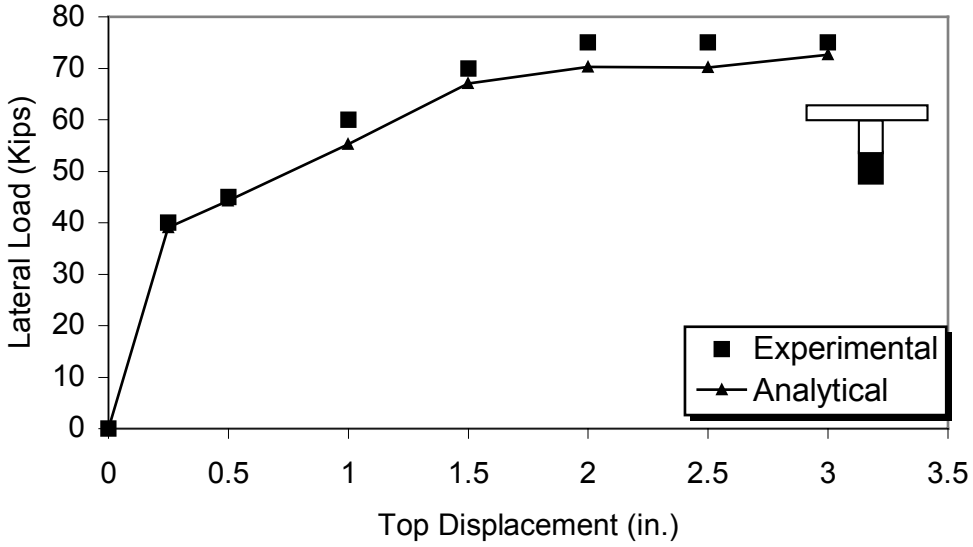

Figure 5.4 Load vs. Top Displacement

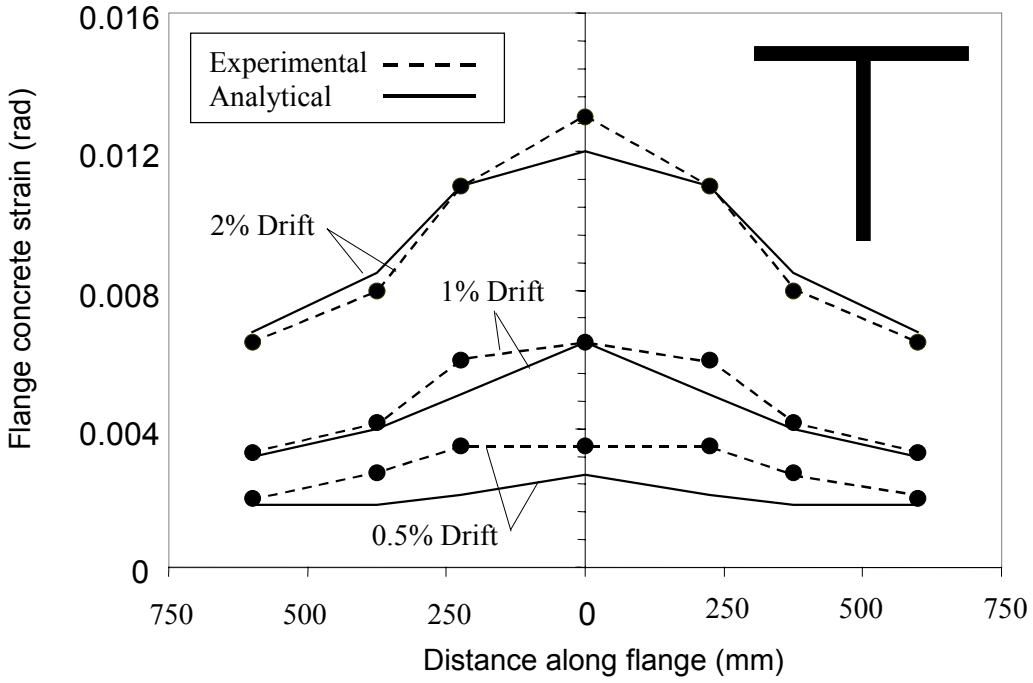

Figure 5.5 Measured and computed tension flange strain profile for specimen TW2

5.5.1 Elastic Results

A few elastic analyses are also conducted to investigate the effect of wall height on the effective width of walls under pure flexure. Figure 5.6 shows that the effective flange width for the walls with 15 ft and 30 ft flanges does not change much as the wall height is increased from 6-floors to 12-floors. For example, the effective width of the walls with the 15 ft flange increased by 11% as the wall height doubled. The corresponding increase was 25% in the walls with the 30 ft flanges. Although these elastic results are largely irrelevant to the behavior of RC walls with flanges under tension because the flanges crack early, they do provide some insight into the effect of an important parameter such as wall height.

5.5.2 Inelastic Results

Figure 5.7 shows representative plots of the steel stress distribution along the flange of a 12-story wall. The plots shown are for walls with 30 ft flange under pure flexure and $P = 0.05 f_c^{'} A_g$. It is clear from the figure that the flange becomes more 'effective' (i.e. more of the flange is mobilized) as the drift level increases. Another observation is that the flange become much less effective as the axial load increases from zero to $P = 0.05 f_c^{'} A_g$. These trends are quantified and discussed next.

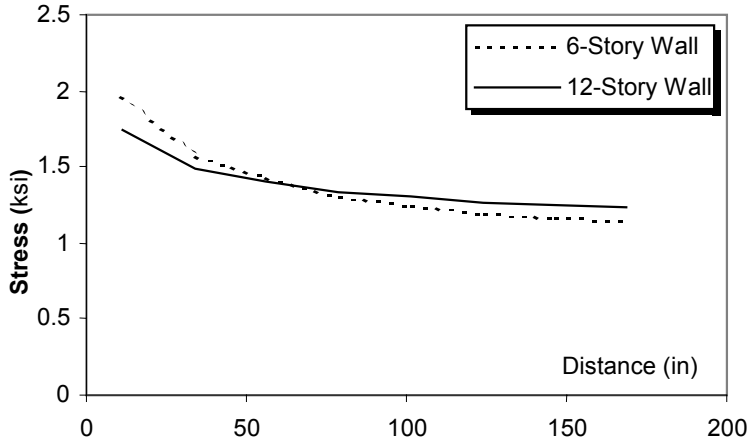

a) Flange Width=15 ft

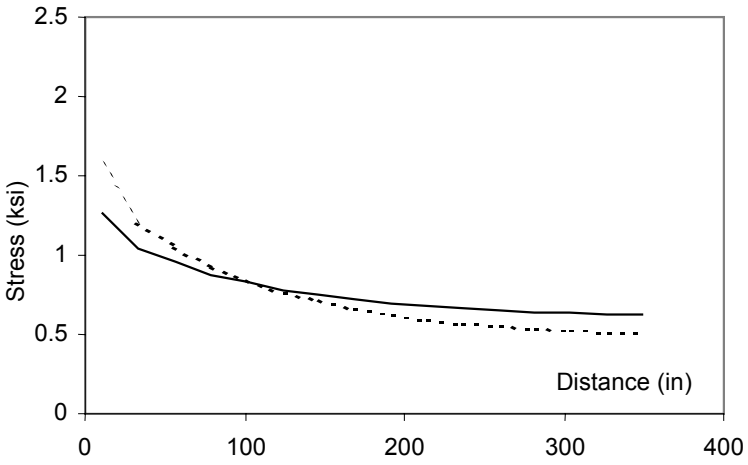

b) Flange Width 30 ft

Figure 5.6 Elastic stress distribution in tension flange

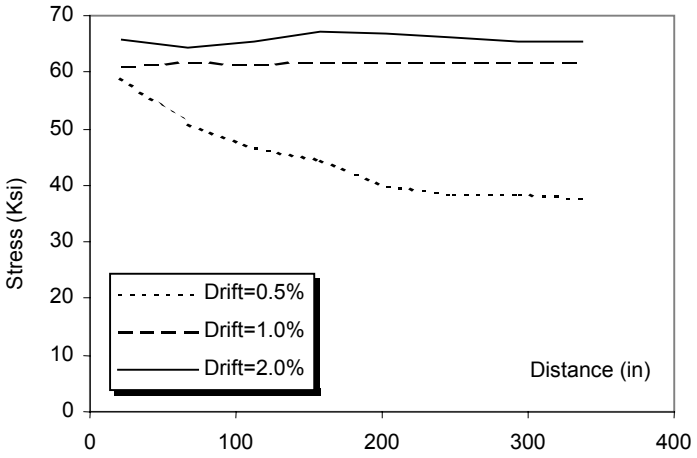

a) Wall Under Pure Bending

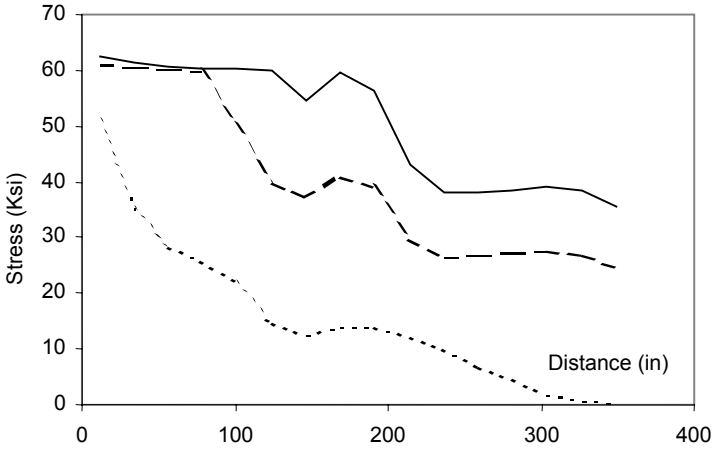

b) Wall Under Compressive Stress 0.05 f_c'

Figure 5.7 Steel tensile stresses along flange of 12-story wall with 30 ft flange.

Since the elastic analyses indicate that wall height is not an important parameter, the effective width is calculated as a function of the wall length, *d*, which is also in accord with previous research on T-beams (Pantazopoulou and Moehle 1991). Results of the 24 inelastic analyses are presented in Tables 5.2 and 5.3 and Figure 5.8. The only results that do not seem to conform to a discernable trend are those for the 6-story wall with 30 ft flange subjected to $0.08 f_c^{'} A_g$; for example, compare the bottom curves in Figures 5.8e and 5.8f. Unlike all other cases, the effective width of this particular wall is considerably lower than that in the 12-story wall for all deformations levels. The reason behind this discrepancy appears to be severe crushing in the compression zone, which relieved the tension flange of large demands thereby reducing its effectiveness. Concrete crushing did not occur in any of the other walls. The following conclusions can be drawn from Figure 5.8 and Tables 5.2 and 5.3:

Table 5.2 Effective Width for the 6-Story Wall

Flange Width	15.0 ft.			22.5 ft.			30.0 ft.		
Axial Load Level	0.5%	1.0%	2.0%	0.5%	1.0%	2.0%	0.5%	1.0%	2.0%
F_s=0.4 F_y	F.E[1]	F.E	F.E	F.E	F.E	F.E	F.E	F.E	F.E
Pure Flexure	F.E	F.E	F.E	0.87*d*	F.E	F.E	0.75*d*	F.E	F.E
$P = 0.05 f_c^{'} A_g$	0.49*d*	F.E	F.E	0.47*d*	0.87*d*	1.02*d*	0.40*d*	0.82*d*	1.03*d*
$P = 0.08 f_c^{'} A_g$	0.38*d*	0.68*d*	F.E	0.34*d*	0.73*d*	0.82*d*	0.28*d*	0.47*d*	0.50*d*

[1] FE indicates Fully Effective

Table 5.3 Effective Width for the 12-Story Wall

Flange Width	15.0 ft.			22.5 ft.			30.0 ft.		
Axial Load Level	0.5%	1.0%	2.0%	0.5%	1.0%	2.0%	0.5%	1.0%	2.0%
Fs=0.4 Fy	F.E	F.E	F.E	F.E	F.E	F.E	F.E	F.E	F.E
Pure Flexure	F.E	F.E	F.E	0.86d	F.E	F.E	0.79d	F.E	F.E
$P = 0.05 f_c^{'} A_g$	0.59d	F.E	F.E	0.55d	0.86d	1.02d	0.44d	0.94d	1.15d
$P = 0.08 f_c^{'} A_g$	0.44d	0.66d	F.E	0.47d	0.82d	0.95d	0.42d	0.81d	1.09d

Wall Height: Similar to what was observed in the elastic analyses, doubling the wall height does not have a significant impact on the effective flange width.

Axial Load: Axial load strongly influences the effective width. The flanges of all walls under tension, and most of the walls under pure flexure were fully effective. As the level of axial load increases from zero (pure flexure) to $P = 0.05 f_c^{'} A_g$, the flanges become much less effective. However, increasing the load to $P = 0.08 f_c^{'} A_g$ does not further change the effective width significantly.

Drift: The effective width is a strong function of drift, increasing rapidly as the drift increases from 0.5% to 1%, then slowing down somewhat as the drift continues to increase from 1% to 2%.

5.6 Design Implications and Recommendations

It is clear from Figure 5.8 that the ACI-318 specifications do not accurately predict the tension flange effective width, especially in the presence of compressive axial load. In the 6-story walls, current provisions can underestimate the effective width especially for higher drift levels; see for example, Figures 5.8c and 5.8e. On the other hand, the specifications overestimate

the effective width in many of the 12-story walls with axial compression (Figure 5.8b, 5.8d, and 5.8f). For example, in the 12-story wall with 30 ft flange, the ACI specifications suggest that the flange is fully effective, whereas the analysis shows that only a portion of it is active (1.15*d* or 81% of the flange for $P = 0.05 f_c^{'} A_g$ and 1.09*d* or 76% of the flange for $P = 0.08 f_c^{'} A_g$ at 2% drift).

Another issue with the ACI provisions is that the effective width is tied to wall height and not wall length. The results presented here and by others based on their work on T-beams (Pantazopoulou and Moehle 1991) suggest that wall length is a more influential variable. A calibration based on wall height is certainly reasonable and acceptable if wall length is proportional to wall height. However, in many cases, wall dimensions are constrained by architectural requirements and so a preset relation between wall height and wall length cannot always be assumed. One such example is the coupled wall systems considered in this work, where the efficiency of the system allows engineers to design individual walls with aspect ratios that are significantly different than in equivalent isolated walls.

Perhaps the greatest drawback of the current fixed effective width provisions is that they are not suitable for performance-based evaluation of wall behavior. The results presented herein and by others (Pantazopoulou and French 2002) clearly show that the effective width depends strongly on drift level. For example, in 12-story walls with 30 ft flanges under compression load, the effective width increases by more than 150% as the drift level increases from 0.5% to 2% (Figure 5.8f). Thus, accurate evaluation of structural behavior at a specific performance level is difficult to achieve unless a deformation-based effective width is adopted.

With this point in mind, the following criteria are proposed based on the limited study presented herein. Extensive analytical and experimental studies are still needed to confirm and refine these recommendations.

Walls Subjected to Tension: Such walls can occur in strongly coupled systems where the force *T* resulting from coupling is greater than the gravity force in the wall. It is recommended that the flange be taken as fully effective regardless of the wall and flange dimensions.

Walls Subjected to Pure Flexure: Such a situation can occur in a moderately coupled system where the coupling force *T* is equal to the gravity force in the wall. The results presented in Tables 5.2 and 5.3 suggest that the flange is fully effective in most of the pure flexure cases considered. Since the largest flange width considered in Table 5.3 is 30 ft, two more analyses were conducted with flange widths of 40 ft and 50 ft subjected to pure flexure. The results from these analyses are in substantial agreement with recommendations in Pantazopoulou and Moehle (1991). Based on the analyses it is recommended that: for 0.5% drift use an overhanging effective width of 0.9*d*; for 1% drift use 1.5 *d*; and for 2% drift use 2.0 *d.*

Walls Subject to Gravity Compression: For compression levels similar to those considered here (representative of gravity loading), the recommended effective width is: for 0.5% drift use an overhanging effective width of 0.6.*d*; for 1% drift use 0.95.*d*; and for 2% drift use 1.15.*d*. These values are obtained by choosing the largest numbers in the relevant columns in Tables 5.2 and 5.3 and then rounding-off.

5.7 Impact of Analysis Results on HCW Modeling

The conclusions drawn from the study presented herein are directly applied to the structural wall modeling in chapter 6. The flanges of the walls are lumped into 2-node truss

element having cross sectional area equal to the steel reinforcement within the flange effective width. Since coupling ratio is limited to 30%, the Tension force resulting from coupling is still less than the gravity loads on either of the shear walls LSW and RSW. Therefore, the flanges are constantly under compressive force. Based on the conclusions stated above and on 2% expected drift, the effective width of the left and right walls is taken as 1.15 *d* where d is the wall depth resulting in fully effective flange width. By applying this conclusion, an 85% reduction in the finite element model size is achieved.

5.8 Summary

The effect of a number of influential parameters on the tension flange effective width in flanged RC shear walls is investigated using detailed finite element analyses. The numerical model accounts for nonlinearities in steel and concrete behavior and was verified through comparison to test data. Analysis results showed that although the tension flange effective width does not vary significantly as a function of wall height, it is strongly dependent on the drift level, axial force level, and wall length.

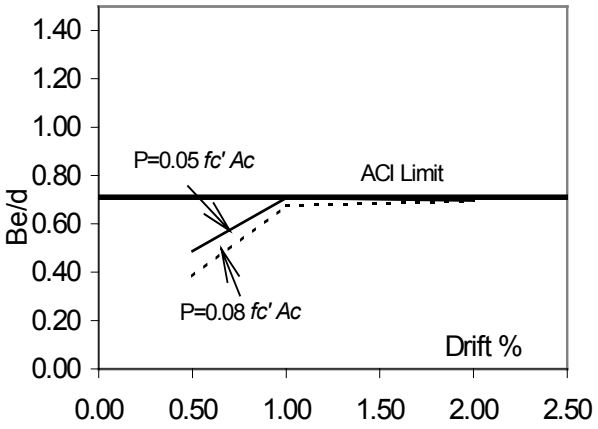

a) 6-floor wall with 15 ft flange

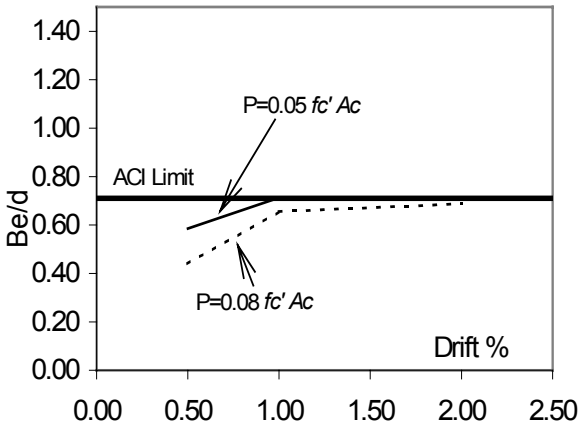

b) 12-floor wall with 15 ft flange

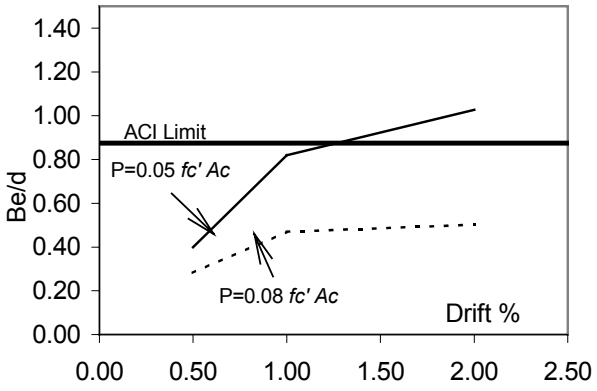

c) 6-floor wall with 22.5 ft flange

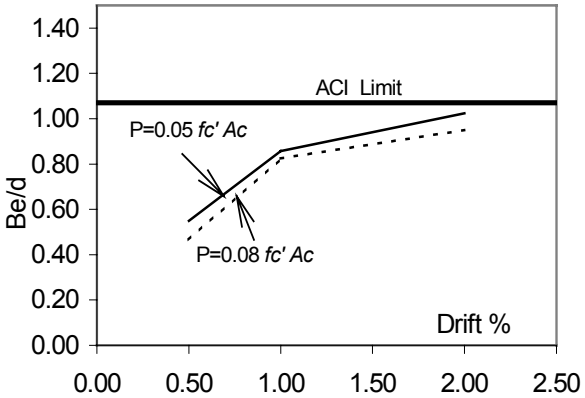

d) 12-floor wall with 22.5 ft flange

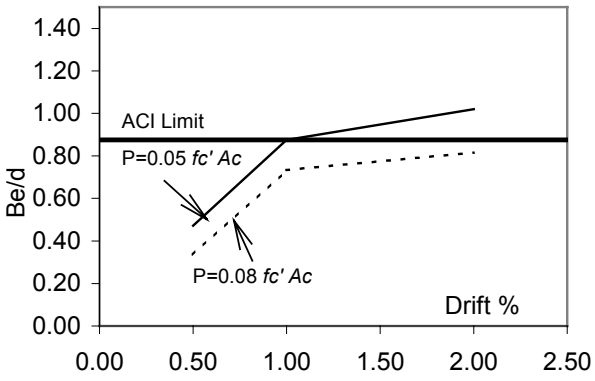

e) 6-floor wall with 30 ft flange

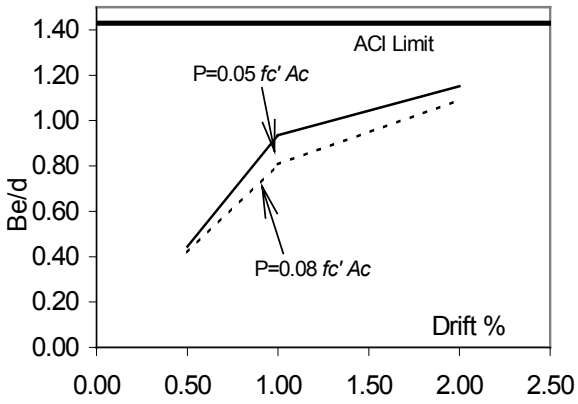

f) 12-floor wall with 30 ft flange

Figure 5.8 Effective Width vs. Drift Ratio and Level of Axial Load

CHAPTER 6: ANALYSIS RESULTS

Dynamic nonlinear time history analysis is regarded as the most accurate and comprehensive type of analysis. Compared to pushover analysis, time history analysis simulates the true effect of cyclic loading associated with the ground motions. Structural dynamic characteristics such as damping, frequency content of ground motions and its ability to trigger different higher modes as well as possible strength/stiffness degradation due to of cyclic loading are considered. However, the computational cost of performing such analysis is significantly higher than other types of analyses. In this chapter, the results of time history analysis of the prototypes designed in chapter 3 are presented. Also presented are the characteristics of the ground motion acceleration records that were used in analysis, the basics of time history analysis, description of the finite element model used in analysis as well as the analysis results. Structural performance is evaluated against the requirement and acceptance criteria of FEMA-356.

6.1 Parametric Study

Sixty transient analyses are conducted to better understand the seismic behavior of HCW systems. Three systems are analyzed, HCW-12-U, HCW-12-30 and HCW-18-30. A suite of 10 earthquakes (discussed later in this chapter) is used for each building and for two hazard levels as discussed in section 6.3. The structural behavior of the three systems is then examined at the two specified levels of seismic risk by evaluating a number of performance parameters. The performance parameters considered include story drift ratios, wall rotations, wall shear

distortions, coupling beam chord rotations (as defined in FEMA-356), as well as various other stress and strain measures at critical points. Wall rotations are calculated by assuming that plane sections remain plane at different floor heights, while shear distortions are computed from the diagonal deformations of each wall panel. The calculated demands are then compared to values obtained from pushover analyses and to acceptance criteria (when available) in FEMA-356.

6.2 Performance Level

FEMA-356 defines three discrete performance levels namely: immediate occupancy, life safety and collapse prevention that can be used in performance based design. *Immediate occupancy* means very limited structural damage has occurred due to an earthquake and both gravity load and lateral force resisting systems remain almost intact maintaining most of their stiffness and strength. Minor repair work may be required but normal occupancy is possible immediately after the earthquake. *Life safety* means significant damage to the structure has occurred but the system is not brought to the collapse limit. Some structural elements may experience severe damage but the risk of falling debris that is considered as a life threat is relatively low. *Collapse prevention* performance level means the building is on the verge of experiencing partial or total collapse. Substantial damage to the structure has occurred, including the potential for significant degradation in strength and stiffness of the lateral system and large inelastic deformations are possible. However, all significant components of the gravity load resisting system will preserve sufficient strength against the gravity demands.

6.3 Level of Seismic Hazard

Conventionally, the probability of exceedance in 50 years and the return period are used to categorize earthquake ground shaking. Ground shaking hazard is typically characterized by a hazard curve, which indicates the probability that a given value of a ground motion parameter, for example peak ground acceleration, will be exceeded over a certain period of time. The most commonly used levels of seismic hazard include:

- 2% in 50 years (referred to hereafter as 2/50), also known as the *maximum considered earthquake* (MCE): this is the most severe level of ground shaking. The return period for this event is 2475 years. This earthquake is used for design of new building by most design codes in the United States.
- 10% in 50 years (referred to hereafter as 10/50). These are moderate earthquakes with a return period of 475 years.
- 50% in 50 years (referred to hereafter as 50/50). These represent the most frequent earthquakes with a return period of 72 years.

The United States Geological Survey (USGS) has developed a suite of ground shaking hazard maps for both 2/50 and 10/50 ground shaking for a damping ratio of 5% for use in seismic design. The spectral acceleration at short period and at 1-second period is obtained from the maps and used to construct a response spectrum for the desired hazard level. This procedure was illustrated in Chapter 3. In order to obtain a response spectrum for a 50/50 ground motion, FEMA-356 provides an exponential function by which the spectral acceleration for any hazard level can be interpolated

$$S_i = S_{i(10/50)} \left(\frac{P_R}{475}\right)^n \tag{6.1}$$

$$P_{R(50/50)} = \frac{1}{1 - e^{0.02\ln(1-P_{50/50})}}) \quad (6.2)$$

Where:

S_i: spectral acceleration (i = s for short period, i = 1 for 1-secod period) for 50/50 ground motion.

$S_{i(10/50)}$: Spectral Acceleration for the 10/50 motion obtained from USGS maps.

$P_{R(50/50)}$: mean return period for 50/50 earthquake and is calculated from Equation 6.2 for a value of $P_{50/50} = 0.5$ (50%), Thus $P_{R(50/50)} = 72.6$ *years*

n: defined in Table 2-11 of FEMA-356 and depends on the location of the building, for Los Angeles, n= 0.44 and hence, $S_{i(50/50)} = 0.43\ S_{i(10/50)}$

6.4 Performance Objective

The performance objective defines the desired performance level of a building when subjected to an earthquake ground motion of specific hazard level. For example, according to the '*Basic Safety Objective'* in FEMA-356, which essentially defines the basic seismic design philosophy in the guidelines, a building structural system must be able to deliver Collapse Prevention performance for a 2/50 event and Life Safety for a 10/50 event. In other words, buildings designed for the Basic Safety Objective are expected to experience little damage from relatively frequent, moderate earthquake (10/50), but should not collapse in spite of significant damage from severe, infrequent earthquakes (2/50).

One of the problems with the Life Safety performance level is that it is not well defined, both in terms of actual structural behavior and in post-earthquake outcome. As a result, FEMA-350 (2000), which addresses performance-based design of steel frames, drops Life Safety as a performance objective. Instead, only two performance levels are defined, Immediate Occupancy

and Collapse Prevention. Both of these performance levels have readily identifiable consequences associated with the post-earthquake disposition of the building, and are easily quantifiable in technical terms. The Immediate Occupancy performance level is defined in conjunction with a frequent, but mild earthquake, i.e. 50/50 earthquake, while the Collapse Prevention level is defined with a severe, but infrequent event, i.e. a 2/50 earthquake. These two performance levels are adopted in this work.

6.5 Ground Motions Used

Response of nonlinear structural systems to an earthquake ground motion is strongly affected by the frequency content, magnitude, strong motion duration and pulse sequencing that characterize the motion. Therefore, several ground motions representing a range of amplitudes and frequencies should be used to predict the upper and lower bounds of nonlinear behavior of a system. The use of a large number of motions becomes crucial when the structure is anticipated to experience large inelastic deformations. For this purpose, historical earthquake ground motion records may be used

Recently, the SAC (Acronym for *Structural Engineers Association of California* 'SEAOC', *Applied Technology Council* 'ATC' and *California University for Research in Earthquake Engineering* 'CUREe') steel project has developed a large set of response spectra and associated time history ground motions for use in seismic investigations. Three locations across the United States were chosen, Los Angeles, Seattle and Boston representing seismic zones 4,3 and 2 respectively (SAC Draft Report 1997). Time history motion records were developed to simulate different levels of seismic hazards and suits of records for 2/50, 10/50 and 50/50 hazard levels were given for various soil conditions.

Acceleration time histories were derived from historical strong motion ground records as well as physical simulations. Records were given in pairs of two orthogonal components. These records were scaled such that the weighted summation of the square error between the response spectrum of the acceleration record and the response spectrum of NEHRP 1997 at four periods of 0.3, 1.0, 2.0 and 4.0 seconds is brought to its minimum value. The motivation behind this scaling technique is to ensure that the resulting acceleration records have similar trends as the smooth response spectrum of NEHRP 1997 without altering other characteristics of the original acceleration record such as frequency content and phasing (SAC Report, 1997).

As required by FEMA-356 (2000), for a given performance level, the maximum response of three ground motion records or the median response of seven records should be used in a performance evaluation. The use of the maximum response of three records appears to serve as a penalty for not using a larger set of ground motion records. In this work, a set of ten-ground motion records are used in order to better characterize the scatter that can occur due to the variability of ground motions. Ten 2/50 records and 10 50/50 records are selected from SAC ground motion records for the city of Los Angeles where the prototype buildings are located. The records are selected from the motions denoted 'LA21 through LA59*'*. Since the main objective of the current work is to study the behavior of coupled walls, analyses were performed only in the coupled wall direction and records with odd-only numbers (21, 23 etc) are used. Details of the original SAC records, moment magnitude, epicentral distance and the peak ground acceleration (PGA) of each record are presented in tables 6.1 and 6.2.

Table 6.1 Original SAC Record for 2/50 Ground Motions

Rec.	SAC	Record	Mag.[1]	Distance[2]	PGA	Strong Motion		
						Duration	From	**To**
1	LA21	1995 Kobe	6.9	3.4	1.28	25	4	29
2	LA23	1989 Loma	7	3.5	0.42	12.5	2.65	15.15
3	LA25	1994 Northridge	6.7	7.5	0.87	12.5	.005	12.50
4	LA27	1994 Northridge	6.7	6.4	0.93	25	0.02	25.02
5	LA29	1974 Tabas	7.4	1.2	0.80	25	3.28	28.28
6	LA31	Elysian Park	7.1	17.5	1.30	12.5	5.46	17.96
7	LA33	Elysian Park	7.1	10.7	0.78	12.5	6.4	18.9
8	LA35	Elysian Park	7.1	11.2	0.99	12.5	4.38	16.88
9	LA37	Palos Verdes	7.1	1.5	0.71	25	0.02	25.02
10	LA39	Palos Verdes	7.1	1.5	0.48	25	4.14	29.14

Table 6.2 Original SAC Record for 50/50 Ground Motions

Rec.	SAC	Record	Mag.[1]	Distance[2]	PGA[3]	Strong Motion		
						Duration	From	To
1	LA41	Coyote Lake,	5.7	8.8	0.59	12.5	0.01	12.51
2	LA43	Imperial	6.5	1.2	0.14	12.5	1.92	14.42
3	LA45	Kern, 1952	7.7	107	0.14	50	0.02	50.02
4	LA47	Landers, 1992	7.3	64	0.34	50	0.02	50.02
5	LA49	Morgan Hill,	6.2	15	0.32	25	0.02	25.02
6	LA51	Parkfield, 1966,	6.1	3.7	0.78	25	0.02	25.02
7	LA53	Parkfield, 1966,	6.1	8	0.69	25	0.02	25.02
8	LA55	North Palm	6	9.6	0.52	25	0.02	25.02
9	LA57	San Fernando,	6.5	1	0.25	25	0.02	25.02
10	LA59	Whittier, 1987	6	17	0.77	25	0.02	25.02

[1]Moment magnitude, [2]Epicentral distance, [3]Peak ground acceleration

6.5.1 Strong Motion Duration

Records are provided in terms of ground acceleration at time intervals as small as 0.02 second or less. To reduce the computational effort, analysis is focused on a specific part of the ground motion duration where most of the earthquake energy is delivered to the building, i.e. the strong motion duration. The duration is calculated such that at least 90 percent of the seismic energy is delivered. The technique used is based on a method proposed by Trifunac and Brady (1975) and is expressed by the following equations:

$$E(T) = \int_0^T a^2(t)\,dt \tag{6.3}$$

$$E_m = E_{(T100\%)} = \int_0^{T_{100\%}} a^2(t)\,dt \tag{6.4}$$

$$D_{sm} = T_{(0.95E_m)} - T_{(0.05E_m)} \tag{6.5}$$

Where:

E_m is the total energy delivered by the earthquake ground motion

a is the acceleration at time t

D_{sm} is the duration of the strong motion considered in analysis.

$T_{(0.95Em)}$ and $T_{(0.05Em)}$ are the time instance at which 95 and 5 percent of the total energy is delivered respectively.

In this work, a fixed number of time steps is used for all analyses to reduce the effort required to extract the data from the output files. This results in a usage of durations of 12.5, 25 and 50 seconds depending on the time interval of each record. The starting and ending point of the strong motion duration used in the analysis is presented in the last two columns of table 6.1 and 6.2. Figure 6.1 shows a schematic for the strong motion duration of an earthquake record.

The time-period encompassed by the dashed lines in the figure represents the strong motion duration.

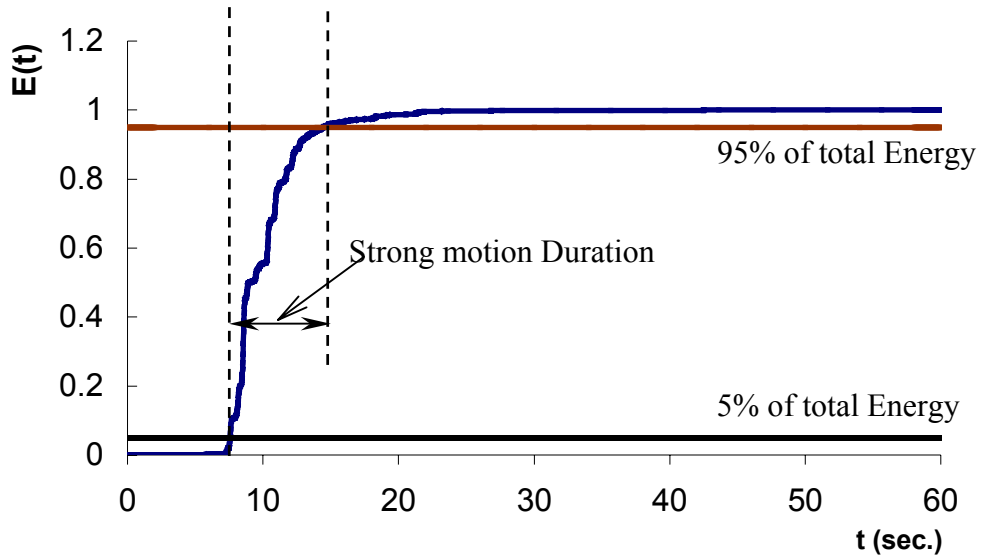

Figure 6.1 Strong Motion Duration

6.5.2 Scaling of Records

Properly chosen scaling of earthquake records can reduce the required number of nonlinear analysis without introducing bias (Shome et al, 1997). According to Shome et al (1997), the nonlinear response measured from a suite of records; which are chosen from a narrow magnitude and distance interval (or 'bin') display wide dispersion. However, when the records are scaled to the bin-median spectral acceleration at the fundamental frequency of the structure, the same median response measures can be obtained with reduced variability compared to those of the unscaled ones. They concluded that scaling of ground motion records to the 5% damped spectral acceleration at the fundamental frequency of the structure is the best among the alternative scaling methods they investigated. The "median" mentioned in the study refers to the

geometric mean, which was defined as the exponential of the average of the natural logarithms of data, while the "variability" refers to the dispersion, which was defined as the standard deviation of the natural logarithms of data.

For the analysis of the 12-story system, analyses were performed twice; once with the unscaled records obtained directly from SAC and a second time with records scaled as proposed by Shome et al (1997). To prepare the second set of records, the median spectral acceleration at the '*fundamental period'* (T_1) of the structure is computed for every response spectrum in each suite of records. Each record is then scaled so that its spectral acceleration at the fundamental period of the structure matches this median value. Figure 6.2 shows the scaled response spectra of all records versus the FEMA-368 design response spectrum for both 2/50 and 50/50 hazard levels.

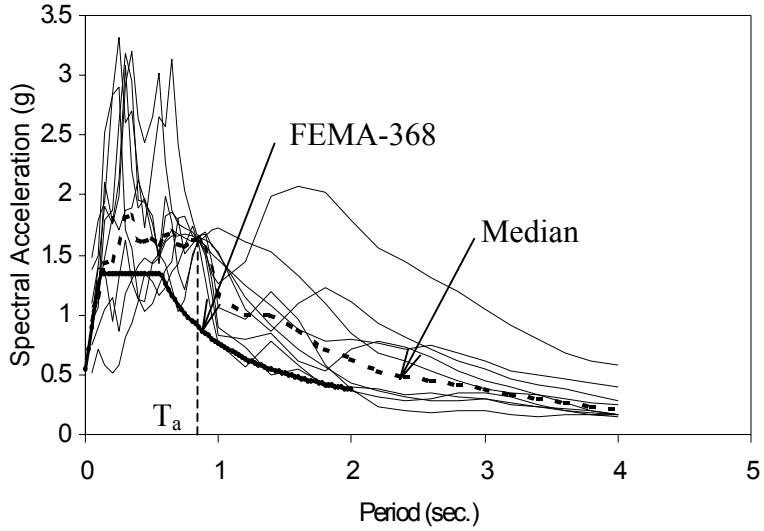

a) 2/50 Earthquakes

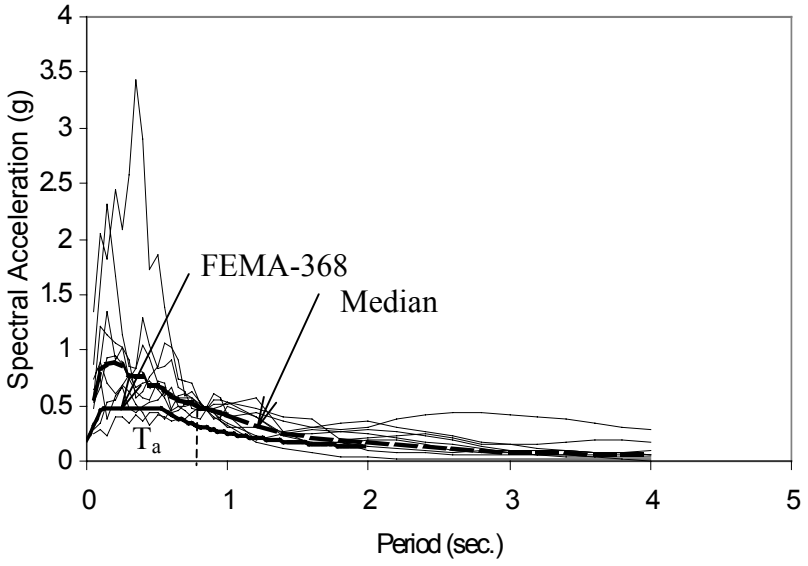

b) 50/50 Earthquakes

Figure 6.2 Elastic Response Spectra (5% damped) Scaled to median spectral Acceleration at The fundamental Period of the 12-Story System

For the 18-story system, the same technique is used except that the records are scaled at both the fundamental period (T_1) and the fundamental period of the system after all the coupling

beams yield (T_u). The reason behind this approach is it was noted that all the coupling beams reach the yield limit early and the system behaves essentially as an uncoupled system. T_u is computed using the following expression:

$$T_u = T_i \sqrt{\frac{K_i}{K_u}} \tag{6.6}$$

Where T_i is the fundamental period of the elastic system, K_i and K_u are the stiffness of the system before and after the coupling beam yield respectively. Tables 6.3 through 6.6 present the scaling factors of all records scaled at T_1 for both 12-story and 18-story systems. Table 6.7 presents the scaling factor for the 2/50 records scaled at T_u for the 18-story system only.

Table 6.3 Original and Scaled PGA's in g for the 2 /50 Records For 12-Story Systems

Record name	Original PGA	S_a[1]	Scaling Factor	PGA[2]
LA21	1.28	2.86	0.54	0.70
LA23	0.42	1.53	1.02	0.43
LA25	0.87	1.84	0.85	0.74
LA27	0.93	1.37	1.13	1.05
LA29	0.80	1.63	0.96	0.76
LA31	1.30	1.66	0.94	1.22
LA33	0.78	1.40	1.11	0.87
LA35	0.99	1.62	0.96	0.95
LA37	0.71	1.61	0.97	0.69
LA39	0.48	0.87	1.80	0.86
MEDIAN[3]		1.58		

Table 6.4 Original and Scaled PGA's in g for the 50 /50 Records For 12-Story Systems

Record name	Original PGA	S_a[1]	Scaling Factor	PGA[2]
LA41	0.59	0.99	0.52	0.31
LA43	0.14	0.28	1.84	0.26
LA45	0.14	0.30	1.70	0.24
LA47	0.34	0.36	1.45	0.49
LA49	0.32	0.51	1.01	0.32
LA51	0.78	0.43	1.20	0.94
LA53	0.69	0.47	1.11	0.76
LA55	0.52	0.67	0.77	0.40
LA57	0.25	0.27	1.89	0.47
LA59	0.77	2.36	0.22	0.17
MEDIAN[3]		0.52		

[1]Spectral Acceleration at T_1=0.84 sec., [2] Scaled PGA, [3] Geometric Mean

Table 6.5 Original and Scaled PGA's in g for the 2% /50 Records For 18-Story System

Record name	Original PGA	S_a[1]	Scaling Factor	PGA[2]
LA21	1.28	2.53	0.47	0.60
LA23	0.42	0.72	1.67	0.70
LA25	0.87	1.67	0.71	0.62
LA27	0.93	0.93	1.28	1.19
LA29	0.80	0.83	1.45	1.16
LA31	1.30	1.46	0.82	1.07
LA33	0.78	1.40	0.86	0.67
LA35	0.99	1.02	1.18	1.17
LA37	0.71	1.40	0.85	0.60
LA39	0.48	0.88	1.35	0.65
MEDIAN[3]		1.2		

Table 6.6 Original and Scaled PGA's in g for the 50% /50 Records For 18-Story System

Record name	Original PGA	S_a[1]	Scaling Factor	PGA[2]
LA41	0.59	0.75	0.55	0.32
LA43	0.14	0.20	2.04	0.29
LA45	0.14	0.30	1.35	0.19
LA47	0.34	0.33	1.24	0.42
LA49	0.32	0.44	0.93	0.30
LA51	0.78	0.33	1.24	0.97
LA53	0.69	0.45	0.9	0.62
LA55	0.52	0.50	0.82	0.43
LA57	0.25	0.20	1.98	0.50
LA59	0.77	1.35	0.30	0.23
MEDIAN[3]		0.41		

[1]Spectral Acceleration at T_1=1.0 sec., [2] Scaled PGA, [3] Geometric Mean

Table 6.7 Original and Scaled PGA's in g for the 2% /50 Records For 18-Story System (Scaled at a fundamental period of the inelastic system)

Record name	Original PGA	S_a[1]	Scaling Factor	PGA[2]
LA21	1.28	0.34	1.14	0.60
LA23	0.42	0.27	1.4	0.70
LA25	0.87	0.33	1.15	0.62
LA27	0.93	0.51	0.74	1.19
LA29	0.80	0.32	1.18	1.16
LA31	1.30	0.26	1.44	1.07
LA33	0.78	0.49	0.77	0.67
LA35	0.99	0.85	0.45	1.17
LA37	0.71	0.58	0.65	0.60
LA39	0.48	0.2	1.93	0.65
MEDIAN[3]		0.38		

[1]Spectral Acceleration at T_e=1.7 sec., [2] Scaled PGA, [3] Geometric Mean

6.6 Finite Element Modeling

El-Tawil et al (2002a) developed detailed finite element models for the 6 and 12-story prototype structures discussed in chapter 3 (Figure 6.3.a). The models are described in El-Tawil et al (2002a) and account for the effect of material inelasticity, concrete cracking, tension stiffening, crushing, steel yielding, contact between concrete and coupling beams. A fine plane stress finite element mesh was used to represent the concrete wall and the coupling beams as well. The transition zone between the fine mesh at the beam and the relatively coarser one at the wall was achieved by using triangular element. Contact between the coupling beams and surrounding concrete was represented by a special contact element that simulates the opening and closure of the gap. This element has almost no stiffness or strength in tension but provides very large stiffness when bearing against concrete (Figure 6.4). The models were thoroughly validated through comparisons with test data and were shown to be accurate for a wide range of conditions. However, in this work, it is not possible to use these detailed models for the planned transient finite element analyses because of their large size. Instead, simplified models that are

more computationally tractable are developed and calibrated to the detailed models for use in the parametric study.

To reduce the size of the simplified models used in this work a number of measures were taken including:

- Each coupling beam is represented by a shear flexible beam element instead of an assembly of continuum elements as explained in Chapter 4. The beam is embedded in the concrete wall for a short distance so that a full fixity can develop at the beam end points.
- Gaps are not allowed to open or close; i.e. the contact element of the refined model is eliminated and replaced with a fully rigid connection
- Wall flanges are modeled using plane stress elements in the plane of the wall with a thickness equal to the wall effective width as concluded from the analyses performed in chapter 5.

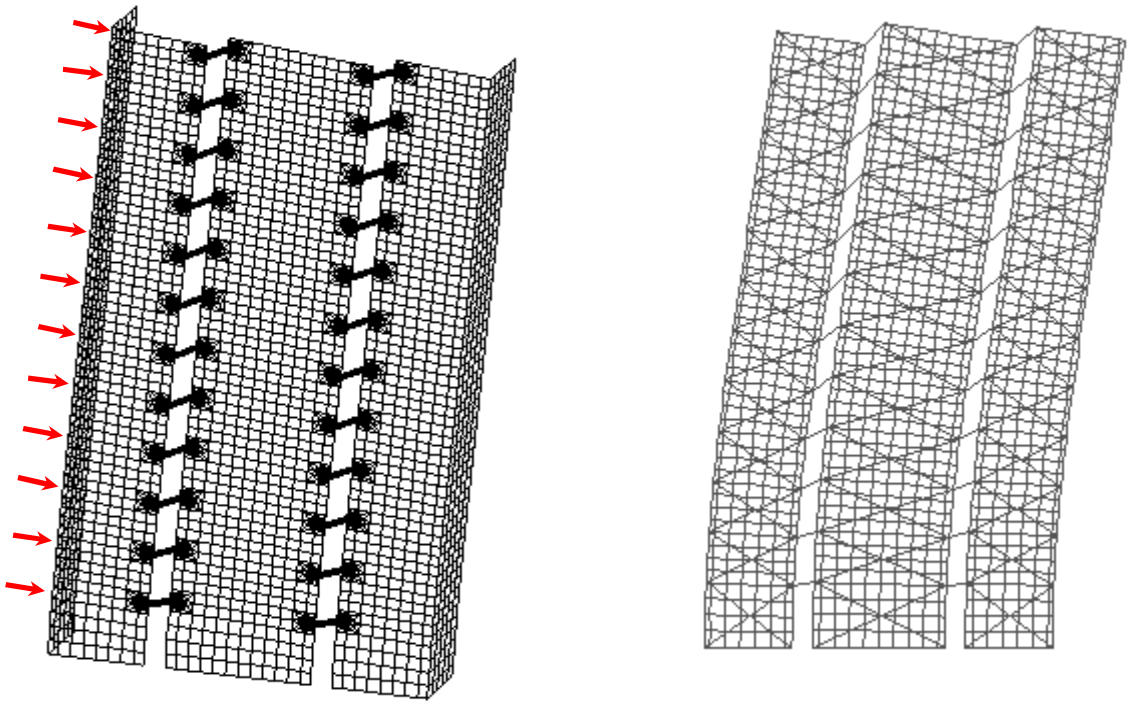

a) El-Tawil et al (2002a,b) Model (3-D) b) Current Model (2-D)

Figure 6.3 Refined and coarse finite element meshes (deformed)

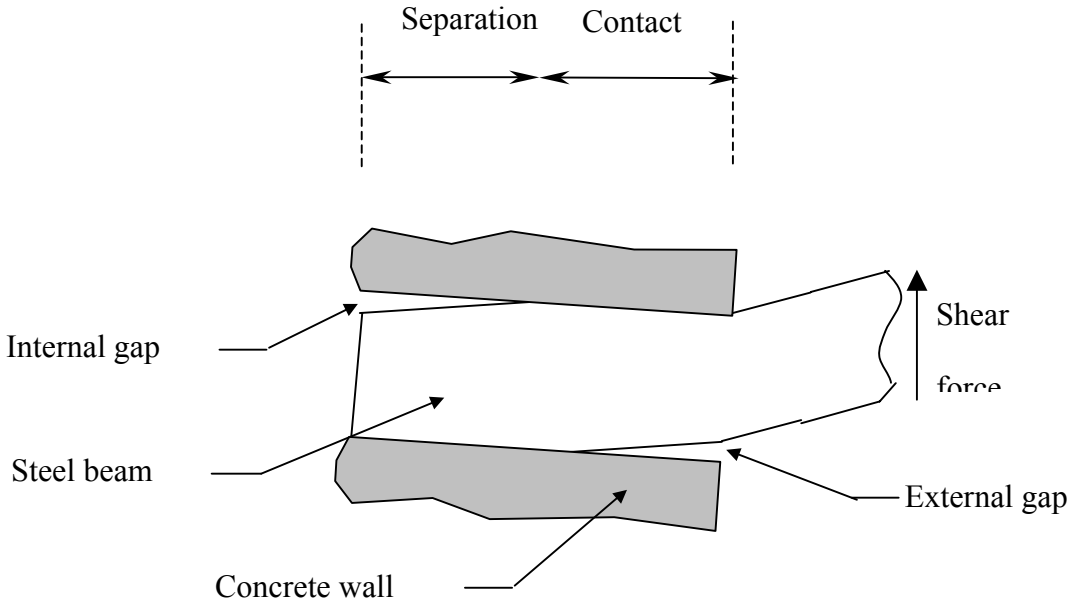

Figure 6.4 Contact Element in the Connection

Gap elements between the beams and the walls are not modeled because the refined model showed that the overall effect of gap opening/closing on behavior is small. In addition to that, the steel beam response is dominated by shear rather than flexure and hence most of the beam rotation comes from the difference in vertical displacement between its ends and not from possible connection rotation. Web reinforcement is modeled as smeared, while the main flexural reinforcement is modeled using bar elements. These modifications reduced the simplified model size dramatically (shown in Figure 6.3.b) to about 15% of the refined model size. A comparison between the pushover responses of both models is shown in Figure 6.5a and 6.5b for both HCW-12-U and HCW-12-30; where base shears are plotted against the roof displacements. Good agreement is obtained.

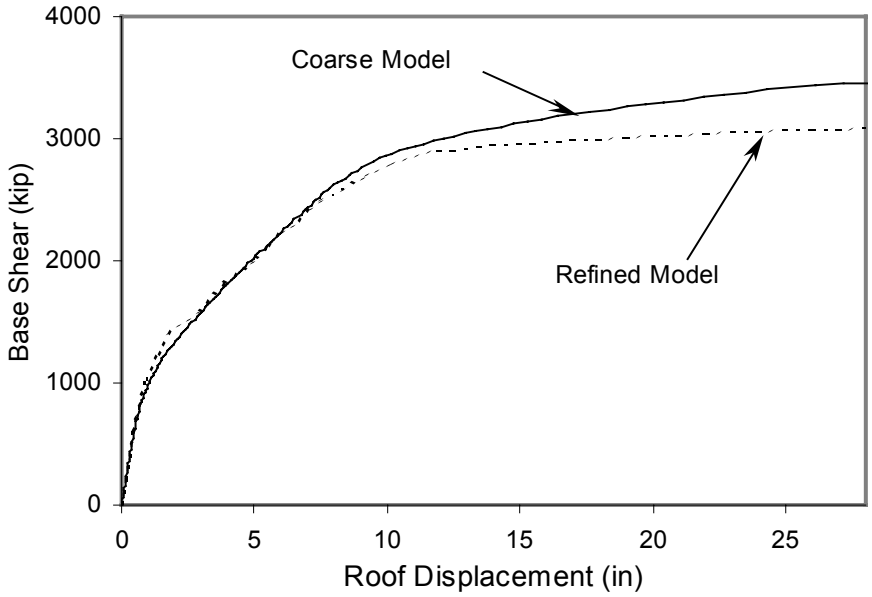

a) HCW-12-U (uncoupled)

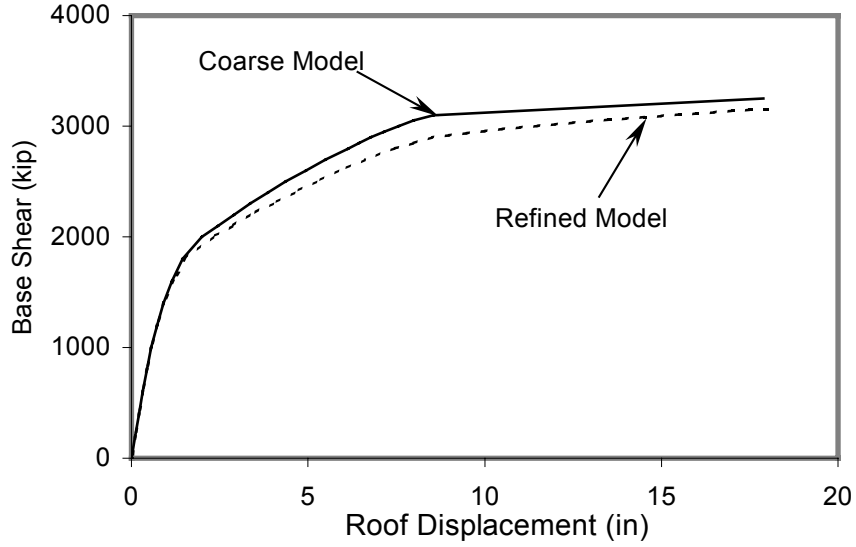

b) HCW-12-30 (with 30% coupling)

Figure 6.5 Base shear versus roof displacement for refined and coarse models

6.1.1 Gravity Loads

Prior to the beginning of earthquake loads, gravity loads, due to dead and live loads, are first applied according to the combinations required by FEMA-356 (2000) as 1.1 x sum of dead load plus live load. This load is applied in 10 increments before the seismic loads take place.

6.1.2 Floor Masses

Floor mass is represented as lumped point masses placed at the floor levels. Since the floor diaphragms are considered rigid, i.e all the nodal points at the floor level undergo the same displacement, the point mass can be placed at any node along the floor level. Masses for the floor level are taken as 2.47 kips sec^2/in. and 1.55 kips sec^2/in. for the typical floors and the roof respectively.

6.1.3 Damping

Discrete dashpots are introduced at the floor levels to model damping. The dashpots have zero structural stiffness and provide 5% of critical damping. To calculate the damping, a Raleigh mass proportional damping model is assumed. According to this method, damping is expressed by the following equation:

$$c = \alpha m + \beta k \tag{6.7}$$

Where c is the viscous damping, m is the mass at floor level and k is the stiffness of the floor. α and β are constants. Since the damping is assumed mass proportional, β is zero and α is determined from the following equation:

$$c = \alpha m = 2\xi \varpi m,\ \alpha = 2\xi \varpi \tag{6.8}$$

Where ξ is the damping ratio taken as 5%. ω is the fundamental frequency of the structure in radians. c is taken as 2.02 and 1.53 for 12 and 18-story systems respectively. Dashpot dampers and mass representation are depicted in Figure 6.6.

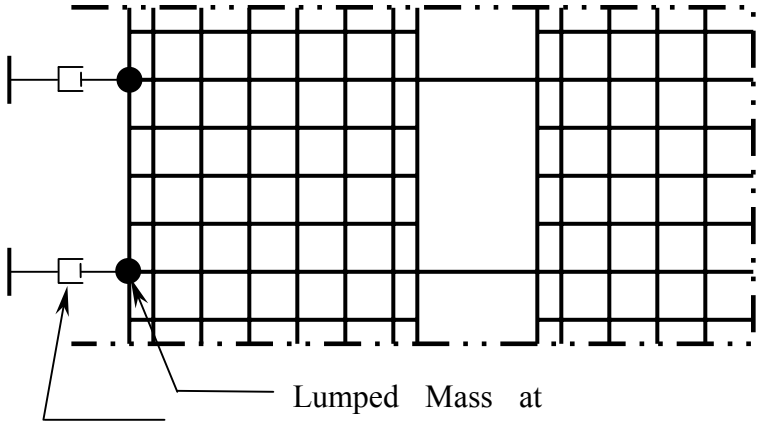

Figure 6.6 Lumped Masses and Dashpot Dampers

6.1.4 Direct Time Integration

The system of governing equations for a transient dynamic problem at time t are generally written as

$$M\ \ddot{u}(t)+C\dot{u}(t)+f_{\text{int}}(u,\dot{u},\varepsilon,\sigma,t)=f_{ext}(t) \tag{6.9}$$

Where M is the mass matrix, C the damping matrix and f_{ext} the external force vector, and $\ddot{u}$, $\dot{u}$ and u are the resulting acceleration, velocity and displacement vectors, ε and σ are the strain and stress fields. Vector f_{int} is the internal set of forces opposing the displacements. For geometrical or physical nonlinear analysis or both, f_{int} must be calculated for the actual stress distribution satisfying all nonlinear conditions.

$$f_{\text{int}}=\int B^T\,\sigma\,dA \tag{6.10}$$

Where B^T is the strain-displacement matrix as described in Chapter 4 and A is the area of the element.

For the transient response of a nonlinear analysis, the solution of the second-order differential equation (6.9) is obtained by *direct time integration* techniques. The solution for the dynamics problem is determined at a number of discrete time points: *t-Δt, t, t+Δt...etc*. Solution at time *t* is known, equation 6.9 holds:

$$M\,{}^{t}\ddot{u} + C\,{}^{t}\dot{u} + {}^{t}f_{\text{int}} = {}^{t}f_{ext} \tag{6.11}$$

Two time-integration schemes are examined, *Newmar*k method and *Wilson-θ* theta method, which is considered an extension to *Newmark* method. A comparison between both methods indicates that *Wilson-θ* method produce smoother and more stable base shear history curves than does *Newmark* method. Therefore, *Wilson-θ* method is chosen as the time integration scheme. The method is basically an extension of the *Newmark* scheme with $\gamma=1/2$ and $\beta=1/6$. The acceleration is assumed to vary linearly in time from *t* to $t=\theta\,\Delta t$ with $\theta>1.0$ (Figure 6.7). With this assumption the following equations is derived for ${}^{t+\theta\Delta t}\dot{u}$ and ${}^{t+\theta\Delta t}\ddot{u}$.

$${}^{t+\theta\Delta t}\ddot{u} = \frac{6}{\theta^2\Delta t^2}\left({}^{t+\theta\Delta t}u - {}^{t}u\right) - \frac{6}{\theta\Delta t}\,{}^{t}\dot{u} - 2\,{}^{t}\ddot{u} \tag{6.12}$$

$${}^{t+\theta\Delta t}\dot{u} = \frac{3}{\theta\Delta t}\left({}^{t+\theta\Delta t}u - {}^{t}u\right) - 2\,{}^{t}\dot{u} - \frac{\theta\Delta t}{2}\,{}^{t}\ddot{u} \tag{6.13}$$

The dynamic equilibrium equation is considered at $t+\theta\Delta t$:

$$M\,{}^{t+\theta\Delta t}\ddot{u} + C\,{}^{t+\theta\Delta t}\dot{u} + {}^{t+\theta\Delta t}f_{\text{int}} = {}^{t+\theta\Delta t}f_{ext} \tag{6.14}$$

In this equation the external load vector on the right-hand side, just like the acceleration, is assumed to vary linearly in the time interval: $t \rightarrow t+\theta\Delta t$

$$ {}^{t+\theta\Delta t}f_{ext} = {}^{t}f_{ext} + \theta({}^{t+\Delta t}f_{ext} - {}^{t}f_{ext}) \tag{6.15} $$

The *Wilson-θ* scheme is unconditional stable for $\theta \geq 1.37$.

The analyses are conducted using DIANA (2000). However, the analyses employed user-defined material models (as described in chapter 4) that provided cyclic concrete behavior that is superior to the standard models available in DIANA (2000).

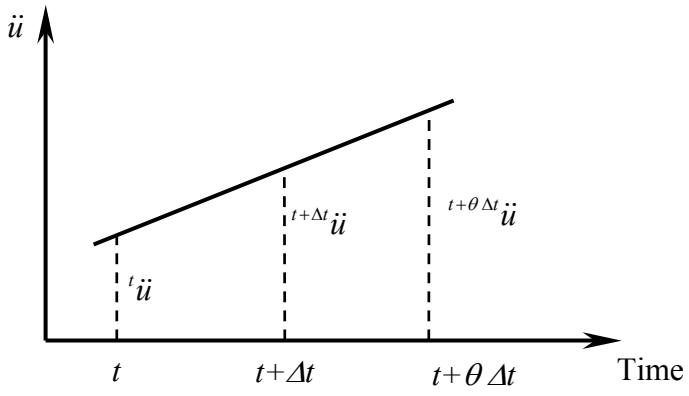

Figure 6.7 Wilson-θ Scheme of Time Integration

6.7 Analysis Results

The performance measures calculated from the parametric analyses are compared to corresponding pushover results and examined for evidence of behavioral trends. The data gleaned from the analyses is used to judge the effect of pertinent parameters, including the effect of record scaling, higher modes, and dynamic shear magnification. The term "median" in the following discussions refers to the geometric mean, which is the exponential of the average of the natural logarithms of data. Following is a summary of the various results obtained.

6.7.1 Scaled vs. Unscaled Ground Motions

To investigate the effect of ground motion scaling on structural response, some of the analyses are conducted twice. For the two 12-story systems, analysis is conducted once with scaled ground motions and once more with the original unscaled records. For the 18-story system, analysis is conducted twice for the 2/50 records only; once scaled at the fundamental period T_1, and once more for scaling at the fundamental period of the structure after all the coupling beam have yielded T_u. A summary of the time history analyses performed in this work is given in Table 6.8

Table 6.8 Summary of all Performed Nonlinear Time History Analyses

Records / System	Original Records (Unscaled)		Records Scaled at T_1		Records Scaled at T_u	
	2/50	50/50	2/50	50/50	2/50	50/50
HCW-12-U	[2]10	[2]10	-	-	-	-
HCW-12-30	[1]10	[1]10	[2]10	[2]10	-	-
HCW-18-30	-	-	[1]10	[2]10	[2]10	-

[1] Analyses were conducted to examine the scaling scheme.

[2] Final results presented are based on the output of these analyses.

The coefficient of variation (*COV*) is used as an indication of the dispersion of results. It's expressed as a ratio between standard deviation and the mean of the results of a specific response parameter; such as roof displacement, base shear, story drifts etc. a large *COV* indicates a wide dispersion and hence greater scatter in the obtained results.

$$COV = \frac{Sandard\ Deviation}{Mean} = \frac{\sqrt{\dfrac{n\sum x^2 - (\sum x)^2}{n(n-1)}}}{\sum x / n} \tag{6.16}$$

Where n is the number of data points (10 points) and x is the response parameter (roof displacement or base shear).

6.7.1.1 Results for HCW-12-30

The maximum roof displacements resulting from both sets of records are presented in Figure 6.8. In the 2/50 cases, although large differences are observed in two of the earthquakes (first and last columns in Figure 6.8a), all the other analyses show small differences between scaled and unscaled records.

The *COV's* are 48% for the scaled records and 52% for the unscaled set, and as is clear from the figure, the medians of both sets are almost identical. In 50/50 cases however (Figure B1, Appendix B), individual differences and *COV*'s are much larger, but the medians for both scaled and unscaled sets are also very close (Figure 6.8b). The *COV* is 14% for the scaled records and 74% for the unscaled ones. By comparing scaled record data in Figures 6.9a and 6.9b, it is obvious that the 2/50 records result in greater scatter compared to the 50/50 records. Similar trends are obtained for the base shear. These analyses support Shome et al's (1997) suggestion that record scaling does not significantly influence the median, but can considerably reduce dispersion in the response parameters.

The variation in base shear is shown in Figure 6.9 for 2/50 records. Like the roof displacements, both scaling schemes yielded close *COV* for the 2/50 records with medians of 4826 and 4895 kips for the scaled and unscaled records respectively and an equal *COV* of 14%. Though 50/50 records show a similar median value for the base shear (2921 and 2840 kips for scaled and unscaled respectively), *COV's* for both scaled and unscaled were 14% vs. 34%

respectively. Again, the results support the success of the scaling scheme to reduce the dispersion in results. Base shears for 50/50 records is show in Figure B2, Appendix B.

6.7.1.2 Results for HCW-18-30

A comparison is made between the two scaling schemes; scaling at T_1 vs. scaling at T_u as previously explained. Figure 6.10.a shows roof displacements for both scaling schemes. Smaller dispersion is observed for the records scaled at T_u. The *COV* is 33% and 57% for T_u scaling vs. T_1 scaling respectively. A remarkable difference in median roof displacements is obtained. Median roof displacements for both cases are 26.5 and 33.5 inches. For the base shear however (Figure 6.10b), T_1 scaling resulted in less dispersion and less *COV* of 18% vs. 32% for T_u scaling. Therefore, no definite conclusion can be drawn to establish which scaling technique is better. The rest of the analysis results presented in the next sections are based on the T_u scaling scheme.

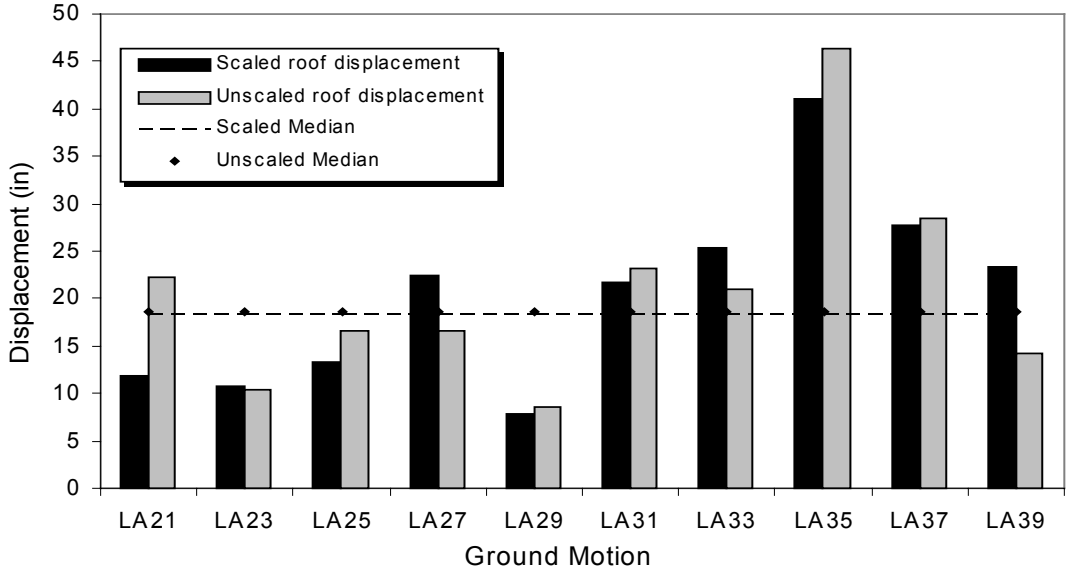

Figure 6.8 Maximum Roof Displacement in HCW-12-30 for Scaled and Unscaled Records for 2/50 records

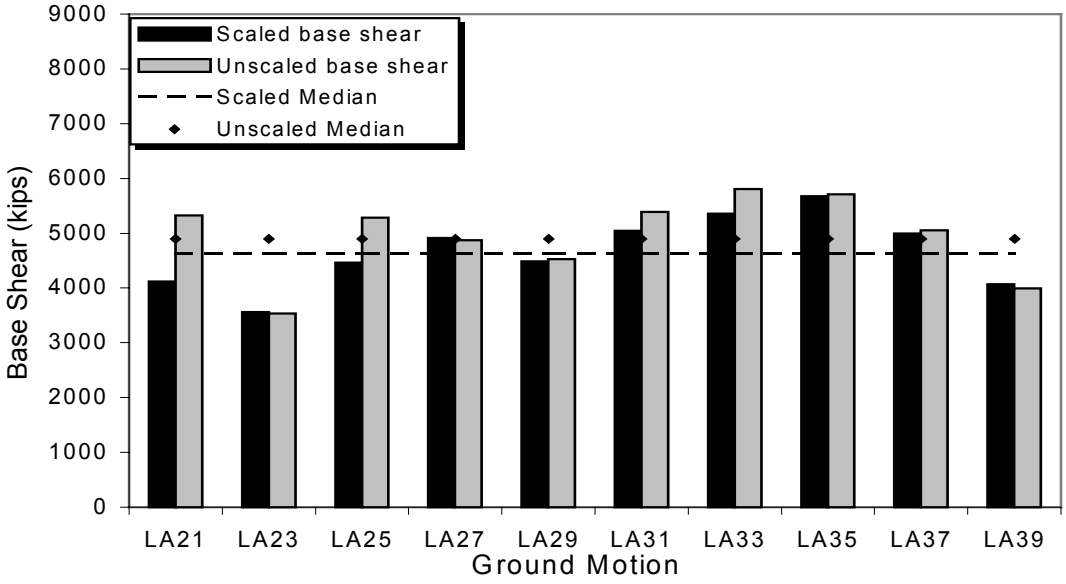

Figure 6.9 Maximum Base Shear in HCW-12-30 for scaled and unscaled ground motions for 2/50 records

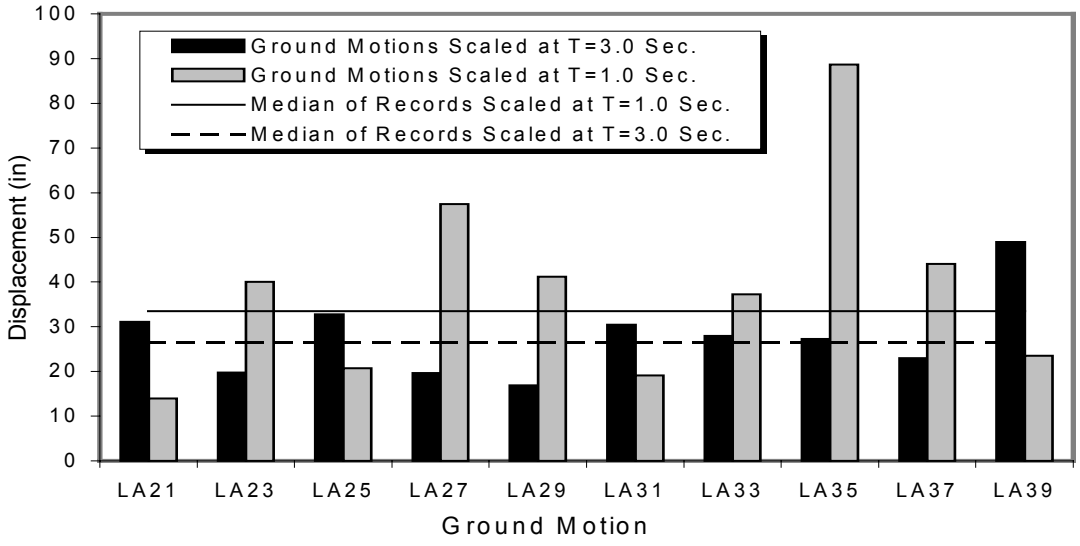

a) Roof Displacement for 2/50 Records

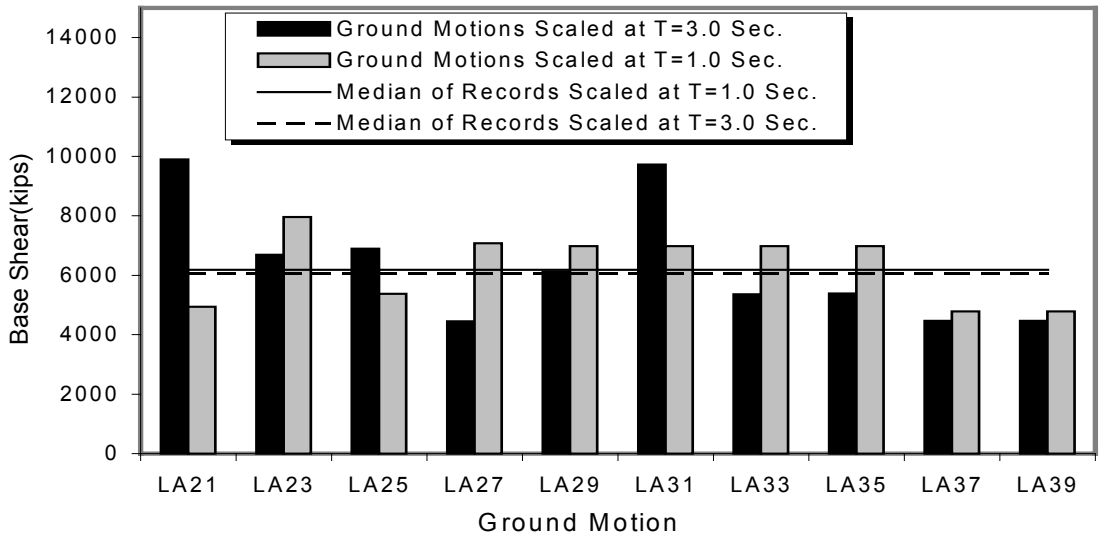

b) Base Shear for 2/50 Records

Figure 6.10 Maximum Roof Displacement and Base Shear in HCW-18-30 for Different Scaling Schemes

6.7.2 Maximum Roof Displacement

Although roof displacement is not used as a response parameter to evaluate the building performance, it is a general indicator of the extent of nonlinear response, story drift and plastic rotation at the base of the wall. Maximum roof displacements are obtained from the displacement history of the each ground motion at the roof level. In order to assess the validity of static nonlinear procedures, roof displacements from time history analyses are compared to the target displacements predicted by the pushover analyses using the FEMA-356 equation:

$$\delta_t = C_0 C_1 C_2 C_3 S_a \frac{T_e^2}{4\pi^2} g \tag{6.17}$$

Where:

C_0, C_1, C_2 and C_3 are modification factors determined according to section 3.3.3.3 of FEMA-356.

S_a = Spectral response acceleration at the effective fundamental period of the structure

g = Acceleration of gravity

T_e is the effective fundamental period as determined from the expression:

$$T_e = T_i \sqrt{\frac{K_i}{K_e}} \tag{6.18}$$

Where:

T_i = Elastic fundamental period in the direction under consideration calculated by elastic dynamic analysis.

K_i = Initial lateral stiffness of the system.

K_e = Effective lateral stiffness of the system (secant stiffness when $V_{BASE} = 0.6V_{YIELD}$)

The determination of the initial and effective lateral stiffnesses is shown in Figure 6.11.

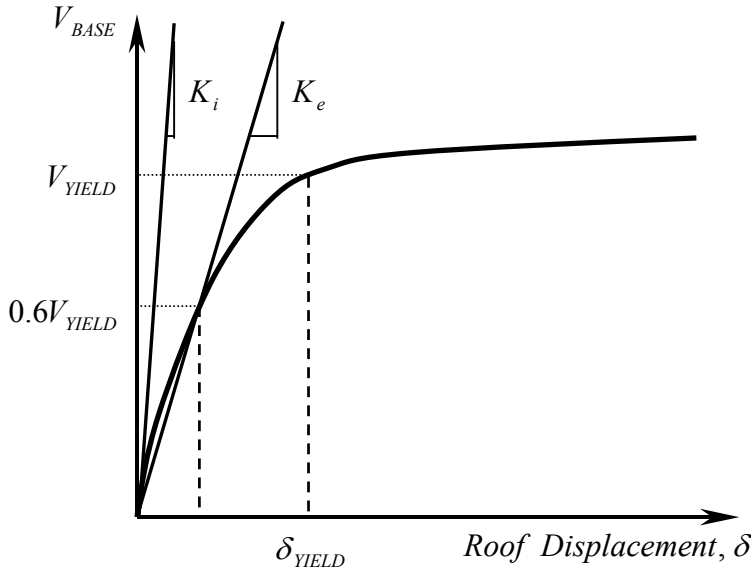

Figure 6.11 Determination of Initial and Effective Lateral Stiffnesses

6.7.2.1 Results for HCW-12-30 and HCW-12-U

Figure 6.12 shows representative displacement histories for ground motion LA31. Displacements at all floor level are plotted against the time for both HCW-12-30 and HCW-12-U. The general trend suggests that that the fundamental mode is dominating the structure's maximum deformational response. Displacements at all floor level mostly attain their maximum level at the same time.

The beneficial effect of coupling can be seen by comparing median values in Figure 6.13 (uncoupled walls) and Figure 6.8 (coupled walls). For example, the median of the maximum roof displacements decreased from 25.4 in for HCW-12-U to 18.6 in for the HCW-12-30 for 2/50 cases. It is instructive to compare these median roof displacements to the target roof

displacement suggested by FEMA-356 (2000), which are 28.2 in for the uncoupled systems and 16.8 in for the coupled system.

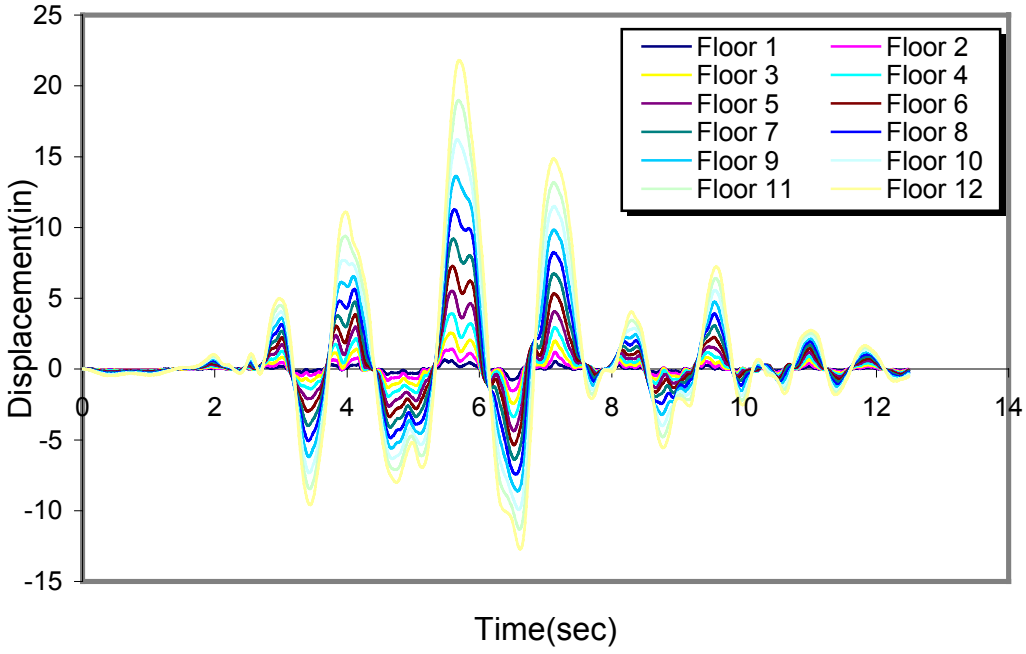

a) HCW-12-30

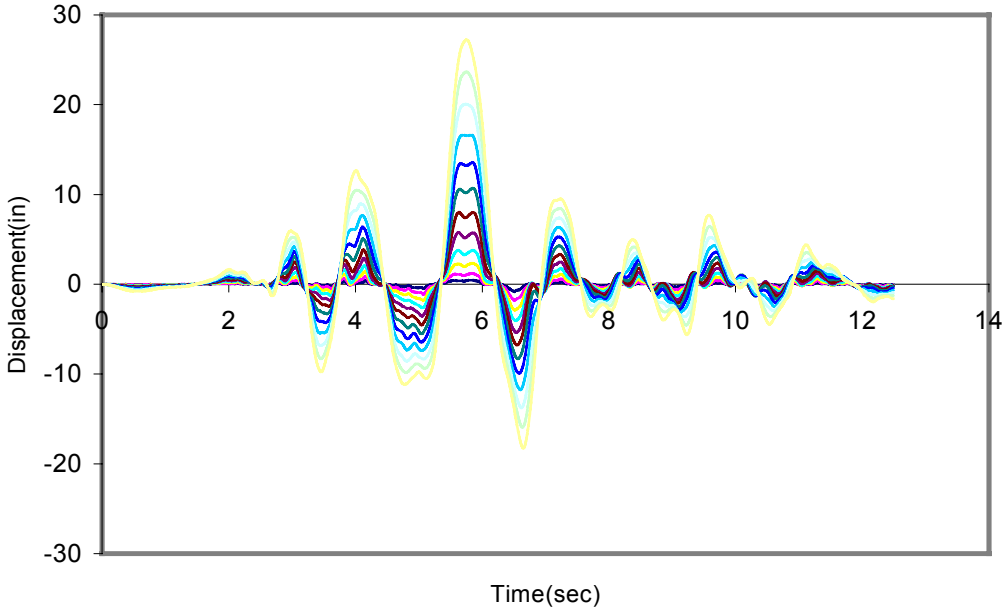

b) HCW-12-U

Figure 6.12 Displacement History for Ground Motion LA31

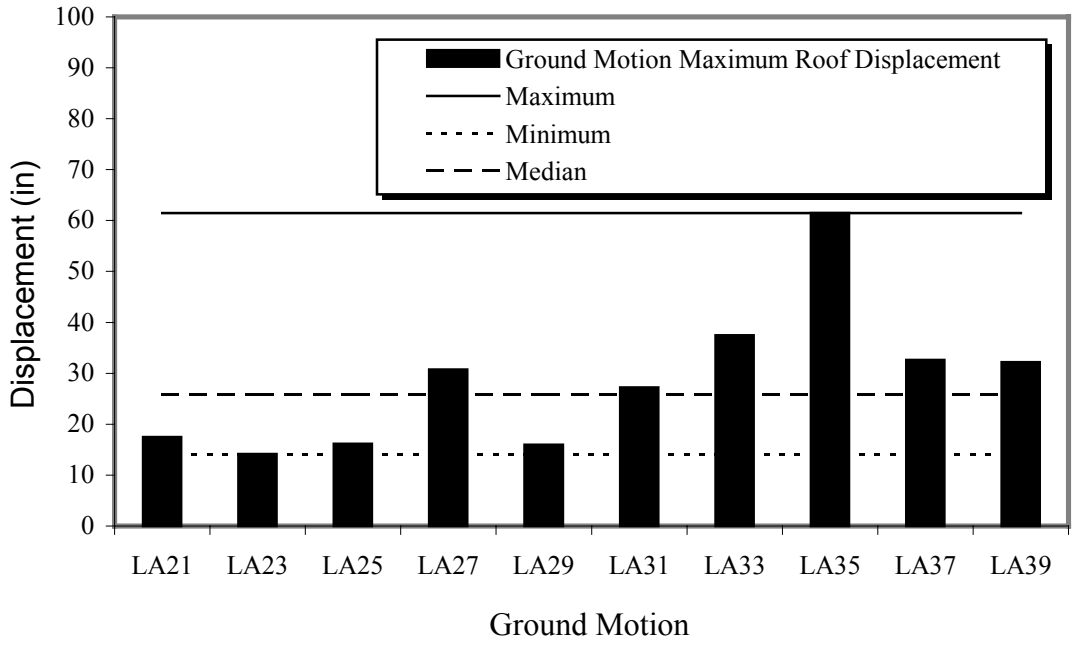

Figure 6.13 Maximum roof displacement in HCW-12-U for 2/50 records

Although the FEMA-356 (2000) target displacement is conservative for the uncoupled wall, it under predicts the coupled wall displacements. In any case, both target displacements estimates are within 11% of the dynamic data, which is rather good considering the inherent unknowns in this situation.

For the 50/50 records (shown in Figure B3, Appendix B), HCW-12-30, roof displacement varies from 3.2 in to 5.3 in with a median of 4.3 in and a *COV* of 14%. Calculated target displacement is 3.8 in which is a conservative estimate compared to the median. For HCW-12-U, median roof displacement is 6.4 in with a COV of 19%, very close to the target displacement of 6.45 in.

6.7.2.2 Roof Displacement Results for HCW-18-30

Roof displacements are presented in Figure 6.10a for 2/50 records. Displacement history at different floor levels is presented in Figure 6.14 for ground motion LA33. Displacement history trends are similar to those observed in the 12-story building. Displacements of all floors attain their peak value almost simultaneously indicating that the maximum deformational response is still dominated by first mode. Median roof displacement is 26.5 and 5.632 for the 2/50 and 50/50 records.

For the 2/50 motion records, the median of maximum roof displacements increased from 18.6 in to 26.5 in due to the increase in height from 147 ft in the 12-story building to 219 ft in the 18-story one. Unlike elastic behavior of cantilever shear walls where the increase in displacement with height can be exponential (4^{th} order), increase in inelastic displacement is approximately proportional to the increase in building height. Target displacement using FEMA-356 equation yielded 30.4 in which is closer to the one obtained from the records scaled at T_1 (33.5 in). This latter result suggests that T_1-scaling in addition to being more conservative could be more reliable as well.

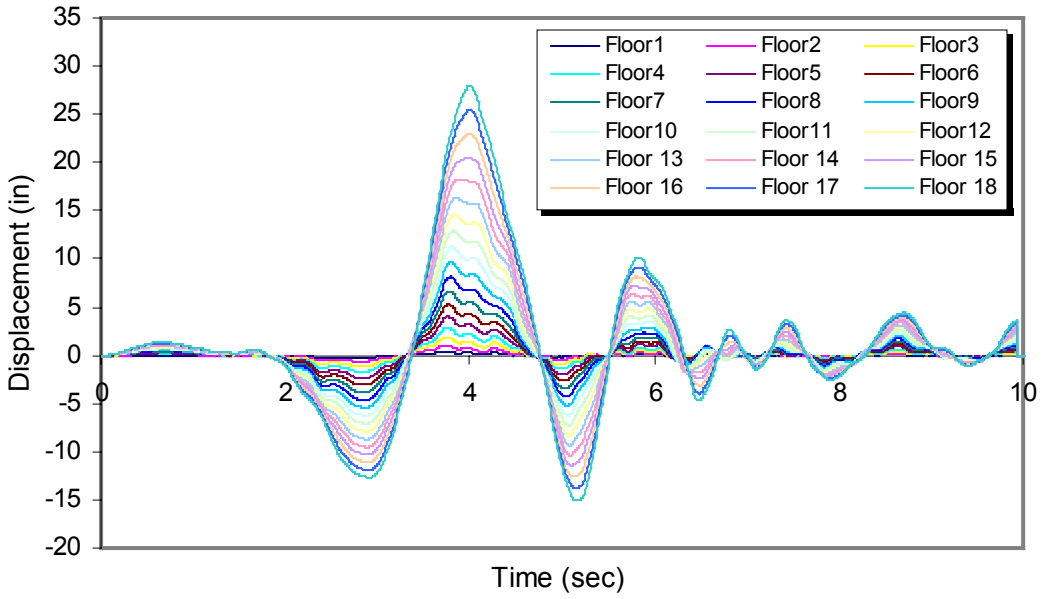

Figure 6.14 Displacement History for Ground Motion LA33 in HCW-18-30

For the 50/50 records as shown in Figure B4, Appendix B, maximum roof displacement varies from 4.3 in to 14.8 in with a median of 5.6 in with a *COV* of 47% when all ten-motion records are considered and *COV* of 14% if LA43 record is excluded. Target displacement calculation resulted in a value of 7.7 in which is greater than the median estimate of the time history analyses. Displacements resulting from the 50/50 ground motions are significantly small compared to those of the 2/50 records.

6.7.2.3 Deflection Amplification Factor

The deflection amplification factor was discussed earlier in section 3.7.2. In that section, it's suggested to resolve the displacements resulting from an elastic model of the system in which the coupling beams are replaced by vertical forces representing their nominal capacity, into two components, $(\delta_{xe})_w$ and $(\delta_{xe})_{cb}$. The magnification factor C_d is applied only to $(\delta_{xe})_w$ since $(\delta_{xe})_{cb}$ already takes into account the nonlinearity in the coupling beams. This technique yielded

magnified roof displacements for HCW-12-30 and HCW-18-30 equal to 21.5 in and 29.45 in respectively. The medians of the maximum roof displacements resulting from the dynamic analyses are 18.6 in and 26.5 in for the 12-story and 18-story systems respectively. Compared to the values predicted by the deflection amplification factor, the variation is as large as 15%. If the magnification factor is directly applied to the displacement resulting from the elastic model with vertical forces replacing the coupling beams, the displacement resulting from amplifying these displacements would have been 82.25 in for the 18-story system, nearly tripling the roof displacement. For the 12-story system, the magnified displacement would have been 25.65 in with 37% increase compared to the displacement from the dynamic analysis.

6.7.3 Base Shear Magnification

As explained before in chapter 3, dynamic loading can excite a structure's higher modes other than the fundamental (first) mode. Based on the frequency content of ground motion acceleration, higher modes that are triggered could cause the building to behave as a simple beam with overhang instead of a cantilever; thus, attracting higher base shear. This is known as dynamic magnification of base shear. Paulay and Priestley (1992) suggested the following equation to account for the increase in the base shear demands:

$$\omega = 1.3 + n/30,\ \omega \le 1.8 \qquad (6.19)$$

Where ω is the shear magnification factor and n is the number of stories. This equation was considered in the design of the shear walls, and yielded a dynamic base shear magnification factor of 1.7 for the 12-story building and 1.8 for the 18-story building.

Table 6.9 Base Shear for All Analyses in kips

System \ Records		Original Records (Unscaled)		Records Scaled at T_1		Records Scaled at T_u	
		2/50	50/50	2/50	50/50	2/50	50/50
HCW-12-U	Minimum	4975	1474	-	-	-	-
	Maximum	7735	5409				
	Median	5986	3291				
HCW-12-30	Minimum	3540	1840	3357	2225	-	-
	Maximum	5812	5286	5680	3559		
	Median	4895	2840	4626	2921		
HCW-18-30	Minimum	-	-	4783	2173	4455	-
	Maximum			7960	4243	9892	
	Median			6172	3132	6082	

6.7.3.1 Results for HCW-12-30 and HCW-12-U

Static pushover analyses (see Figure 6.5) indicate that total base shears for both coupled and uncoupled systems are almost identical and equal to 3195 kip. Time history analyses for both systems show that the base shears do increase substantially beyond this value under dynamic loading. The computed base shears for all 2/50 records are shown in Figure 6.15 and 6.9 for HCW-12-U and HCW-12-30 respectively. The figures show that the median base shear for the uncoupled system (5986 kip) is larger than the base shear for the coupled system (4626 kip); an increase of 30%. When compared to pushover results, dynamic base shear magnification reaches 44% for the coupled system and 87% for the uncoupled. These figures indicate that higher mode effects are somewhat more prominent in the uncoupled walls versus the coupled walls. Furthermore, it appears that Equation 6.19 is rather inaccurate and needs to be refined to more accurately pick up differences in structural characteristics.

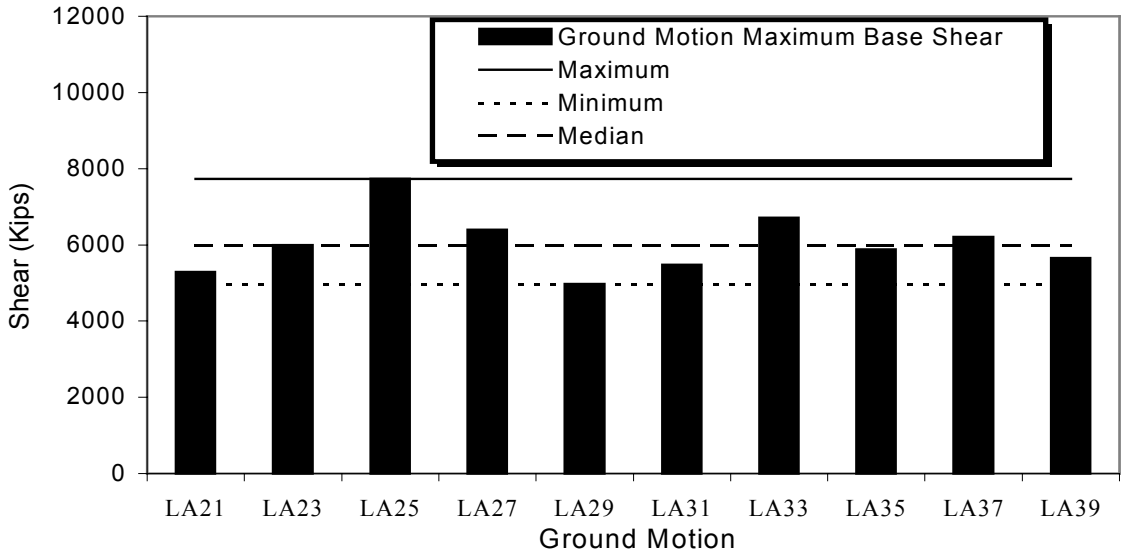

Figure 6.15 Maximum Base Shear in HCW-12-U for 2/50 records

Figure 6.16a and 6.17.b show the displacement and drift profiles along the height of HCW-12-U at the time at which the base shear reach its maximum value for earthquake LA31 that produces a maximum base shear of 5044 kips; closest to the median of all 2/50 records which was 4626 kip. Profiles at 10 time intervals before and 10 intervals after the maximum base shear time instant are also plotted to show the progress of the profile around the targeted time instant. The figure shows that an inflection point exits at about 3/4 of the height, and that the building seems to be unfurling around this point as the time steps progress, clearly indicating higher mode effects. Higher mode effects are also evident in the drift plots, which show that drifts at the top stories are increasing at a faster rate than at the bottom floors, reflecting the whiplash effect that is taking place. Figure 6.17 presents a profile of the floor forces at the instants of maximum base shear for all 2/50-motion records. Story forces are obtained by adding the inertial forces at floor levels to the damping forces. Patterns of all records indicate additional evidence of higher mode participation in the computed base shears. Inertial forces and hence,

floor accelerations attain their maximum values at the lower portion of the wall and gradually decrease towards the top of the wall. In some instants, such as record LA31, floor forces at the top level are in the opposite direction indicating maximum participation of the higher modes. Maximum Base Shear for 50/50 records is shown in Figure B5, Appendix B for further reference.

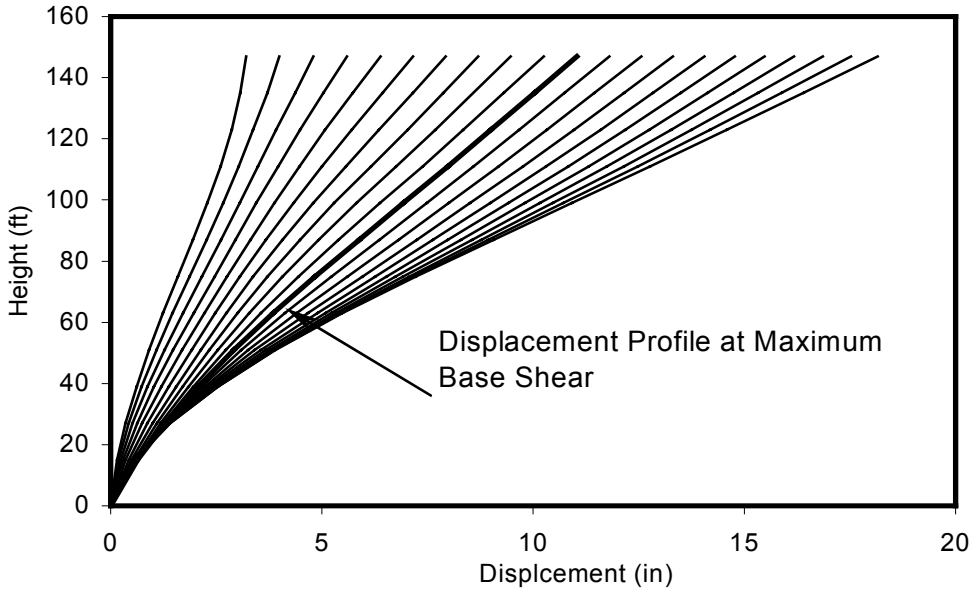

a) Displacement Profile

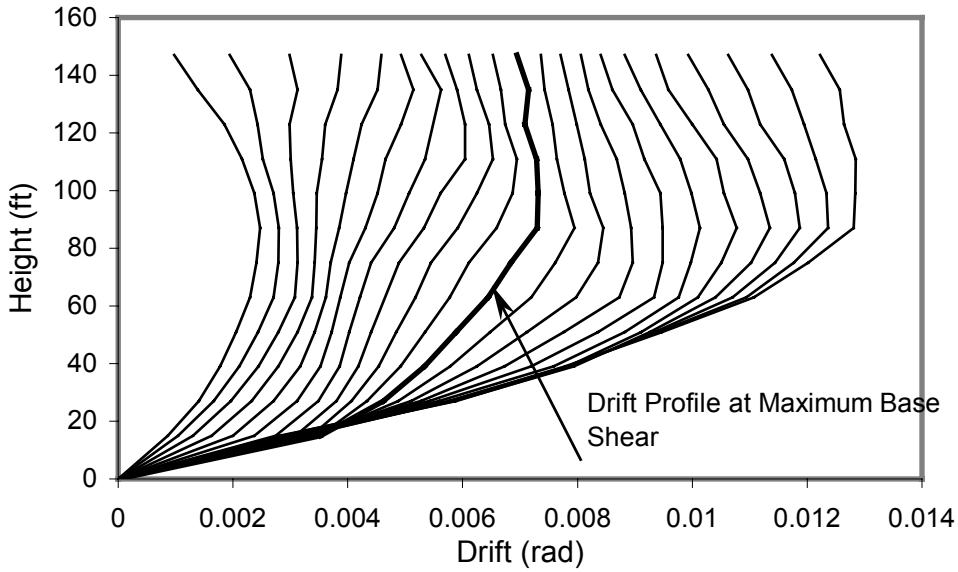

b) Interstory Drift Ratios

Figure 6.16 Displacement and Drift Profiles at the Maximum Base Shear and Adjacent Time Intervals for Earthquake LA31 (HCW-12-30)

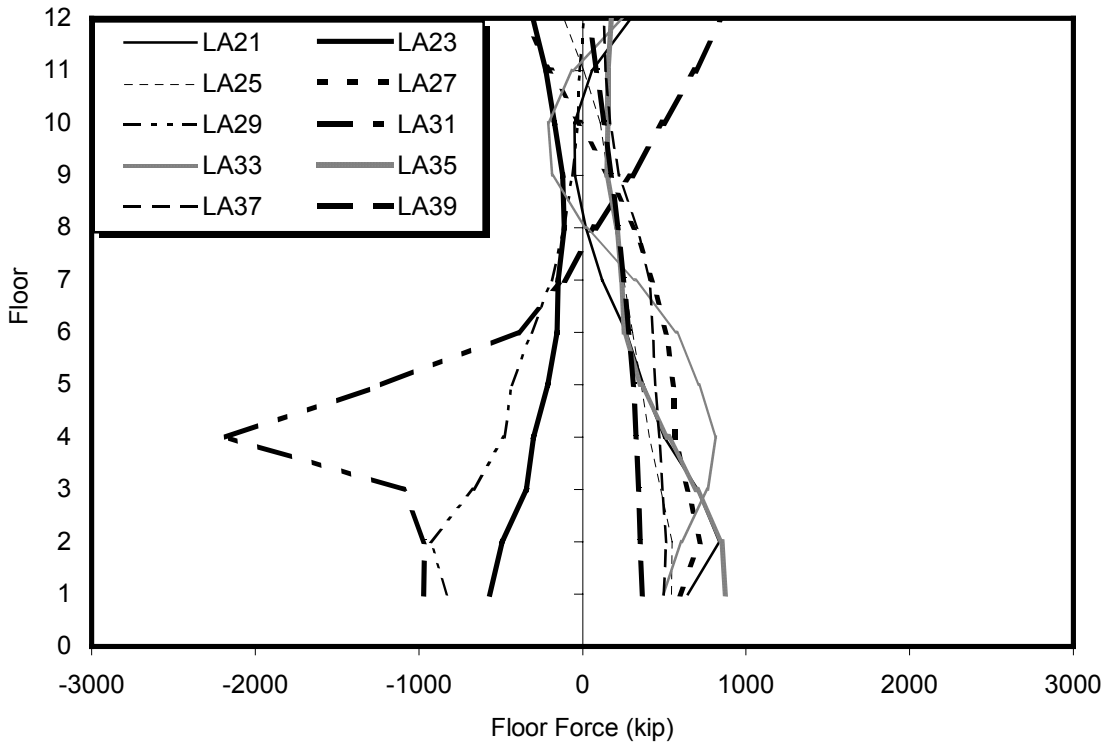

Figure 6.17 Floor Forces at Maximum Base Shear for 2/50 Records in HCW-12-30

6.7.3.2 Base Shear Results for HCW-18-30

The base shear resulting from static push over analysis is 3900 kips as shown in Figure 6.18. Dynamic analysis indicates a median base shear for the 2/50 motion records equal 6082 kips (Figure 6.10b), i.e. the dynamic shear magnification factor is 1.55 which is less than the factor predicted by equation 6.19. This factor is higher than the one of HCW-12-30 (1.44); which is consistent with the trend suggested by equation 6.19.

As was done for HCW-12-30, the displacement and drift profiles for the time intervals adjacent to the instant of maximum base shear are plotted in Figures 6.19a and 6.19b for record LA29; which has a base shear closest to the median of the 2/50 records. The maximum base shear occurred at a roof displacement of 13 in, which is less than the median roof displacement of 26.5 in. Drift profile at maximum base shear indicates an inflection point at a height of 171 ft;

70% of the total building height. Figure 6.20 shows floor forces at the maximum base shear for LA29. Higher mode participation is even more evident compared to the 12-story building. The force distribution shows three-time direction reversal which indicates that higher modes up to the 4^{th} mode are present at this instant of the load history.

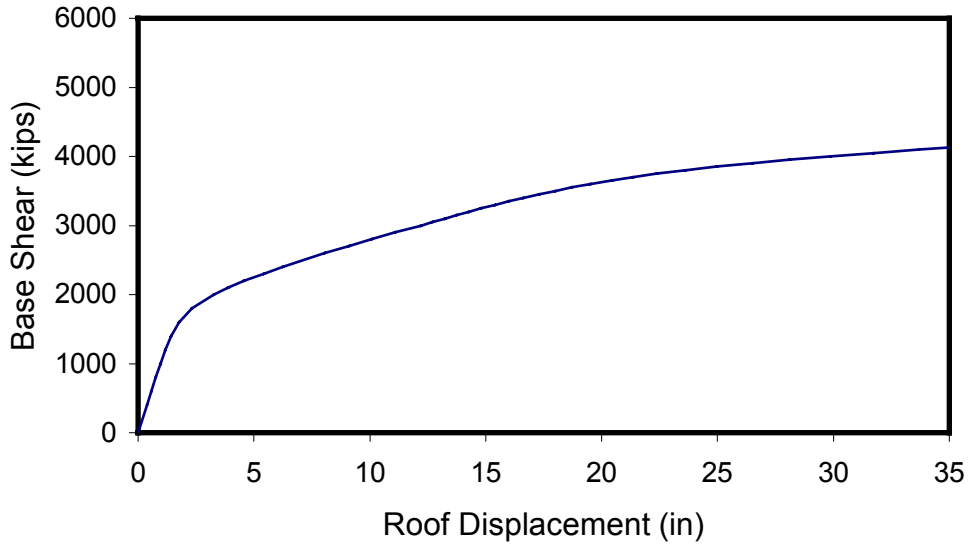

Figure 6.18 Push Over Base Shear Versus Roof Displacement for HCW-18-30

It's clear that although the first mode controls the maximum deformational response of the building; in terms of maximum roof displacement, higher mode effects are controlling the maximum base shear. Hence, it's necessary to design for this magnified base shear in order to avoid possible brittle failure modes associated with lack of shear strength. Different design codes (UBC-1997, IBC- 2000 and ASCE7 1997) don't clearly address this issue.

Base shears for 50/50 records are shown in Figure B6, Appendix B for further reference. The base shears range from 2173 kips to 4243 kips with a median value of 3132 kips. From pushover analysis, base shear at target displacement 5.6 in is 2300, which is lower than the yield limit of the wall flexural steel but well past the coupling beam yielding.

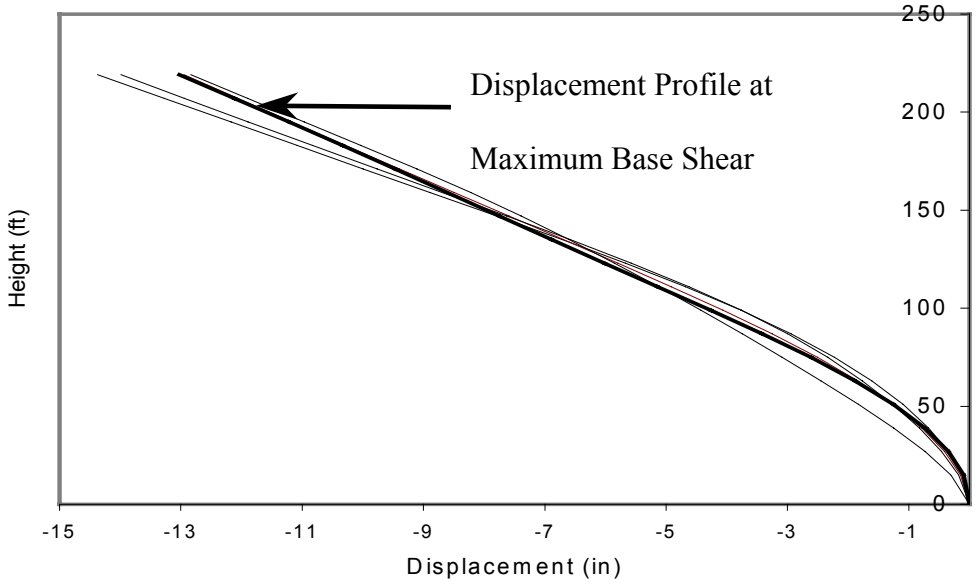

a) Displacement Profile Ratios

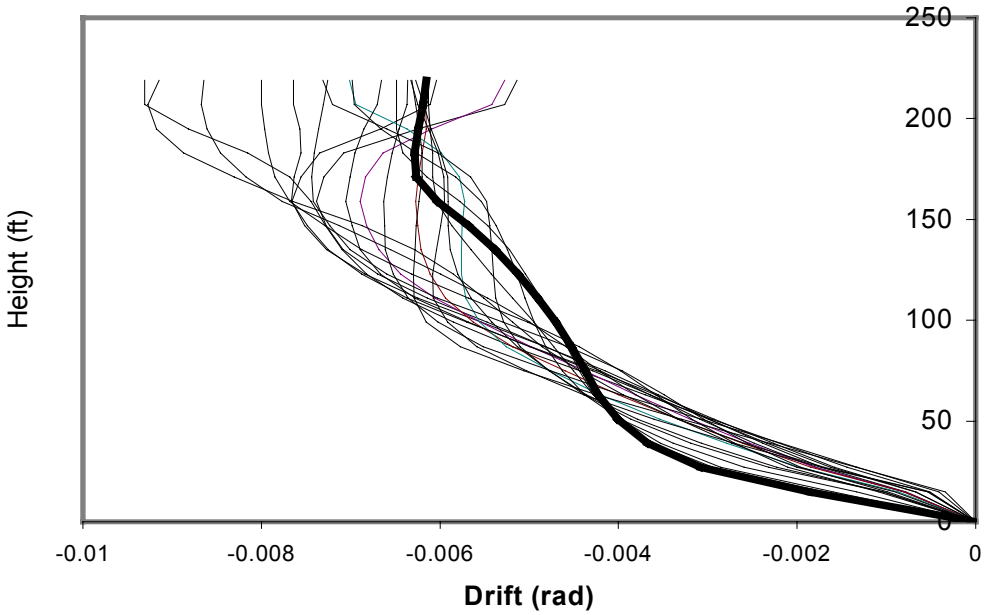

b) Interstory Drift Ratios

Figure 6.19 Displacement and Drift Profiles at the Maximum Base Shear and Adjacent Time Intervals for Earthquake LA29 (HCW-18-30)

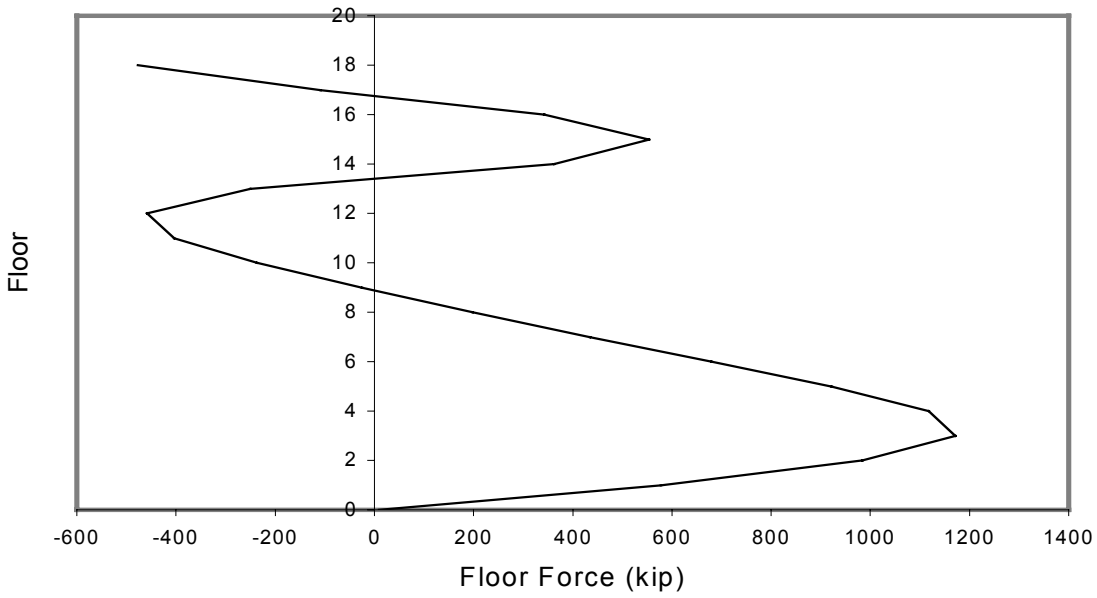

Figure 6.20 Floor Forces at Maximum Base Shear for LA29 Record in HCW-18-30

6.7.4 Concrete Crushing at Base

Examining concrete compressive strains at the base is an important measure to ensure no crushing occurs in concrete. For this reason, principal stresses are computed at each element at the wall base and compressive stresses are plotted against the wall length for all three walls LSW, MSW and RSW. Complete set of plots can be found in Appendix B Figures B7 through B12.

6.4.1.1 Results for HCW-12-30 and HCW-12-U

The median concrete principal compressive strains for the 2/50 runs are well below the crushing point for both coupled and uncoupled systems. The crushing compressive strain is 0.0022 for unconfined concrete at the wall web and 0.008 for confined concrete within the boundary element where heavy transverse reinforcement is provided.

Although strains in some of the boundary elements are as high as 0.005, the heavy confining reinforcement generally protects the concrete against crushing. Only one ground motion (LA35) causes crushing in the boundary elements as well as in some portions of the wall webs. On the other hand, concrete compressive strains are quite low in all 50/50 runs.

6.7.4.2 Results for HCW-18-30

For 2/50 motion records, the maximum compressive strain for HCW-18-30 is 0.0038; which is well below the crushing strain of 0.008 for confined concrete. The median value is generally less than 0.003 at the boundary zones. Concrete at the web experiences strain levels substantially lower than the limit of 0.0022. For 50/50 records, median strains are less than 0.001 even within the boundary zone indicating very limited damage taking place.

6.7.5 Interstory Drift

Interstory drift is an important measure of performance for buildings. Drift at a given story is calculated based on the difference in lateral displacement between the floors divided by the story height. Maximum drifts are computed along the height for every ground motion. Drifts resulting from each record are plotted as scatter while the maximum, minimum and median values of all records are plotted as continuous lines.

6.7.5.1 Results for HCW-12-30 and HCW-12-U

Interstory drift ratios for the coupled building are plotted along the height in Figure 6.21 for the 2/50 set of analyses. The maximum of the median story drift ratios is 1.43%, while the maximum story drift for all earthquakes is 2.68%. These numbers reflect the inadequacy of the

static pushover procedure, where the maximum predicted drift demand is 1% (El-Tawil et al 2002b). In other words, the static pushover analysis significantly underestimates drift demands in this particular building. An opposite observation is made for the 50/50 runs (Figure B13, Appendix B), where the maximum of the median drifts is 0.31%, while the maximum drift is 0.38%. The corresponding demand predicted by the pushover technique in FEMA-356 (2000) is 0.54%.

HCW-12-U interstory drifts, as in Figure 6.22, show a 2% story drift at the building top floors for the 2/50 earthquakes with a similar trend to the coupled system. Because of the coupling effect, drifts are significantly higher than those of the coupled system, while drifts from pushover analysis is 1.8% at the same hazard level. For 50/50 records (Figure B14, Appendix B), maximum drift is 0.57% vs. 0.4% a predicted by pushover analysis.

6.7.5.2 Results for HCW-18-30

The Interstory drift for HCW-18-30 as depicted in Figure 6.23 for 2/50 records, shows a different trend of behavior. Unlike the 12-story where the drift increases with the height up to ¾ of the building height and then declines, story drift increases in magnitude along the entire wall height. However, the rate of change itself decreases up to 2/3 of the building height at which it begins to increase again up to the roof level. The difference in behavior between the 12-story and the 18-story buildings is attributed to the reduction in wall thickness that takes place at the 12^{th} floor. Maximum drift from push over analysis at the target displacement (at 2/50 level) is 1.34%. This value is less than the median of the time history analyses; which is 1.81%. The locations of the maximum drift along the height are also different, in the push over analysis, maximum drift takes place at about 2/3 of the building height while in the time histories, the maximum occurs

almost at the roof level. Story drifts for 50/50 records are shown in Figure B15, Appendix B for further reference.

6.7.5.3 Comment on the Drifts as a Performance Measure

Story drifts are widely used by design codes as a performance measure. They are even used from the beginning of the design process to judge the stiffness of the system by magnifying the elastic displacements with the C_d factor. However, the use of drifts as indicator for the deformational demand can be misleading particularly in the case of walls dominated by flexural behavior. The systems considered herein, which are representative of mid-height shear wall systems, deform predominantly in flexure rather than shear. The drift calculated at the top floor does not represent true distortion in the wall profile but mostly pure rigid body rotation because of the large rotational demands at the base of the wall. In other words, the large drifts at the upper floors actually do not reflect the extent of deformation at these levels. Rather, shear distortions are better representative for the extent of deformation.

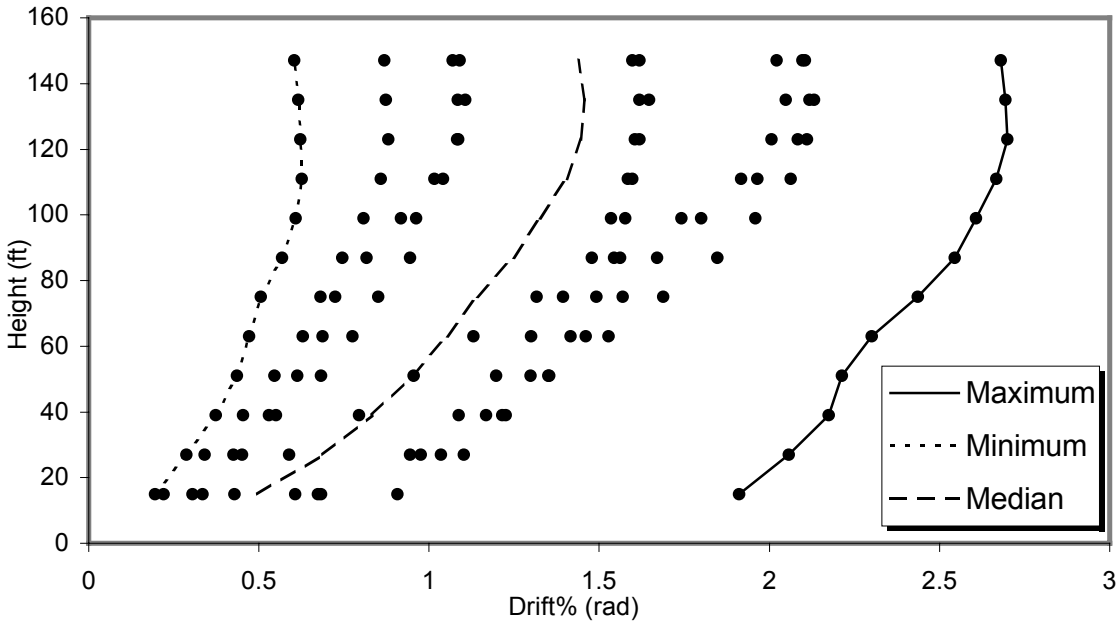

Figure 6.21 Story drift ratios along height for HCW-12-30 for 2/50 records

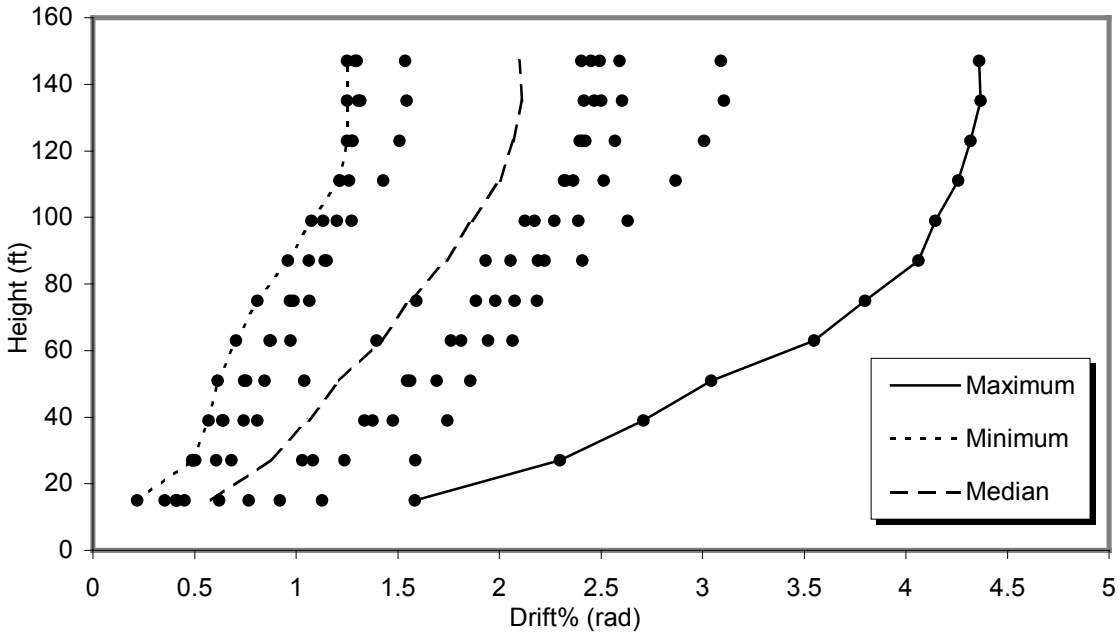

Figure 6.22 Story drift ratios along height for HCW-12-U for 2/50 records

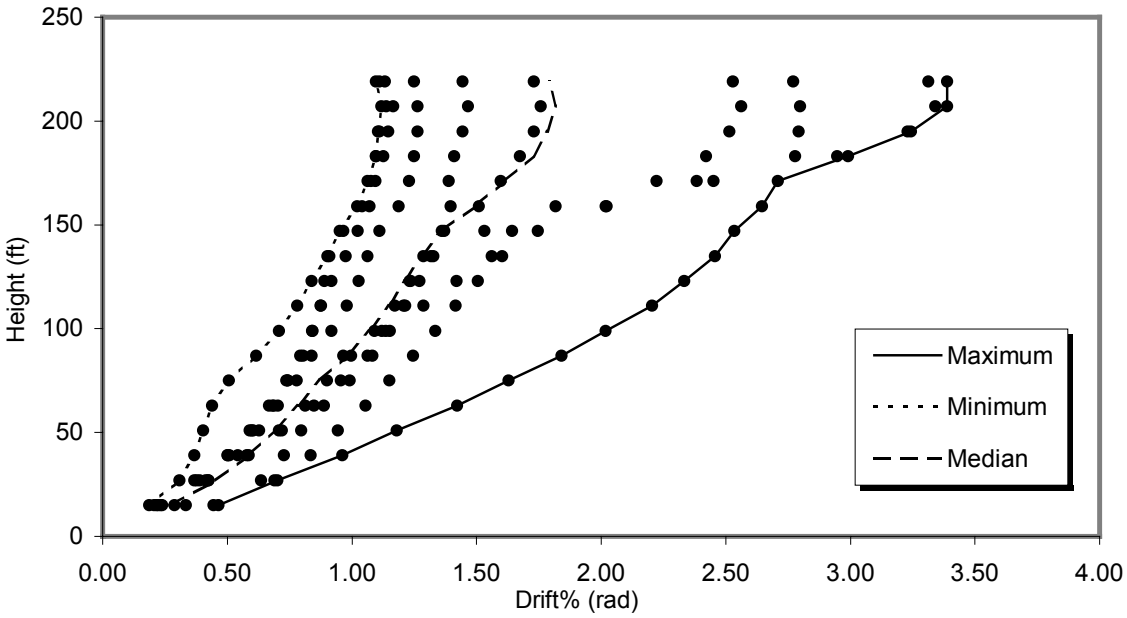

Figure 6.23 Story drift ratios along height for HCW-18-30 for 2/50 records

6.7.6 Shear Deformation

Although shear distortions are not one of the parameters used to evaluate the building performance, they are important in predicting the potential for brittle failure modes. Since concrete is a brittle material, significant shear distortions are undesirable and should be avoided. Average shear deformations at each story is calculated using two diagonal members that have small stiffness such that they do not affect the results (Figure 6.24). Average shear distortions are computed using the following equation suggested by Oesterle et al (1976):

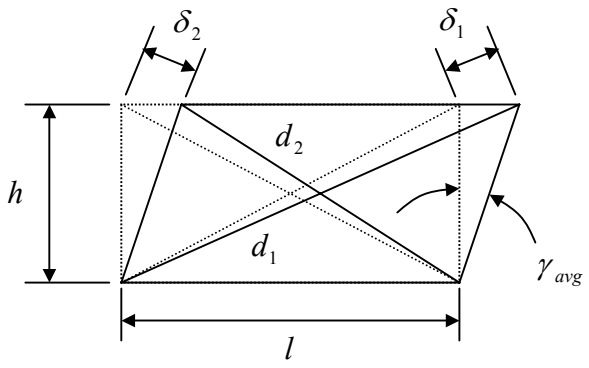

Figure 6.24 Calculation of Average Shear Distortions

$$\gamma = \frac{\delta_1 d_1 - \delta_2 d_2}{2hl} \tag{6.20}$$

Where: $\delta_1, \delta_2 =$ Change in lengths of Wall Diagonals

$d_1, d_2 =$ Lengths of wall panel diagonals

$h =$ Story Height

$l =$ Length of wall

The calculated distortions are then plotted along the wall height for the three walls.

6.7.6.1 Results for HCW-12-30 and HCW-12-U

Median base shear distortions both systems is approximately 0.003 radians with a general trend as shown in Figure 6.25a. Shear distortions reach their maximum value at the wall base then they decrease dramatically in the first two stories and constantly decrease over the rest of the height but with much smaller decay rate. The median value of shear distortion is quite high compared to the wall rotation as discussed in the next section. The contribution of shear deformation to the total roof displacement results only from the first two stories. Therefore, it is considered less significant compared to the wall rotation.

6.7.6.2 Results for HCW-18-30

Median shear distortions for this system are significantly less than that of the 12- story systems. This is expected since a taller wall experience less shear strains and is more sensitive to flexural deformation. The trend in Figure 6.25b is different from that of the 12-story systems since the reduction in wall thickness at the 6^{th} and 12^{th} floor level reduces the shear stiffness of the wall. Maximum distortion at the wall base is 0.0012 radians, which is also comparable in terms of contribution to overall deformations. Thus, the contribution of shear deformation to the total displacement at the roof is considerable and should not be ignored in any rational analysis.

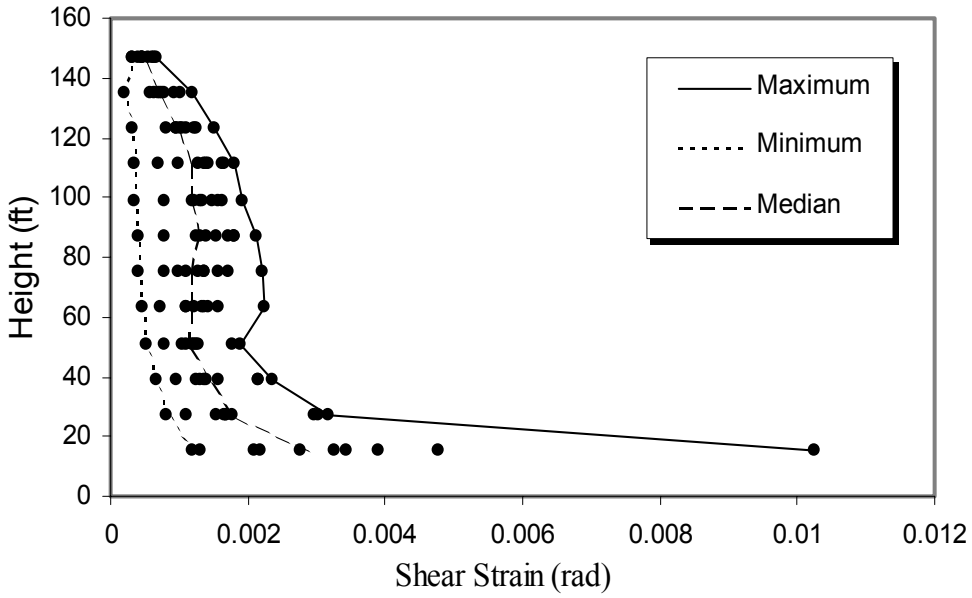

a) HCW-12-30

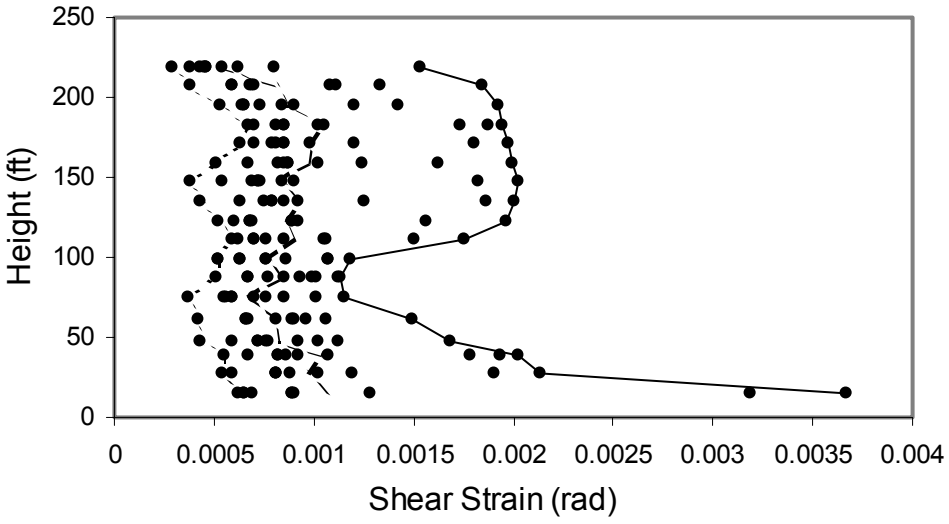

b) HCW-18-30

Figure 6.25 Shear Distortion for 2%50 Records

6.7.7 Wall Rotations

As shown in Figure 6.26, wall rotations are calculated based on the vertical displacements of the wall edges at floor levels using the following equations:

$$\theta_{i+1}^{net} = \theta_{i+1} - \theta_i \tag{6.21}$$

$$\theta_{i+1} = \frac{y_1 - y_2}{l} \tag{6.22}$$

Where: θ_{i+1}^{net} is the net rotation of story $i + 1$

$\theta_i, \theta_{i+1} =$ Wall rotations of floors i and $i+1$, respectively

$y_1, y_2 =$ Vertical displacements of the left and right wall edges, respectively

$l =$ Length of wall

Net plastic rotation at story $i + 1$ is calculated by subtracting the yield rotation of floor $i +$ 1 from the total rotation θ^{net}

$$\theta_{i+1}^{p} = \theta_{i+1}^{net} - \theta_{i+1}^{y} \tag{6.23}$$

Plastic rotations are plotted for all earthquake records along the wall height as scatter while maximum; minimum and median of each set of records are indicated by lines.

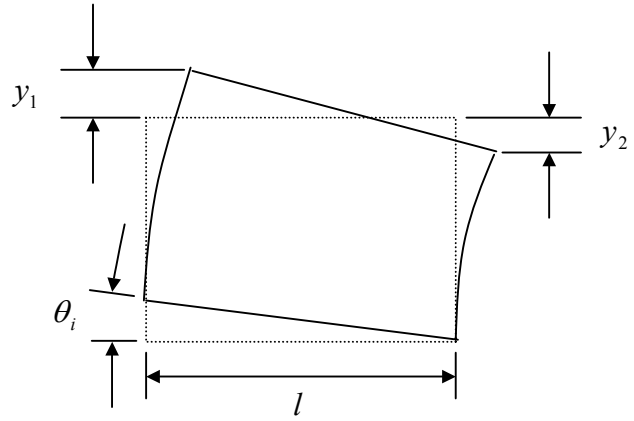

Figure 6.26 Calculation of Plastic Wall Rotations

6.7.7.1 Results for HCW-12-30 and HCW-12-U

Maximum wall rotations occur at the wall base and have almost equal values for the three walls; then they drop suddenly at the second floor then decrease gradually with the height where they reach small values at the top (Figure 6.27). The rotations reach a maximum value of 0.005 radians for the coupled system subjected to 2%50 ground motions, while for the uncoupled system, the maximum wall rotation for the same hazard level is 0.007. For the static analyses, maximum wall rotations are 0.005 and 0.01 for coupled and uncoupled systems respectively. The limits of FEMA-356 depend on whether the wall has a boundary element or not. A more stringent limit is specified for walls that doesn't have boundary element in their compression zone and hence, RSW has tighter acceptance limit than LSW and MSW. In the case of dynamic analysis however, drifts in both directions were nearly equal and either outside walls can experience a state of maximum drift while its boundary element is in the tension side. Therefore, since a boundary element is not provided in both wall edges, the wall is considered not confined. Since MSW has a boundary element in both sides, it is considered as a wall with confined boundary. All the three walls in the coupled system pass the criteria of FEMA-356. The computed wall rotation limit for the collapse prevention objective according to FEMA-356 is 0.009 radians for MSW and 0.005 radians for LSW and RSW. For the uncoupled system, FEMA-356 limits for the LSW and RSW is 0.007 and 0.013 for MSW; therefore, all walls pass the acceptance check.

For 50/50 records, maximum base rotations are 0.001and 0.0015 for the coupled and uncoupled system respectively. The limit for the immediate occupancy objective is 0.0015 for RSW and LSW and 0.005 for MSW; therefore, all the rotations are within the acceptance limit.

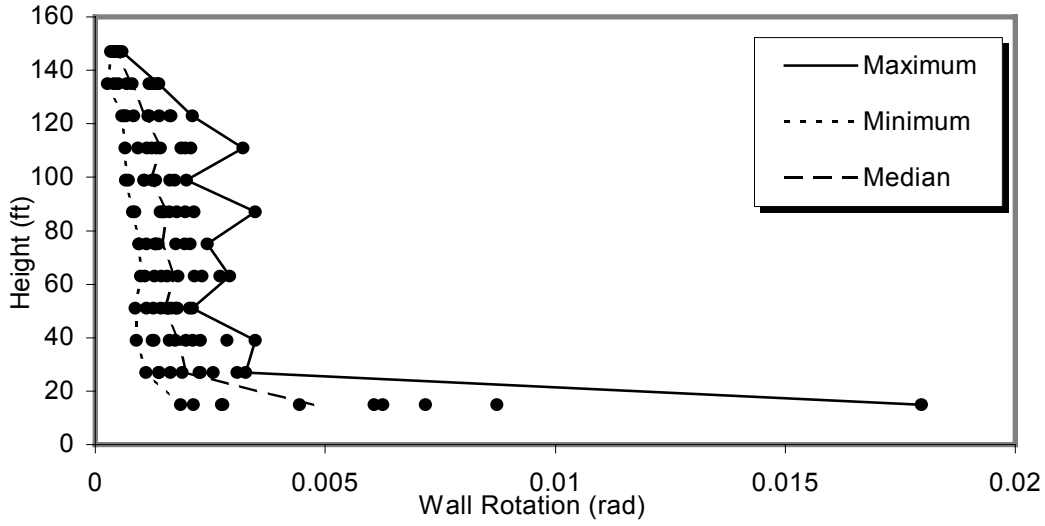

Figure 6.27 Wall Rotation Along Height in HCW-12-30 for 2/50 Earthquakes (LSW)

6.7.7.2 Results for HCW-18-30

Wall Rotations for HCW-18-30 is considerably lower than rotation in HCW-12-30. The median rotation at the wall base is 0.0026 radians; only 52% of the rotation at the wall base in HCW-12-30. However, the average wall rotation based on the maximum roof displacement divided by the wall height (i.e. roof drift angle) is almost identical for both systems and equals 1%. Figure 6.28 shows the distribution of wall rotation along the wall height. Obviously, plastic hinge rotation is not as large in HCW-18-30 compared to HCW-12-30 and less concentration of rotation is observed at the base. Although the design procedures were the same, a stiffer wall design is obtained in case of 18-story wall. The reduction in wall rotation at the base of the wall is attributed to the following reasons:

- The total over-strength of the HCW-18-30 is more than that of HCW-12-30. Wall over-strength depends on system characteristics and design aspects that will be discussed later in this chapter

- The results are obtained from the records scaled at T_u as previously explained, which generated less deformational response than those of the records scaled at T_1. For example, roof displacement for T_u records is 80% of that of T_1 records. Therefore, wall rotations are expected to decrease in the same proportion.

The strong response of HCW-18-30 at the base is not a desired one. In addition to the extra cost of erecting such a strong system, the system does not consume sufficient energy at its base through plastic rotation as it is supposed to do. This strong behavior may cause other member of the system to fail in brittle modes; members such as the joints between wall and slabs or floor diaphragms or brittle shear failure in the walls themselves.

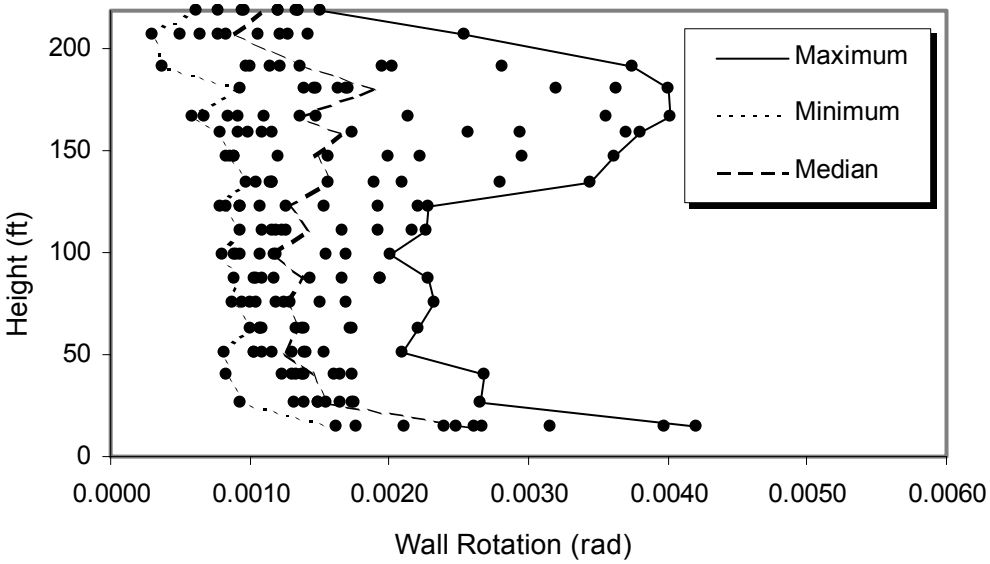

Figure 6.28 Wall Rotation Along Height in HCW-18-30 for 2/50 Earthquakes (LSW)

Static push over analysis for the wall resulted in wall rotations of 0.008 for LSW and MSW; and 0.01 for RSW while the acceptable limits of FEMA-356 are 0.004 for LSW and RSW and 0.0125 for MSW. To investigate the dramatic difference between the pushover and time history predicted wall rotations, displacement profiles along the wall height for both type of

analysis are plotted in Figure 6.29a. The pushover shows significant rotation concentrated at the wall base while the time history shows rotation accumulating over the height. Roof displacement at the time history is extracted from LA33; which yields the closest displacement to the median of all 2/50 records. The push over profile is plotted at the same roof displacement value. Force distribution along the height, story shears and story overturning moment for both static and dynamic analyses are plotted in Figures 6.29b, 6.29c and 6.29d respectively. Dynamic results are extracted at the same time instance of the maximum roof displacement in Figure 6.29a. The Force distribution in Figure 6.29.b shows completely different profiles; while the pushover yields uniform distribution, time history results in a force distribution clearly dominated by higher modes. As the rotation is a product of the integration of moments along the height of the wall, the large difference in overturning moment in 6.29d explains the dramatic difference in wall rotations between the two types of analysis.

It's clear from this comparison that pushover, in case of the 18-story system, is not reliable in predicting the deformation demands on the system. Although target displacements estimated by the pushover is close to the maximum roof displacement from the time history, the prediction of rotational demand on the wall is erroneous and gives a false indication of the level of inelastic deformation.

A comparison between plastic rotations obtained from static and dynamic analyses are shown in Table 6.10.

Table 6.10 Comparison with FEMA-356 Wall Rotation Limits at the collapse prevention limit

Analysis	FEMA Limits	Wall Rotation		
		LSW	MSW	RSW
HCW-12-U	Dynamic	Pass	Pass	Pass
	Static	Pass	Pass	**Fail**
HCW-12-30	Dynamic	Pass	Pass	Pass
	Static	Pass	Pass	Pass
HCW-18-30	Dynamic	Pass	Pass	Pass
	Static	**Fail**	**Fail**	**Fail**

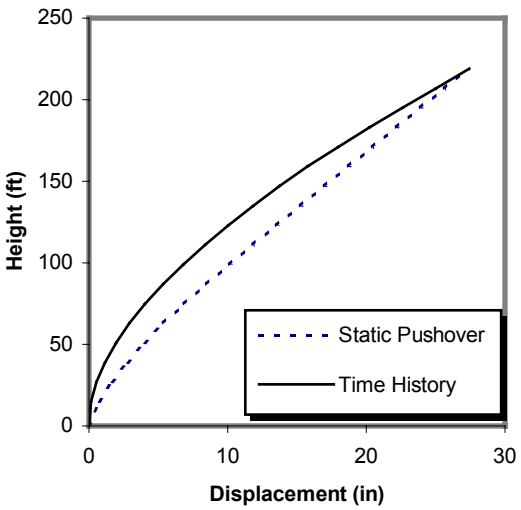

a) Roof Displacement

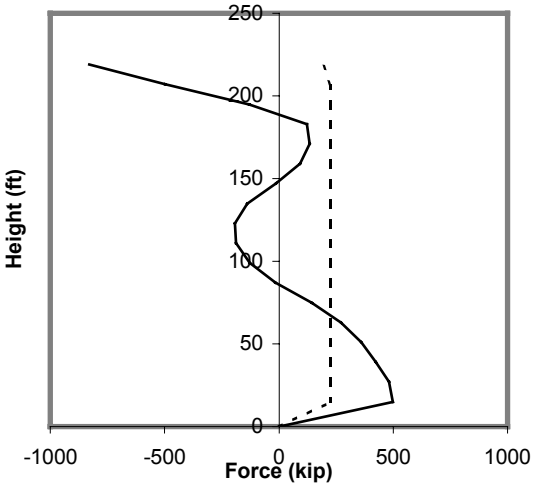

b) Floor Forces

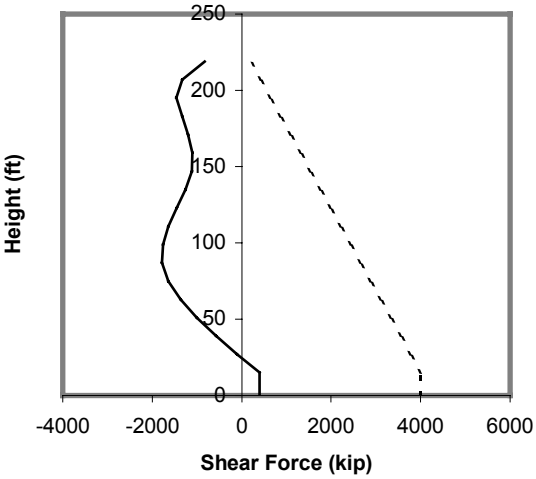

c) Shear Force

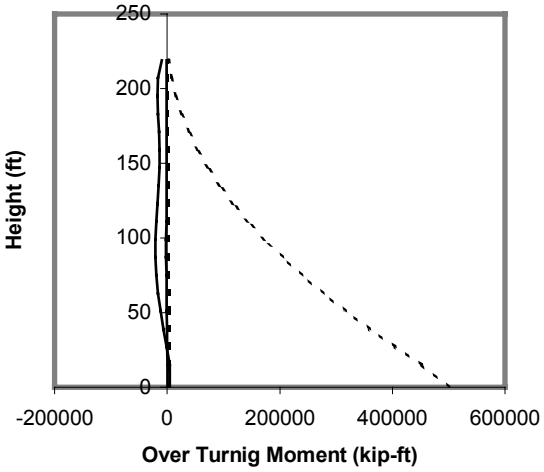

d) Over Turning Moment

Figure 6.29 Comparison Between Pushover and Time History at the Maximum Roof Displacement In HCW-18-30

6.7.8 Coupling Beam Rotation

The total coupling beam rotation accounts for the total rotation of the left and right walls, θ_{WL} and θ_{WR} respectively, as depicted in Figure 6.30. The average of the wall rotations at the beam left and right ends is added to the beam shear distortion to obtain the beam total rotation according to the following equation.

$$\theta_{CB} = \theta_1 + \frac{1}{2}\left(\theta_{WL} + \theta_{WR}\right) \tag{6.24}$$

Where: θ_{WL}, θ_{WR} = Total wall rotations for left and right shear walls

The rotations for both sets of coupling beams are plotted over the height of the structure.

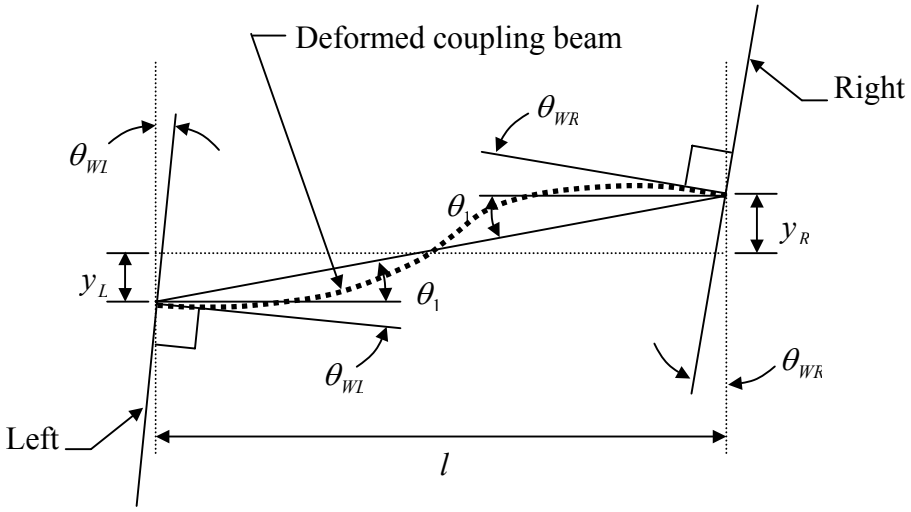

Figure 6.30 Calculation of Coupling Beam Rotation

6.7.8.1 Results for HCW-12-30 and HCW-12-U

For the 50/50 records, the median coupling beam plastic rotation is 0.015 with a coefficient of variation of 15%. The median value just satisfies the FEMA-356 (2000) shear link limits for immediate occupancy (0.015). As shown in Figure 6.31, the median estimate for the

2/50 records is 0.07 with a coefficient of variation of 40%. This median value is quite close to that predicted by the pushover analyses and well within the collapse prevention limit (0.15) permitted by FEMA-356 (2000) for shear links. It is clear that there is much room for additional coupling beam deformations, especially for the collapse prevention limit state. These results emphasize the inherent ductility of HCW systems.

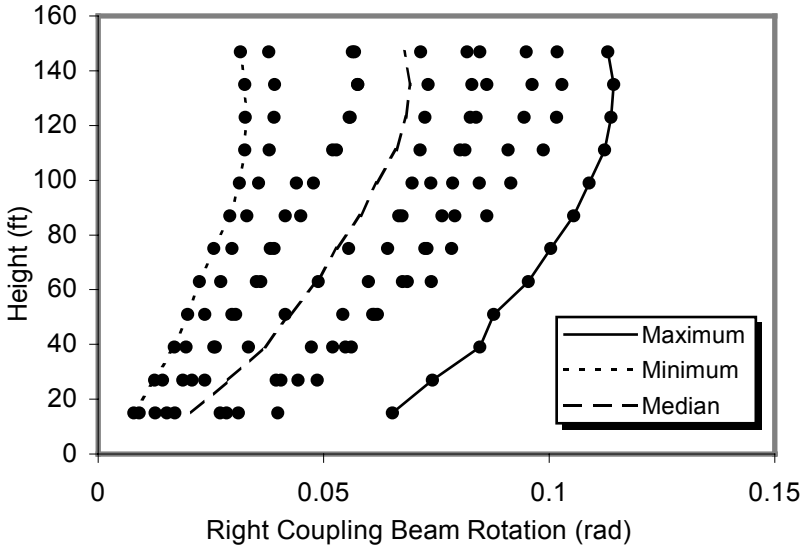

Figure 6.31 Coupling Beam Rotation Along Height in HCW-12-30 for 2/50 Earthquakes

6.7.8.2 Results for HCW-18-30

Maximum coupling beam rotation for HCW-18-30 is 0.09 for the 2/50 records; which is well below the limit allowed by FEMA-356 for collapse prevention (0.15). Static pushover analysis results in a maximum plastic rotation of 0.05 at 2/3 of the wall height. Coupling beam rotations increase gradually with the height up to the 12th story, then they increase at a higher rate up to the roof level as shown in Figure 6.32.

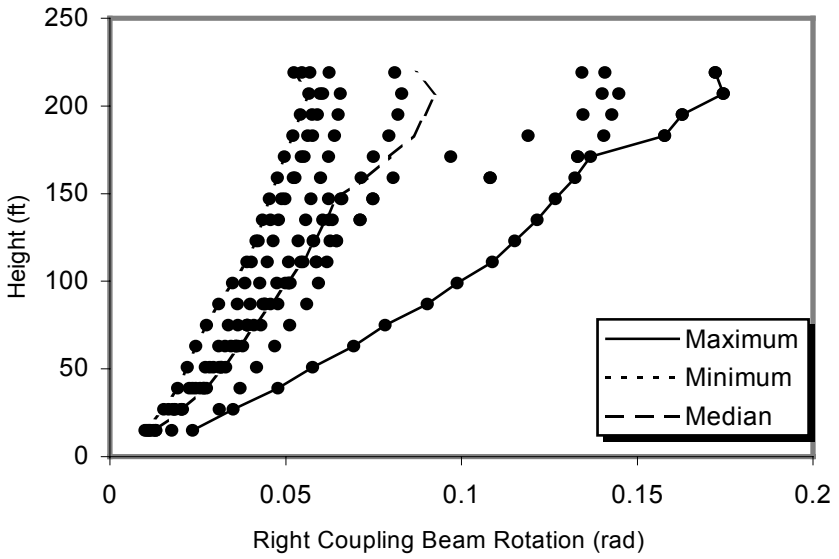

Figure 6.32 Coupling Beam Rotation Along Height in HCW-18-30 for 2/50 Earthquakes

Time history analysis indicates that the coupling beams reach the yield limit early and experience some strain hardening when subjected to 2/50 records. This can be seen in Figure 6.33a, which shows shear force history for an average record (LA33). Shear forces in all 18 coupling beams between LSW and MSW are plotted in the figure. Push over analyses also confirm this result; which is considered a major advantage of the coupled wall system as the early yielding of coupling beams increases the ductility and energy dissipation capacity of the system. The presence of the coupling beams becomes even more important in HCW-18-30 where significant over-strength is observed in the system and coupling beam yielding become the main energy dissipation mechanism.

The 50/50 records on the other hand, do not cause the beams to strain harden. Figure 6.33b shows the shear force history in the coupling beams between LSW and MSW for record LA57; which represents the average response of all 50/50 records. It is observed that even though the beams do not strain harden; they often reach their yield point most of the time.

Pushover analysis indicates that coupling beam also reach the yield limit before the 50/50 target displacement. Although the beams provide the system with high ductility capacity, this can be a low cycle fatigue problem since ground motions of low acceleration input are more frequent.

Although rotational demands on the wall are low as explained in the previous section, rotational demands on the coupling beams indicate that the beams experience significant inelastic deformations. These two results are not contradictory; rotational demands on the coupling beams do not depend only on the wall rotations but also on the overall growth or shortening at the wall edges due to flexural action in the walls and axial forces imposed by the coupling beams. They also depend on story drift, which as discussed in section 6.7.5, is higher in HCW-18-30 compared to HCW-12-30.

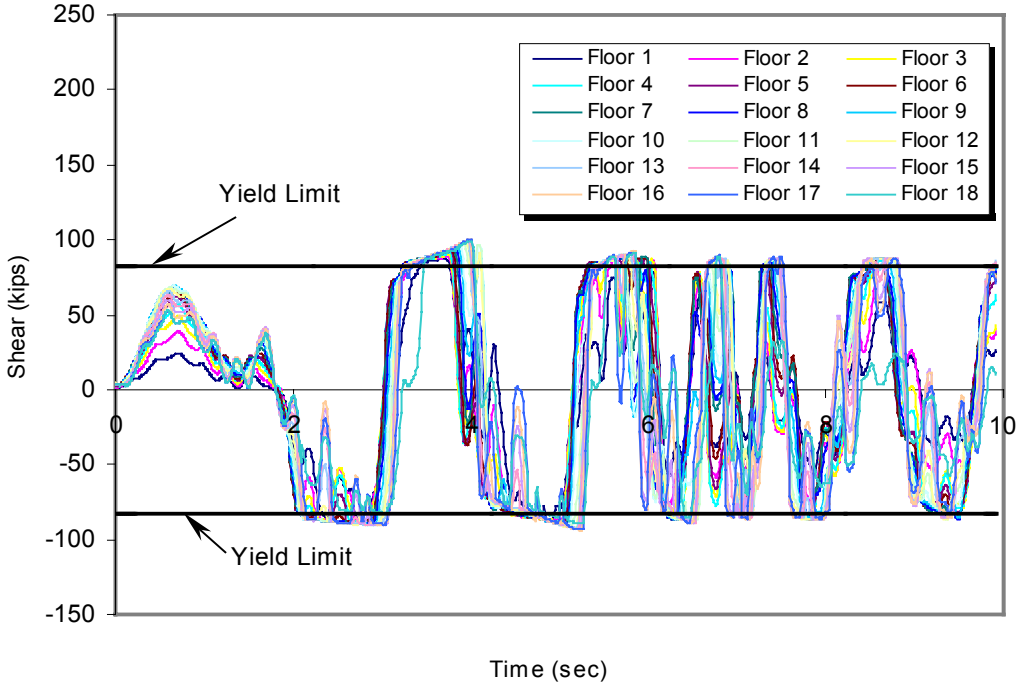

a) LA33

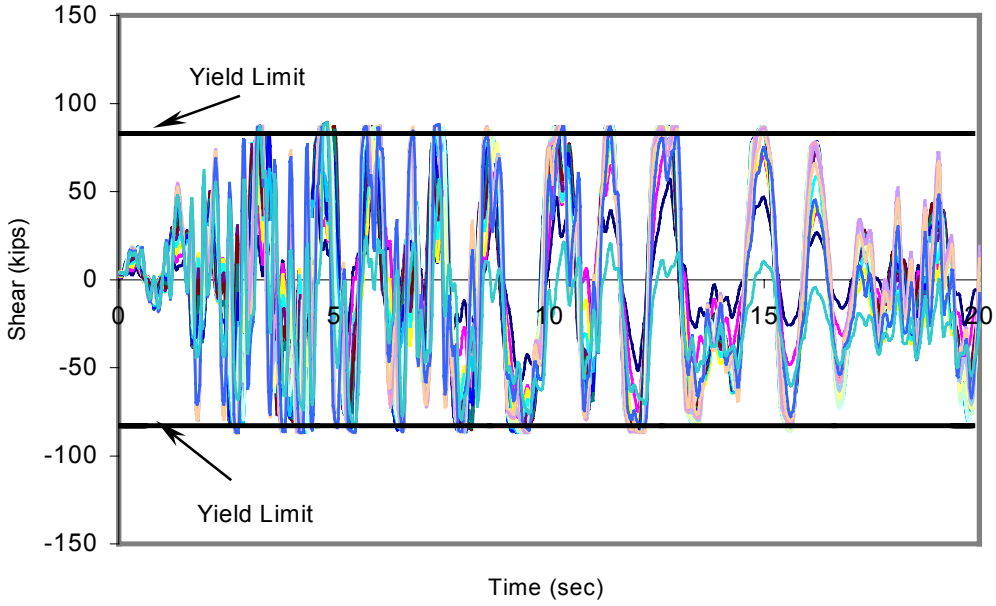

b) LA57

Figure 6.33 Coupling Beam Shear Force History along Time in HCW-18-30

6.7.9 Stiff Behavior of HCW-18-30

As discussed in section 6.7.7.2, HCW-18-30 exhibits significantly less inelastic deformations compared to HCW-12-30. In particular, rotational demand on the walls in HCW-18-30 is significantly less than that of HCW-12-30 although the design procedures are essentially the same. Elastic fundamental period of both 18-story and 12-story wall are 1.0 and 0.84 second respectively indicating that both systems have close dynamic characteristics prior to coupling beam yielding. The design spectral accelerations for both systems, and hence the design base shear, are proportional to the fundamental periods of the elastic systems (i.e. prior to the coupling beam yielding). This resulted in spectral acceleration equal to 0.7g and 0.9g for the 18-story and 12-story system respectively. However, immediately after the coupling beams yield, eign value analyses of both buildings result in fundamental periods of 2.5 and 1.3 seconds corresponding to spectral accelerations of 0.3g and 0.58g for the 18-story and 12-story building respectively. It follows that calculating the base shear of both systems based on the elastic fundamental period results in over-designed walls. Since the reduction in fundamental period due to coupling beam yielding is more dramatic in the 18-story building, this system shows even stronger and stiffer response.

In order to better understand the stiff response of HCW-18-30 compared to HCW-12-30, moment profiles were plotted along the height for both systems for all 2/50 earthquake records and the moment profiles were captured at the instance of maximum bending moment at the base of LSW. Figure 6.34a and 6.34b show both groups of plots. Moment profiles for the 12-story system indicate a response dominated by the first mode (cantilever shape). The 18-story system on the other hand, exhibits moment profiles that are affected by the higher modes.

Strain distributions at the same instances of maximum moments were plotted for both systems as shown in Figure 6.34c and 6.34d; their medians are also shown in Figure 6.34e. The following observations can be made:

- Strain profiles are not linear as conventionally assumed by design interaction equations. The steel strains are significantly less than those predicted by section analysis.
- For HCW-18-30, a check of the amount of steel distributed along the web indicates that steel reinforcement is not much over that required by the interaction equation; only a 15% safety margin is made as shown in Figure 6.35. Reducing steel reinforcement at the web to 50% percent of this amount could cause the seismic demand (moment and axial force) to be exactly on the interaction curve with no safety margin but the reinforcement would not have been adequate to resist moments in the transverse direction.

In summary: a design with less reinforcement at the web could still have yielded acceptable wall rotations even though it might not satisfy the design interaction equation.

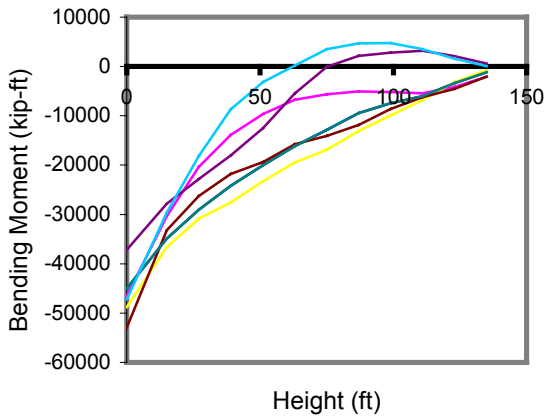

a) LSW/HCW-12-30 Moment (k-ft)

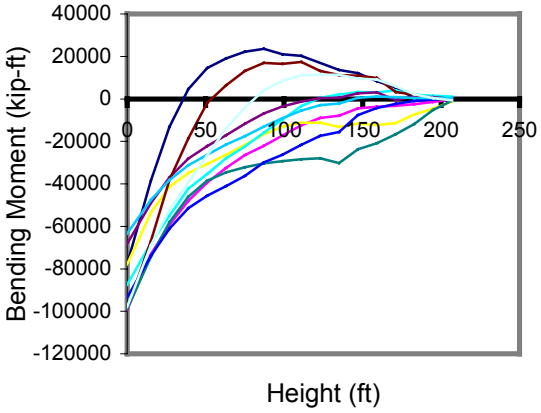

b) LSW/HCW-18-30 Moment (k-ft)

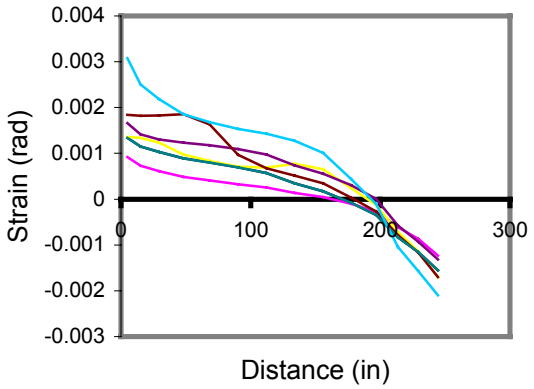

c) LSW/HCW-12-30 Normal Strain (rad)

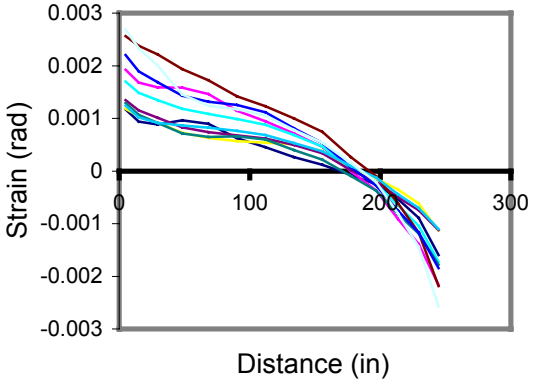

d) LSW/HCW-18-30 Normal Strain (rad)

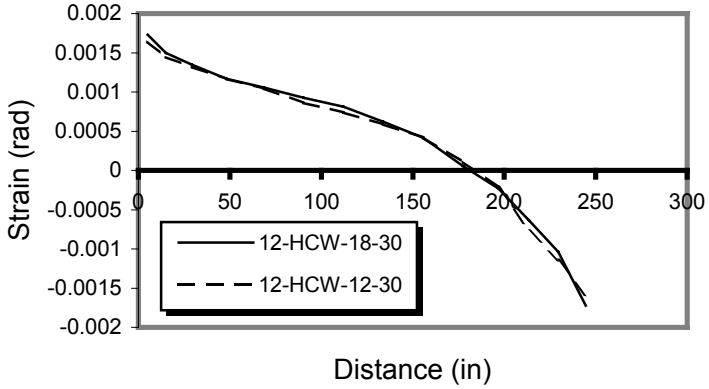

e) Median Normal Strain (rad)

Figure 6.34 Analysis of Moment and Strain Profiles for LSW/HCW-18-30

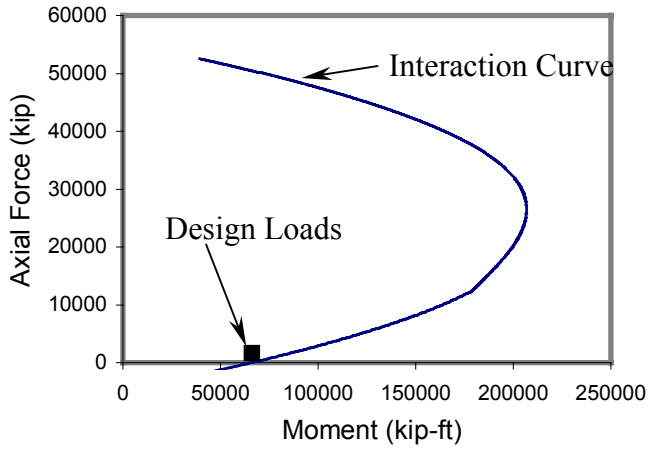

Figure 6.35 Interaction Diagram for LSW/HCW-12-30 at the Base

6.7.10 Deformed Shape

Deformed shapes of all three systems are plotted in Figures 6.36 through 6.38. These profiles were captured at a moment of maximum roof displacement for representative earthquakes. As in HCW-12-U, pure cantilever response can be observed. HCW-12-30 shows an inflection point in the lateral displacement at about 2/3 of the building, above which the walls rotate as rigid bodies. Rotations of the coupling beams are affected by this behavior where the coupling beams in the top 1/3 of the building have almost the same rotation. In HCW18-30, coupling beam rotations continue to increase with height along the entire height of the building. Magnified view of the lower part of the wall (Figure 6.39) shows the effect of floor diaphragm on the deformed shape. The diaphragm restrains the wall tendency for lateral expansion or contraction at the floor levels. This behavior of the floor diaphragm prevents the transverse reinforcement from reaching the yield stress. The diaphragm affects the shear strength of the wall by simulating a shear tie with infinite cross sectional area. However, removing the floor diaphragm completely to avoid such behavior resulted in an unstable system and no convergence

could be attained. Furthermore, this is not a realistic representation of the situation, since a large slab does exist at every floor level. A more comprehensive analysis would also include the slab in the model, but this would result in an intracable finite element solution. The magnified shape also shows that horizontal mesh lines do not remain straight and hence, the traditional assumption that the plane remains plane is not valid for shear walls with such dimensions. Therefore, use of a frame element to represent the wall might lead to inaccurate results.

6.7.11 Crack Patterns

Crack patterns are captured for the three systems at 100 time step intervals. For further reference, the pictures of the cracks are plotted in Appendix B Figures B16 through B45. Cracks start at the boundaries of the walls where tension occurs and then spread over the wall height. Cracks for the 18-story system at the middle of the wall have a tendency to close after the strong motion duration is past while for the other systems, cracks remain open even at the very end of the load duration

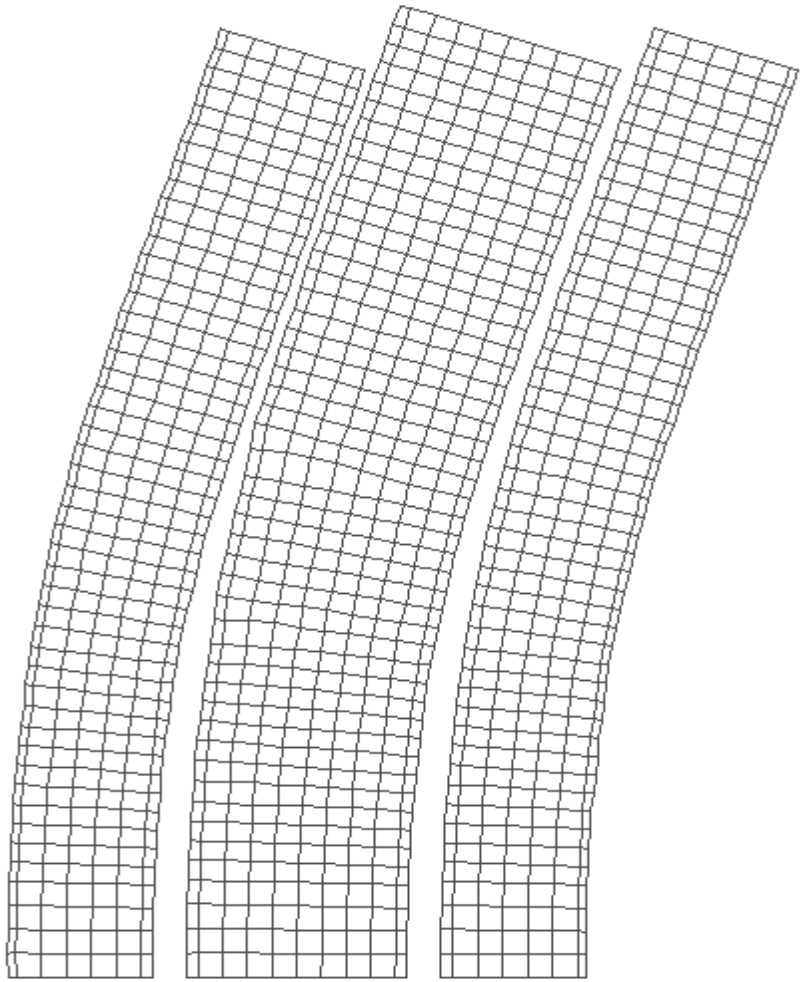

Figure 6.36 Deformed Shape at Time 5.9 second for Earthquake LA31 (HCW-12-U)

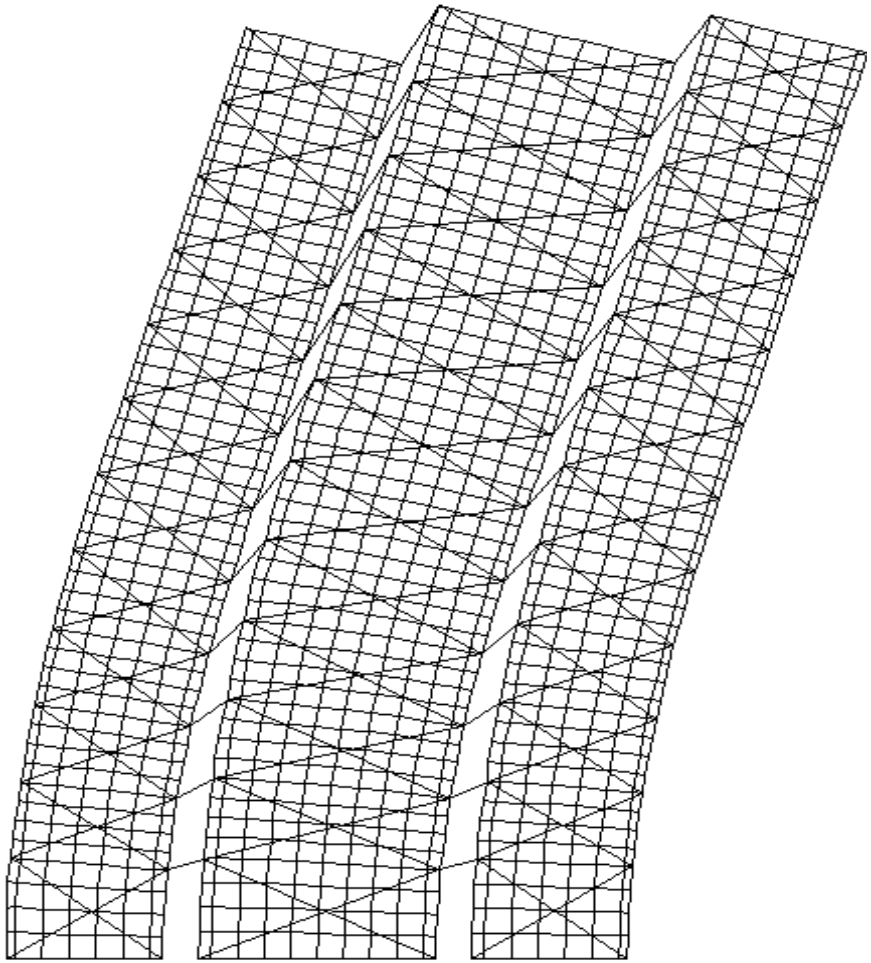

Figure 6.37 Deformed Shape at Time 5.9 second for Earthquake LA31 (HCW-12-30)

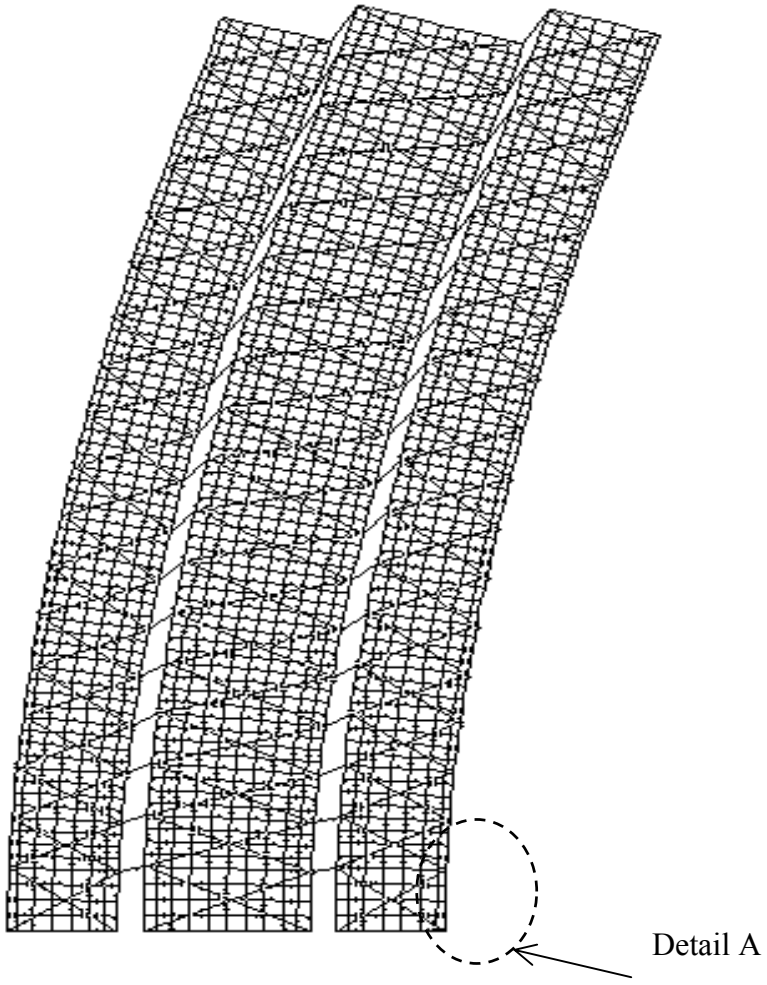

Figure 6.38 Deformed Shape at Time 4.05 second for Earthquake LA33 (HCW-18-30)

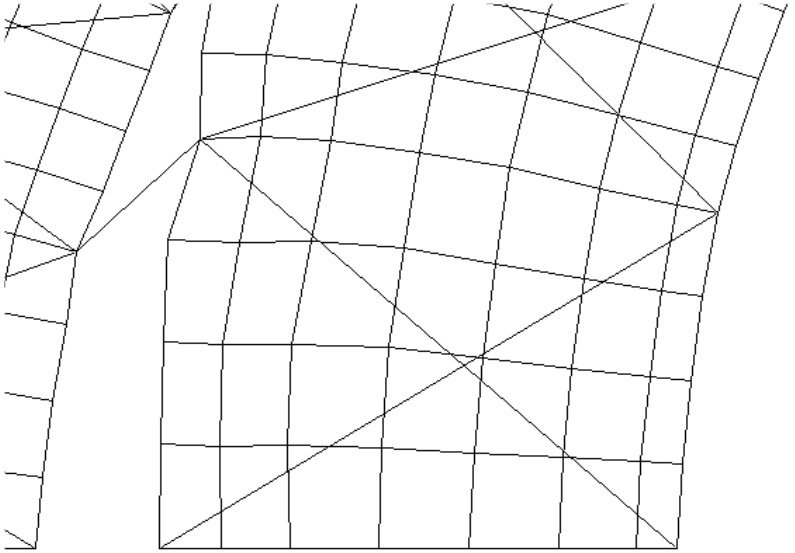

Figure 6.39 Magnified View for Detail “A”

6.8 Rational Method for Computing Shear Magnification Factor

Equation 6.19 proposed by Paulay and Priestley (1992) is used to predict the magnification in base shear due to dynamic effects. Although the equation yields fair results for the two cases considered in this work, it must be kept in mind that it's a function only in the number of stories and does not reflect the dynamic characteristics of the structural system. Hence, the equation may not always result in accurate estimates of the base shear magnification factor. A rational yet simple analysis is proposed in this section to estimate the effect of higher modes on base shear.

A simple example was discussed in Chapter 3, where a cantilever of a total height of 10 ft with distributed mass along the height was analyzed twice; once with a fixed base condition and the second time with hinged base condition. The example demonstrates the effect of higher modes (2^{nd} mode) on the calculation of base shear. The same technique is applied to the HCW system. The system is solved on two increments. In the first increment, the system attracts total base shear equals to its plastic capacity, V_p. This value is obtained directly from the pushover analysis but it can also be obtained using other analytical techniques such as fiber analysis considering the actual flexural reinforcement of the walls. In the second increment, a hinge (plastic hinge) is assumed to form at the wall base and all the coupling beams are assumed to have yielded. The plastic hinge is simulated by reducing the modulus of elasticity of the elements of the 1^{st} story to 1%, 0.1%, 0.01% and 0.001% of the elastic modulus, to study the effect of residual stiffness on response. The shear stiffness of the first floor is retained by using fictitious braces that have axial stiffness computed such that the shear stiffness provided by the braces equals to the shear stiffness of the cracked concrete in the first floor. Linear elastic analyses are

performed on the softened models. A modal combination for both first and second mode is performed to compute the total base shear of the system with different degrees of stiffnesses.

The results of modal combination are presented in Tables 6.11, 6.12 and 6.13. The structural periods for both modes are calculated and the spectral acceleration is obtained from the response spectrum derived at the building site as explained in Chapter 3.

The Base story forces at different story levels for every mode is computed using the following expression (Chopra, 1995):

$$f_n = \Gamma_n \begin{Bmatrix} m_1\ \phi_{1,n} \\ m_2\ \phi_{2,n} \\ .... \\ mi\ \phi_{i,n} \\ .... \\ m_{18}\ \phi_{18,n} \end{Bmatrix} A_n \qquad (6.25)$$

Where:

f_n is the force vector corresponding to mode n

$m_1, m_2, \ldots, m_{18}$ are the masses at floor levels

$\{\phi_{1,n}, \phi_{2,n}, \ldots, \phi_{18,n}\}$ is the modal shape vector of mode n

A_n is the spectral acceleration corresponding to the first mode and obtained from the response spectrum curve.

$$\Gamma_n = \frac{L_n^h}{M_n} \qquad (6.26)$$

$$L_n^h = \sum_{i=1}^{N} m_i\, \phi_{i,n} \qquad (6.27)$$

$$M_n = \sum_{i=1}^{N} m_i\, \phi_{i,n}^2 \qquad (6.28)$$

Where n denotes the n^{th} mode and N denotes the number of degrees of freedom of the structure, 18 in this case.

Following computing the story forces of mode *n*, the total base shear is calculated by adding all the story forces:

$$V_{(base)_n} = \sum_{i=1}^{N} f_{i,n} \tag{6.29}$$

The modal base shears are then combined together using the well-known SRSS method as following:

$$V_{(base)} = \sqrt{\sum_{i=1}^{n} V_{(base),n}^2} \tag{6.30}$$

In the current work only modes 1 and 2 are considered, i.e. n is equal 2.

Table 6.11 Modal Combinations for Base Shear in HCW-18-30 system softened at the base

Stiffness Reduction Factor	Vp	1%	0.10%	0.01%	0.001%
Mode		Spectral Acceleration (g)			
1		0.05	0.02	0.02	0.02
2		1.09	1.05	1.05	1.05
		Structural Period (sec)			
1		14.0	43.0	142.0	500.0
2		0.71	0.72	0.73	0.73
		Effective Weight1 (mg)			
1		13.9	13.6	13.6	13.6
2		2.4	2.3	2.3	2.3
		Base Shear2 (kips)			
1		0.039	0.015	0.015	0.015
2		0.145	0.136	0.136	0.136
Combined Base Shear	0.25	0.15	0.137	0.137	0.137
Magnification Factor		1.60	1.55	1.55	1.55

[1]m is the mass of one story
[2]Shear force is divided by the structure's total weight, W

Table 6.12 Modal Combinations for Base Shear in HCW-12-30 system softened at the base

Stiffness Reduction Factor	Vp	1%	0.10%	0.01%	0.001%
Mode		Spectral Acceleration (g)			
1		0.15	0.03	0.02	0.02
2		1.35	1.35	1.35	1.35
		Structural Period (sec)			
1		5.2	26.3	83.3	263.1
2		.34	.35	.35	.35
		Effective Weight1 (mg)			
1		9.05	9.1	9.1	9.1
2		1.78	1.78	1.78	1.78
		Base Shear2 (kips)			
1		0.075	0.015	0.016	0.01
2		0.134	0.134	0.134	0.134
Combined Base Shear	0.27	0.153	0.134	0.134	0.134
Magnification Factor		1.57	1.50	1.50	1.50

[1]m is the mass of one story

[2]Shear force is divided by the structure's total weight, W

Table 6.13 Modal Combinations for Base Shear in HCW-12-U system softened at the base

Stiffness Reduction Factor	Vp	1%	0.10%	0.01%	0.001%
Mode		Spectral Acceleration (g)			
1		0.18	0.03	0.02	0.02
2		1.35	1.35	1.35	1.35
		Structural Period (sec)			
1		4.1	23.8	76.9	238.1
2		.30	.30	.30	.30
		Effective Weight1 (mg)			
1		9.05	9.1	9.1	9.1
2		1.79	1.77	1.77	1.77
		Base Shear2 (kips)			
1		0.091	0.015	0.010	0.010
2		0.134	0.133	0.133	0.133
Combined Base Shear	0.23	0.161	0.134	0.133	0.133
Magnification Factor		1.70	1.58	1.58	1.58

[1]m is the mass of one story

[2]Shear force is divided by the structure's total weight, W

For HCW-18-30, the Shear magnification obtained for the case of 1% stiffness reduction factor and less yields almost the same magnification from the dynamic analysis (1.60 from the proposed method vs.1.55 from dynamic analysis). For HCW-12-30, modal combination yields a factor of 1.57 vs. 1.44 from dynamic analysis and for HCW-12-30, the values are 1.7 from modal combination vs. 1.87 from dynamic analysis.

Better estimation for the shear magnification factor is obtained from the modal combination than that of the thump suggested by equation 6.19, which yields a factor of 1.8 for HCW-18-30 and 1.7 for both HCW-12-30 and HCW-12-U.

The proposed technique for shear magnification takes into account the real dynamic characteristics of the system in terms of structural period, height of building, distribution of mass along the building height and the strain hardening characteristics of the system.

6.9 Limitation of FEMA-368 on Building Height

FEMA-368 sets a height limit of 160 ft for special reinforced concrete shear wall structures (Table5.2.2, FEMA-368, 2000). This height limitation is ignored in the design process and a reduction factor for seismic demand R, is taken as 5.0. The limits set by FEMA-368 on height were intended for RC shear wall systems. Since the coupled wall system shows fundamentally different behavior in terms of strength, stiffness and energy dissipation capacity, the height limitation is not directly applicable to the coupled wall systems. The results from the system analysis suggest that it can serve as the sole lateral system in buildings with heights beyond the 160 ft limit and still shows acceptable performance.

6.10 Evaluation of the Capacity Design Method

The Capacity design method (proposed by El-Tawil et al (2002a) is discussed in details in Chapter 3. The basic assumption of the method is that all coupling beams yield early enough before the flexural reinforcement in the walls reaches the yield point, i.e. all the beams are assumed to reach their capacities prior to formation of plastic hinge in the walls. This assumption is attractive to designers because it eliminates the need for a lengthy iterative design procedure to size the coupling beams. In addition to that, the coupling ratio becomes a parameter that the engineer can have control over. Furthermore, all coupling beams can be designed to have the same size, which is convenient for both detailing and construction.

The method was proposed based on the observation made by El-Tawil et al (2001a) that in pushover analysis of a 12 story coupled system, all the coupling beams reached the yield limit early. However, they reported that the method is not directly applicable to system with significant higher mode effect.

Higher mode effects are investigated for both 12 and 18-story systems. It is found that the major effect of higher modes is that they cause significant base shear magnification. However, the roof displacement demand on the systems predicted by the pushover analysis is reasonably close to the one predicted by the dynamic analysis (variation is less than 11%). Since the pushover analysis shows the effect of first mode only, it could be concluded that computing the displacement demand based on first mode can be reasonable.

Considering the deformed shape of a coupling beam as shown in figure 6.30, the rotation of the coupling beam increases with the increase of the roof drift demand on the wall and vice versa. Figure 6.33a shows that all coupling beams reach the yield limit often along the time

history analysis for an average 2/50 record implying that the deformational demands in the walls are enough to mobilize the forces in them most of the time.

The only situation that can arise up and hinder the coupling beams from reaching the yield point is when the displacement profile is totally dominated by higher modes during the time history. Even if such assumption is present, the overturning moment at the base reaches its maximum when floor forces are monotonically increasing along the height, which indirectly endorses a first mode profile Hence coupling beams are expected to be fully mobilized when first mode dominates and the overturning moment is maximum. Hence the capacity design method proposed by El-Tawil et al (2002a) is reasonable for mid rise systems such as those considered in this dissertation.

6.11 Summary

Dynamic time history analyses are conducted on three systems; a 12-story systems with zero coupling and another with 30% coupling as well as one an 18-story system with 30% coupling. Two sets of earthquake records were used with 2/50 and 50/50 hazard levels; each set contains ten ground motions. Different scaling techniques were examined to obtain results with less dispersion. Data extracted from analyses includes floor displacement, wall rotations along the height; shear distortion, coupling beam rotation and other deformation response parameters. Shear forces, bending moments are also extracted to evaluate the inelastic demand against the design loads. Demands from time history analysis are compared to those obtained from pushover analysis to evaluate the validity of the static pushover procedures with different building heights.

The performance of the systems is evaluated against the acceptance criteria of FEMA-356 provision for seismic rehabilitation of existing buildings for the strong ground motion

represented by the 2/50 records and the moderate and more frequent motions represented by the 50/50 records. The guidelines provided by FEMA-368 for the design of new buildings are discussed in light of the results obtained from the dynamic time history analyses. The height limitation of FEMA-368 on special concrete shear walls is discussed and the difference in behavior between isolated shear walls and coupled wall system is pointed out. The applicability of the displacement amplification factor as defined be FEMA-368 to the displacements resulting from the capacity design method proposed by El-Tawil et al is evaluated and alternative simplified technique is suggested.

The rationale behind the dynamic shear magnification is explained and the shortcoming of the equation given by Paulay and Priestly is discussed. An alternative rational analysis is suggested to estimate shear magnification factor that takes into account the dynamic characteristics of the system is proposed. Finally, the capacity design method for coupling beams is discussed and its validity is examined in light of the dynamic analysis results.

CHAPTER 7: SUMMARY, CONCLUSIONS AND RECOMMENDATION FOR FUTURE WORK

7.1 Summary

The objective of this work has been to investigate the inelastic response of hybrid coupled wall systems subjected to ground shaking. The prototype theme structure used in the study is based upon plans developed for the US-Japan cooperative research program. A thorough review of previous related work was conducted. In the previous study, the performance of systems with different heights and different coupling ratios was investigated using static pushover analysis. Since pushover nonlinear analysis does not represent true dynamic characteristics of seismic loading such as frequency content and strong motion duration, nor does it capture the effect of higher modes on structural behavior, it was decided to conduct dynamic analysis on systems with selected coupling ratios and heights. Based on observation reported in the previous study, buildings with 12 and 18 stories with coupling ratio of 30% were considered in addition to an uncoupled 12-story system, which served as a reference line for comparison.

Seismic loads on the buildings were determined in accordance with procedures prescribed in FEMA-368 (2000) and system design was carried out in accordance to provisions of ACI-318 (2002) for the concrete walls and AISC-LRFD (2002) for the steel coupling beam. PCI Guidelines were used to compute the necessary embedment of the coupling beams into the concrete walls.

A simple, but robust constitutive model for concrete was developed and implemented a s user-define module in DIANA (2000). The model works well in spite of the random load reversal associated with seismic loading. The model accounts for all major aspect of nonlinear behavior such as cracking, tension stiffening, and compression behavior for both confined and unconfined concrete. Shear behavior is accounted for by constantly updating shear stiffness according to the status of cracking in concrete. The model is validated by comparing analysis results to previously published test results and is found to be satisfactory.

Since large computational demand associated with time history analysis impose limitation on the finite element model size, it was necessary to create a coarse yet sufficiently accurate finite element model. The concept of effective flange width is utilized such that the effective flange width is represented by a single plane stress element and the reinforcement within that effective width is represented by bar (truss) elements. A parametric study is conducted to specify the effective width of tension flange subjected to various levels of axial load. Both 6- and 12-story walls are considered in the study. The findings of the study were then implemented in the finite element model resulting in a dramatic reduction in its size.

The inelastic dynamic behavior of HCW systems is investigated using transient finite element analyses of the developed models. Designs of a 12-story uncoupled system, a 12-story HCW system with 30% coupling as well as an 18-story coupled system with 30% coupling are used in the investigation. Sixty transient analyses are conducted to investigate a variety of parameters including hazard level, earthquake record scaling, dynamic shear magnification, interstory drift, shear distortion, coupling beam rotation, and wall rotation. Performance measures calculated from the parametric analyses are compared to corresponding pushover

results and examined for evidence of behavioral trends. A number or conclusions can be drawn based on this limited study.

7.2 Conclusions

Conclusions drawn from this research effort are summarized as follows:

7.2.1 Finite Element Analysis and Constitutive Modeling

- Simplified and robust constitutive modeling can adequately represent concrete behavior subjected to highly random load reversals that occur during dynamic analysis.
- Separation of shear stiffness properties from normal stiffness properties especially when significant shear distortions are expected to occur could prevent premature concrete crushing. Constitutive models that apply a reduction factor to the shear stiffness while tying both properties together may not realistically represent true shear deformation. A comparison between the shear distortions obtained from the model used in this study and the built-in model of DIANA (which ties both properties together) shows that the used model agrees better with experimental results.

7.2.2 Effective Width of Tension Flanges

- Comparisons between the numerical results and ACI-318 specifications indicate that the ACI provisions do not accurately specify the tension flange effective width, especially in the presence of compressive axial load. Another issue with the ACI provisions is that the effective width is tied to wall height and not wall length, even though wall length is a more influential variable. Although a calibration based on wall height is certainly reasonable and acceptable if wall length is proportional to wall height, in many cases such a predetermined relationship between height and length cannot always be assumed. Another drawback of the current fixed effective width provisions is that they cannot be used for an accurate evaluation of structural behavior at a specific drift level as required in performance-based design.
- Design criteria that are a function of wall length, drift, and axial force level are proposed for determining the tension flange effective width. Although more complicated than the current criteria in ACI-318, the proposed specifications are more reasonable in that they account for the effect of important variables and are suitable for implementation in performance-based design codes. Extensive analytical and experimental studies are still needed to confirm and refine the proposed criteria
- Walls Subjected to Tension: It is recommended that the flange be taken as fully effective regardless of the wall and flange dimensions.
- Walls Subjected to Pure Flexure: It is recommended that: for 0.5% drift use an overhanging effective width of 0.9.d; for 1% drift use 1.5.d; and for 2% drift use 2.0.d.

- Walls Subject to Gravity Compression: The recommended effective width is: for 0.5% drift use an overhanging effective width of 0.6.d; for 1% drift use 0.95.d; and for 2% drift use 1.15.d.

7.2.3 Inelastic Behavior of HCW Systems

- Hybrid coupled wall systems are particularly well suited for use in regions of high seismic risk. For the 12-story system, compared to cantilever RC walls, the coupled walls considered in this study had lower roof drifts (median 25.4 in versus 18.6 in), interstory drifts, and wall rotations. Maximum shear distortions were quite low and the coupling beams had plenty of reserve plastic rotation capacity for the 2/50 hazard level (median demand was 0.07 versus the FEMA-356 limit for shear links of 0.15). The maximum dynamic base shear magnification was also considerably lower (44% versus 87%).
- This study supports Shome et al's (1997) suggestion that record scaling does not significantly influence the median. However, it is observed that while scaling considerably reduced dispersion in the response parameters of the 50/50 cases, it did not significantly reduce dispersion in the 2/50 runs.
- Records scaled at the fundamental period of the structure (T_1) result in more roof displacement than the records scaled at the period of the structure after coupling beams have yielded (T_u). Therefore, use of records scaled at T_1 can yield more conservative results.
- Although the pushover procedure in FEMA-356 managed to compare well to the median dynamic results in some cases, there were several instances where discrepancies were observed. For example, in the 12-story system, the interstory drift

ratio from the pushover analysis (1%) is about 30% less than the median value from the dynamic runs (1.43%). More disturbing is that fact that some of the records produced interstory drift demands that significantly exceeded the median value. It is clear that a probabilistic approach similar to that used in FEMA-350 (2000) for steel frames is needed for hybrid wall systems.

- The normal strain distribution along the wall base suggests that the design assumption that a plane cross section remains plane after deformation is not appropriate for walls of dimensions similar to those considered in the study. The flexural reinforcement does not reach the strain levels predicted by the design procedures as prescribed by the design codes (the flexure-axial interaction diagram).
- The behavior of the 18-story system is considerably stiffer compared to the 12-story system. For example, the maximum base rotation for HCW-18-30 is 52% of that of HCW-12-30, although the design procedures are the same for both buildings. A comparison between moment profiles of both systems indicates that the tendency for deforming in double curvature is more obvious in the case of the 18-story building. The linear static procedure based on the first mode cannot reflect such behavior.
- FEMA-368 pushover procedure dramatically overestimates the base rotation demand for the 18-story building compared to the time history analysis. Comparisons between the displacement profiles for both procedures indicate that the higher mode effects in the 18-story building cannot be ignored.
- The capacity design method assumption that all coupling beams yield before the yield of flexural reinforcement in walls seems to be valid for both 12 and 18-story systems. Although the displacement profile of the 18-story systems suggests that the wall can

deform in double curvature and hence decrease the rotation demand on the coupling beams, it is observed that the coupling beams reach their yield point all the time along ground motion duration.

- Estimation of shear magnification based on the rule-of-thumb suggested by Paulay and Priestly does not reflect the true dynamic characteristics of the building. A proposed rational method to estimate the magnification factor seems to yield reasonable answer compared to the results obtained from the time history analysis.
- Although FEMA-368 sets limits on building height for special reinforced concrete shear wall building of 160 ft, this limit does not seem appropriate for the hybrid coupled wall system. The 18-story system, being 219 ft high, shows sufficient strength, stiffness as well energy dissipation capacity.
- Story drifts do not represent the true extent of nonlinear deformations in the walls considered in this study since flexural deformations dominates the wall behavior. Rather, adopting shear distortions as deformation measure is more realistic.

7.3 Recommendation for Future Work

This research effort was primarily dedicated to investigate the behavior of HCW systems under dynamic loading. In light of observations and findings obtained from this research, the following research areas are worthy of further investigation:

- Investigate the validity of the capacity design method in taller systems with more than 30 stories
- Investigate the effect of low cycle fatigue on the strength and ductility capacity of coupling beams due to frequent ground shaking of 50/50 probability of exceedance.

- For evaluating the performance of HCW systems and RC shear wall system in general, a probabilistic approach similar to that used in FEMA-350 (2000) for steel frames is needed rather than the deterministic approach in FEMA-356.
- Development of a comprehensive displacement-based design procedure for wall sections subjected to combined axial and bending taking into account the nonlinear normal strain distribution along the wall system rather than the current prevailing assumption that strain distributions are linear.
- Development of comprehensive analytical procedure based on modal combination to compute the shear magnification factor. The procedure suggested in section 6.8 needs further refinement to assume realistic material properties at the hinge region. In addition, factors such as loading history and strength degradation due to cyclic loading needs be considered.
- The pushover procedure of FEMA-356 needs further refinement to reflect the effect of higher modes on mid-rise and taller buildings. Incremental nonlinear modal analysis procedure is needed in order to simulate the constant change in building dynamic characteristics due to material nonlinearity.
- Investigate the effect of elastic foundation on the stiffness characteristics of HCW systems.
- Investigate the validity of the prevailing assumption that floor slabs constitutes perfectly rigid diaphragms. Such study will take into account the true material and geometric properties of floor slabs and incorporate them into the finite element model.

APPENDIX A: PCA WALLS: TEST RESULTS VS. ANALYTICAL RESULTS

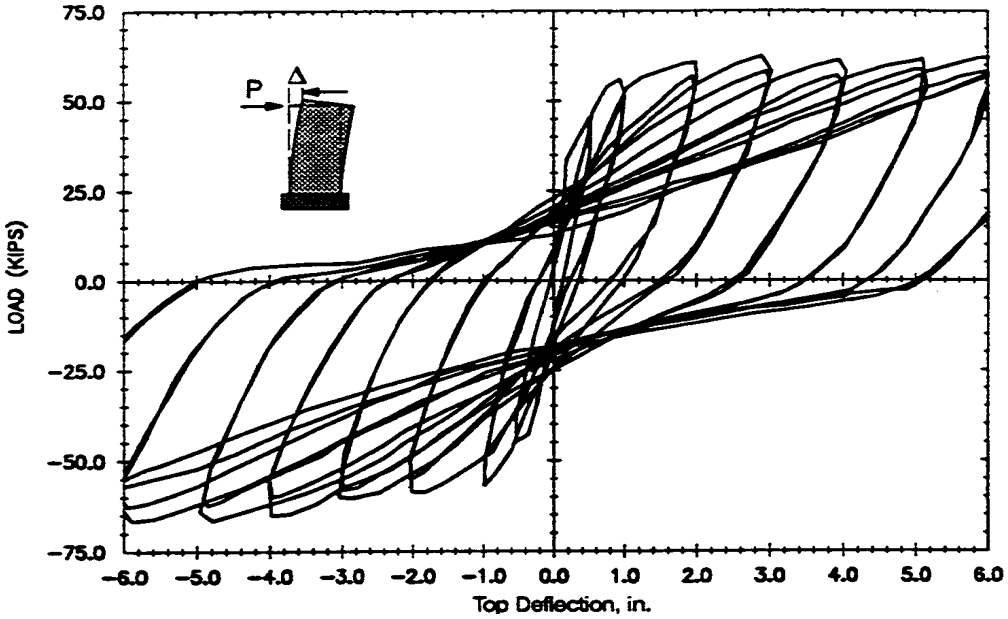

a) Experimental Result

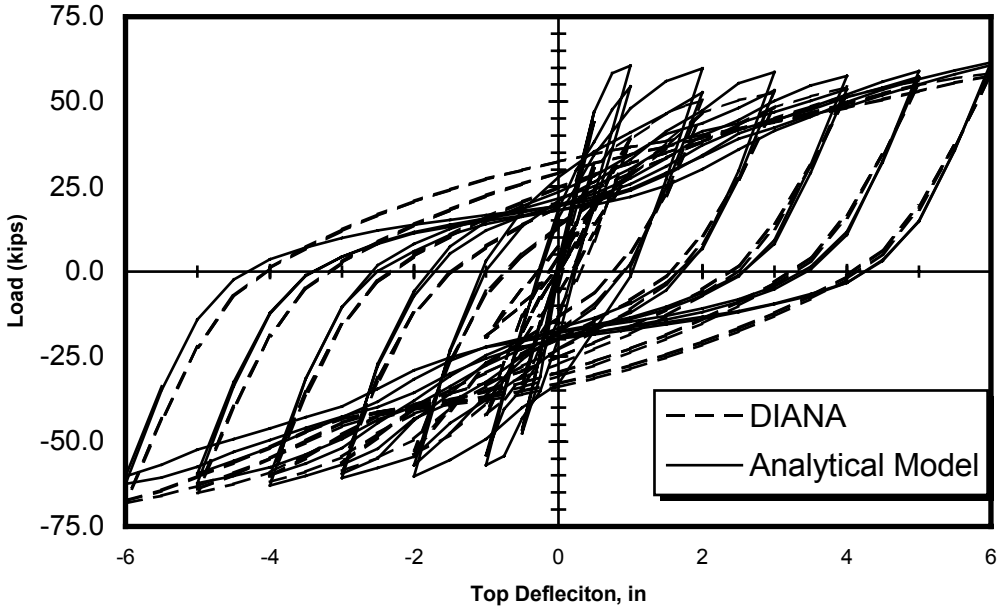

b) Analytical Result

Figure A.1 Load vs. Displacement Comparison for Wall B3

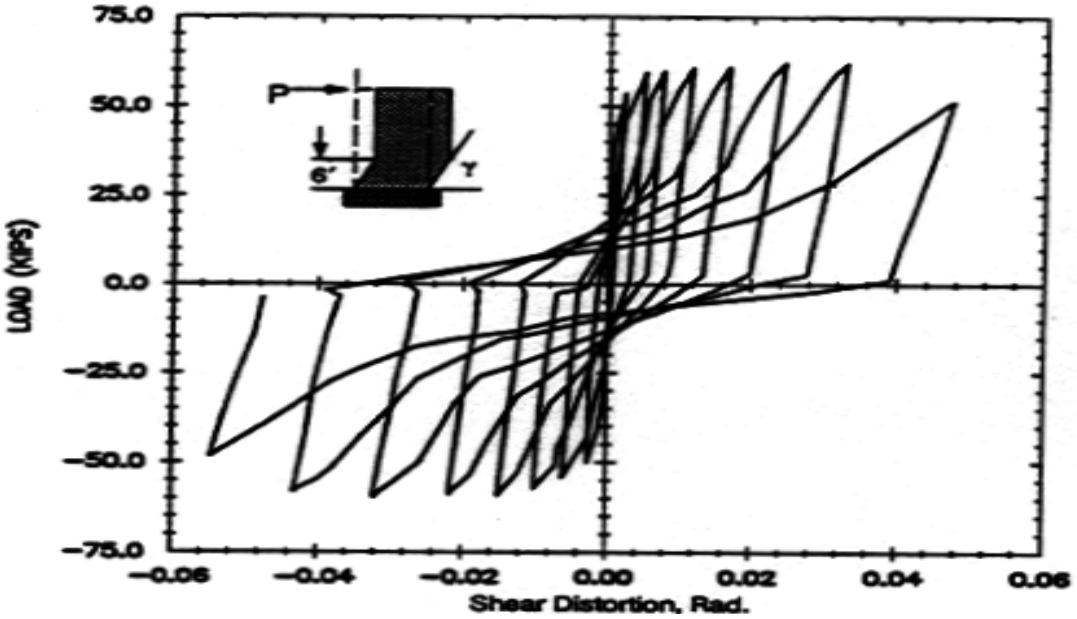

a) Experimental Result

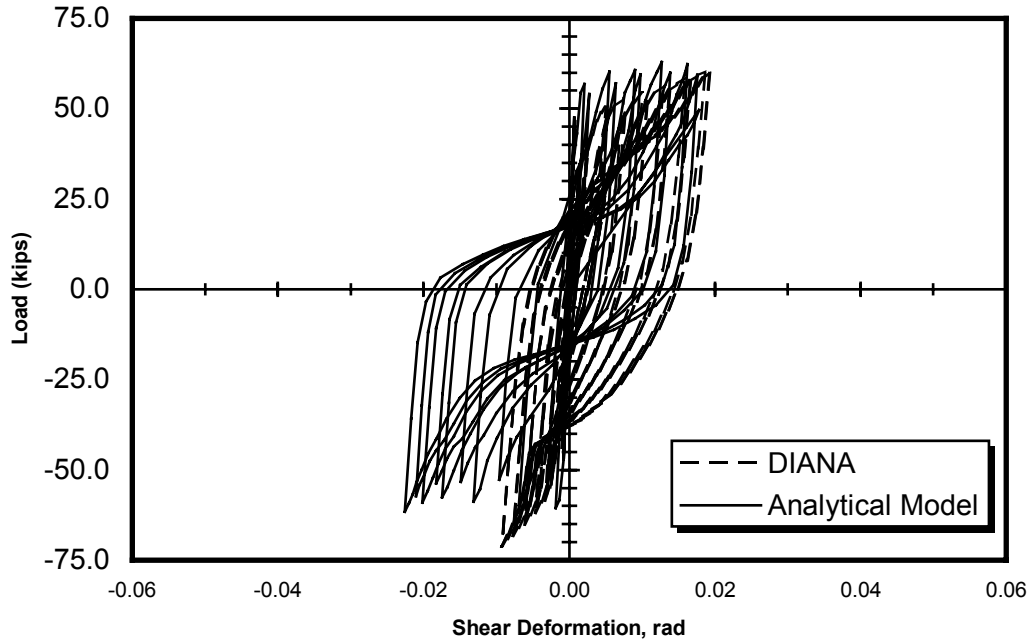

b) Analytical Result

Figure A.2 Load vs. Shear Distortion Comparison for Wall B3

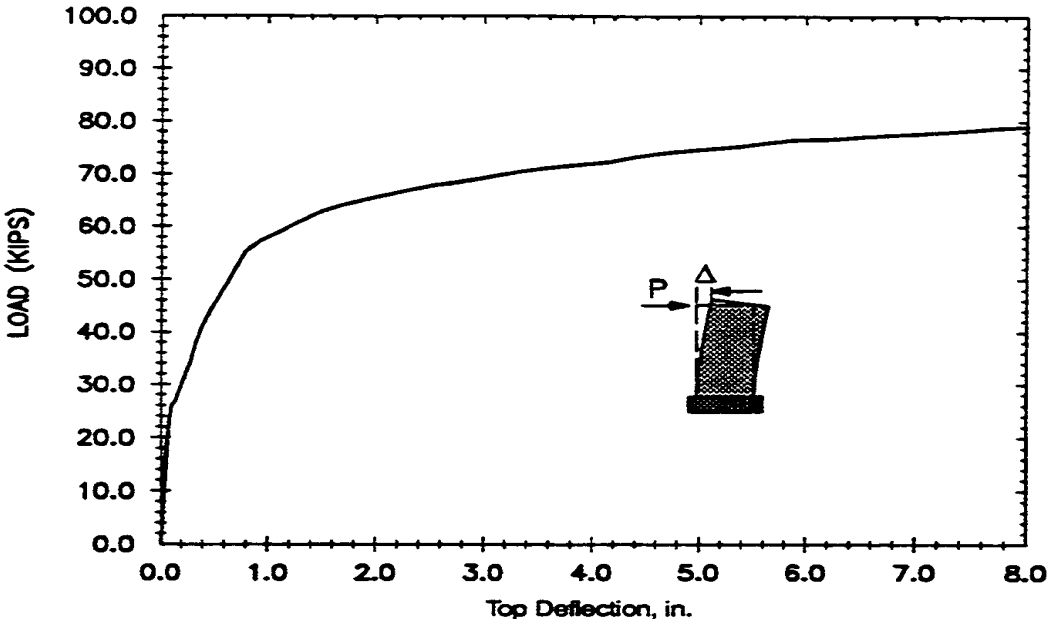

a) Experimental Result

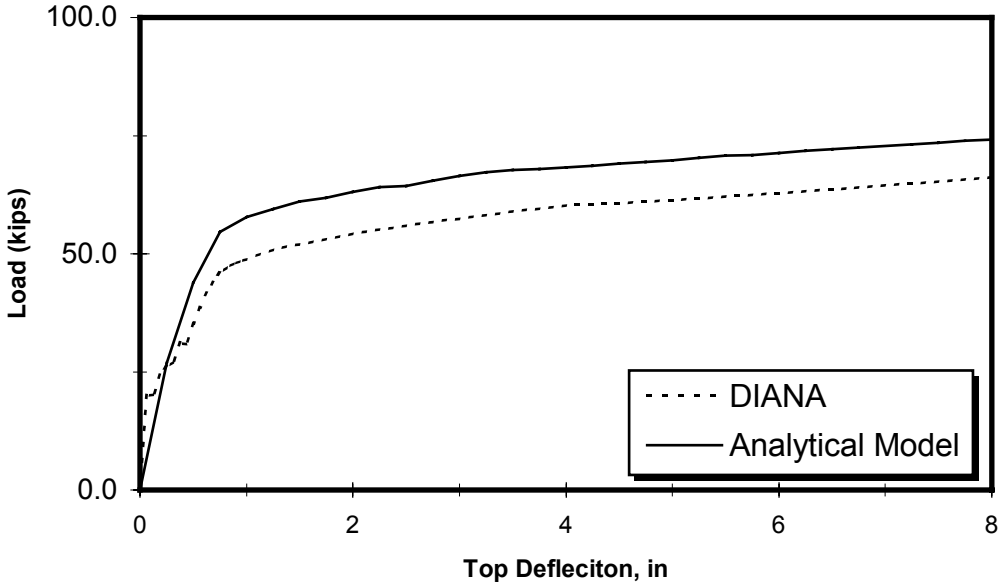

b) Analytical Result

Figure A.3 Load vs. Displacement Comparison for Wall B4

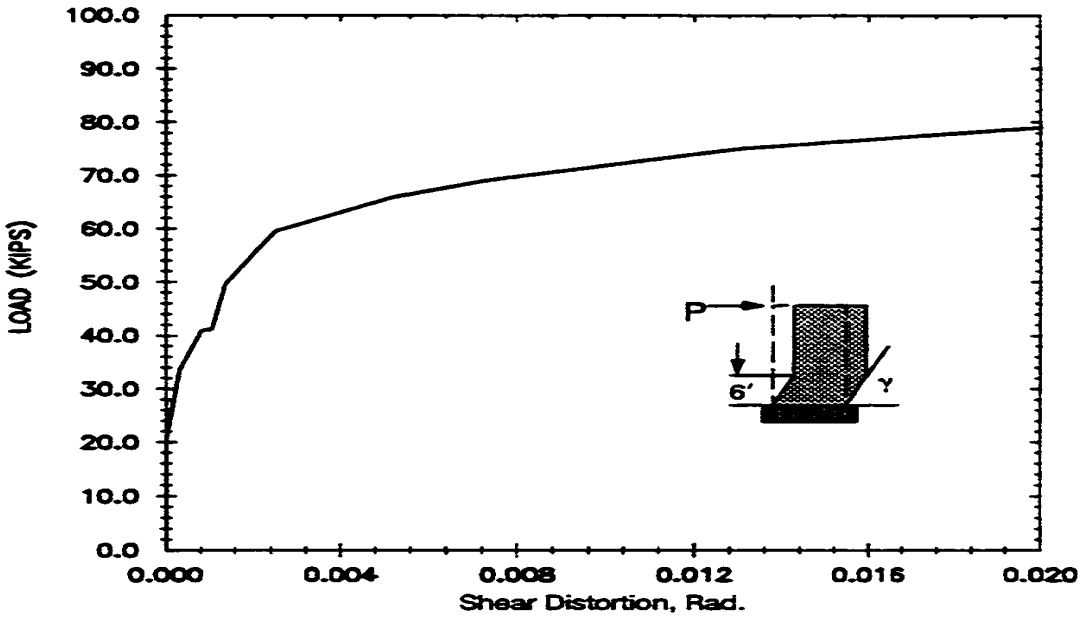

a) Experimental Result

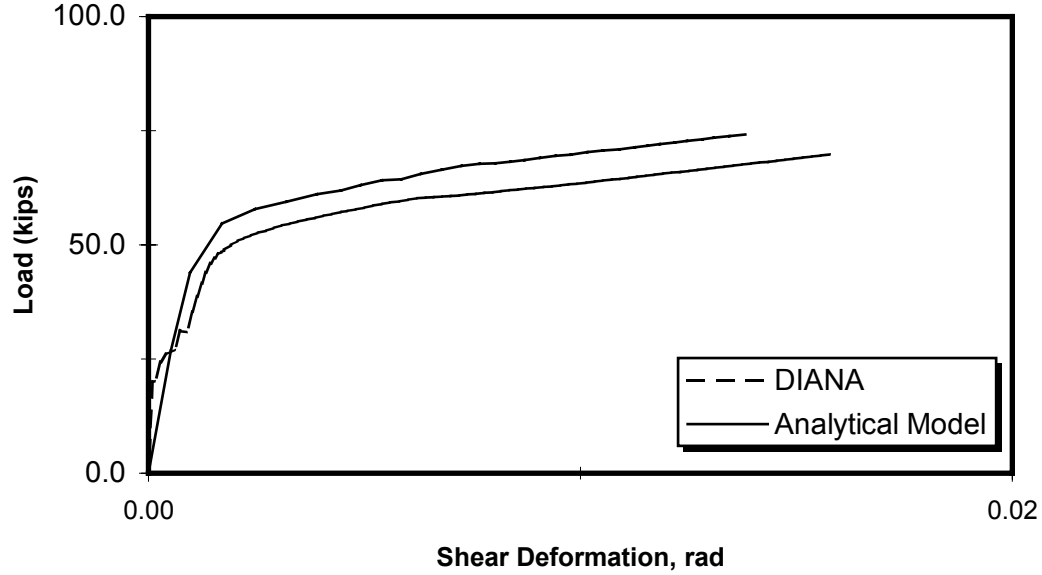

b) Analytical Result

Figure A.4 Load vs. Shear Distortion Comparison for Wall B4

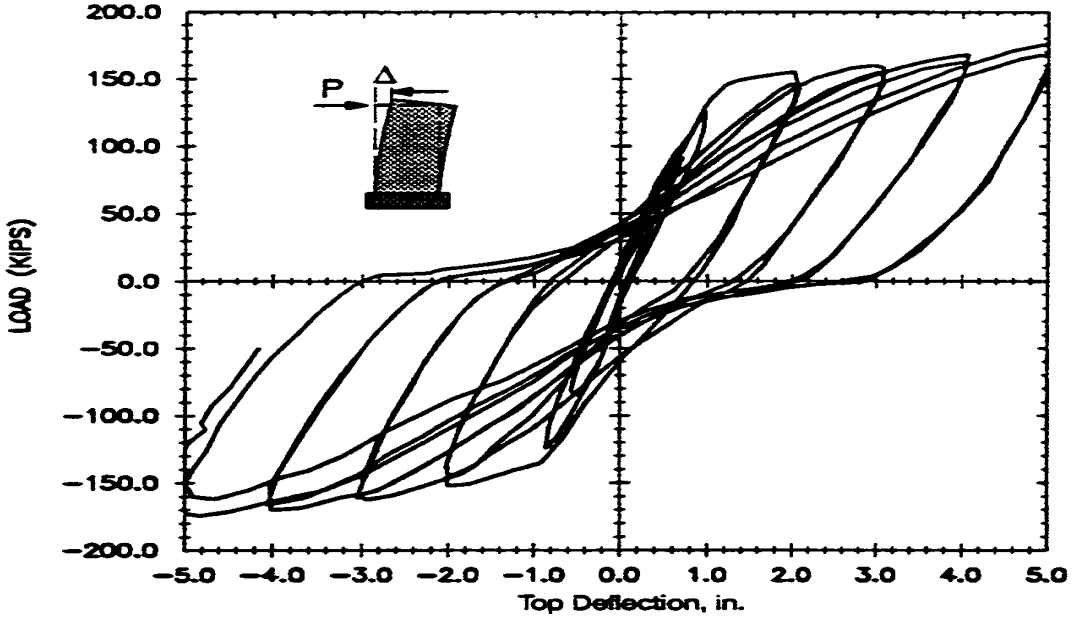

a) Experimental Result

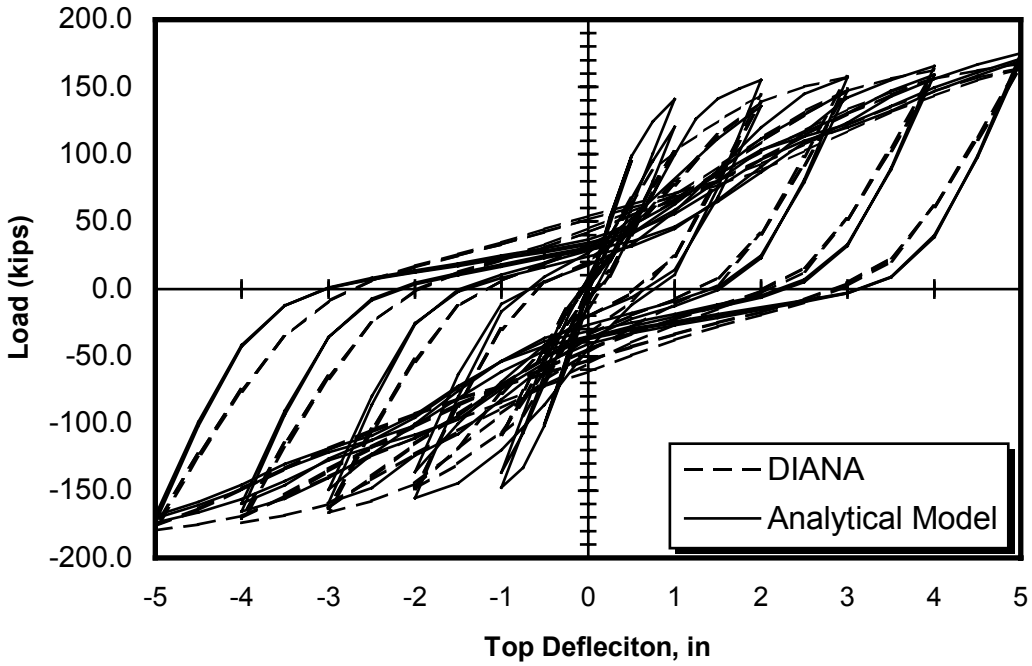

b) Analytical Result

Figure A.5 Load vs. Displacement Comparison for Wall B5

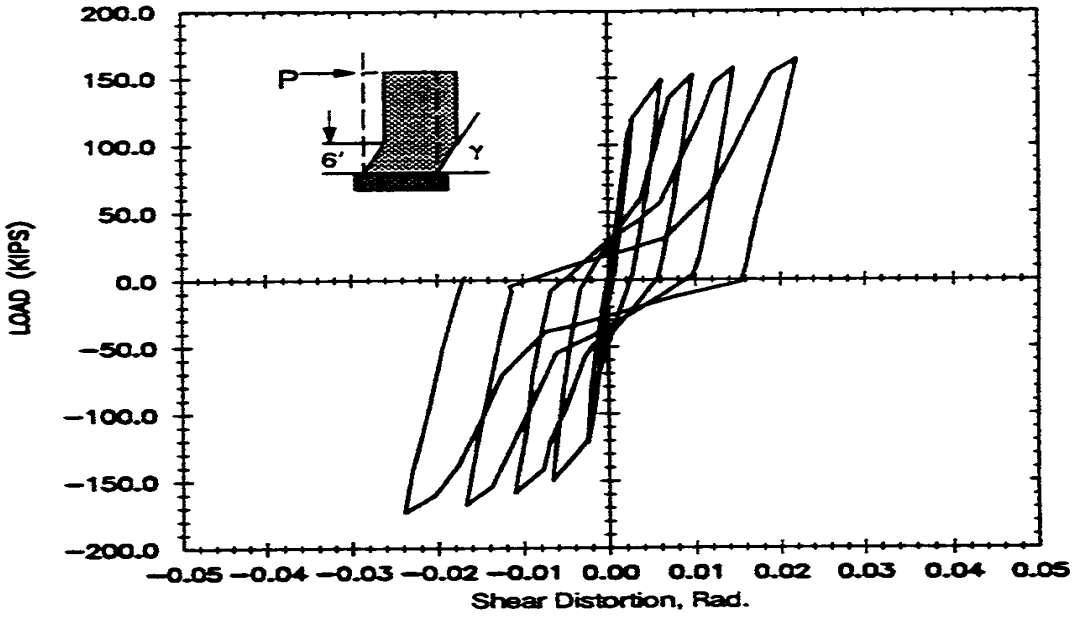

a) Experimental Result

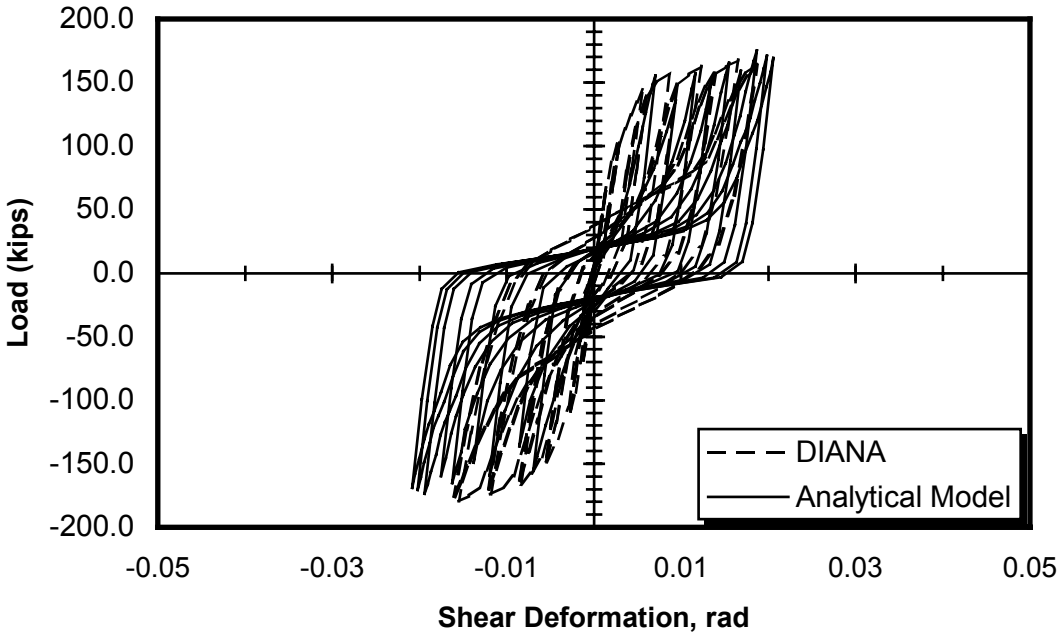

b) Analytical Result

Figure A.6 Load vs. Shear Distortion Comparison for Wall B5

APPENDIX B: SELECTED OUTPUT FROM TIME HISTORY ANALYSIS

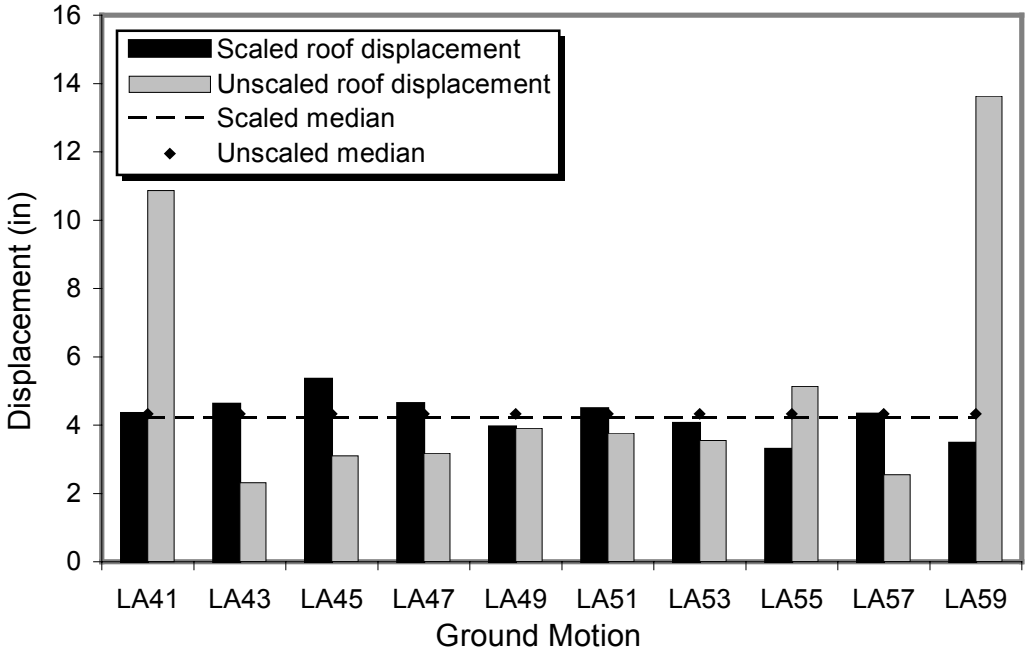

Figure B1 Maximum Roof Displacement in HCW-12-30 for Scaled and Unscaled Records for 50/50 Records.

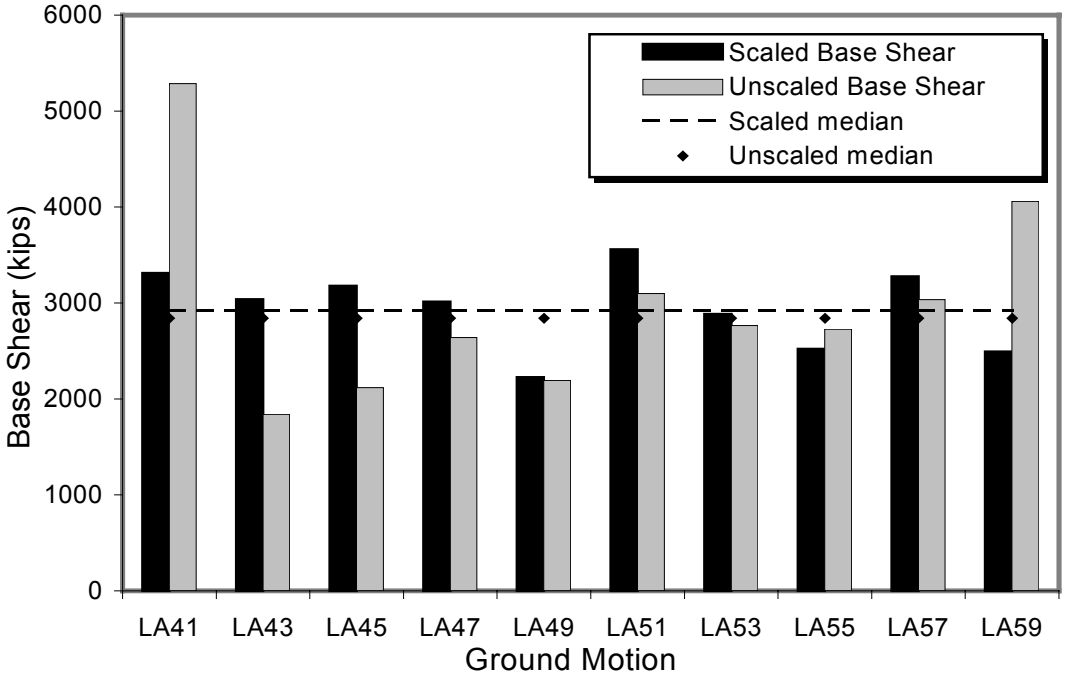

Figure B2 Maximum Base Shear in HCW-12-30 for Scaled and Unscaled Ground Motions for 50/50 Records.

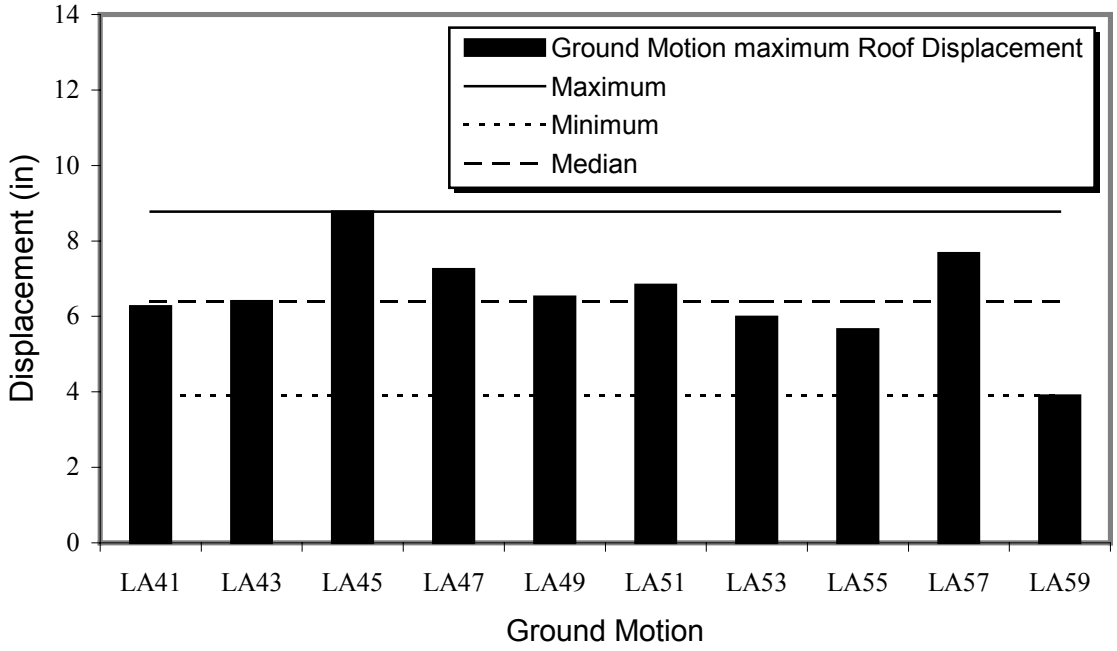

Figure B3 Maximum Roof Displacement in HCW-12-U for 50/50 Records.

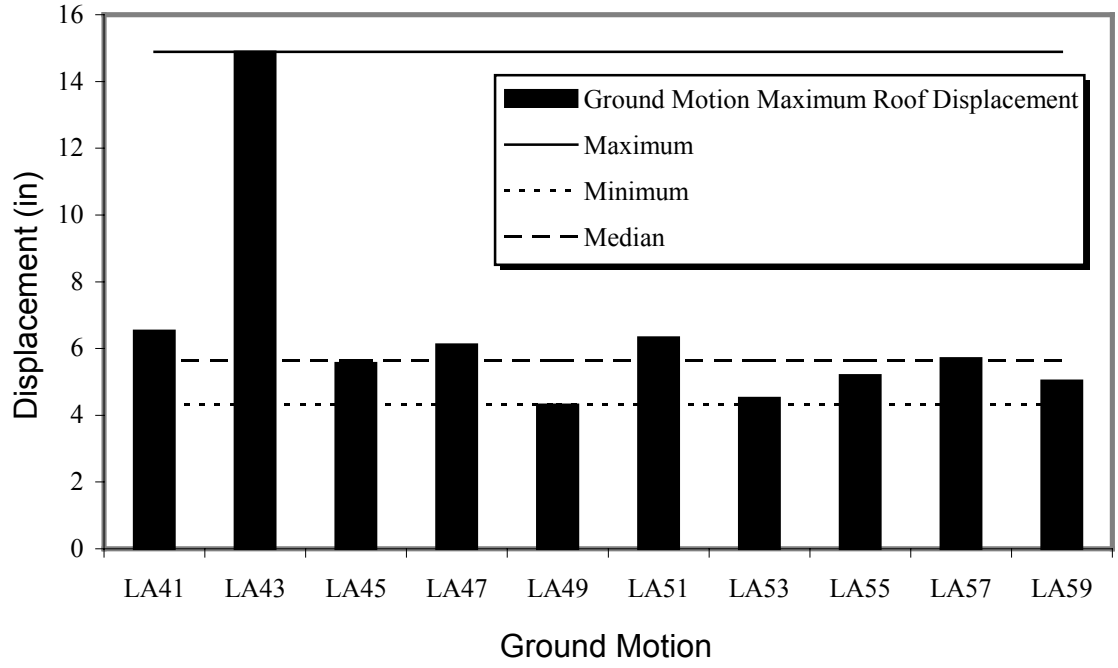

Figure B4 Maximum Roof Displacement in HCW-18-30 for 50/50 Motion Records

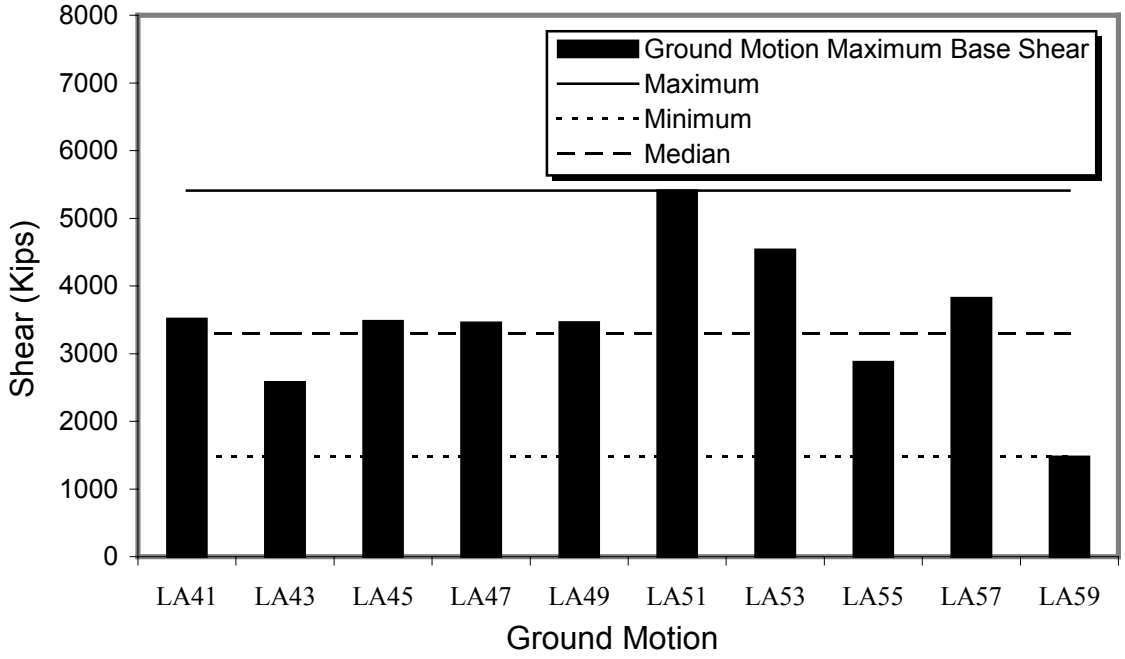

Figure B5 Maximum Base Shear in HCW-12-U for 50/50 Records.

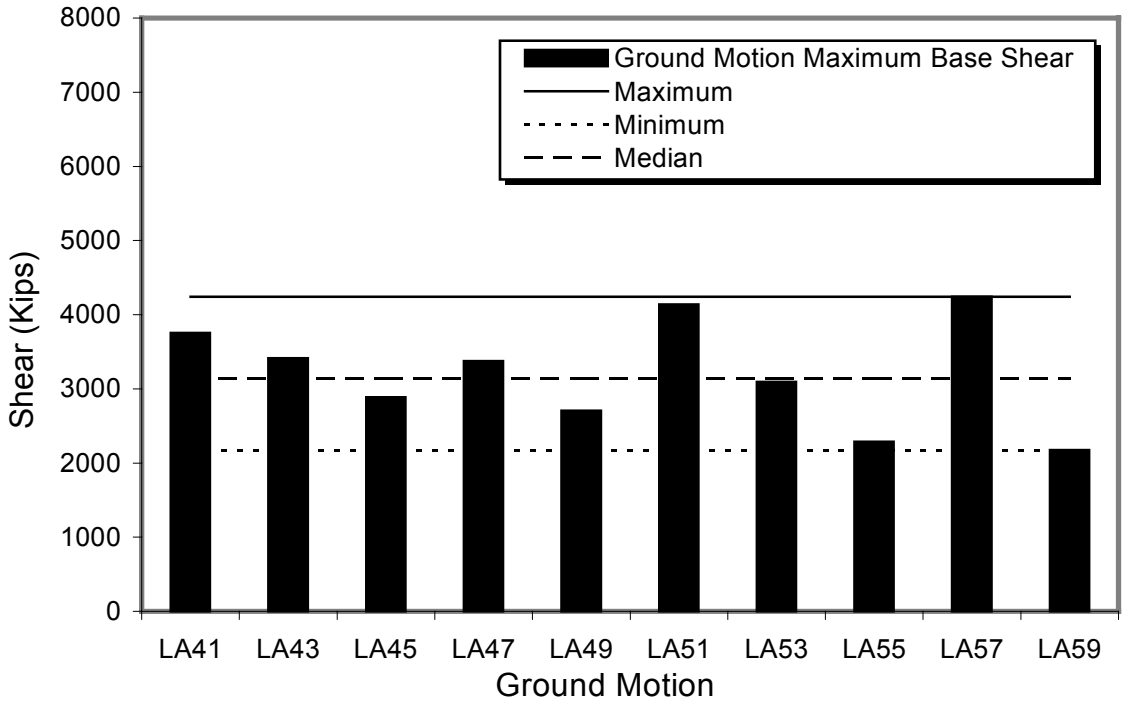

Figure B6 Maximum Base Shear in HCW-18-U for 50/50 Records

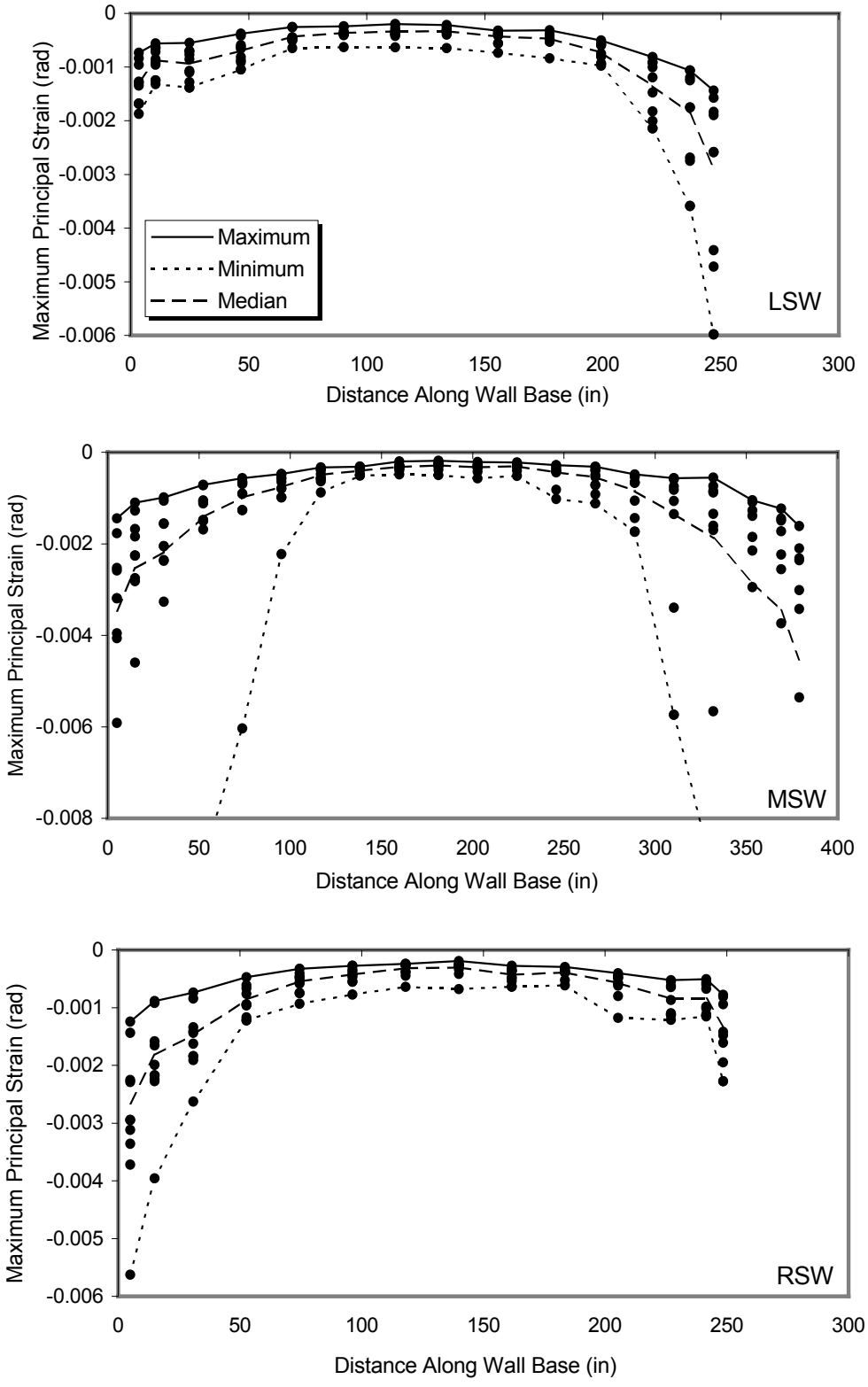

Figure B7 Maximum Principal Strains at the Base in HCW-12-30 for 2/50 Earthquakes

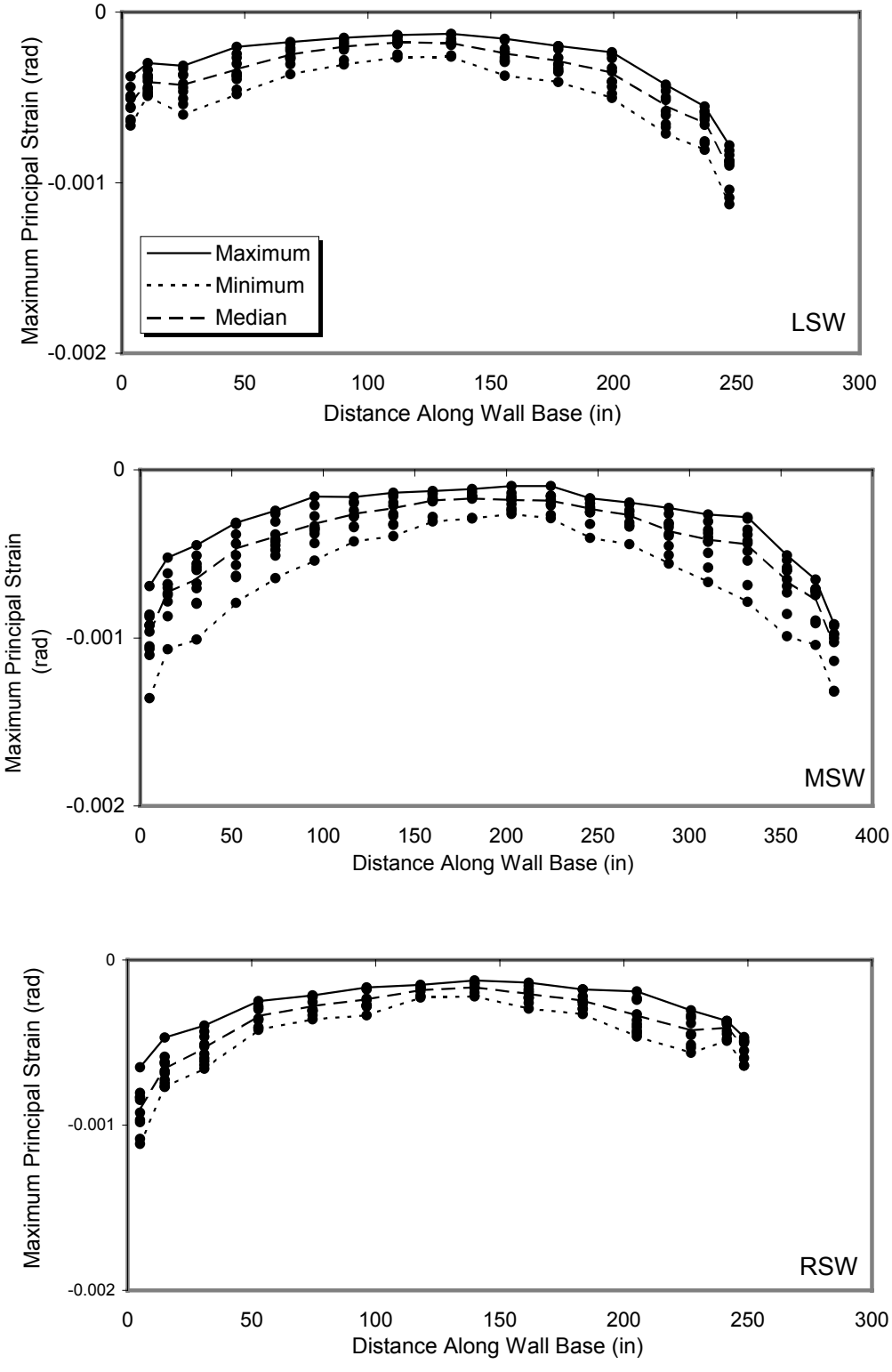

Figure B8 Maximum Principal Strains at the Base in HCW-12-30
for 50/50 Earthquakes

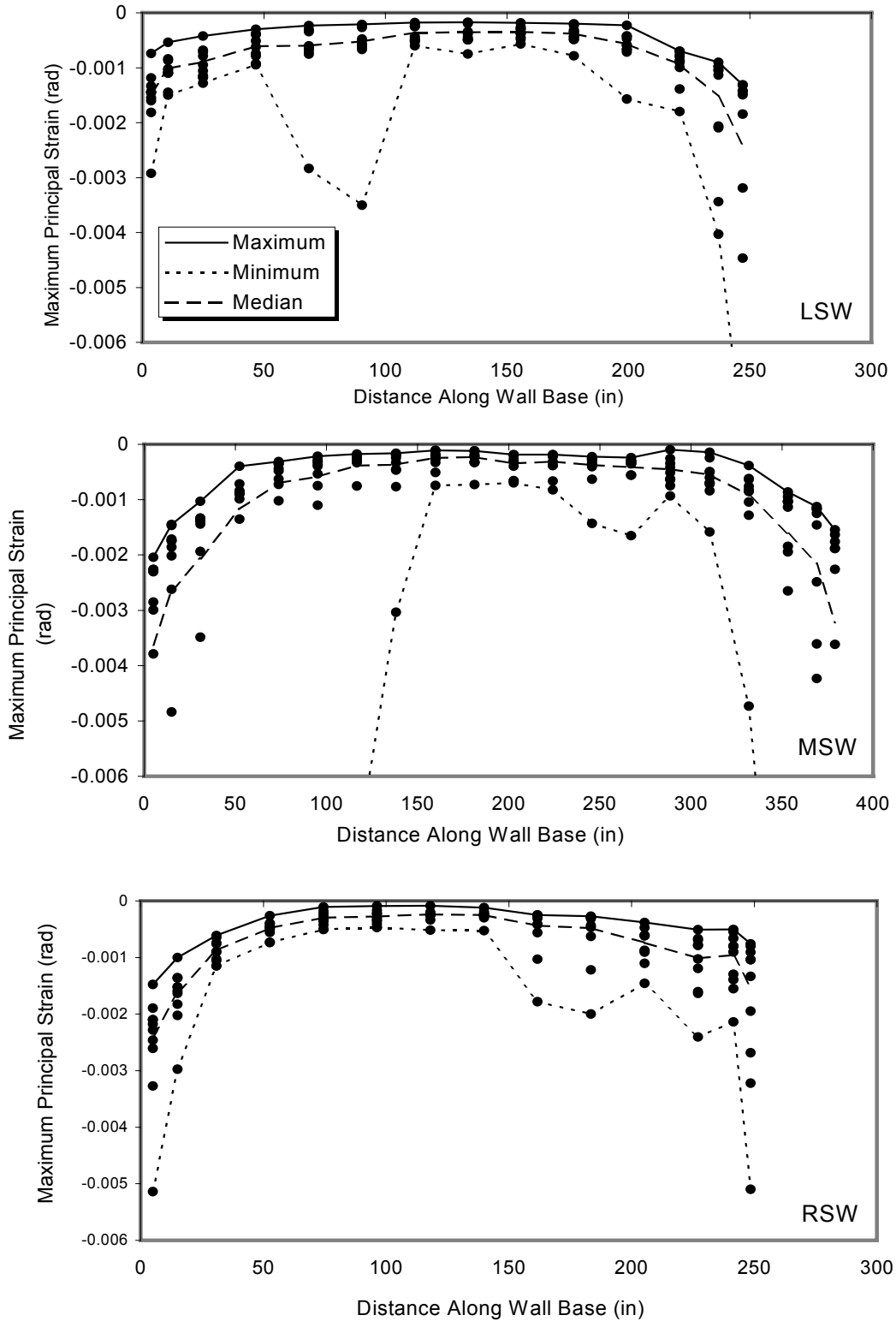

Figure B9 Maximum Principal Strains at the Base in HCW-12-U
for 2/50 Earthquakes

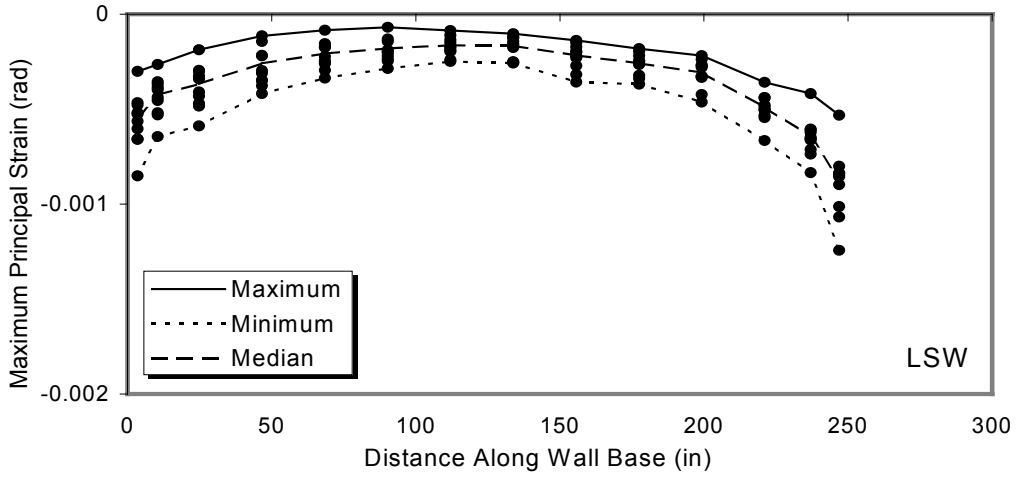

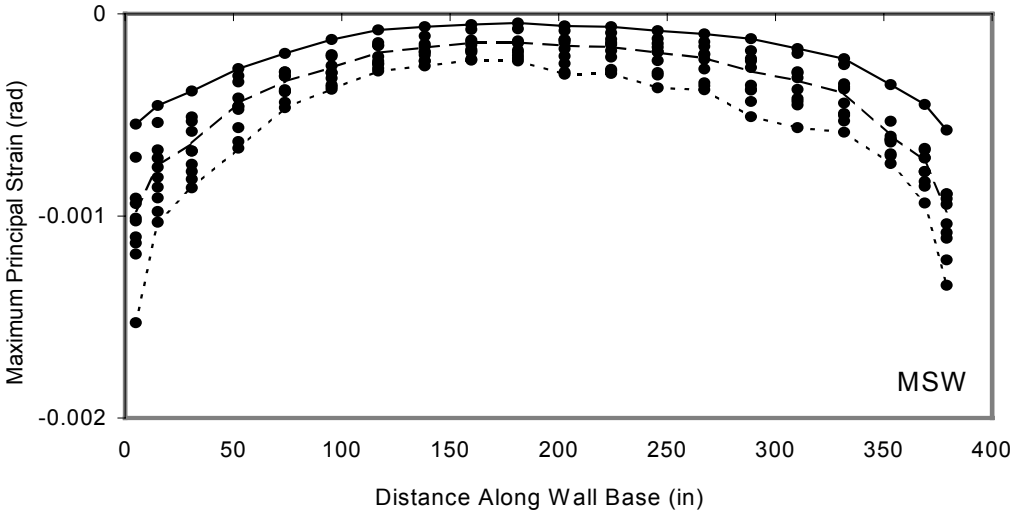

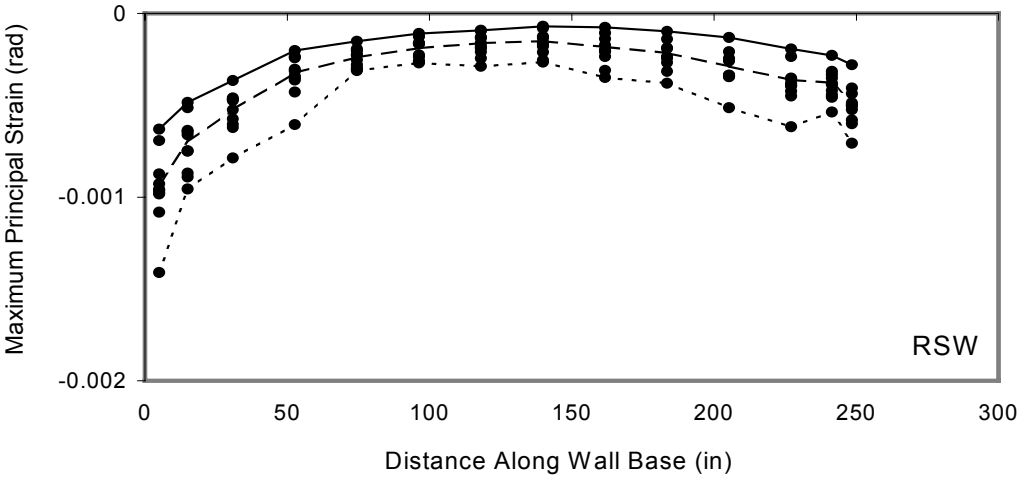

Figure B10 Maximum Principal Strains at the Base in HCW-12-U for 50/50 Earthquakes

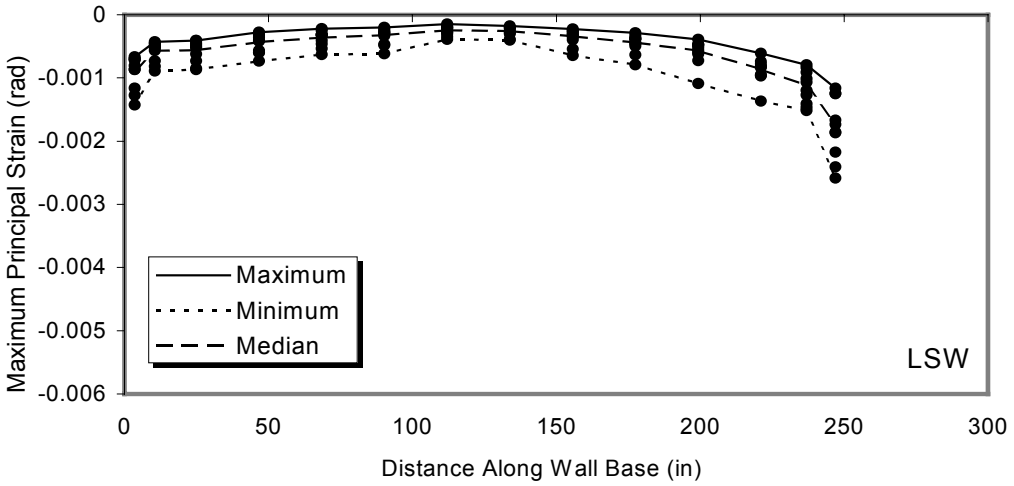

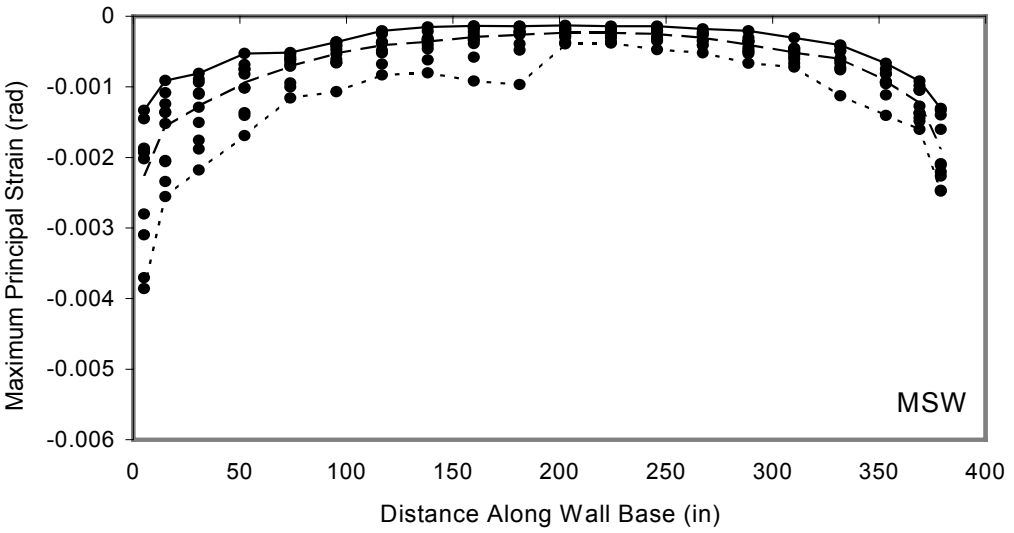

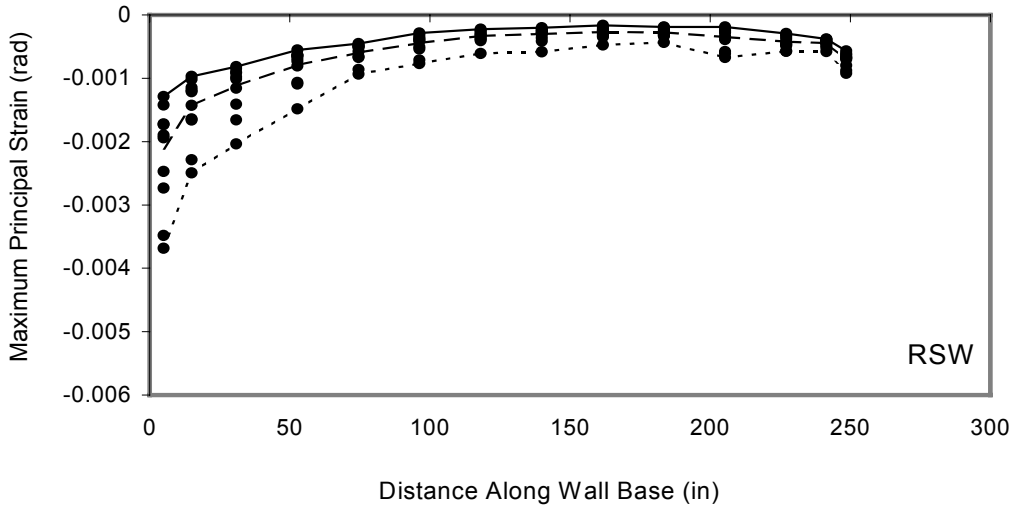

Figure B11 Maximum Principal Strains at the Base in HCW-18-30 for 2/50 Earthquakes

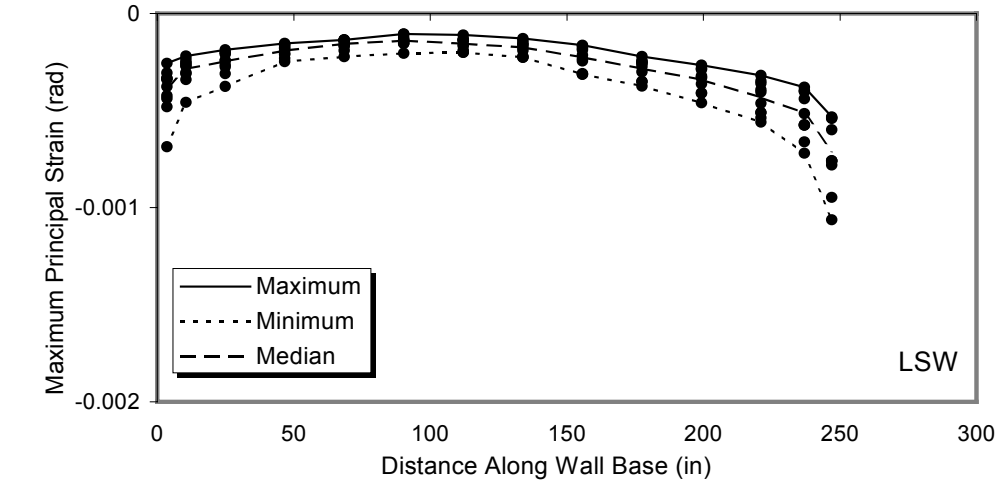

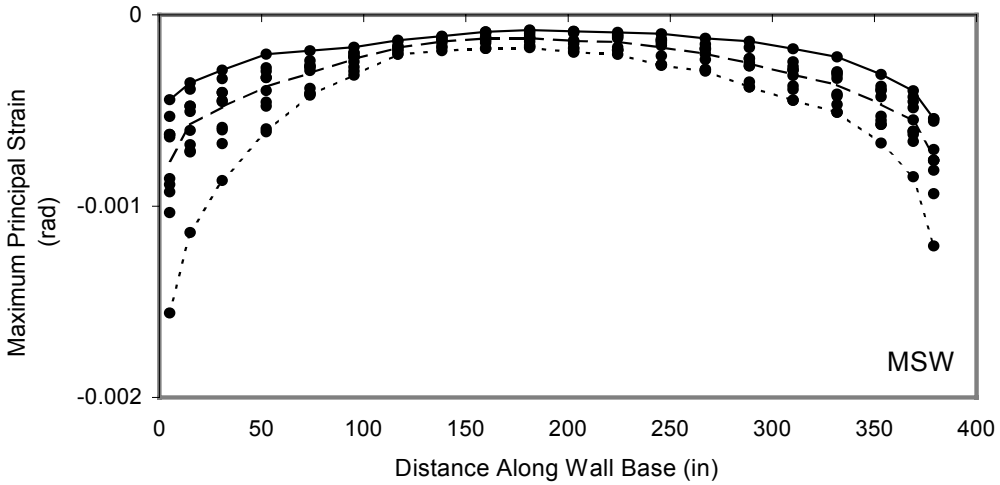

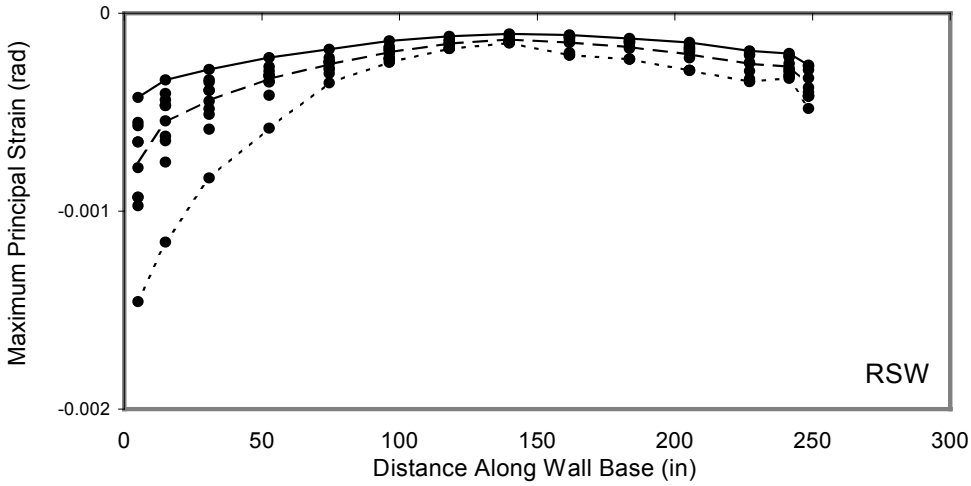

Figure B12 Maximum Principal Strains at the Base in HCW-18-30 for 50/50 Earthquakes

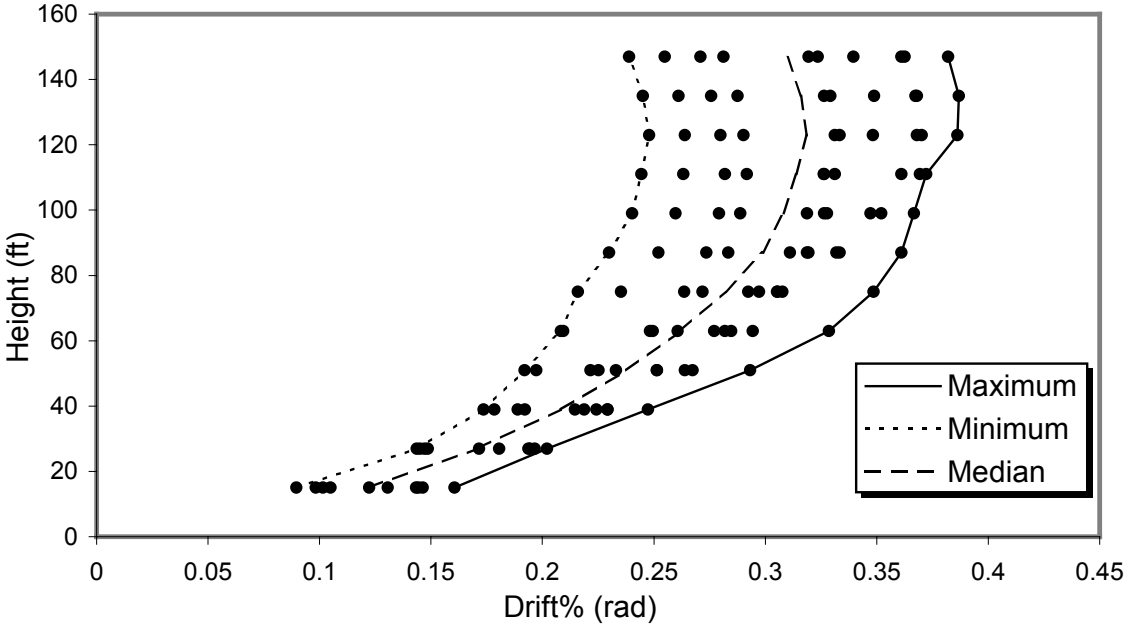

Figure B13 Story Drift Ratios along Height for HCW-12-30 for 50/50 Records.

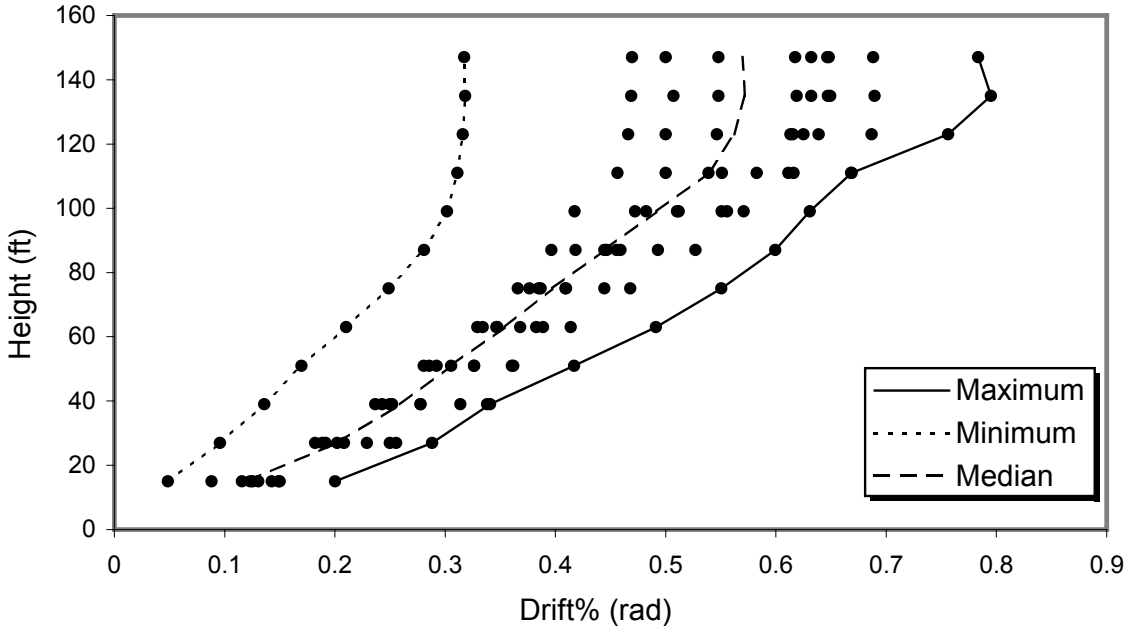

Figure B14 Story Drift Ratios along Height for HCW-12-U for 50/50 Records.

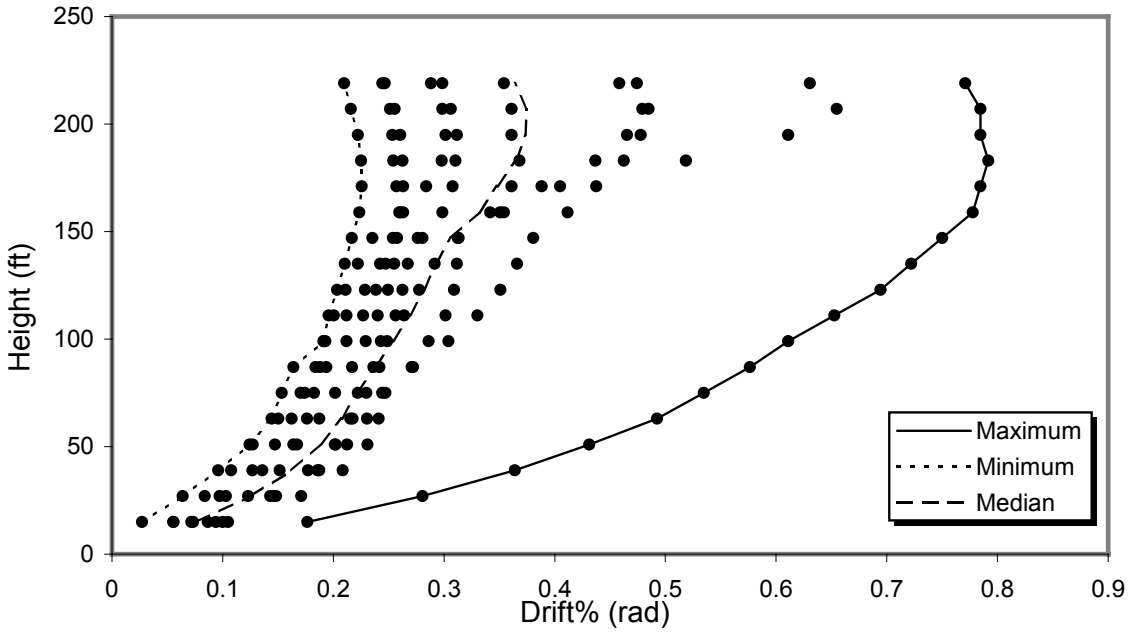

Figure B.15 Story Drift Ratios along Height for HCW-18-30 for 50/50 Records.

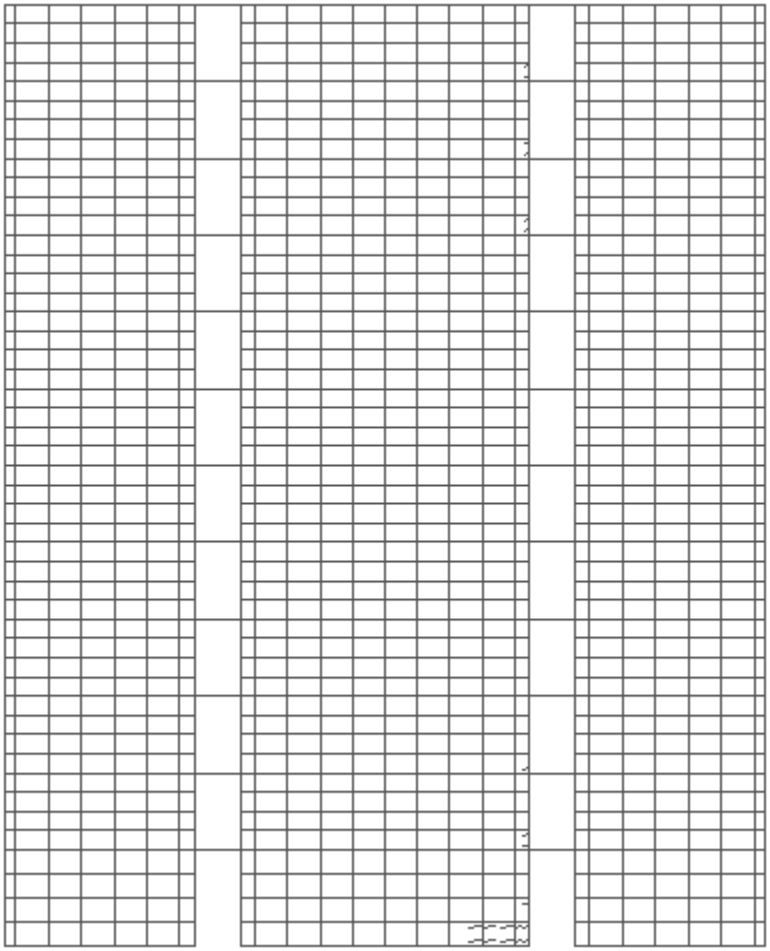

Figure B16 Crack Pattern at Time 0.9 second for Earthquake LA31 (HCW-12-30)

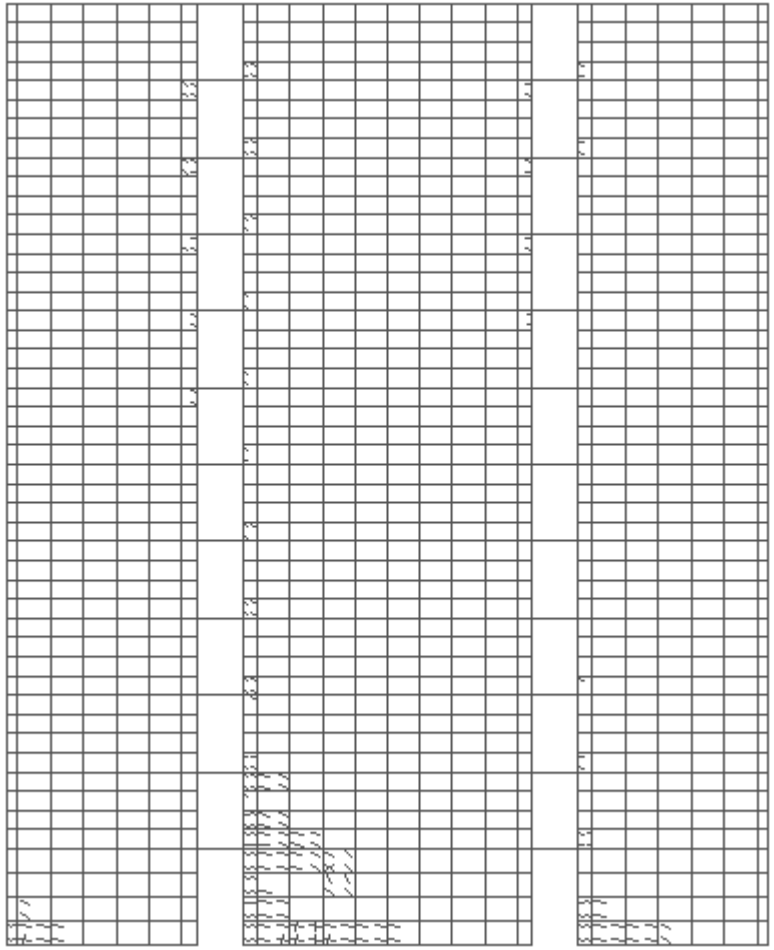

Figure B17 Crack Pattern at Time 1.9 second for Earthquake LA31 (HCW-12-30)

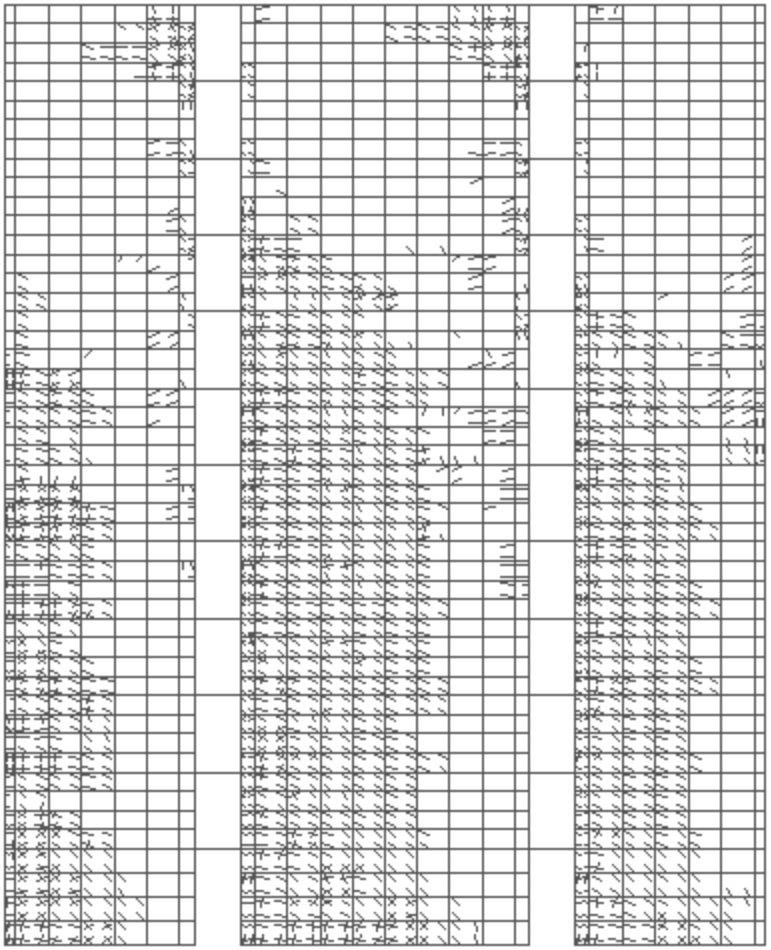

Figure B18 Crack Pattern at Time 2.9 second for Earthquake LA31 (HCW-12-30)

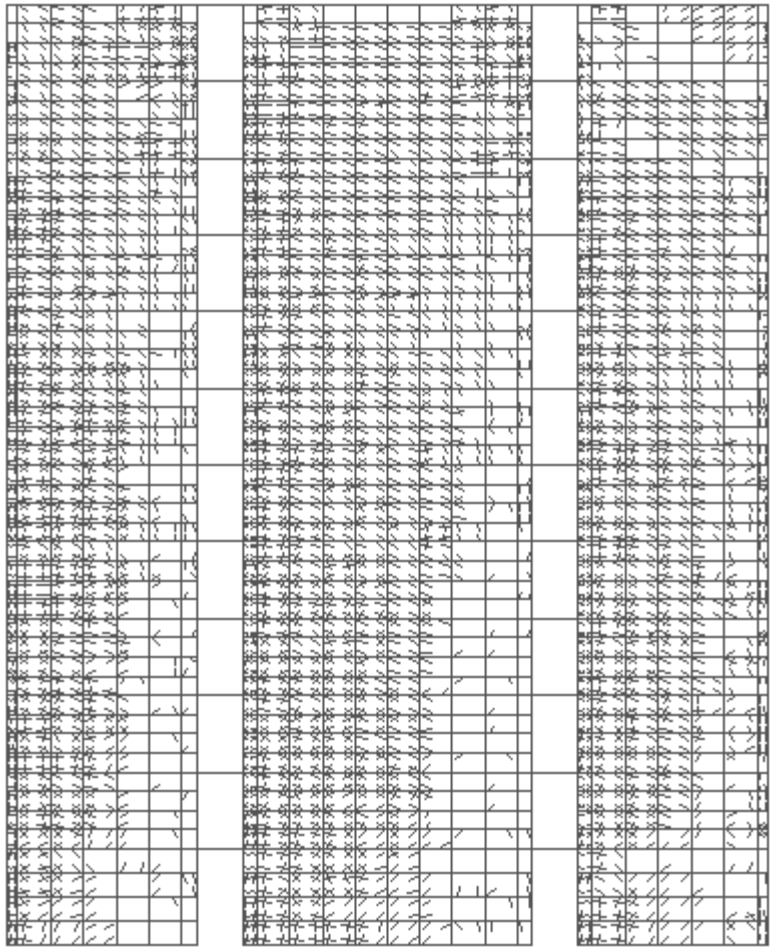

Figure B19 Crack Pattern at Time 3.9 second for Earthquake LA31 (HCW-12-30)

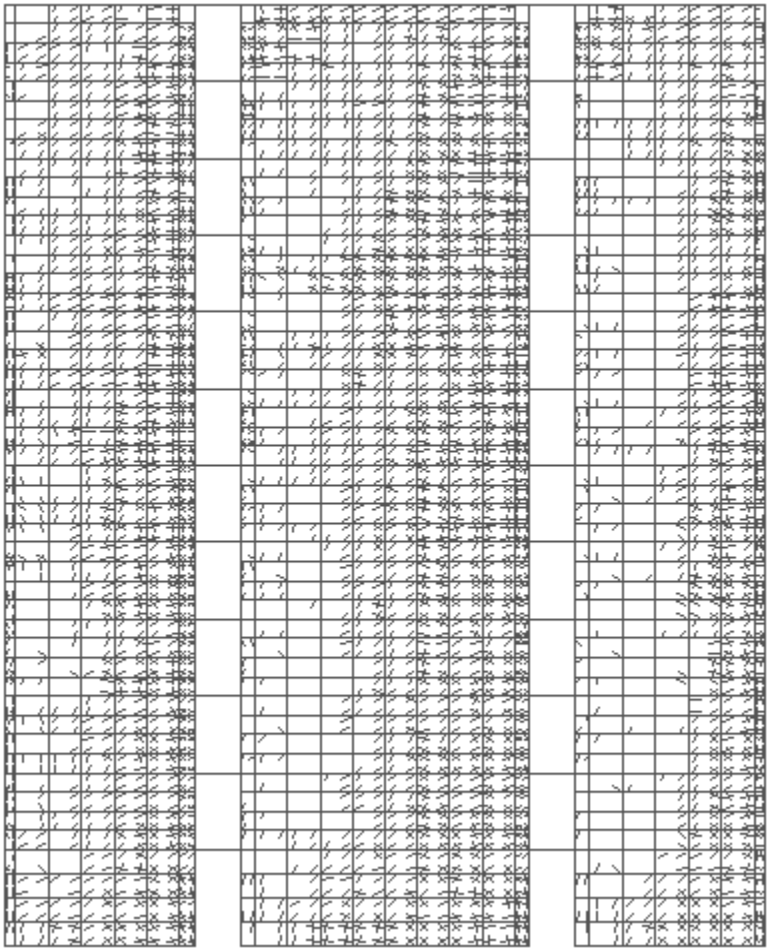

Figure B20 Crack Pattern at Time 4.9 second for Earthquake LA31 (HCW-12-30)

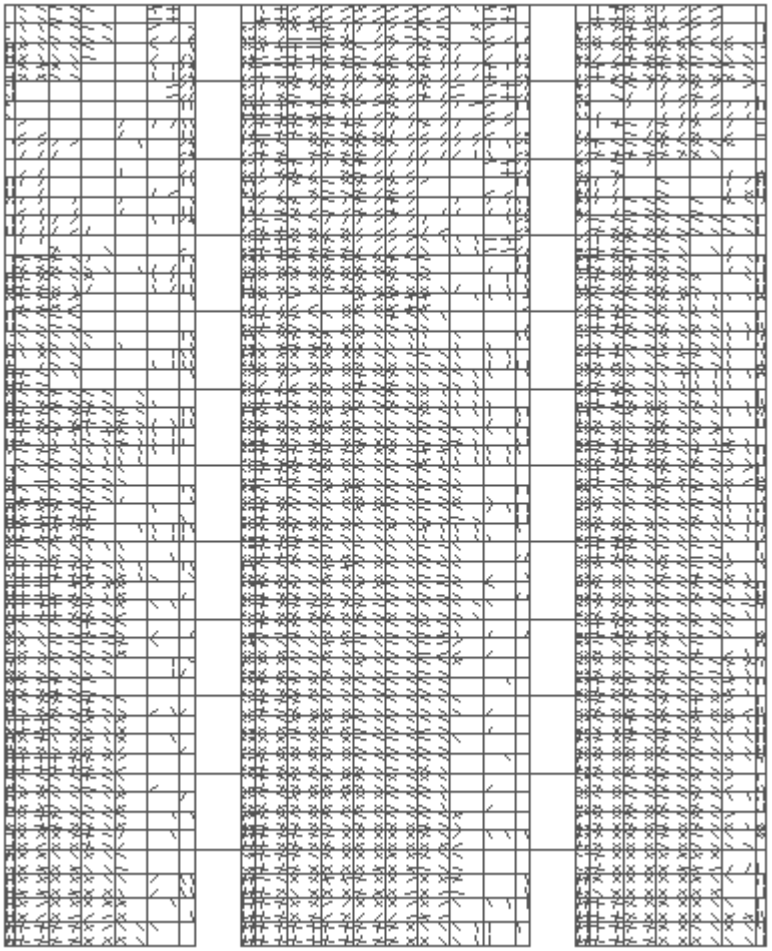

Figure B21 Crack Pattern at Time 5.9 second for Earthquake LA31 (HCW-12-30)

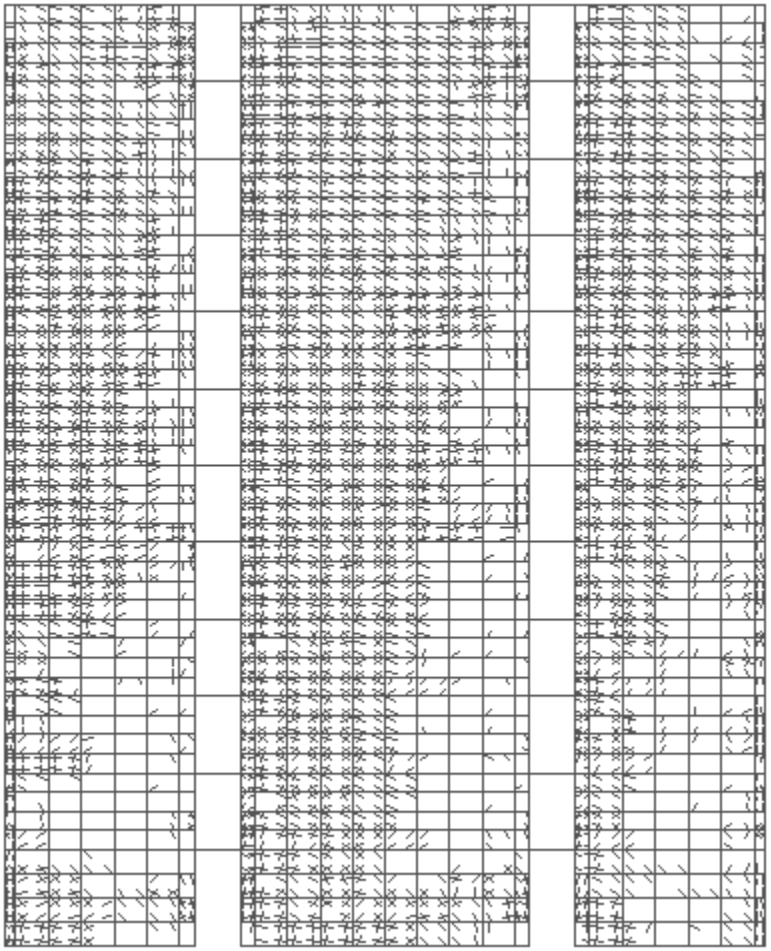

Figure B22 Crack Pattern at Time 6.9 second for Earthquake LA31 (HCW-12-30)

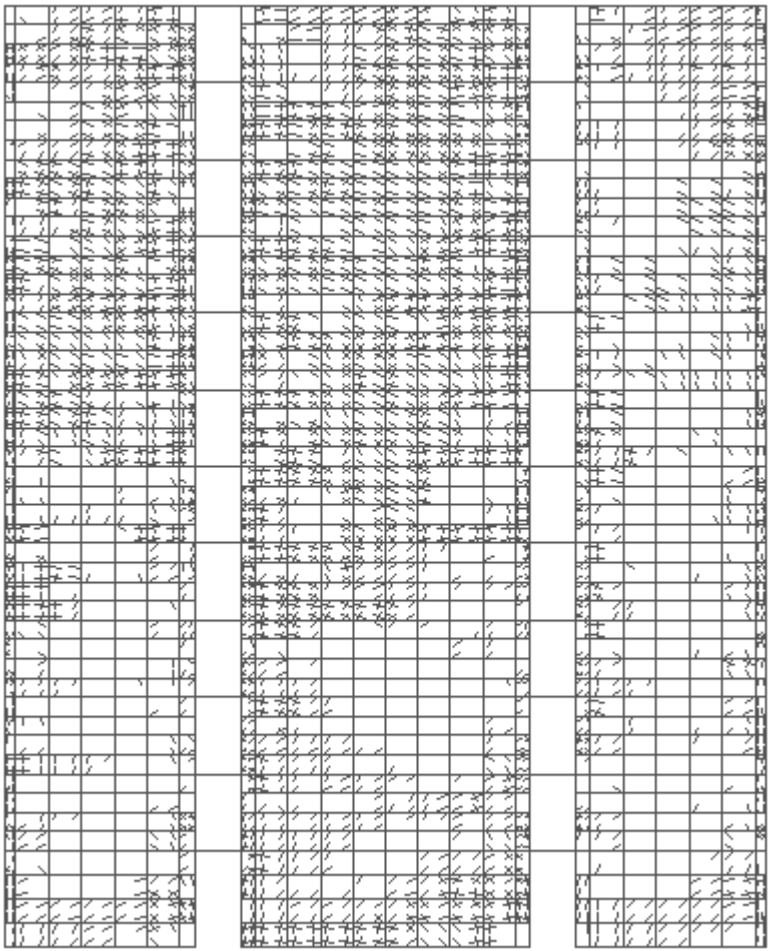

Figure B23 Crack Pattern at Time 7.9 second for Earthquake LA31 (HCW-12-30)

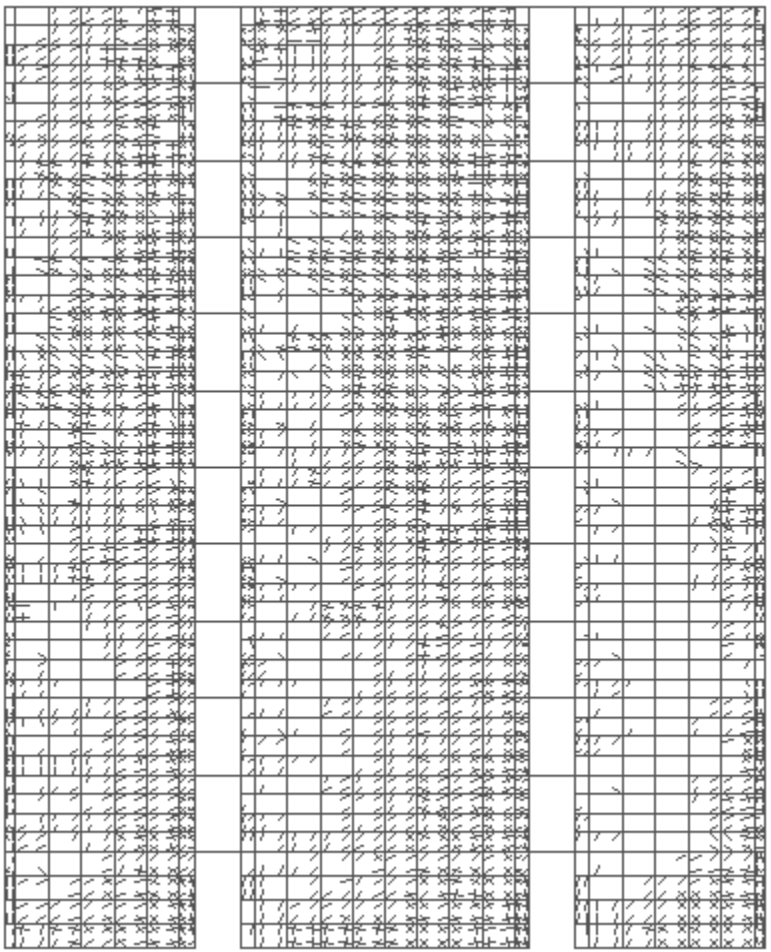

Figure B24 Crack Pattern at Time 8.9 second for Earthquake LA31 (HCW-12-30)

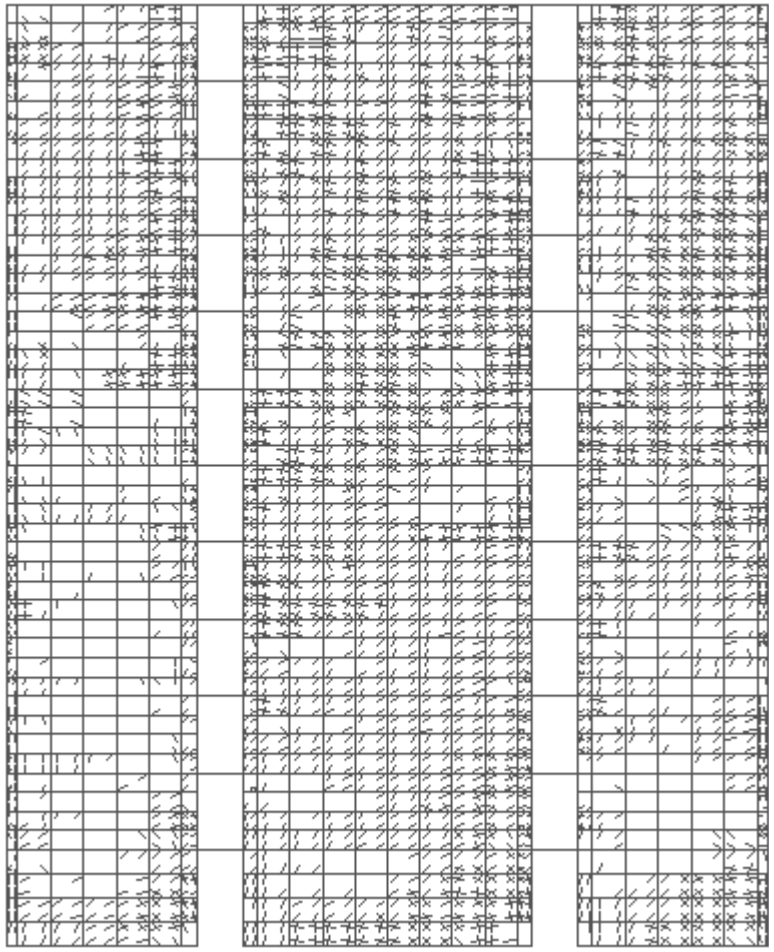

Figure B25 Crack Pattern at Time9.9 second for Earthquake LA31 (HCW-12-30)

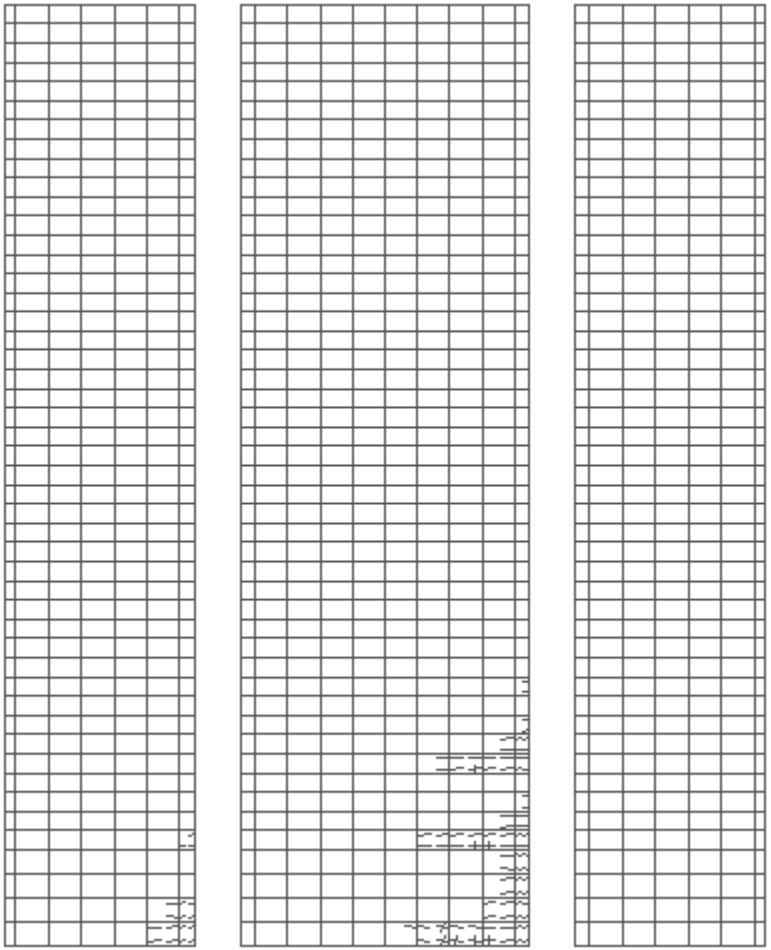

Figure B26 Crack Pattern at Time 0.9 second for Earthquake LA31 (HCW-12-U)

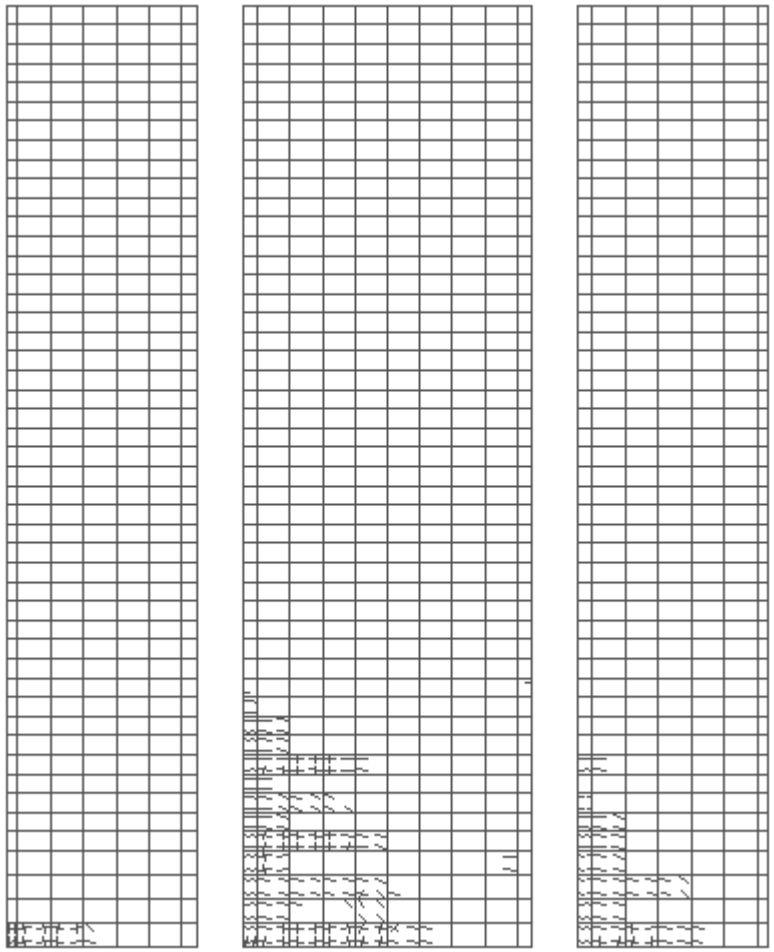

Figure B27 Crack Pattern at Time 1.9 second for Earthquake LA31 (HCW-12-U)

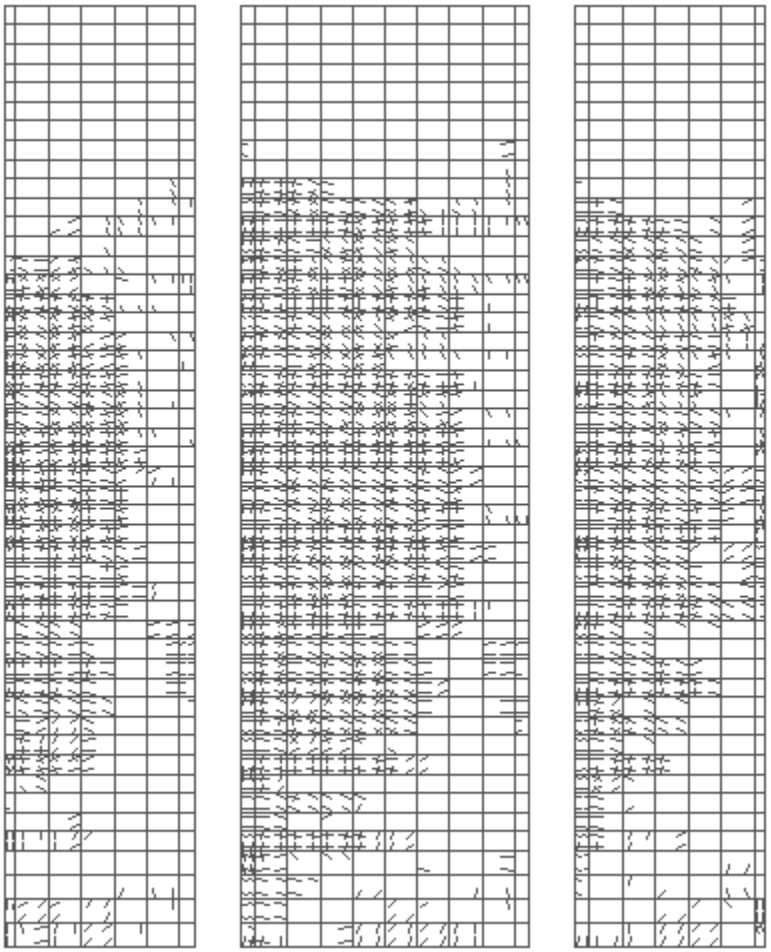

Figure B28 Crack Pattern at Time 2.9 second for Earthquake LA31 (HCW-12-U)

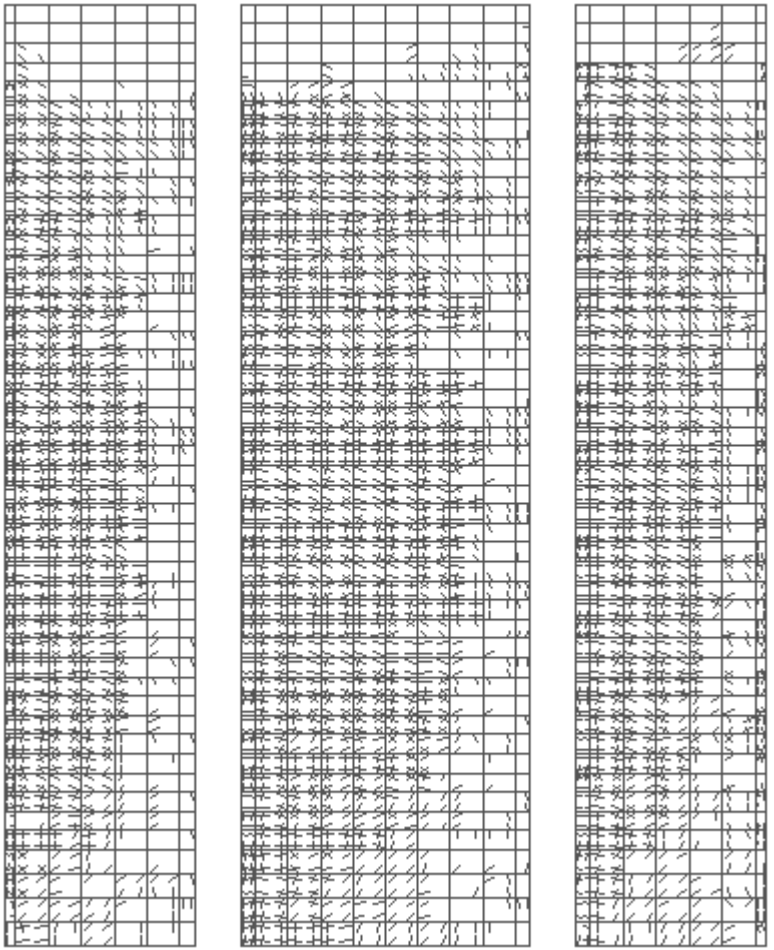

Figure B29 Crack Pattern at Time 3.9 second for Earthquake LA31 (HCW-12-U)

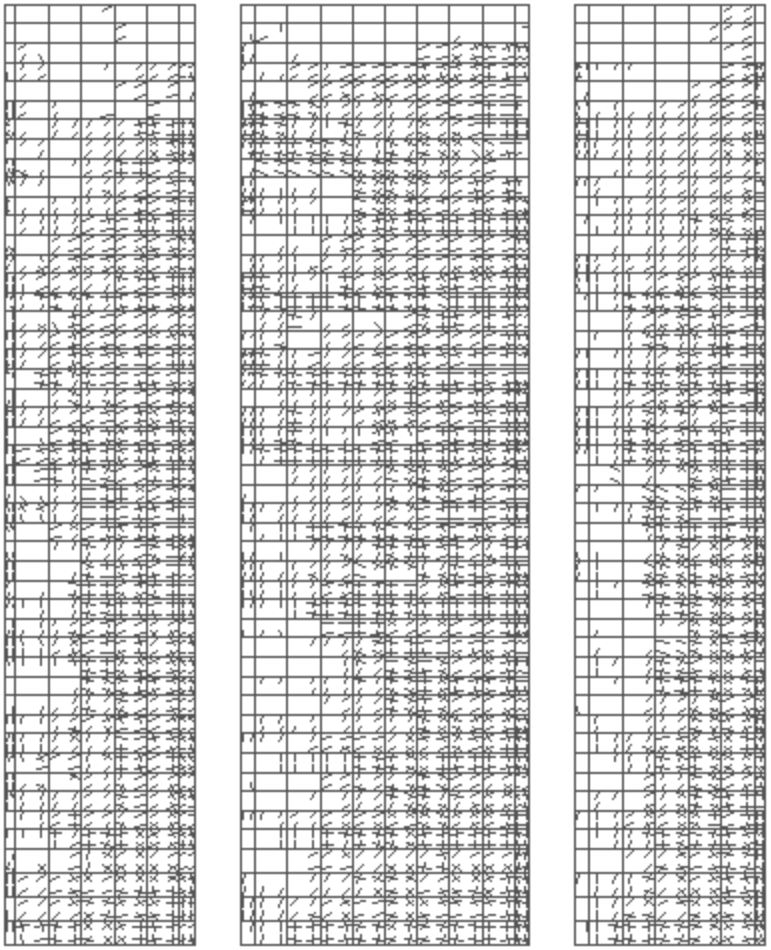

Figure B30 Crack Pattern at Time 4.9 second for Earthquake LA31 (HCW-12-U)

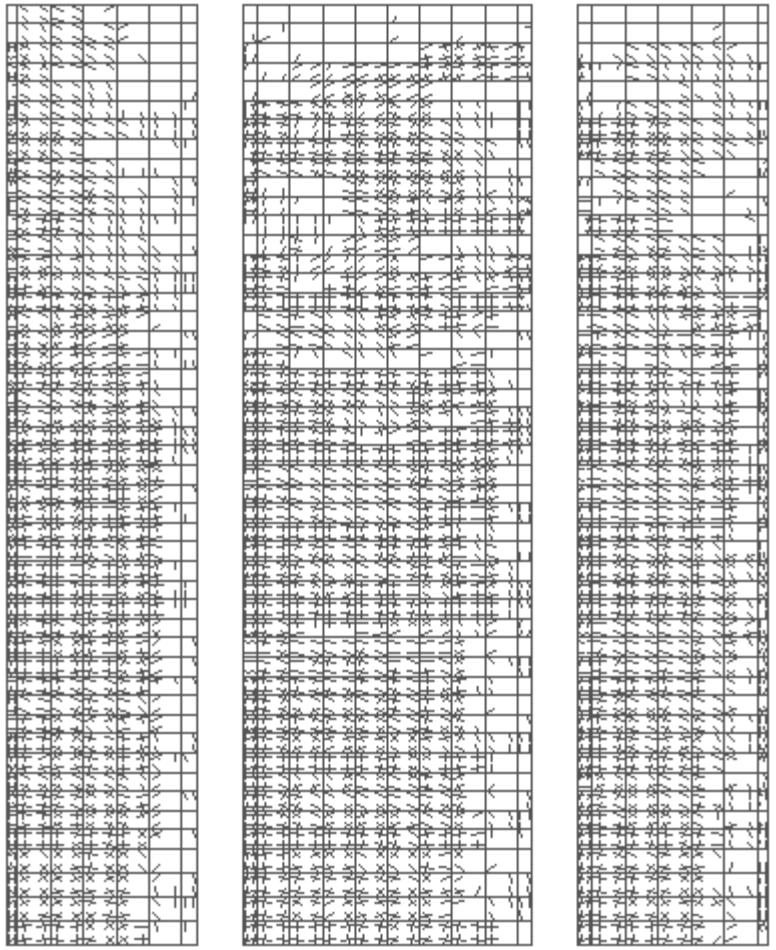

Figure B31 Crack Pattern at Time 5.9 second for Earthquake LA31 (HCW-12-U)

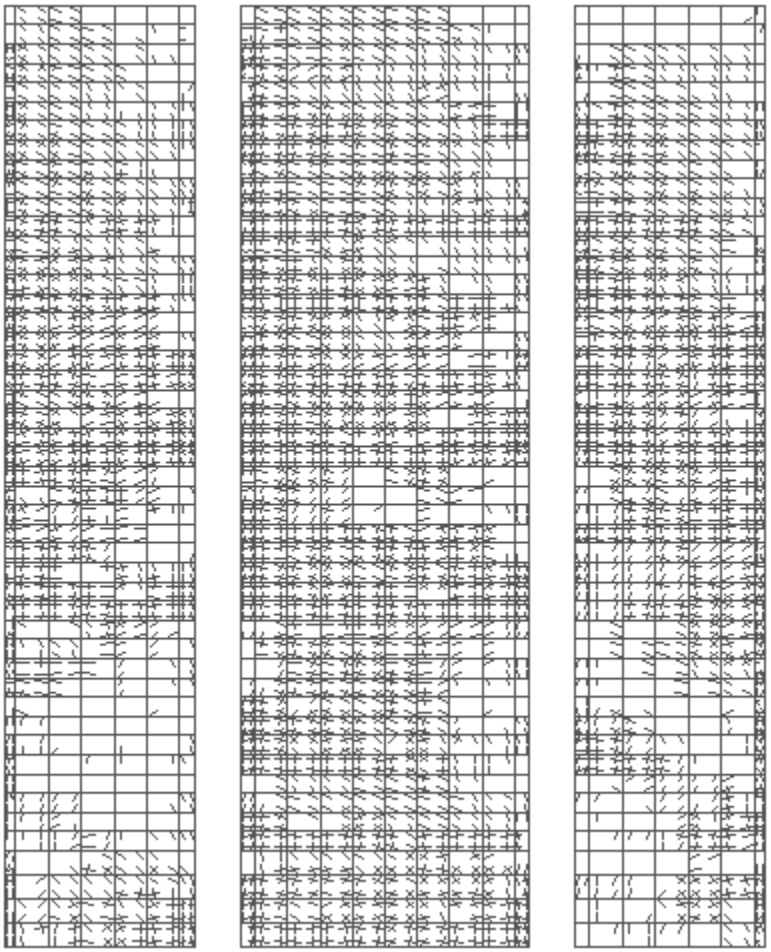

Figure B32 Crack Pattern at Time 6.9 second for Earthquake LA31 (HCW-12-U)

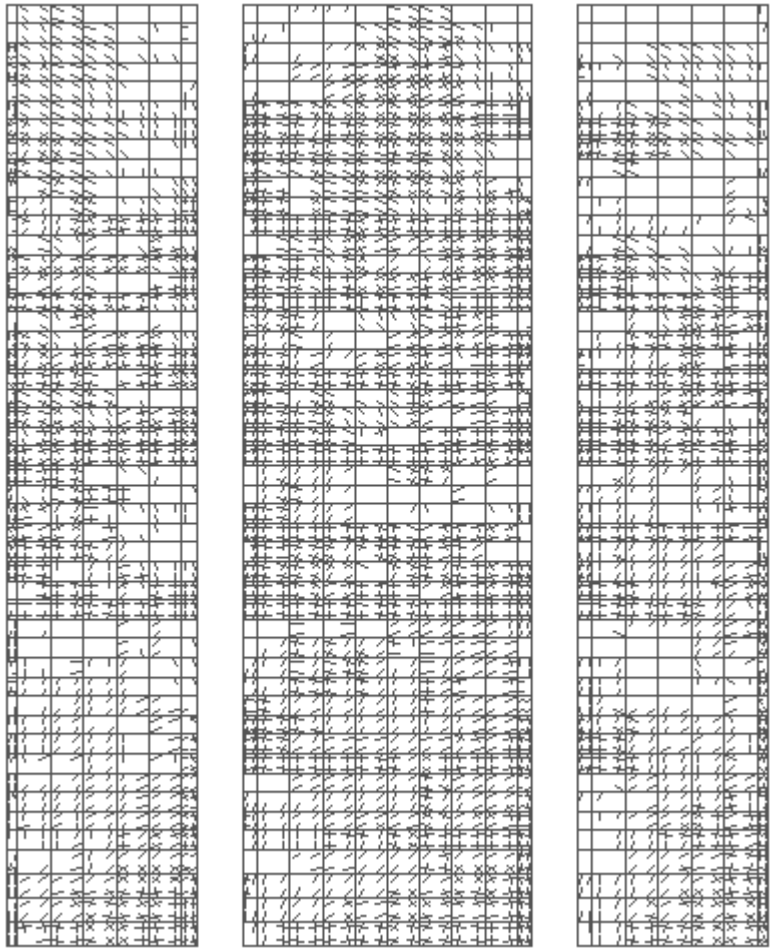

Figure B33 Crack Pattern at Time 7.9 second for Earthquake LA31 (HCW-12-U)

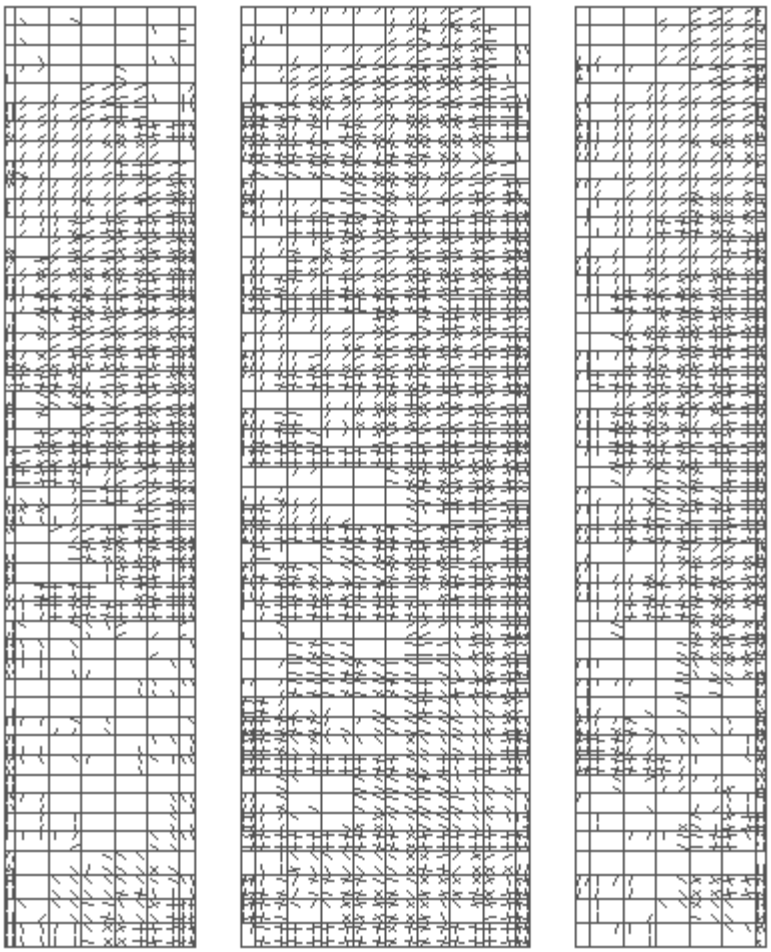

Figure B34 Crack Pattern at Time 8.9 second for Earthquake LA31 (HCW-12-U)

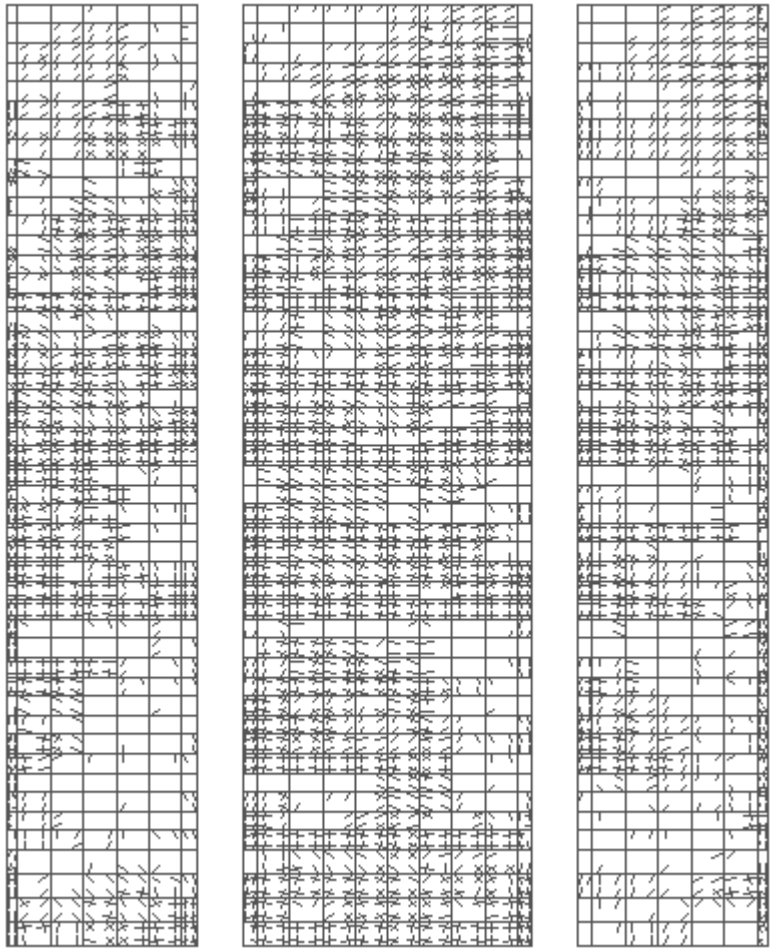

Figure B35 Crack Pattern at Time9.9 second for Earthquake LA31 (HCW-12-U)

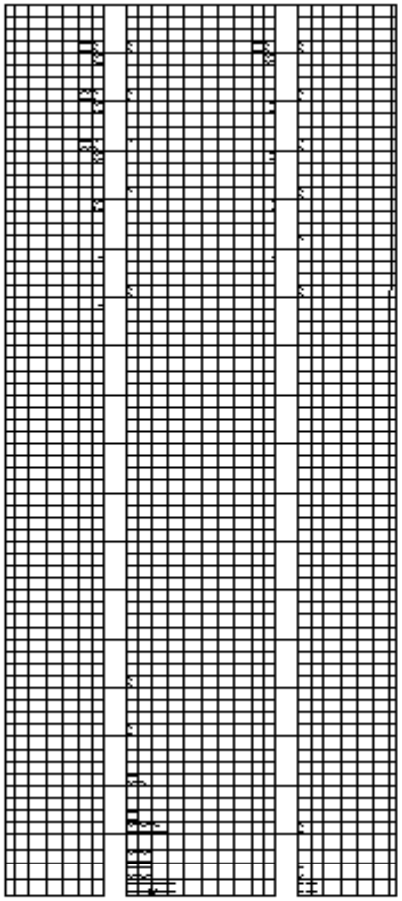

Figure B36 Crack Pattern at Time 0.9 second for Earthquake LA33 (HCW-18-30)

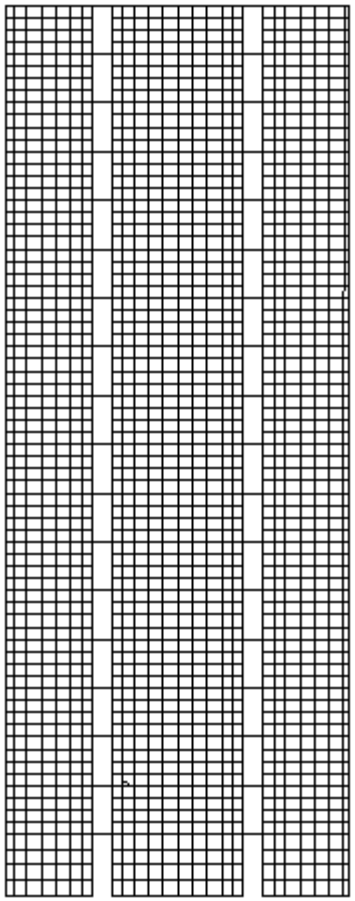

Figure B37 Crack Pattern at Time 1.9 second for Earthquake LA33 (HCW-18-30)

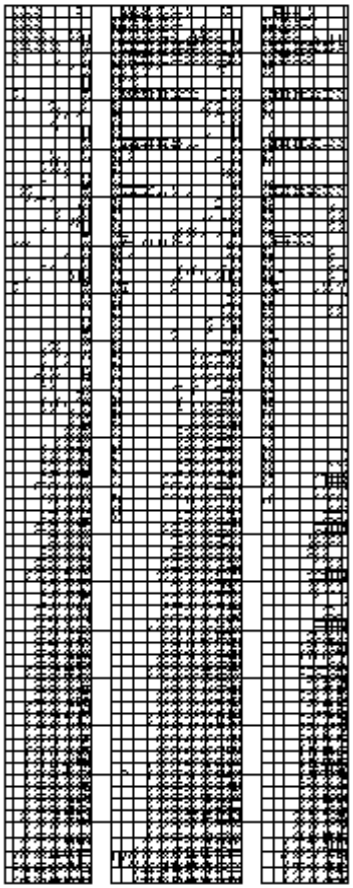

Figure B38 Crack Pattern at Time 2.9 second for Earthquake LA33 (HCW-18-30)

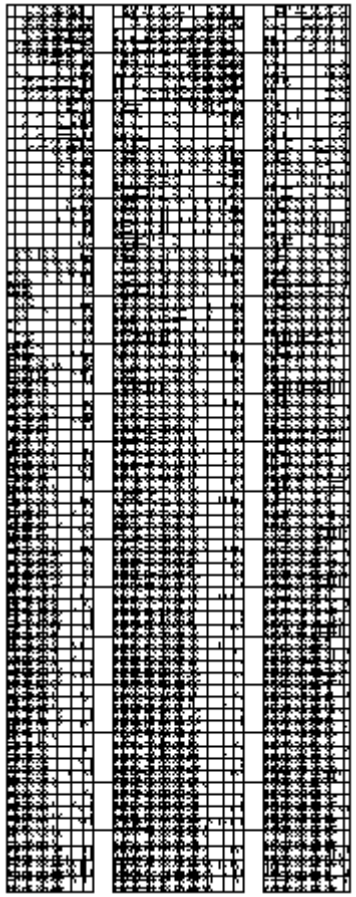

Figure B39 Crack Pattern at Time 3.9 second for Earthquake LA33 (HCW-18-30)

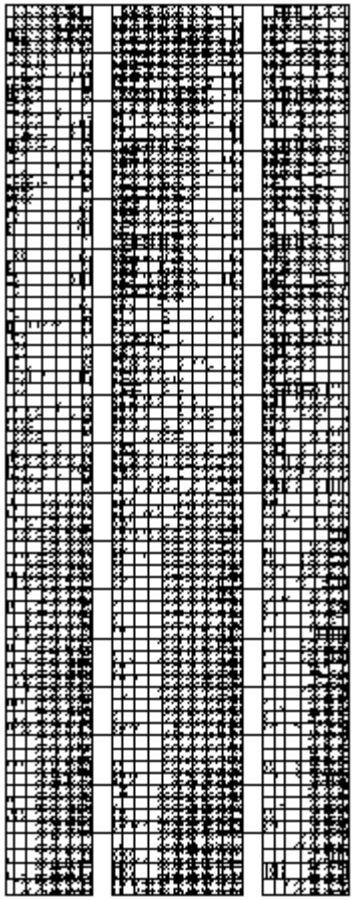

Figure B40 Crack Pattern at Time 4.9 second for Earthquake LA33 (HCW-18-30)

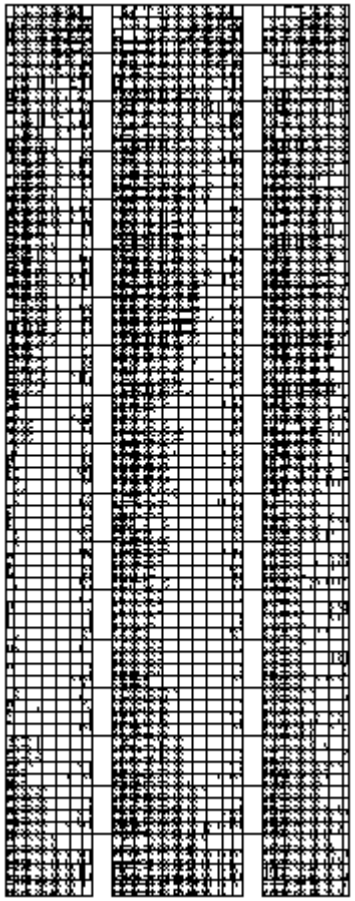

Figure B41 Crack Pattern at Time 5.9 second for Earthquake LA33 (HCW-18-30)

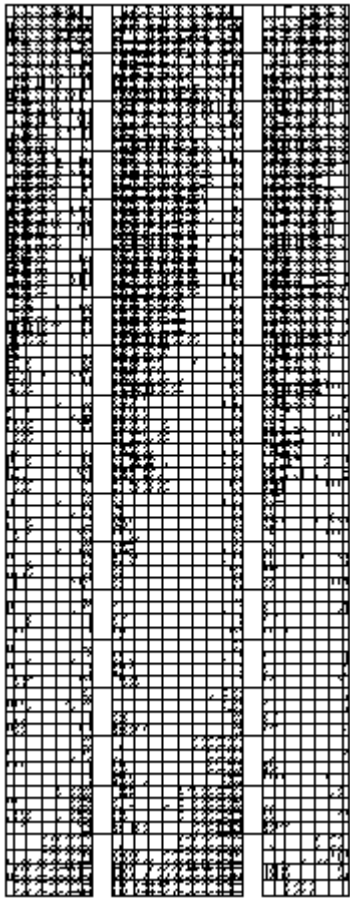

Figure B42 Crack Pattern at Time 6.9 second for Earthquake LA33 (HCW-18-30)

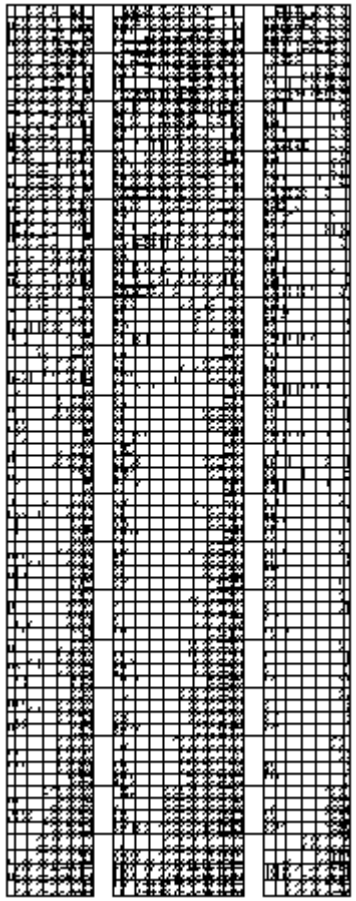

Figure B43 Crack Pattern at Time 7.9 second for Earthquake LA33 (HCW-18-30)

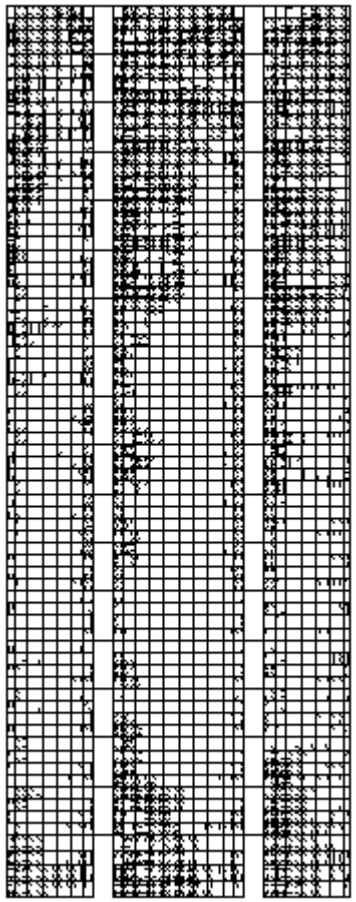

Figure B44 Crack Pattern at Time 8.9 second for Earthquake LA33 (HCW-18-30)

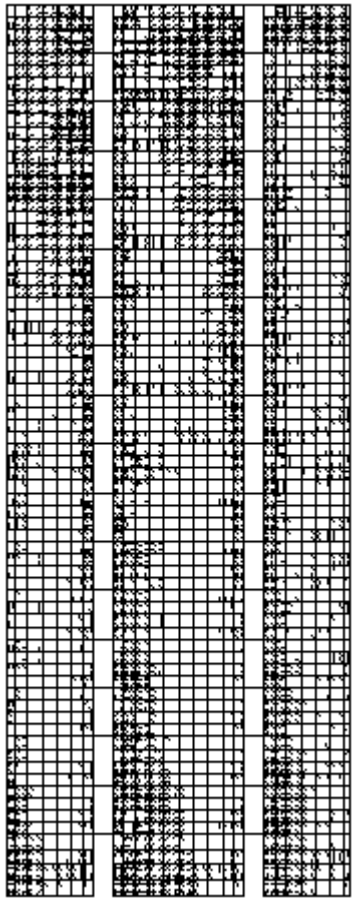

Figure B45 Crack Pattern at Time9.9 second for Earthquake LA33 (HCW-18-30)

LIST OF REFERENCES

ACI (1984), "Earthquake Effects on Reinforced Concrete Structures, US-Japan Cooperative Earthquake Research Program," ACI Special Publication SP-84, American Concrete Institute, Detroit, 1984

AISC Seismic (1997), "*Seismic Provisions for Structural Steel Buildings*, American Institute of Steel Construction (AISC)", Chicago, Illinois.

Aktan, A.E. and Hanson, R.D., Nonlinear Cyclic Analysis of Reinforced Concrete Plane Stress Members," Special Publication Sp63-6, American Concrete Institute, 1980, pp. 135-152

Balakrishnan, S. and Murray, D. W., "Concrete Constitutive Model for NLFE Analysis of Structures," Journal of Structural Engineering, ASCE, Vol. 114, No. 7, July 1988, pp. 1449-1466

Bazant, Z.P., Comments of Orthogonal Models for Concrete and Geomaterials," Journal of the Engineering Mechanics, ASCE, Vol. 109, No. 3, June 1983, pp. 849-865.

Bazant, Z. P. and Cedolin, L., "Fracture Mechanics of Reinforced Concrete," Journal of Engineering Mechanics Division, ASCE, Vol. 106, No. EM6, December 1980, pp. 1287-1306.

Bolander, J. and Wight, J. K. "Finite Element Modeling of Shear Wall Dominant Buildings," ASCE, "Journal of Structural Engineering, Vol. 117, No. 6, June 1991, pp. 1719-1739

Bolander, J. E. and Wight, J. K., "Towards Realistic FE Model for Reinforced Concrete Shear Walls Dominant Buildings Subjected to Lateral Loadings," Report No. UMCE89-2,

Department of Civil Engineering, The University of Michigan, Ann Arbor, Michigan, January, 1989, pp. 192

Brown, J. R. “Fatigue Characteristics of Reinforcing Bars Under Simulated Seismic Loading.” Master’s thesis, University of Central Florida, Orlando, Florida, 1998.

Cardenas, A. E, Hanson, J. M., Corley, W. G. and Hognestad, E., “Design "Previsions for Shear Walls,” ACI Journal Proc., 70(3), American Concrete Institute, Detroit, March 1973, pp. 221-230

Cervenka, V., “Constitutive Model for Cracked Reinforced Concrete,” Journal of the American Concrete Institute, Vol. 82, No. 6, November-December, 1985, pp.877-882

Chitty, L., “On the Cantilever Composed of a Number of Parallel Beams Interconnected by Cross Bars”, London, Edinburgh and Dublin Philosophical Magazine and Journal of Science, Vol. 38, October 1947, pp. 685-699

Chitty, L., and Wan, W., J., “Tall Building Structures Under Wind Load”, 7th International Conference for Applied Mechanics, Vol. 1, 1948, pp. 254-268

Collins, Michael P.; Mitchell, Denis; and MacGregor, James G. “Structural Design Considerations for High-Strength Concrete,” Concrete International, May 1993, pp. 27-34.

Coull, A. and Stafford-Smith, B., “Tall Buildings”, Pergamon Press Ltd., Oxford, UK, 1967

Daniel, J. I., Shiu, K. N. and Corley, W. G., “Openings in Earthquake Resistant Structural Walls,” Journal of Structural Engineering,” ASCE, Vol. 112, No. 7, July 1986, pp. 1660-1976

Darwin, D. and Pecknold, D. A. W., Analysis of RC Shear Panels Under Cyclic Loading,” Journal of the Structural Division, ASCE, Vol. 107, No. ST2, February 1976, pp. 335-369

De Borst, R. and Nauta, P., "Non-Orthogonal Cracks in Smeared Finite Element Method", Engineering Computation, Vol. 2, March 1985, pp. 35-46.

DIANA 7.0 (2000), Users Manual, DIANA Analysis, P.O. Box 113, 2600 AC Delft, The Netherlands.

Ehsani, M., and Wight, J. K. (1985), "Effects of Transverse Beams and Slab on Beam-to-Column Connections" *ACI Structural Journal*, V.82, No. 2, Mar.-Apr., pp. 188-195.

El-Tawil, S, Kuenzli, C. M. and Hassan (2002a), M., "Pushover of Hybrid Coupled Walls. I: Design and Modelling," ASCE, Journal of Structural Engineering, Vol. 128, No. 10, pp. 1272-1281

El-Tawil, S and Kuenzli, C. M. (2002b), "Pushover of Hybrid Coupled Walls. II: Analysis and Behavior," ASCE, Journal of Structural Engineering, Vol. 128, No. 10, pp. 1282-1289

El-Tawil, Sherif M., and Deierlein, Gregory G. (1996) "Fiber Element Analysis of Composite Beam-Column Cross-Sections." Report No. 96-6, Cornell University, Ithaca, New York.

Fajfar, P. and Fischinger, M., "Mathematical Modelling of Reinforced Concrete Strural Walls for Nonlinear Seismic Analysis," Proc. European Conference on Structural Dynamics, Eurodyn '90, Bochum, A.A. and Rotterdam, 1991

Fan, H. M. ad Heins C. P. (1974), "Effective Slab Width of Simple Span Steel I-Beam Composite Bridges at Ultimate Load", C. E. Report No. 57, University of Maryland, College Park, MD.

FEMA-350 (2000), "Recommended Seismic Design Criteria For New Steel Moment-Frame Buildings", FEMA 350/July 2000, Building Seismic Safety Council, Washington, D.C.

FEMA-356 (2000), NEHRP Guidelines for the Seismic Rehabilitation of Buildings. FEMA-356, Applied Technology Council (ATC-33 Project), Redwood City, California.

FEMA-368 (2000), "*NEHRP Recommended Provisions for Seismic Regulations for New Buildings and Other Structures"*, Building Seismic Safety Council, Washington, D.C.

Fintel, M., "Performance of Buildings with Shear Walls in Earthquakes of the last thirty years", PCI Journal, V.40, NO. 3, May-June 1995, pp. 62-78, No. 2, March-April,

Furlong, R. W., "Effective Stiffness of Composite Shear Walls", Composite Construction in Steel and Concrete, Proceedings of an Engineering Foundation Conference, ASCE, V.III, June 1996, pp. 250-257

Gilbert, R.I. and Warner, R. F., "Tension Stiffening in Reinforced Concrete Slabs", Journal of the Structural Division, ASCE, Vol. 104, No. ST12, December 1978, pp. 1885-1900.

Gong, Bingnian and Shahrooz, Bahram M., Seismic Behavior of Composed Coupled Wall Systems, Report No. UC-CII 98/01, College of Engineering, University of Cincinati, June 1998

Harries, K. A., Gong, B., and Shahrooz, B. M. (2000), "Behavior and Design of Reinforced Concrete, Steel, and Steel-Concrete Coupling Beams," Earthquake Spectra, Volume 16, No. 4, pp. 775-799.

Harries, K. A., Mitchell, D., Redwood, R. G., and Cook, W. D. (1998), "Nonlinear Seismic Response Predictions of Walls Coupled with Steel and Concrete Beams," Canadian Journal of Civil Engineering, 25(5), pp. 803-818.

Harries, K. A., Mitchell, D., Cook, W. D., and Redwood, R. G. (1993), " Seismic Response of Steel Beams Coupling Concrete Walls," Journal of Structural Engineering, ASCE, 119(12), pp. 3611-3629.

Hawkins, N. M., Mitchell, D. and Roeder, C. W., "Moment Resisting Connections for Mixed Constructions," Engineering Journal, AISC, Vol. 17, No. 1, 1980, pp 1-10

Hernandez, O. B. and Zermeno, de L. M. E., "Strength and Behavior of Structural Wall with Shear Failure," Proceedings of 7th World Conference on Earthquake Engineering, Vol. 4, Istanbul, Turkey, September 1980, pp. 121-124

Hosoya, H and Abe, I. and Kitagawa, Y., and Okada, T. (1994), "Shaking table tests of Three-Dimensional Scale Models of Reinforced Concrete High-Rise Frame Structures with Wall Coulumns," ACI Structural Journal, V.92, No.6, pp. 765-780.

Hiraishi, H., Nakata, S., Kitagawa, Y. and Kaminosono, T., "Static Tests on Shear Walls and Beam-Column Assemblies and Study Between Shaking Table Tests and Pseudo Dynamic Tests," Publication SP-84, American Concrete Institute, Detroit, 1985, pp. 11-48

Inoue, N., Koshika, N. and Suzuki, N., "Analysis of Shear Walls Based on Collins Panel Tests", Finite Element of Reinforced Concrete Structures, ASCE, May 1985, pp. 288-299.

Kabeyasawa, T., Shiohara, H., Otani, S. and Aoyama, H., "Analysis of Full Scale Seven-Story Reinforced Concrete Test Structure: Test PSD-3," Proceeding 3rd Joint Technical Coordinating Committee, US-Japan Cooperative Earthquake Research Program, Building Research Institute, Tsukuba, Japan, 1982

Kanno, R., "Strength, Deformation and Seismic Resistance of Joints Between Steel Beams and Reinforced Concrete Columns," Ph. D Dissertation to Cornell University, August 1993.

Karsan, I.D. and Jirsa, J.O., "Behavior of Concrete Under Compressive Loading", Journal of the Structural Division, ASCE, Vol. 95, No. ST12, December, 1969, pp. 2543-2563

Kuenzli, C. M. (2001), "Seismic Behavior and Design of Hybrid Coupled Wall Systems", MS Thesis, Department of Civil and Env. Eng., University of Central Fl, Orlando, FL 32816.

Kupfer, H.B. and Hilsdorf, H. K., "Behavior of Concrete under Biaxial Stresses," Journal of the American Concrete Institute, Vol. 66, No. 8, August 1969, pp. 656-666

Lefas, I. And Kotsovos, M. D., "Behavior of Reinforced Concrete Structural Walls: Strength, Deformation Characteristics, and Failure Mechanism," ACI Structural Journal, Vol. 87 No. 1, Jan-Feb 1990, pp. 23-31

Linde, P. "Numerical Modeling and Capacity Design of Earthquake-Resistant Reinforced Concrete Walls," Ph.D. Dissertation, Institute of Structural Engineering, Swiss Federal Institute of Technology, Zurich, August 1993.

Iliya, R. and Bertero, V. V., "Effects of Amount and Arrangement of Wall Panel Reinforcement on Hysteretic Behavior of Reinforced Concrete Walls," Report No. EERC- 84/04, Earthquake Engineering Research Center, University of California, Berkeley, February 1980

MacLeod, I., A., "Lateral Stiffness of Shear Walls with Openings in Tall Buildings", Symposium in Tall Buildings, Pergamon Press, Oxford, 1967, pp. 223-244.

Mander, J. B.; Priestley, M. J. N.; and Park, R. "Theoretical Stress-Strain Model for Confined Concrete." *Journal of Structural Engineering* 114 August 1988, pp. 1804-26.

Marcakis, K. and Mitchell, D., "Precast Concrete Connections with Embedded Steel Members," Prestressed Concrete Institute Journal, PCI, Vol. 25, No.4, July-August 1980, pp. 88-116

Mattock, A. H. and Gaafar, G.H., "Strength of Embedded Steel Sections as Brackets," ACI Journal, Vol. 79, No. 2, March-April 1982, pp. 83-93

Milford, R.V., "Nonlinear Behavior of Reinforced Concrete Cooling towers," Ph.D. Dissertations, Department of Civil Engineering, University of Illinois at Urbana-Champaign, Urbana, Illinois, 1984.

Morgan, B., Hiraishi, H. and Corley, W. G., "Medium Scale Wall Assemblies: Comparison of Analysis and Results," Publication SP-84, American Concrete Institute, Detroit, 1985, pp. 241-269

Oesterle, R. G., Aristizabal-Ochoa J. D., Sihu K, N. and Corley W. G., "Web Crushing of Reinforced Concrete Structural Walls", ACI Structural Journal, Vol. 81, No. 3, 1984, pp. 231-241

Oesterle, R. G. and Fiorato, A. E., "Seismic Design of Reinforced Concrete Walls," 8th World Conference on Earthquake Engineering," San Francisco, 1984, pp. 515-552

Oesterle, R. G., Fiorato, A. E. and Corley, W. G., "Design of Earthquake Resistant Structural Walls," Proceedings of the Fourth Canadian Conference on Earthquake Engineering, Vancouver, Canada, June 1983, pp. 81-91

Oesterle, R. G., Fiorato, A. E., Johal, L. S., Carpenter, J. E., Russell, H. G., and Corley, W. G. (1976), "*Earthquake Resistant Structural Walls-Tests of Isolated Walls"*, Report No. NSF/RA-760815, Construction Technology Laboratories, Portland Cement Association, Skokie, Illinois.

Oesterle, R. G., Aristizabal-Ochoa, J. D., Fiorato, A. E., Russell, H. G., and Corley, W. G. (1979), "*Earthquake Resistant Structural Walls-Tests of Isolated Walls-Phase II"*, Report No. NSF/RA-790275, Construction Technology Laboratories, Portland Cement Association, Skokie, Illinois.

Okamoto, S., Nakata, S., Kitagawa, Y., Yoshimura, M. and Kaminosono, T. " A Progress Report on the Full Scale Seismic Experiment of a Seven-Story Reonforced Concrete Building- Part of the US-Japan Cooperative Program" B.R.I Research Paper No. 94, Building Research Institute, Ministry of Constructio, Japan, March 1985

Pantazopoulou, S. J. and French C.W. (2001), "Slab participation in Practical Earthquake Design of Reinforced Concrete Frames" *ACI Structural Journal*, V.98, No. 7: 479-489, July-Augest 2001.

Pantazopoulou, S. J. and Moehle J.P. (1990), “Identification of effect of Slabs on Flexural Behavior of Beams” *Journal of Structural Engineering*, ASCE, V.116, No. 1, pp. 91-104, January 1990.

Paulay, T. and Priestley, M. J. N. (1992), Seismic Design of Reinforced Concrete and Masonry Buildings, New York: John Wiley & Sons, Inc., 1992.

PCI Design Handbook-Precast and Prestressed Concrete, Prestressed concrete institute, Chicago, 1985

Pilakoutas, K., “Earthquake Resistant Design of Reinforced Concrete Walls,” PhD Dissertation, University of London, 1990

Popovics, S. (1973), "A Numerical Approach to the Complete Stress-Strain Curve for Concrete," *Cement and Concrete Research*, 3(5), pp. 583-599.

Popovics, S. (1970), "A State-of-the-Art Report: A Review of Stress-Strain Relationship for Concrete”, journal of the American Concrete Institute, Vol. 67, March 1970, pp. 243-248.

Qi, X., and Pantazopoulou, S. J. (1991), “Response of RC Frames under Lateral Loads,” *Journal of Structural Engineering*, ASCE, V.117, No. 4, pp. 1167-1188.

Rashid, Y. R., “Analysis of Prestressed Concrete Vessels,” Nuclear Engineering and Design, Vol. 7, No. 4, April 1968, pp. 334-344

Raths, C. H., “Embedded Structural Steel Connections,” “Journal of Pre-Stressed Concrete Institute,” Vol. 19, No. 3, May-June 1974, pp. 104-112

Reisner, E. (1964), "Analysis of Shear Lag in Box Beams by Principle of Minimum Potential Energy," *Quarterly Journal of Mechanics and Applied Mathematics*, Vol. 4, No. 3, pp. 268-278.

Rosman, R., “Approximate Analysis of Shear Walls Subject to Lateral Loads”, American Concrete Institute Journal, Vol. 61, N0. 6, 1964, pp. 717-732

Scanlon, A. and Murray, D.W., “Time Dependent Reinforced Concrete Slab Deflections,” Journal of the Structural Division, ASCE, Vol. 100, No. St4, September 1974, pp. 1911-1924

Schade, H. H. (1951), “The Effective Width of Stiffened Plating Under Bending Loads", Vol. 59, *Society of Naval Architects and Marine Engineers*.

Schwaighofer, J., “Analysis of Shear Wall Structures Using Standard Computer Programs,” ACI Proceedings, Vol. 66, No. 12, 1969

Sechler, E. E. (1952), “*Elasticity in Engineering*, California Institute of Technology”, Pasadena, California.

Shahrooz, B. M., Remmetter, M. and Qin, F. “Seismic Design and Performance of Composite Coupled Walls,” Journal of Structural Engineering, Vol. 119, No. 11, 1993, pp. 3291-3309

Shahrooz, B. M., and Pantazopoulou, S. J. (1992), “Modeling Slab Contribution in Frame Connections,” *Journal of Structural Engineering*, ASCE, V.118, No. 9, pp. 2475-2492.

Sheikh, T. M., Deierlin, G. G., Yura, J. A. and Jirsa, J. O., “Beam-Column Moment Connections for Composite Frames Part I and Part II,” ASCE, Journal of Structural Division, Vol. 115, No. 11, 1989, pp. 2858-2896

Shome, N., Cornell, C. A., Bazzurro, P. and Carballo, J. E. (1997). “Earthquakes, Records, and Nonlinear Responses”. *Earthquake Spectra*, Vol. 14, No. 3, pp. 469-500

Sinha, B.P., Gerslte, K.H. and Tulin, L.G., “Stress-Strain Relations for Concrete Under Cyclic Loading”, Journal of the American Concrete Institute, Vol. 61, No. 2, February, 1964, pp. 195-211

Sittipunt, C. and Wood, S.L. (1995), "Influence of Web Reinforcement on the Cyclic- Response of Structural Walls," ACI Structural Journal, V. 92, No. 6, pp-745-756

Stevens, N.J., Uzumeri, S.M. and Collins, M.P., "Analytical Modeling of Reinforced Concrete Subjected to Monotonic and Reversed Loading", Publication No. 87-1, Department of Civil Engineering, University of Toronto, Toronto, Canada, January, 1987.

Task Committee on Finite Element Analysis of Reinforced Concrete Structures, 'State of the Art Report on Finite Element Analysis of Reinforced Concrete," American Society of Civil Engineering, New York, N.Y., 1982, pp. 545.

Thorenfeldt, E.; Tomaszewicz, A.; and Jensen, J. J. (1987). "Mechanical Properties of High Strength Concrete and Application in Design." *Proceedings of the Symposium "Utilization of High Strength Concrete,"* Stavanger, Norway, June 1987, Tapir, Trondheim, pp. 149-59.

Timoshenko, S. P. and Goodier, J. N. (1970), "*Theory of Elasticity"*, 3rd Edition, McGraw-Hill, New York.

Trifunac, M. D., and Brady, A.G., "A Study of the Duration of Strong Earthquake Ground Motion, " Bulletin of Seismological Society of America, Vol. 65, 1975

UBC (1994), "*Uniform Building Code"*, International Conference of Building Officials, Whittier, California, USA, 1994.

U.S.-Japan Planning Group (1992), "Recommendations for U.S.-Japan Cooperative Research Program, Phase 5-Composite and Hybrid Structures." Report UMCEE 92-29, University of Michigan, Ann Arbor, Michigan.

Vecchio, F.J. and Collins, M.P., "The Modified Compression Field Theory for Reinforced Concrete Elements Subjected to Shear," Journal of American Concrete Institute, Vol. 83, March-April 1986, pp. 219-121.

Vecchio, F.J. and Collins, M.P., "Response of Reinforced Concrete to Inplane Shear and Normal Stresses," Publication No. 82-03, Department of Civil Engineering, University of Toronto, March 1982.

Vulcano, A., Bertero, V. V. and Colotti, V., "Analysis Models for Predicting the Lateral Response for RC Shear Walls," Report No. UCB/EERC-88/17, Earthquake Engineering Research Center, University of California, Berkeley, 1987

Wallace, J. W. (1996), "Evaluating of UBC-1994 Provisions for seismic Design of RC Structural Walls", *Earthquake Spectra*, Vol. 12(2), pp. 327-347.

Wang, T. T., Betero, V. V. and Popov, E., P., "Hysteretic Behavior of Reinforced Concrete Framed Walls", Report No. EERC 75-23, Earthquake Engineering Research Center, University of California, Berkeley, December 1975

Yamanouchi, H., Izaki, Y. and Nishiyama, I., "Seismic Behavior of Joint Panels in Mixed Systems," The 13rd Congress of the International Association for Bridge and Structural Engineering (IABSE), Helsinki, June, 1988